Thèse n° 9492

Miniature and Minimalistic Neutron Detectors for Online High-Resolution Experiments in the Zero-Power Reactor CROCUS

Présentée le 5 septembre 2022

Faculté des sciences de base
Laboratoire de physique des réacteurs et de comportement des systèmes
Programme doctoral en energie

pour l'obtention du grade de Docteur ès Sciences

par

Fanny VITULLO

Acceptée sur proposition du jury

Prof. C. Ludwig, président du jury
Prof. A. Pautz, Dr V. Lamirand, directeurs de thèse
Prof. T. Downar, rapporteur
Dr P. Schillebeeckx, rapporteur
Prof. C. G. Theiler, rapporteur

École
polytechnique
fédérale
de Lausanne

2022

Acknowledgments

The journey that has led me to the submission of this Ph.D. thesis has been anything than straightforward. In the last two years, the worldwide COVID-19 pandemic has challenged in many ways everyone's, and in particular mine, life and work. If I am here today presenting this thesis, a great deal of hardworking, dedication and perseverance was necessary, but it would have never been possible without the support from my supervisors, colleagues, family, and friends.

My deepest gratitude goes to Prof. Andreas Pautz for giving me the opportunity to work on this doctoral project. You have always believed in me since the beginning of my studies in the Joint Nuclear Engineering Master at EPFL, ETH, and PSI. I would like to thank you for your continuous support and guidance during these years.

A special thank goes to my supervisor Dr. Vincent Lamirand. Your knowledge, guidance, wisdom, and patience have been invaluable during this journey. I will always be grateful to you for having taught me how to grow professionally and personally on every occasion. During the pandemic, you have been for months the only person I was seeing when none else was allowed on campus, and I am proud to say that we have done a remarkable job at not getting infected at work.

The LRS experimental team has played an irreplaceable role in carrying out this work. My gratitude goes to Dr. Pavel Frajtag for his immense support in the reactor operations and in allowing me to become a licensed operator of CROCUS; to Laurent Braun for his thoroughness in the development of the electronics needed for this work; to Daniel Godat for his promptness in producing, reviewing and supporting all my crazy designs for the mechanical pieces needed for the experiments presented in this work. A special mention goes to the mechanical atelier of the EPFL physics section for producing promptly the huge amount of mechanical pieces of SAFFRON.

I would also like to thank the rest of the LRS team. Dr. Mathieu Hursin and Dr. Carlo Fiorina, you have been great inspirational models for my career. Alessandro Scolaro, Stefan Radman, and Edoardo Brunetto, you are formidable colleagues and, most of all, special friends outside the office. Daniel Siefman, Oskari Pakari, Tom Mager, Thomas Ligonnet, and Klemen Ambrozic, thank you for your precious help and for the great time we had together.

This work would not have been possible without the contribution of the Paul Scherrer Institut (PSI). My gratitude goes to the LTP and LRT teams. In particular, to Dr. Jean-Baptiste Mosset for his incredible research and for the support given me every time I needed it. Also, many thanks to Dr. Gregory Perret and Alexander Wolfertz for the continuous sharing of information and equipment.

Although these last weeks might have proven me the contrary, life is not only work, and my life would not be the same without all the people that I love and admire. I would like to start with my friends in Milan, who have always been my safe place and source of joy whenever I needed them

during this journey. In particular, my friend Pier, who is my rock in the happiest and saddest moments. To my hometown and lifetime friends: even if we don't live each other on a daily basis, every summer, Christmas, and Easter (ah no, Easter has become optional lately) with you is an adventure, as if no day had passed since high school. Marianna and Emeline, we always struggle to find time to see each other, but when we do, it is always a blast.

Last but not least, I am eternally grateful to my parents and family for their unconditioned love, support, and dedication. In spite of the distance, you always had, have, and will have a special place in my heart.

Lausanne, 14 June 2022

Abstract

The continuous strive for more efficient and reliable nuclear power plants is leading to increasing complexity in the design and operations of reactors. As a consequence, comprehensive analyses are required to assess the reactor's safety during normal and accidental conditions. Validated simulation tools with high-fidelity capabilities, i.e., at the pin or sub-pin scale, are necessary to predict local neutronics effects in the core. However, the scarcity of high-resolution in-core experimental data imposes limitations to the validation of such high-fidelity pin-resolved neutronics codes. The challenges in performing online high-resolution in-core experiments are numerous: from the accessibility of in-core locations to the availability of neutron detection technologies with adequate dimensions and online capabilities. In the present thesis, the development of a novel miniature and minimalistic (MiMi) neutron detection technology is presented, allowing unprecedented spatial resolution for the online study of the neutron flux in zero-power research reactors. The MiMi neutron detectors are tested in the EPFL zero-power reactor CROCUS and used to build a data set of high-resolution neutronics experiments in CROCUS, including measurements of local gradients and directionality of neutron flux, and the local impact of a fuel rod displacement. As the next level of development, a three-dimensional (3D) full-core mapping system named SAFFRON, consisting of 149 MiMi neutron detectors distributed in-core, is designed and installed in CROCUS. Static thermal neutron flux maps are measured in absolute terms and between different core configurations, e.g., water level vs. control rod operation at criticality. The obtained results open up the investigation of a variety of space-dependent neutronics phenomena in CROCUS.

Keywords

High-resolution neutronics, in-core neutron detection, miniature scintillators, high-fidelity neutronics codes, zero-power reactor, CROCUS.

Résumé

La quête d'une production d'énergie nucléaire efficace, compétitive et soutenable entraîne une complexité croissante dans la conception et l'exploitation des réacteurs. En conséquence, des analyses toujours plus approfondies sont requises pour évaluer la sûreté et la fiabilité des réacteurs, dans des conditions d'opération normales et accidentelles. Dans cette perspective, des outils de simulation avec des capacités de haute-fidélité sont développés pour la prédiction des effets neutroniques locaux en cœur de réacteur, jusqu'à l'échelle du crayon ou inférieure. Cependant, la rareté des données expérimentales à haute résolution en cœur de réacteur limite la validation de ces codes neutroniques haute-fidélité résolus à l'échelle du crayon. La réalisation d'expériences en cœur à haute résolution pose de nombreux défis, de l'accessibilité des emplacements en cœur, à la disponibilité de technologies de détection de neutrons adéquates. Dans le présent manuscrit de thèse, une nouvelle technologie de détecteur de neutrons miniature et minimaliste (MiMi) pour les applications en réacteur à puissance nulle est présentée, permettant une résolution spatiale sans précédent pour l'étude du flux neutronique. Au cours de son développement, un ensemble de données expérimentales neutroniques à haute résolution est établi dans le réacteur à puissance nulle CROCUS de l'EPFL, de la mesure de gradients locaux et de la directionnalité du flux neutronique, à l'impact local du déplacement d'un barreau de combustible. Dans un développement ultérieur, un système de cartographie tridimensionnel (3D) appelé SAFFRON est conçu et installé dans CROCUS. Il est composé de 149 détecteurs de neutrons MiMi répartis dans le cœur du réacteur. Des cartes statiques de flux de neutrons thermiques sont mesurées en termes absolus et entre différentes configurations du cœur, par exemple entre états critiques obtenus par variation du niveau d'eau et par insertion d'une barre de contrôle. Les résultats de mesure ouvrent la voie à l'étude d'une variété de phénomènes neutroniques à dépendance spatiale.

Mots-clés

Neutronique haute-résolution, détection de neutrons en cœur de réacteur, scintillateurs miniatures, codes neutroniques haute-fidélité, réacteur à puissance nulle, CROCUS.

Contents

List of Figures

List of Tables

List of Abbreviations

3D	Three-dimensional
CAD	Computer-Aided Design and drafting
COLIBRI	CROCUS Oscillator for Lateral Increase Between U_{met} Rods and Inner zone
CRUD	Chalk River Unidentified Deposits (historical), or corrosion products
EPFL	École polytechnique fédérale de Lausanne
FPGA	Field-Programmable Gate Array
KUCA	Kyoto University Critical Assembly
LRS	Laboratory for Reactor Physics and Systems Behaviour
LTP	Laboratory for Particle Physics
LWR	Light Water Reactor
M&S	Modeling and Simulation
MCA/MCB	Multichannel analyzer/multichannel buffer
MiMi	Miniature and Minimalistic neutron detectors
MSD	Moving Sum after Differentiation
NPP	Nuclear Power Plant
PCB	Printed Circuit Board
POM-C	Polyoxymethylene-Copolymer
PSI	Paul Scherrer Institut
Pu-Be	Plutonium-beryllium neutron source
SAFFRON	Scintillator Array with optical Fibers For high-Resolution Online Neutron counting
SCA	Single Channel Analyzer
SiPM	Silicon Photomultiplier
TRAX	Translateur Radial Axial (in French)
V&V	Verification and Validation
WLS	Wavelength Shifting Fibers

Chapter 1

Introduction

In a world with limited resources and increasing electricity demand, optimizing the performance of nuclear power plants (NPPs) while improving their safety and reliability has become the primary focus of the nuclear industry. The continuous strive for a more efficient, competitive, and sustainable power generation is driving power uprates [1], fuel utilization enhancements, higher burnup levels [2], and lifetime extensions [3] for the current fleet of operating light water reactors (LWRs). At the same time, optimized reactor concepts are under development for the next generation of NPPs [4]. In this process, particular attention is set on addressing a series of safety-related issues recently observed in the operating fleet of LWRs, e.g., CRUD deposition [5], fuel deformations [6], and fuel vibrations [7]. The increasing complexity in reactors' design and operation deriving from such optimization efforts and safety enhancements must be supported by comprehensive analyses to assess the safety and reliability of the reactor during normal and accidental conditions.

The prediction of the rate of interaction of neutrons with the different reactor materials is the backbone of reactor safety analyses. This prediction requires the knowledge of the materials' cross-sections and, more importantly, of the distribution of the neutron population in space, direction, energy, and time, which is commonly called a *neutron flux map.* As neutrons are responsible for propagating the chain reaction and producing energy through fission, the reactor power profile directly depends on the distribution of the neutron population. Related safety parameters such as the fuel temperature and integrity are intertwined with the power distribution and thus with the neutron flux map. In the same way, the evolution of the fuel composition is strictly connected to the level of exposure to neutrons and, in turn, it affects back the neutron flux distribution through feedback effects. Furthermore, the time evolution of the neutron population gives indications of the reactor state and stability. Therefore, the ultimate goal of reactor analyses is to determine the distribution and evolution of the neutron population in a nuclear reactor core, which is mathematically described by the solution of the *neutron transport* equation.

Since the early stages of the nuclear industry, integral experiments in general, and critical mock-up facilities in particular, have played an important role in understanding the physics of nuclear reactors [8],[9]. However, due to the large costs involved with building nuclear test facilities and performing experiments, it has become common practice to predict the neutron flux map and its evolution in

NPPs by solving the neutron transport equation with dedicated computer codes. Such codes, also known as *neutronics codes*, are classified into *deterministic* or *stochastic (Monte Carlo)*.

As of today, Monte Carlo codes (see Section 2.2.2) represent the state-of-the-art of computer codes for steady-state neutronics simulations. Their stochastic approach allows simulating with high resolution and fidelity the whole range of neutron interactions happening in a reactor core without solving the neutron transport equation analytically and without significant geometry approximations. Despite the high-fidelity capabilities, their required computational power is burdensome for their routine use in operating NPPs and becomes massive for time-dependent simulations. Instead, deterministic methods (see Section 2.2.1) have been widely employed by the industry and by regulators to solve – in a time-effective manner – the neutron transport equation with numerical methods and different levels of discretization and approximation. Standard deterministic codes used for full-core LWRs calculations produce flux and power maps within homogenized fuel assembly volumes, and then the pin-by-pin power levels are reconstructed with dedicated techniques. Neutron kinetics simulations instead are often performed following the *point-kinetic* model for which the neutron flux distribution is assumed fixed in space and only the amplitude, or power-level, changes.

More recently, the exponential growth of computing power is driving refinements of the spatial discretization in the numerical solution of the neutron transport equation by deterministic methods for both steady-state and kinetics simulations. As of today, three-dimensional (3D) full-core time-dependent methods with pin-resolved details are becoming more and more prominent in the field of neutronics simulations. Such *high-fidelity deterministic neutronics codes* have the capability to predict the steady-state neutron flux map directly at the pin or sub-pin scale and to simulate space-dependent neutron kinetics. Their capability to simulate local neutronics effects, whether embedded within advanced high-fidelity multi-physics modeling and simulation (M&S) tools or not, could pave the way for the improvement of the more conservative reactor operational safety margins set in the past. At the same time, developing codes with a higher spatial resolution promotes the inclusion of complex elements in reactor designs to optimize power plant performance and improve safety. An example is the diffusion of heterogeneous fuel assemblies in LWRs to achieve better axial and within-assembly power profiles while reducing dryout margins with spacers [10].

Neutronics code must undergo a *verification* and *validation* (V&V) process before being used to perform safety assessments for operating or future reactors. Verification aims at checking if the code is robust and reliable and if the underpinning models are solved correctly. For neutronics simulations, verification procedures consist of code-to-code comparisons. In particular, the results of a deterministic code are compared against the equivalent results obtained with another deterministic code or a Monte Carlo code. On the other hand, the validation step is of the uttermost importance because it ensures that the code fulfills its intended purpose and represents the reality of a physical phenomenon. The validation of neutronics codes requires the comparison of the code results against adequate experimental data (accompanied by their uncertainty) measured in reference critical or subcritical facilities. Therefore, *high-resolution neutronics measurements* within reference reactor cores are of essence for the validation of high-fidelity neutronics codes aiming at resolving local and space-dependent phenomena in nuclear reactors.

However, the availability of high-resolution in-core – i.e., *inter-pin* and *intra-pin* – neutronics measurements is limited. In the vast majority of commercial LWRs, the instrumentation in place to detect neutrons is narrowed down to the essential for monitoring purposes and often consists of detectors placed in ex-core positions, i.e., outside the fuel lattice. On the other hand, in-core experimental data from heavily instrumented LWRs are often proprietary and hardly available to the scientific community. The accessibility to locations of interest, e.g., within the fuel lattice and inside fuel pins, remains the main limitation for localized measurements in operating NPPs. With these premises, *zero-power research reactors* play a crucial role in producing high-quality in-core validation data. Indeed, the availability and flexibility in the operation of research reactors open the possibility of investigating neutronics effects at a local scale with inter-pin and intra-pin measurements and of observing space-dependent phenomena with *3D mapping* measurements. In addition, in zero-power reactors, the limited temperature and burnup feedbacks allow measuring "pure" neutronics effects. The comparison of such results with Monte Carlo simulations can provide feedback for the evaluation of the underlying nuclear data.

Nevertheless, the experimental observation of neutronics phenomena at a fine spatial scale is a non-trivial task even in research reactors. Considering the limited space available in inter-pin and intra-pin positions and the spatial scale of the phenomena of interest, i.e., in the mm range, the need for neutron counting techniques on small active volumes is essential. Neutron activation methods are a valid option if the time evolution of the neutron population is not required and the achievable uncertainty is sufficient. Otherwise, *online miniature neutron detectors* with an active volume of a few cubic millimeters are needed to resolve neutronics effects at the pin or sub-pin level, i.e., the cm range. While the perturbation to the neutron flux map induced by such detectors must be minimal, their miniature dimensions must not translate into a reduced sensitivity. At the same time, the detector design must be flexible and versatile to accommodate the experimental needs. If spatial-dependent phenomena are to be investigated, the detector parallelization and the construction of detector arrays must be possible at an affordable cost. Most of the conventional measuring instruments in research reactors, including miniature fission chambers, do not satisfy the totality of these requirements.

In this context, advanced miniature and minimalistic (MiMi) neutron detectors for online in-core thermal neutron counting are developed at the Laboratory for Reactor Physics and Systems Behaviour (LRS) at the École polytechnique fédérale de Lausanne (EPFL), Lausanne, Switzerland. With an active volume smaller than one mm^3, these detectors enable a wide range of high-resolution neutronics measurements in low-flux reference research reactors like CROCUS, the zero-power reactor operated by LRS on the EPFL campus. Local neutron flux gradients, flux directionality dependences, and effects of the fuel pitch variations are experimentally investigated in CROCUS with the MiMi neutron detectors. The peculiar simplicity and versatility of the detector design allow to multiply the number of available detector units and build a three-dimensional (3D) full-core mapping system in the CROCUS reactor, called SAFFRON (Scintillator Array with optical Fibers For high-Resolution Online Neutron counting). SAFFRON allows measuring detailed neutron flux maps and opens to the investigation of spatial-dependent neutronics phenomena with kinetics, modulation, and noise experiments. In this work, the experimental data are compared with the results of Monte Carlo simulations, as they represent the state-of-the-art of high-fidelity simulations. Nonetheless, the experimental data presented in this thesis provide valuable points for the future

validation of high-fidelity deterministic neutronics codes in general, and in particular for the validation of the high-fidelity model of CROCUS under development at LRS [11].

1.1 Aim of the thesis

The main goal of this thesis is to develop miniature neutron detectors to perform high-resolution neutronics experiments in the reference zero-power reactor CROCUS with the intent to provide validation points for high-fidelity neutronics codes. In more detail, the goals of the current work can be summarized as follows:

- **Develop a miniature neutron detector based on the ZnS(Ag):^{6}LiF scintillator technology for in-core reactor applications:** build a detector with miniature dimensions fitting the available in-core positions in CROCUS, with minimal and localized flux perturbations, online capabilities, and potential parallelization. Test the detector behavior in mixed neutron/gamma fields by characterizing the thermal neutron sensitivity and the insensitivity to gamma radiation;

- **Apply the ZnS(Ag):^{6}LiF-based miniature detector for online high-resolution in-core neutronics measurements:** investigate the detector's capability to resolve mm-wise in-core neutronics phenomena. Create a dataset of high-resolution in-core experiments in CROCUS, available for the validation of the high-fidelity model of CROCUS currently under development and the future validation of high-resolution neutronics codes;

- **Develop a three-dimensional (3D) full-core mapping system in CROCUS**: build a system consisting of a large number of miniature neutron detectors distributed in the inter-pin spaces of CROCUS for measuring neutron flux maps. Open up new experimental prospects in the investigation of space-dependent reactor physics phenomena, including neutron kinetics, modulation, and noise experiments.

1.2 Thesis Outline

The present thesis is structured into seven chapters. After the introductory chapter, Chapter 2 presents the fundamental concepts of reactor physics and neutron detection and reviews the computational and experimental tools available to resolve localized in-core neutronics effects. Chapter 3 introduces the design, instrumentation, and experimental features of the CROCUS zero-power research reactor. The thesis objectives are addressed in the following three chapters. First, the development of miniature and minimalistic (MiMi) neutron detectors is presented in Chapter 4, from the first prototype to the final version, along with the testing in different irradiation conditions. A series of online high-resolution in-core experiments performed in CROCUS with the MiMi neutron detectors are presented in Chapter 5, accompanied by the comparison of their results against the results of Monte Carlo simulations. Chapter 6 presents the development of the 3D full-core mapping system installed in CROCUS, called SAFFRON, and the obtained first experimental results for absolute and relative neutron flux maps. The conclusions and outlook for this thesis are outlined in Chapter 7.

Chapter 2

High-resolution reactor physics: a short review

The primary objective of this chapter is to provide the reader with an overview of the computational and experimental tools used to investigate the local behavior of neutrons in a nuclear reactor core. Throughout the chapter, the basic principles of both reactor physics and thermal neutron detection are introduced with the intent to ease the understanding of the state-of-the-art techniques in reactor physics simulations and experiments.

In the first Section 2.1, the behavior of neutrons in a nuclear reactor is discussed and formulated mathematically. Section 2.2 presents the computational methods currently available to predict the neutron flux map in a reactor core, followed in Section 2.3 by a review of the high-resolution neutronics codes available as of today. Afterward, a description of the experimental techniques suitable to detect and count thermal neutrons is presented in Section 2.4, focusing on the use of scintillators for neutron detection. Section 2.5 introduces the challenges faced in detecting thermal neutrons in a reactor environment. Finally, a review of previous experiences in performing highly localized in-core thermal neutron measurements is reported in Section 2.6.

2.1 Neutron physics in nuclear reactors

2.1.1 Neutron interactions

Neutrons are subatomic particles with a neutral charge and a mass marginally higher than protons. Because of their neutrality, they are not subject to Coulomb forces with electrons and nuclei of the surrounding matter. However, neutrons can interact with other nuclei via nuclear reactions. Neutrons can change energy and direction of travel after a *scattering* reaction (elastic or inelastic), or they can be captured and replaced by one or more secondary radiations following an *absorption* reaction [12]. Absorption can result in the production of gamma rays via (n, γ) radiative capture reactions, more neutrons with (n, xn) reactions, charged particles via (n, α) and (n, p), or a multitude of different radiations is released by (n, fission) reactions. A visual summary of the neutron-induced reaction is presented in Figure 2.1.

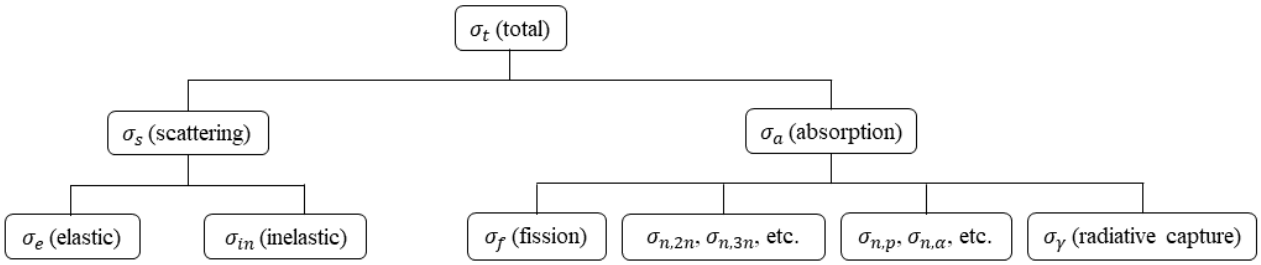

Figure 2.1 – Hierarchy of neutron interactions. Inspired by [13].

A probability of interaction, called *microscopic cross-section* σ (units in barns, i.e., 10^{-24} cm^2), can be defined for each neutron-induced nuclear reaction. The microscopic cross-section is strongly dependent on the energy of the incident neutrons. Neutrons may be divided into two main categories according to their traveling energy: *slow* ($E < 0.5\ eV$) and *fast* ($E > 0.5\ eV$) [12]. In addition, *thermal* neutrons can be identified as slow neutrons at thermal equilibrium with the medium at room temperature around the average energy of 0.025 eV, i.e., the average energy of a Maxwellian neutron spectrum.

Depending on the domain, some neutron-induced interactions become more important than others. For instance, reactions resulting in the neutron disappearance are of interest for shielding applications, while the transformation into charged particles is essential to detect and count neutrons (see Section 2.4). Similarly, the energy generation in a nuclear reactor is strictly intertwined with the occurrence of fission reactions.

2.1.2 Fission and reactor criticality

Fission reactions can be induced by neutrons of any energy, depending on the fissile material and on its corresponding microscopic cross-section. The attention of this thesis is set on systems employing thermal neutrons to induce fission events. Indeed, light water reactors (LWRs), representing the majority of the reactors currently operating in the world, operate in the thermal energy range.

In a typical LWR core, fissile nuclides like ^{235}U undergo a *fission* reaction after interacting with a thermal neutron. As a result of the reaction, the fissile element is split into two or very rarely three daughter nuclei, called *fission products (FP)*, releasing at the same time more than one neutron, gammas, betas, neutrinos, and energy, as shown in Figure 2.2. The average number of neutrons emitted in the fission process, called ν, depends on the fissioning nuclide and on the energy of the incident neutron [14]. For ^{235}U thermal fission, ν is around 2.4. The neutrons released by fission, called also *prompt* neutrons, are born in the fast energy range and thus start to scatter around on light nuclei, i.e. hydrogen in water for LWRs. The energy loss process from fast to thermal energy is called neutron *moderation*. During this procedure, neutrons stream from one collision point to another, with a certain probability of escaping the system. Once thermal, neutrons might get absorbed by other nuclei. The neutron absorption can result in a capture reaction or in a successive fission, propagating the so-called *fission chain reaction*.

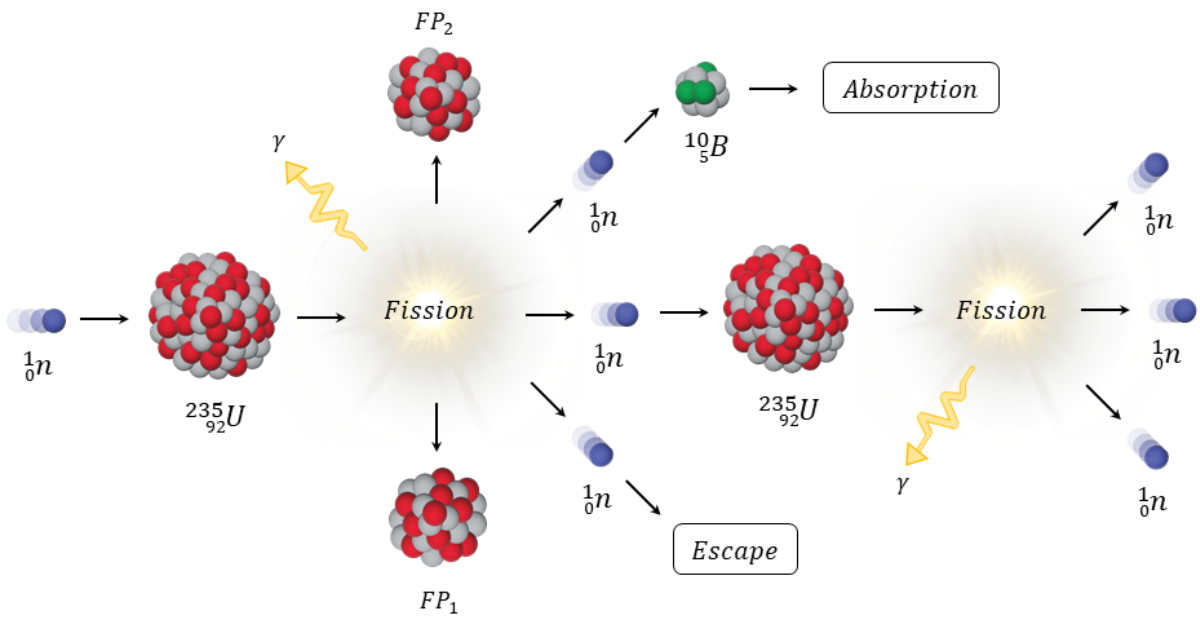

Figure 2.2 – Illustration of the fission chain reaction in a typical LWR reactor core.

By definition, a nuclear reactor is a system designed to sustain a stable fission chain reaction by balancing the production and loss of neutrons. If one defines the *effective multiplication factor* k_{eff} as the ratio between the number of neutrons in two successive generations, a nuclear reactor is said:

- *Critical* ($k_{eff} = 1$) if the neutron population is constant in time and the fission chain is stable;
- *Subcritical* ($k_{eff} < 1$) if the neutron population decreases and the fission chain dies out;
- *Supercritical* ($k_{eff} > 1$) if the neutron population increases and the fission chain diverges.

2.1.3 Basic quantities in reactor physics

Knowledgeable of the physics behind the fission chain reaction, it is immediate that keeping track and predicting the behavior of the neutron population is essential to ensure a safe and reliable operation of a nuclear reactor.

The core neutron population can be described by the angular neutron density $n(\boldsymbol{r}, \boldsymbol{\Omega}, E, t)$ so that $n(\boldsymbol{r}, \boldsymbol{\Omega}, E, t) dV d\Omega dE$ is the number of neutrons present in the infinitesimally small volume dV about $\boldsymbol{r}$ (shown in Figure 2.3), with energy dE about E, moving in direction $\boldsymbol{\Omega}$ in the solid angle $d\Omega$. The product between $n(\boldsymbol{r}, \boldsymbol{\Omega}, E, t)$ and the neutron speed v is called *angular neutron flux*

$$\psi(\boldsymbol{r}, \boldsymbol{\Omega}, E, t) = v \cdot n(\boldsymbol{r}, \boldsymbol{\Omega}, E, t). \tag{2.1}$$

$\psi(\boldsymbol{r}, \boldsymbol{\Omega}, E, t)$ represents the neutron distribution in space $\boldsymbol{r}$ (three dimensional), angle $\boldsymbol{\Omega}$ (two dimensional), energy E, and time t in a reactor core. The prediction of the angular neutron flux ψ is the main objective of reactor analyses and is made by solving the *neutron transport* problem, formulated in the next section.

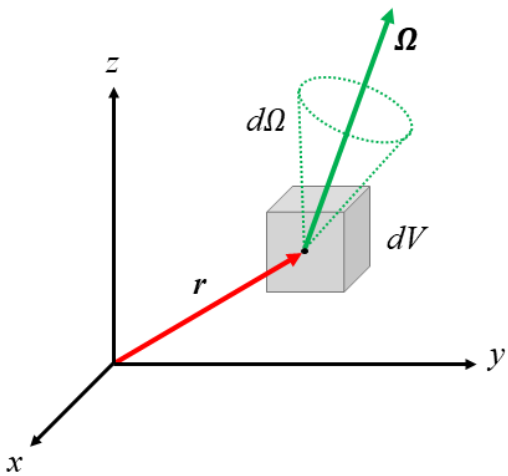

Figure 2.3 – Spatial and angular coordinates of the linear Boltzmann equation for a volume dV at position $\boldsymbol{r}$ and within the angular cone $d\Omega$ at $\boldsymbol{\Omega}$.

Another important quantity in reactor physics is the *scalar neutron flux* (in units of $\mathrm{cm}^{-2}\cdot\mathrm{s}^{-1}$), obtained by integrating the angular neutron flux over the entire solid angle

$$\phi(\boldsymbol{r},E,t) = \int_{4\pi} \psi(\boldsymbol{r},\boldsymbol{\Omega},E,t)d\Omega. \tag{2.2}$$

The *reaction rate* $RR_x(r,E,t)$ for any neutron-induced reaction is given in $\mathrm{cm}^{-3}\cdot\mathrm{s}^{-1}$ by

$$RR_x(\boldsymbol{r},E,t) = \Sigma_x(\boldsymbol{r},E,t)\cdot\phi(\boldsymbol{r},E,t) = \mathrm{N}(\boldsymbol{r},t)\cdot\sigma_x(E)\cdot\phi(\boldsymbol{r},E,t), \tag{2.3}$$

where Σ_x is the macroscopic cross-section, and N is the material density. The fission reaction rate RR_f is a particularly important quantity because its integral over energy is directly proportional to the generated reactor power.

2.1.4 Neutron transport theory

The complexity of neutrons' motion and interactions in a nuclear reactor core is mathematically described by the time-dependent Boltzmann neutron transport equation, also known as the *linear Boltzmann equation*, which is an integro-differential equation formulated with seven variables as

$$\begin{aligned}\frac{1}{v}\frac{\partial\psi}{\partial t}(\boldsymbol{r},\boldsymbol{\Omega},E,t) &= -\boldsymbol{\Omega}\cdot\nabla\psi(\boldsymbol{r},\boldsymbol{\Omega},E,t) - \Sigma_t(\boldsymbol{r},E,t)\psi(\boldsymbol{r},\boldsymbol{\Omega},E,t)\\ &+ \int_0^\infty dE' \int_{4\pi} \Sigma_s(\boldsymbol{r},\boldsymbol{\Omega}'\cdot\boldsymbol{\Omega},E'\to E,t)\psi(\boldsymbol{r},\boldsymbol{\Omega}',E',t)d\Omega'\\ &+ \frac{\chi_p(E)}{4\pi}\int_0^\infty dE' \int_{4\pi} [1-\beta]\nu\Sigma_f(\boldsymbol{r},E',t)\psi(\boldsymbol{r},\boldsymbol{\Omega}',E',t)d\Omega'\\ &+ \frac{1}{4\pi}\sum_{i=1}^{6}\chi_{d,i}(E)\lambda_i C_i(\boldsymbol{r},t) + Q_{ext}(\boldsymbol{r},\boldsymbol{\Omega},E,t).\end{aligned} \tag{2.4}$$

The time-variation of the angular neutron density $n(\boldsymbol{r}, \boldsymbol{\Omega}, E, t)$ is given by the left-hand side of Equation (2.4), while each term on the right-hand side represents a rate of loss or gain of neutrons in $dVd\Omega dE$ about $(\boldsymbol{r}, \boldsymbol{\Omega}, E)$ at time t due to a specific process. The first two terms are the rate of loss of neutrons due to leakages and interactions. The third term gives the rate of gain from internal scattering. The fourth term is the rate of gain due to prompt fission, while the fifth is due to delayed neutrons. The last term represents an external neutron source.

For time-dependent problems, the evolution of the group-wise delayed neutrons precursors density C_i must be solved together with neutron transport. Each equation has the form

$$\frac{\partial C_i}{\partial t}(\boldsymbol{r}, t) = \int_0^\infty dE' \int_{4\pi} \beta_i \nu \Sigma_f(\boldsymbol{r}, E', t)\psi(\boldsymbol{r}, \boldsymbol{\Omega}', E', t)d\Omega' - \lambda_i C_i(\boldsymbol{r}, t), \quad i = 1, \dots, N \tag{2.5}$$

where the rate of appearance of precursor C_i due to fission reactions is counteracted by its rate of disappearance due to decay.

In addition, the study of the fuel composition evolution due to burnup requires the additional solution of the depletion equation. Fuel burnup falls out of the scope of this thesis, but an extensive description of fuel depletion methods can be found in [14].

Because of the seven variables involved, an analytical solution of the linear Boltzmann equation can be found only in simplified cases, while it is impossible to obtain one for real complex systems as a full reactor core. Hence, approximation methods are needed to solve the transport problem. A common method applied since the early stage of nuclear to simplify the transport problem is the *diffusion approximation*.

2.1.5 The diffusion approximation

The transport problem can be simplified by reducing the angular dependency of the angular flux $\psi(\boldsymbol{r}, \boldsymbol{\Omega}, E, t)$ integrating the latter over the entire solid angle. This simplification yields the solution of the linear Boltzmann equation in terms of scalar neutron flux $\phi(\boldsymbol{r}, E, t)$. However, the integration over 4π introduces another variable in the system: the *neutron current density* $\boldsymbol{J}(\boldsymbol{r}, E, t)$. It indicates the net rate at which neutrons pass through a given surface with a given direction and given energy. Equation (2.4) becomes:

$$\begin{aligned}\frac{1}{v}\frac{\partial \phi}{\partial t}(\boldsymbol{r}, E, t) = & -\nabla \cdot \boldsymbol{J}(\boldsymbol{r}, E, t) - \Sigma_t(\boldsymbol{r}, E, t)\phi(\boldsymbol{r}, E, t) \\ & + \int_0^\infty \Sigma_s(\boldsymbol{r}, E' \to E, t)\phi(\boldsymbol{r}, E', t)dE' + Q_{fiss}(\boldsymbol{r}, E, t) + Q_{ext}(\boldsymbol{r}, E, t).\end{aligned} \tag{2.6}$$

A relation between $\phi(\boldsymbol{r}, E, t)$ and $\boldsymbol{J}(\boldsymbol{r}, E, t)$ can be introduced with the *Fick's law* under the assumption that all neutron sources are isotropic:

$$\boldsymbol{J}(\boldsymbol{r}, E, t) = -D(\boldsymbol{r}, E, t)\nabla\phi(\boldsymbol{r}, E, t), \tag{2.7}$$

where $D(\boldsymbol{r}, E, t)$ is the diffusion coefficient.

Fick's law can be included in Equation (2.6) so that the final time and energy-dependent *diffusion equation* has the form

$$\frac{1}{v}\frac{\partial\phi}{\partial t}(\boldsymbol{r},E,t) = \nabla\cdot D(\boldsymbol{r},E,t)\nabla\phi(\boldsymbol{r},E,t) - \Sigma_t(\boldsymbol{r},E,t)\phi(\boldsymbol{r},E,t) + \int_0^\infty \Sigma_s(\boldsymbol{r},E'\to E,t)\phi(\boldsymbol{r},E',t)dE' + Q_{fiss}(\boldsymbol{r},E,t) + Q_{ext}(\boldsymbol{r},E,t). \tag{2.8}$$

The diffusion equation provides a description of the neutron population for problems satisfying a series of assumptions deriving from Fick's law and largely described in classic textbooks [14], [15]. For the purpose of this thesis, it is important to know that the diffusion approximation can be expected not to be accurate in heavily absorbing medium or in regions where there are large anisotropies of the angular flux or high leakages. Therefore, diffusion theory is inaccurate or invalid near vacuum or material boundaries, near strong absorbers, or close to localized neutron sources.

2.2 Computational neutron transport

Approximate solutions to the neutron transport problem can be found with the aid of computer codes, called *neutronics codes*. As of today, neutronics are divided into two macro-categories on the basis of the method applied to obtain an approximate solution: *deterministic* and *stochastic (*or *Monte Carlo)*.

2.2.1 Deterministic neutronics codes

Deterministic neutronics codes solve the linear Boltzmann equation numerically. Finding a numerical solution requires the discretization of the seven independent variables, turning Eq. (2.4) into an algebraic system of equations. The most common discretization methods used for space, angle, energy, and time are briefly described hereafter. A comprehensive explanation of the discretization methods mentioned hereafter can be found in the textbooks by Stacey [14] and Azmy and Sartori [16].

The energy dependence of the angular flux derives from the strong variation of the cross-section data with energy. The common approach for treating the angular flux energy dependence is the *multigroup approximation*. The energy range of interest is divided into a finite number of energy bins *G,* and Equation (2.4) becomes a system of *G* equations for the group flux $\psi_g(\boldsymbol{r},\boldsymbol{\Omega},t)$. The continuous-energy cross-sections are averaged over the energy group and remain constant. A trade-off between results accuracy and the computational cost must be considered in the choice of the number of the energy groups.

The angular dependence of the neutron flux is particularly important in regions with strong flux anisotropies, i.e., heterogenous volumes or strong absorbers. The angular variable $\boldsymbol{\Omega}$ can be discretized with discrete ordinates methods (S_N) or the method of characteristics (MOC), depending on the quadrature set. The result is a set of equations solving neutron transport in selected angular directions. Another option is to expand the angular dependence with spherical harmonics (P_N) or with the simplified spherical harmonics method (SP_N). It is important to remark that the diffusion equation described in Section 2.1.5, simplifying the angular dependence, can be derived from the lowest-order spherical harmonics expansion P_1.

The time variable of the transport equation can be split into timesteps and the time derivatives can be replaced by time differences with explicit or implicit methods, depending on the time scale of the problem to be studied. For steady-state problems, the time-dependence in Equation (2.4) can be eliminated.

The spatial discretization of the neutron transport problem requires the subdivision of the problem geometry with a mesh. In nuclear applications, mesh divisions range from coarse (at the assembly level) to fine (at the sub-pin level). In addition, the mesh type can be structured, mainly Cartesian, or unstructured to represent complex geometries. Depending on the chosen spatial mesh, different schemes can be adopted to discretize the spatial variable. The most common discretization schemes for neutron transport are linked to the angular treatment and are discrete ordinates (S_N) and method of characteristics (MOC). While the first one is straightforward mainly on Cartesian geometries, the second is efficient also with complicated geometries.

For a full three-dimensional (3D) reactor problem, a discretization of each of the seven variables of the linear Boltzmann equation on a 10^2 division would lead to a problem with 10^{14} unknowns [17]. Despite the recent increase in computing capabilities, solving a problem with such a large number of unknowns with computer codes is still extremely challenging, if not impossible. Therefore, computational methods aiming at simplifying the transport problem for full-core LWRs analyses have been developed since the 1950s.

2.2.1.1 Conventional methodology for full-core LWRs calculations

Nowadays, the conventional approach for standard neutronic analyses of full-core LWRs used by industry and regulators relies on a two-step calculation scheme based on the combined use of *lattice codes* and *nodal codes*, as shown in Figure 2.4. The main idea of this methodology is to simplify the geometrical heterogeneities and the spectral dependencies in the core.

Lattice codes solve the neutron transport problem in 2D slices representing axial portions of each fuel assembly in the reactor core. The calculations scheme consists of a series of steps solving the neutron transport at coarser scales, from pin-level to assembly level. At each step, the angular flux distribution in energy and space for the heterogeneous lattice cell is calculated with reflective boundary conditions. The flux distribution is then used to condensate and homogenize the cross-section in the cell in preparation for the successive step in a way that the average physical quantities at the fine level are preserved at the coarse level. The final output is a series of few-group homogenized neutronics data, including macroscopic cross-sections, assembly data, assembly-discontinuity factors, etc., suitable to be used in the successive full-core 3D calculation.

Nodal codes are computational tools used to couple neutron transport and thermal-hydraulics in steady-state and transient simulations [18]. The discussion of the thermal-hydraulic capabilities of such codes is out of the scope of this thesis. At the neutronics level, the core is divided into a coarse mesh of homogenized volumes with a radial dimension corresponding to a fuel assembly and an axial spacing of typically 10 to 20 cm. Such volumes are called nodes, and to each of them corresponds an output of the lattice codes. In most applications, the two-group version of the neutron diffusion equation is solved on this nodal structure to calculate the 3D nodal flux and power distribution.

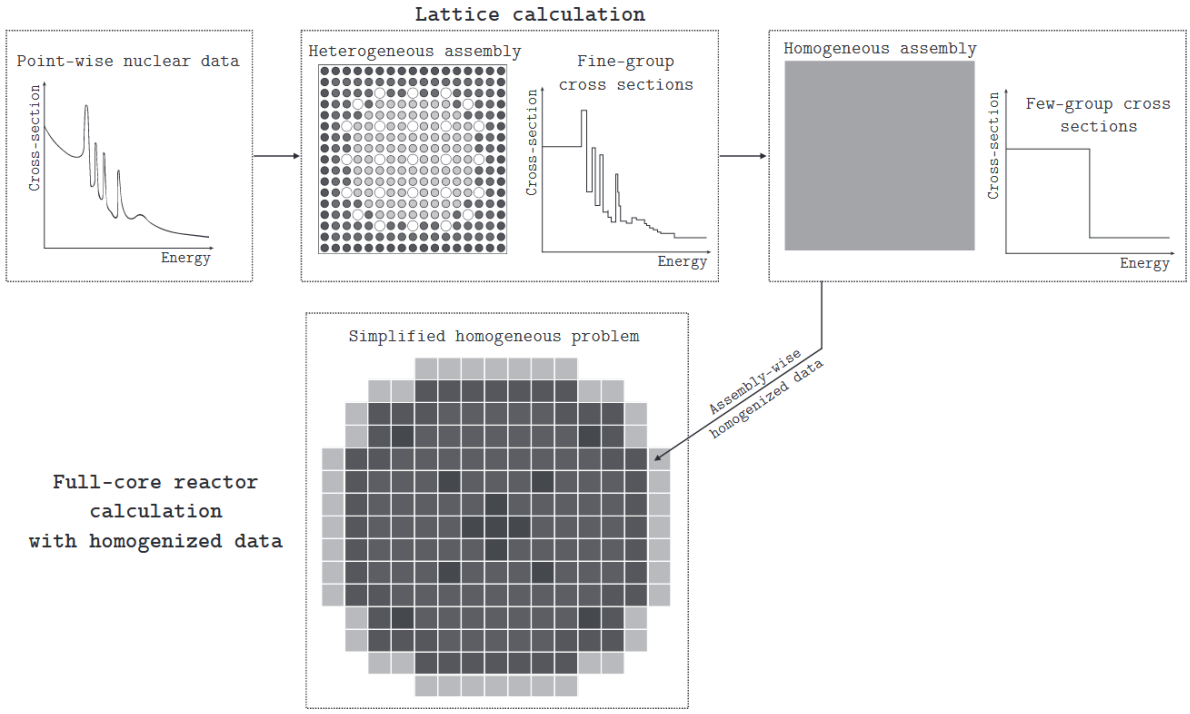

Figure 2.4 – Two-step computational scheme for full-core LWR analysis [19].

Successively, pin-power-reconstruction techniques based on the information of the 2D lattice transport calculation are used to reconstruct the flux and power levels of the single fuel rods in the assembly.

The use of lattice codes together with nodal codes is a solid, well-known, and validated methodology for standard steady-state and transient simulations, widely used by industry and regulators. Neutron flux maps and reaction rate maps are generated for various reactor conditions in an efficient manner. However, the homogenization and condensation schemes do not allow to resolve with high accuracy localized phenomena in the core, especially at the intra-pin and inter-pin levels. The ability to resolve such localized effects becomes particularly relevant if the neutronics solver is coupled with advanced thermal-hydraulics and mechanical solvers looking at phenomena at a more local scale than the fuel assembly. Therefore, the current tendency is to develop high-resolution deterministic neutronics codes to be integrated with the so-called high-fidelity multi-physics codes. The advancements in the development of high-fidelity deterministic neutronics codes are discussed in Section 2.3.

2.2.2 Monte Carlo neutronics codes

Differently from the deterministic approach, Monte Carlo neutronics codes simulate the neutron transport through matter as a stochastic process without solving the linear Boltzmann equation numerically. Individual neutron histories are tracked from the emission point to the final absorption or escape point in an *analog* fashion. The random walk of neutrons is simulated by generating random numbers from probability distributions, including the initial position, energy, and direction, the distance traveled before collision, and the reaction type at the collision point. The probability distribution functions derive directly from the macroscopic cross-sections of the traversed material.

A more mathematical formulation of the Monte Carlo method can be found in textbooks by Stacey [14] or Hébert [20].

Over a large number of simulated neutron histories, it is possible to obtain statistical estimates of the quantity of interest – i.e., neutron flux, reaction rate, k_{eff}, etc. – over a specific volume. The process of recording events is called *tallying* or scoring. Due to the statistical nature of the method, each tally output is represented by the mean value of the scored quantity accompanied by a statistical uncertainty, namely the statistical variance. The statistical uncertainty serves as a measure of computational precision and varies inversely to the square root of the number of simulated histories. Hence, if the number of simulated neutron histories tends to infinity, the statistical uncertainty of any estimate will tend to zero. Obviously, a problem of this magnitude requires either an infinite computing power or an infinite simulation run time.

Contrary to deterministic neutronics codes, the stochastic approach of Monte Carlo allows for modeling three-dimensional complicated geometries with a limited number of approximations. However, while obtaining global parameters averaged on the entire core (e.g., k_{eff}) is straightforward even with standard computing power, recording average quantities on very small volumes – or worst at a point – with good statistical uncertainties becomes extremely computationally expensive. Hence, one of the main drawbacks of Monte Carlo codes is the burdensome and not readily-available generation of detailed flux and reaction rate maps. In turn, a series of variance reduction techniques can be applied to score into optically thin volumes or heavily shielded regions. We usually refer to these techniques as *non-analog* because a certain weight is assigned to neutron histories depending on their importance.

Another inherent advantage of Monte Carlo codes is their capability to employ continuous-energy nuclear data libraries to draw probability distribution functions. Minimizing the approximations in the microscopic cross-section treatment aids in providing feedback on the evaluation of nuclear data if the simulation results are compared against experimental data.

Nowadays, Monte Carlo neutronics codes are considered a reference for steady-state reactor calculations and the golden standard for high-resolution neutronics simulations despite their computational expensiveness. However, their time-dependent capabilities to simulate reactor kinetics and noise are still under development.

The Monte Carlo approach is implemented in popular codes such as the Monte Carlo N-Particle Transport Code (MCNP) and Serpent. MCNP, under development at Los Alamos National Laboratory since the late 1950s, has been a pioneer in the field of particle transport simulations. It was designed to track many particle types over a broad range of energies for various applications, including criticality simulations in nuclear reactors. The latest version released is MCNP6.2 [21]. Serpent [22] is a multi-purpose 3D continuous-energy Monte Carlo particle transport code developed at VTT Technical Research Centre of Finland and publicly released in 2009. As of today, the code has been upgraded to its second version, i.e., Serpent 2, which is the main tool used for the simulation of neutronics effects in this work. The main differences between MCNP6.2 and Serpent 2 are the tracking routine (ray tracing vs. delta-tracking), licensing costs (small fee vs. free), and flexibility in source code modifications (protected vs. publicly available). In addition, MCNP6.2 has other well-

consolidated capabilities, such as the possibility to perform coupled neutron/photon/electron calculations and the capability to apply variance reduction techniques and be coupled with variance reduction tools, i.e., ADVANTG [23]. Although incredible progress has been made in recent years, some of these capabilities are in the first development phase in the Serpent 2 code.

2.3 Towards high-resolution full-core neutronics codes

The research on computational methods to solve the neutron transport problem has been of central interest in the field of reactor physics since the 1950s. Historically, full-core LWRs analyses are performed with legacy codes based on the two-step methodology discussed in Section 2.2.1.1. As already mentioned, legacy solvers introduce a series of approximations and condensations that limit their application for the investigation of small-scale neutronics phenomena occurring in the core, e.g., local flux variations due to fuel deformations [24] or CRUD deposition [25].

In the last 30 years, computational power and computer memory have increased by many orders of magnitude. As a consequence, neutronics solvers modeling phenomena at different spatial scales, with higher levels of sophistication and fewer approximations, have started to be introduced.

Monte Carlo codes became a more realistic alternative to legacy codes for steady-state full-core calculations, but their capabilities to solve time-dependent problems are still under assessment. At the same time, hybrid methodologies combining Monte Carlo and legacy codes have been implemented, in particular, to generate the few-group cross-sections in realistic fuel arrangements to be successively used by nodal codes.

The advancement in the computing capabilities also opened to the development of high-fidelity multi-physics tools, requiring a high level of resolution in the solution of the transport problem to be coupled with thermal-hydraulics and mechanical solvers. The need for accurate and more detailed simulations has been favoring the development of advanced neutronics tools for LWRs within the framework of several projects, such as the Consortium for Advanced Simulation of Light Water Reactors (CASL) [26] in the US. A renowned example of these high-fidelity neutronics tools is the MPACT [27], [28] neutronic solver, developed within the Virtual Environment for Reactor Applications (VERA) of the CASL project. MPACT relies on a 2D/1D method for the whole core transport. The 3D problem is divided into 2D pin-homogenized problems in the radial core direction, usually solved with the method of characteristics (MOC) to represent the radial heterogeneities of the core, and in 1D problems in the axial direction solved with lower-order methods. The solutions from the two problems are then coupled together with axial and radial transverse leakages. The 2D/1D scheme is proven to work efficiently for reactor core geometries having much higher geometric and material variability in the radial direction than the axial direction. Another of the most recent high-fidelity neutronics solvers based on the 2D/1D method is nTRACER [29], developed at Seoul National University.

While both MPACT and nTRACER operate on structured mesh, novel neutronics solvers operating on unstructured meshes are being developed in parallel. Codes such as GeN-Foam [30] are particularly suitable to model complex reactor geometries and allow predicting with a high spatial resolution the steady-state and time-dependent neutron flux distribution. A GeN-Foam model of the CROCUS zero-power reactor is under development at EPFL.

High-fidelity neutronics codes are becoming the state-of-the-art for reactor physics simulations, and they are starting to be also required by regulators for safety analyses. However, their use in the safety assessment of operating or next-generation nuclear reactors requires the prior validation of their underlying computational models. As of today, the validation of high-fidelity neutronics codes still remains a challenge due to the scarcity of highly localized neutronics measurements in reactor cores.

2.4 Thermal neutron detection methods

The detection of subatomic particles is strictly dependent on their mode of interaction with matter. Charged particles can be directly detected after having ionized or excited the detector media by collecting the information carried by the induced charges. Neutrons, on the other hand, cannot be detected directly and must be converted into detectable radiations through one of the neutron-induced nuclear reactions described in Section 2.1.1. As already mentioned, the reaction type strongly depends on the neutron energy. Due to the importance of thermal neutrons in LWRs, this section summarized the thermal neutron detection techniques relevant to this work. For a complete review of low-energy instrumentation, it is possible to refer to the classic textbook by Knoll [12].

Thermal neutrons, due to their low kinetic energy, can transfer only a small amount of energy to the medium via scattering interactions. Hence, thermal neutron detection relies on absorption nuclear reactions converting thermal neutrons into secondary radiations. The neutron-induced secondary radiations can be charged particles – i.e., alphas, protons, recoil nucleus, and fission fragments – or uncharged radiations, such as gamma rays. The conversion into charged particles is the most exploited method to detect thermal neutrons, while the use of secondary gammas is very rare and thus not discussed in this thesis.

The detection of thermal neutrons requires a *converter* material. A converter must have a high cross-section for nuclear conversion reactions in the low-energy range to maximize the chances of interactions. At the same time, the total energy released by the reaction as kinetic energy of the products, called the Q-value, must be as large as possible to ease the successive detection of charged particles with conventional methods and discriminate against other radiation types. However, high exothermic Q-values do not allow for recovering the information on the small energy of thermal neutrons. Popular converters for thermal neutrons are ^{3}He, ^{6}Li, ^{10}B, and ^{235}U, whose cross-sections of interest are shown in Figure 2.5.

After being produced, secondary charged particles are directly detected in a successive step with standard detection methods for charged particles, i.e., gas-filled detectors, semiconductors, and scintillators. The total or partial deposition of the energy of the neutron-induced charged particles indicates a neutron interaction in the detector's sensitive volume. Depending on the detector mode of operation, the neutron interactions can be counted one by one in *pulse mode* operations, or the average rate of neutron interaction can be obtained in *current mode*.

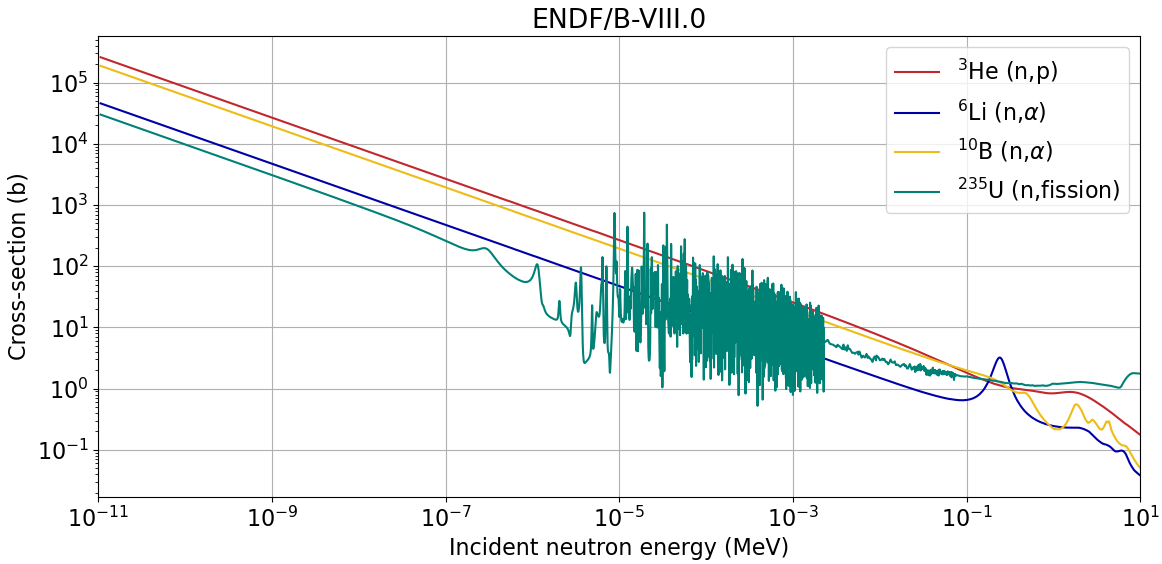

Figure 2.5 – Microscopic cross-sections as a function of the incident neutron energy for some reactions of interest in neutron detection, from the ENDF/B-VIII.0 [31] nuclear data library.

Independently from the detector's mode of operation and application, the reading of a thermal neutron detector over a certain time interval Δt, being single event counts or an average current, is proportional to the rate of interactions with the converter material occurring in the detector volume V over the entire energy range E as

$$detector\ output \propto \int_V \int_E \int_{\Delta t} RR_x(\boldsymbol{r}, E, t) dV dE dt. \tag{2.9}$$

where RR_x is the reaction rate for the selected neutron reaction and neutron converter material. In particular, recalling Equation (2.3), we obtain

$$detector\ output \propto \int_V \int_E \int_{\Delta t} N(\boldsymbol{r}, t) \cdot \sigma_x(E) \cdot \phi(\boldsymbol{r}, E, t) dV dE\, dt, \tag{2.10}$$

Equation (2.10) indicates that the detector output represents the neutron population in a certain region depending on the detector properties – including the detector volume V, the volume-integrated atomic density N of the converter nuclide, and its energy-integrated microscopic cross-section σ_x – and on the scalar neutron flux incident on the detector's active volume, also considering the spectral component. Indeed, the detector output convolutes the neutron spectrum with the energy-dependent cross-section of the converter material.

The proportionality between the detector output and the neutron population in the detector region is given by the detector *intrinsic efficiency* ϵ, or *sensitivity*, defining the general detector capability to translate the neutron population incident on the detector active volume into a measurable quantity:

$$\epsilon = \frac{detector\ output}{number\ of\ incident\ neutrons\ on\ detetctor\ volume}. \tag{2.11}$$

Once the basic principles of thermal neutron detection have been discussed, the use of conventional detection technologies for charged particles in conjunction with thermal neutron converter materials is presented hereafter.

2.4.1 Gas-filled neutron detectors

The use of gas-filled detectors is the most common method to detect thermal neutrons. In the majority of cases, such detectors consist of a chamber filled with a gas acting as both a converter and an ionization medium. Only in particular cases, discussed later, the converter material surrounds the chamber.

The interaction between a thermal neutron and a converter nucleus generates two charged particles emitted in opposite directions. These charged particles ionize and excite the gas molecules along their path, generating ion pairs. If a sufficiently high external voltage is applied, the ion pairs drift in the chamber avoiding recombination and generating a current. In this case, the gas-filled detector works in the ionization region and is said to be an *ionization chamber*. In most applications, ionization chambers are used in current mode. Indeed, the direct measurement of the ionization current gives an indication of the average rate of neutron interactions.

If the applied voltage is sufficiently high, secondary ionizations can occur in the detector gas and multiply the number of ion pairs. In case the ion pairs are multiplied proportionally, the detector is a *proportional counter* and it is usually operated in *pulse mode*. By connecting a pre-amplifier module to the proportional counter, the output consists of a single electronic pulse with an amplitude proportional to the energy released in the detector volume by the charged particles generated following a neutron interaction. The electronic processing of the pre-amplifier output signal, consisting mainly of its amplification, allows counting of single neutron events.

For the sake of completeness, a gas-filled detector works in the *Geiger-Muller* region for extremely high applied voltages causing showers of avalanches of secondary ionizations. The propagation of avalanches always terminates after the same number of avalanches for a fixed applied voltage. As a consequence, the number of collected charges per neutron event and thus the amplitude of the pulses collected from a Geiger Muller counter is always constant and representative of a neutron event independently from the energy released by the charged particles. The use of Geiger-Muller counters for thermal neutron detection is possible but not common.

Most of the gas-filled thermal neutron detectors operate in pulse mode in the proportional region and are either ^{3}He proportional counters or BF_3 proportional tubes. The working principles of these two technologies are similar: both present a cylindrical chamber in which the reaction Q-value can be deposited fully or partially depending on the detector's dimensions, gas pressure, and purity. The partial deposition of the energy of the reaction products is caused by the *wall effect* and should be minimized as much as possible to increase the detector efficiency and avoid problems in the discrimination between thermal neutron events and interactions of gammas in the detector volume. Therefore, the fabrication of ^{3}He detectors of small sizes requires high-pressure chambers, increasing the difficulties in the detectors' manufacturing. While the very high ^{3}He cross-section for (n,p) reactions makes these devices the golden standard for efficient thermal neutron detection, the availability of ^{3}He is extremely limited and its cost is prohibitive. ^{10}B, in turn, is readily available on the market and

compensates for the lower reaction cross-section with a higher reaction Q-value ensuring better gamma discrimination.

Fission chambers are a variation of the previously described gas-filled detectors. The standard design consists of ionization chambers with the inner surface coated with a thin layer of fissile material, being ^{235}U, ^{233}U, or ^{239}Pu. Thermal neutrons are converted into highly energetic fission products emitted in opposite directions. Thus, due to the detector configuration, only one of the fragments moves in the direction of the ionization chamber and has the chance to be detected. Although fission fragments are highly energetic, they are heavy ions, and, as a consequence, the fissile deposit must have a small thickness to minimize the energy loss. Fission chambers can be operated in both pulse mode and current mode, depending on the application.

The main characteristics of the gas-filled detectors used for thermal neutron counting are summarized in Table I, and a complete review of these detectors and their mode of operation can be found in [12].

Table I – Summary of the characteristics of gas-filled detector used for thermal neutron detection, based on the information in [12]. Cross-section values are taken from ENDF/B-VIII.0 [31] nuclear data library.

	^{3}He proportional counter	**BF_3 proportional counter**	**Fission chambers**
Converter isotope	^{3}He	^{10}B	^{235}U (but also ^{233}U, ^{239}Pu, etc.)
Reaction	(n,p)	(n,α)	(n,fission)
Charged particles	${}^{3}_{1}H$, ${}^{1}_{1}p$	${}^{7}_{3}Li$, ${}^{7}_{3}Li^{*}$, ${}^{4}_{2}\alpha$	Fission products
Cross-section at 0.025 eV	5350 barns	3869 barns	590 barns
Q-value	0.764 MeV	2.792 MeV (6%) 2.310 MeV (94%)	~ 200 MeV
Natural abundance	0.0002%	19.8%	0.72%
Gamma discrimination	Good	Good	Excellent
Thermal neutron detection efficiency	25% (1 atm), 76% (5 atm)	~90% (30 cm tube)	< 0.1% (layer < 0.1 μm)
Region of operation	Proportional	Proportional	Ionization
Mode of operation	Pulse	Pulse	Pulse or current
Availability	Very low	High	Restricted
Cost	Very high	Medium	High

2.4.2 Solid-state neutron detectors

Thermal neutrons can also be detected by depositing a thin layer of converter material, mainly ^{10}B or ^{6}Li, on a semiconductor detector. As long as the converter layer has a minimal thickness, one or (less likely) both of the generated charged particles release their entire or partial energy in the semiconductor detector generating electrons and holes along the particle track. In the same way as gaseous detectors, the electrons and holes drift in the crystal if an external voltage is applied to it. For sufficiently high voltages, the charge carriers are collected, and an output signal is generated after electronic processing.

The main constraint of such a design for thermal neutron detection is the fact that the charged particles emitted by the converter layer might not be able to emerge from the latter and be absorbed if the layer

is not thinner than the maximum particle range. This effect significantly limits the detector efficiency for thermal neutron detection to values below 10% [12]. In addition, the higher density of the semiconductor with respect to gases favors the energy deposition of gammas in the detector's active volume. As a consequence, pulse shape discrimination (PSD) techniques must be implemented to separate signals from neutron-induced reactions and gamma interactions.

Typical semiconductors used in combination with ^{10}B or ^{6}Li are silicon-carbide SiC crystals [32] and static chemical vapor deposition (sCVD) diamonds [33].

2.4.3 Scintillator neutron detectors

The detection of thermal neutrons with scintillating materials has gained a renewed interest in recent years [34], and it represents the main focus of this work. Similar to gas-filled detectors, a converter material should be mixed with the scintillating medium. However, an additional conversion step is required during the detection process: the kinetic energy of the charged particles generated by the neutron-induced nuclear reaction is proportionally converted into visible light by scintillating materials. The generated light is then collected and converted again into photoelectrons to output an electronic signal corresponding to a neutron event or a current representing the average rate of neutron interactions. Light conversion techniques are described in Section 2.4.3.1.

Scintillating materials are substances exhibiting luminescence properties when excited by ionizing radiations. The prompt emission of light from a substance excited by primary or secondary charged particles is called *fluorescence* and occurs in a timescale between 10^{-10} to 10^{-7} s [35] from the particle interaction. Other processes, such as *phosphorescence* and *delayed fluorescence*, are both characterized by a slower emission time than fluorescence, i.e., from 10^{-6} to 10 s [35]. A good scintillating material should be transparent to its own light emission or have a small thickness to reduce light attenuation. Additionally, it should have an appropriate refraction index to avoid light dispersion during collection and have a fast decay time of the visible radiation to generate fast pulse signals [12].

Nowadays, two main categories of scintillators are widely available on the market: *organic* and *inorganic* scintillators. An extensive review of the characteristics of both categories of scintillating materials can be found in [12]. Inorganic scintillators show a high light output, but they have a slow decay time, whereas organic crystals are usually faster but with a lower light yield. Scintillators can be found in the form of crystals, plastics, or liquids and are seldom used in the field of thermal neutron detection [12].

Among the wide range of inorganic scintillator compounds available in the market to perform thermal neutron detection, europium-activated lithium iodine LiI(Eu) and silver-activated zinc sulfide ZnS(Ag) are the most widespread. Both LiI(Eu) and ZnS(Ag) thermal neutron detectors employ ^{6}Li as thermal neutrons converter. In the first one, ^{6}Li is already part of the crystalline structure of the inorganic scintillator, while for the second lithium-loaded compounds are usually mixed with the ZnS(Ag) scintillator material. ^{6}Li interacts with thermal neutrons according to the reaction

$$ {}^{6}_{3}Li + {}^{1}_{0}n \rightarrow\rightarrow {}^{3}_{1}H + {}^{4}_{2}\alpha \qquad Q = 4.78\ MeV\ . \tag{2.12} $$

The ^{6}Li reaction cross-section at 0.025 eV is 944 barns [31], and it is considerably lower than the one for neutron-induced ^{10}B(n,α) and ^{3}He(n,p) reactions, as shown in Figure 2.5. In turn, the reaction shows a larger Q-value which can be translated into a high light output of the scintillator. On the contrary to ^{3}He, ^{6}Li has a natural abundance of 7.40% and is available in different forms.

LiI(Eu) detectors show similar characteristics to the classic sodium-iodine NaI(Tl) crystals (used mainly for gamma detection) but with lower light outputs. Although small crystals of LiI can be produced, i.e., in the cm range, their dimensions are not small enough to avoid gamma rays and secondary electrons from depositing relevant portions of their energy in the scintillator volume. In addition, LiI is highly hydrophobic and can be used only in sealed instruments.

On the other side, the dispersion of enriched lithium-fluoride ^{6}LiF in a ZnS(Ag) matrix has achieved growing popularity in the field of neutron detection [34] and is of central interest for this work. The charged particles generated by the ^{6}Li nuclear reaction in (2.12) interact with the surrounding crystals of ZnS(Ag) promoting the migration of electrons from the valence band to an excited state of a luminescence center from which electrons can de-excite emitting photons [12]. ZnS(Ag):^{6}LiF shows a good detection efficiency for thermal neutrons, estimated at around 30%, and a large light output compared to other scintillators. ZnS(Ag):^{6}LiF is well-known for the optimal gamma rejection [36] due to the small thickness in which the screens can be produced. In addition, ZnS(Ag):^{6}LiF is not hydrophobic and can be used to perform measurements in water without sealing. Nevertheless, the light emitted by the ZnS(Ag) fluorescence has a slow decay time, up to a hundred μs, and signal processing techniques are required to perform thermal neutron counting. ZnS(Ag):^{6}LiF showed promising performances for safeguard applications [37], imaging [38], scattering experiments [39], and reactor measurements [40]. Further details on the recent applications of ZnS(Ag) for neutron detectors at Paul Sherrer Institut (PSI) are reported in Section 4.1.

For the sake of completeness, thermal neutron detectors based on inorganic scintillators can also be loaded with gadolinium Gd or boron compounds, e.g., B_2O_3 [41]. Such detectors are less popular than LiI(Eu) and ZnS(Ag):^{6}LiF for thermal neutron detection and thus are not discussed here.

2.4.3.1 Light collection techniques

The light produced by any scintillator must be collected and converted into photoelectrons to obtain a readable electronic signal. Different light conversion techniques are nowadays available to perform the conversion.

Photo-multiplier tubes (PMTs) are historically the devices used in combination with scintillating materials. The scintillator can be directly coupled with the PMT's sensitive layer, or the scintillation light can be transported towards it via light transmission technologies such as optical fibers. A photosensitive layer, called the *photocathode*, converts the incident light photons into photoelectrons. The few hundred generated photoelectrons are proportionally multiplied up to 10^{7}-10^{10} [12] by a series of dynodes positioned in a vacuum tube and held at a positive potential set between 1000 V and 2000 V for most of the commercial models. The amplified charges are collected at the tube output and processed into an electrical pulse with conventional signal processing techniques.

Although the PMTs excellent performances in terms of photon detection efficiency and low noise levels, they are very fragile instruments with a considerable high cost. They require very high voltages to work and suffer from high sensitivity to magnetic fields. In addition, the presence of the vacuum tube limits the size in which PMTs can be built, making them bulky items not suitable for localized applications.

In the last decade, there has been a shift in light conversion techniques from PMTs to semiconductor photodiodes, thanks to the technological advancements in the field of solid-state devices. As of today, different designs of photodiodes can be employed to collect and translate scintillation light with high efficiency, low power consumption, and small dimensions compared to PMTs. Conventional photodiodes (called PIN diodes) are the simplest device to convert, with no internal gain, photons into electron-hole pairs in the semiconductor structure. On the other hand, avalanche photodiodes (APDs) multiply the number of generated charge carriers through the application of an external electronic bias to the semiconductor. For a sufficiently high applied voltage, i.e., above breakdown, the APDs can be used in Geiger mode, in which, as in gas-filled detectors, an avalanche of charges is produced following the initial photon interaction.

A SiPMs is a single-photon sensitive solid-state device made of an array of avalanche photodiodes (APDs) working in Geiger mode and connected in parallel. Each APD is accompanied by its own quenching resistor to cease the avalanche of charges, and the two together form a "pixel" of the SiPM. Although the entire SiPM is externally biased above the APDs breakdown voltage, usually below 100 V, each pixel is electrically independent and is always delivering the same amount of charges upon breakdown due to the quenching process. A picture of a typical SiPM and a simplified electronic scheme of a SiPM are shown in Figure 2.6.

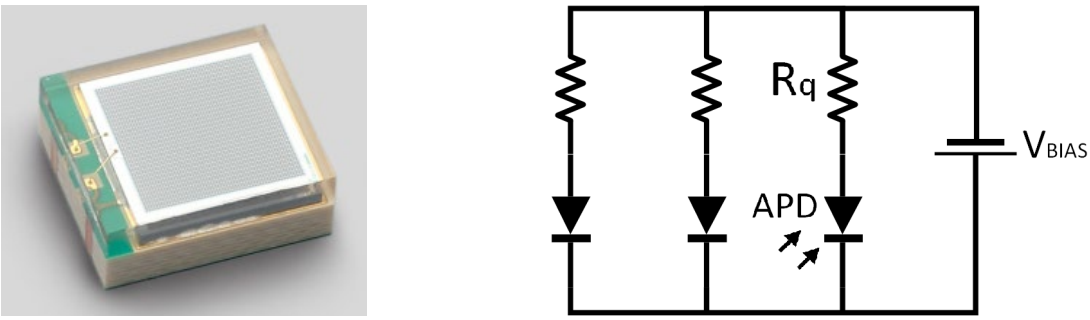

(a) (b)

Figure 2.6 – (a) Picture of a SiPM by Hamamatsu (the S13360-3050PE [42] used in this work) and (b) scheme of a simplified SiPM equivalent circuit.

The SiPM output current is the superimposition of the discharge currents of single APDs. If a single APD discharge is triggered by a single photon, the SiPM output is a fast rise in current due to the avalanche formation, followed by a slow decay of a few tens of ns given by the circuit time constant. In case two or more pixels are fired simultaneously, the SiPM current output is a multiple of the single-photon current depending on the number of triggered APDs. If another photon triggers a different pixel within the decay time of a previous event occurring in another pixel, the discharge current is summed up to the one already flowing at the SiPM output. The three discharge cases are represented in Figure 2.7. The discharged current can then be converted into a voltage signal by a pre-amplification circuit and be used to count the number of scintillation events.

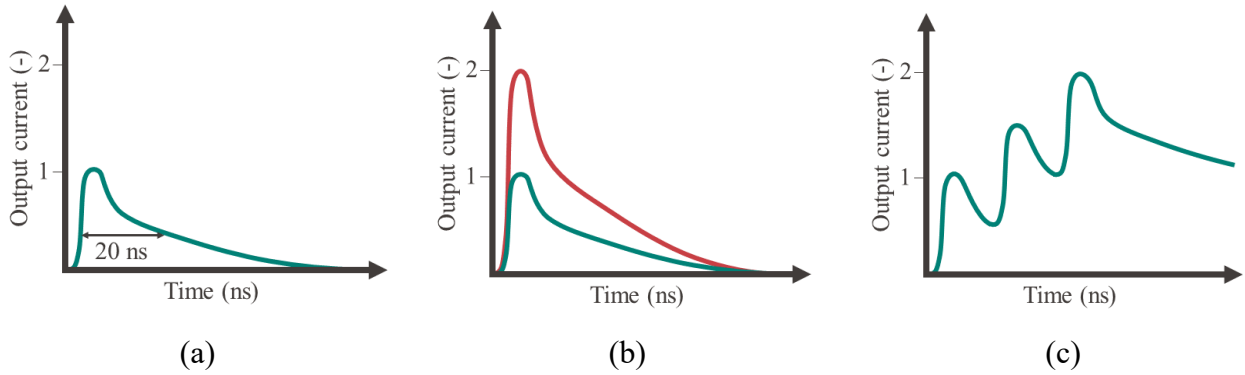

(a) (b) (c)

Figure 2.7 – SiPM output current in different cases: (a) single-photon event, (b) simultaneous single-photon events in different pixels, (c) train of single-photon events in different pixels in a short time.

In general, if an avalanche process is initiated in a pixel, all the neighboring cells are not directly affected and stay ready to detect other photons. However, optical cross-talk occurs due to the possible emission of fluorescence photons during an avalanche triggering the avalanche in a neighboring pixel. Cross-talk becomes more relevant for SiPM with a high fill factor (the pixels are closer to each other) [12]. Another relevant effect in SiPMs is afterpulsing, happening due to the trapping of charges in the impurities of silicon and their consequent exponential decay in time. Last but not least, SiPMs strongly suffer from dark counts generated by the thermal excitation of electrons in silicon.

SiPMs represent a valuable alternative to PMTs for the conversion of scintillation light into electronic signals due to their excellent photon detection efficiency, their mode of operation at a low voltage, their insensitivity to magnetic fields, easy scalability, and small dimensions. However, the high levels of electronic noise due to thermal-generated dark counts drastically increase with radiation damage [43]. Hence, in most applications, SiPMs cannot be used directly coupled to scintillators due to the high irradiation fields to which they would be exposed, but light transmission technologies are employed to transport the scintillation light on the SiPM active surface. Table II summarizes and compares the characteristics of PMTs and SiPMs.

Table II - Comparison between the main characteristics of photomultipliers tubes (PMTs) and silicon photomultipliers (SiPMs). Based on the information available in [12].

	Photomultiplier tubes (PMTs)	**Silicon Photomultipliers (SiPMs)**
Photon detection efficiency	High	High → Need for absolute dark
Resistance	Delicate	Mechanically robust
Applied voltage	High (1000-2000 V)	Low (<100 V)
Dimension	Bulky due to vacuum tube	Small (up to 1x1 mm^2)
Cost	High (few thousand CHF)	Low (about 30 CHF)
Sensitivity to magnetic fields	High	Low
Temperature dependence	Moderate	High → high dark count rate
Radiation damage	Moderate effect on performances	High radiation hardness
Noise level	Low	High
Coupling with scintillator	Direct or via optical fiber	Direct or via optical fiber

2.5 Nuclear reactors instrumentation

The constant monitoring of the neutron population during the operations of a nuclear reactor is essential to ensure a controlled fission chain reaction at all times. Indeed, measuring the neutron population provides direct information both on the average reactor power and on the spatial variations of the neutron flux, contributing to the prevention of unexpected transients which might result in accidental conditions. In LWRs, since the fission chain reaction is sustained by thermal neutrons, their detection is an essential part of the reactor safety systems and is of central interest in this work.

The instrumentation adopted for the detection of neutrons in reactor cores varies according to the reactor power and design. In commercial power reactors, neutron detectors should withstand harsh environmental conditions: high temperatures (up to 300 °C), high pressure (up to 17 MPa), and high radiation levels from both neutrons and gammas. A viable option to measure thermal neutron is the application of *passive* detection with activation techniques, which generally require a certain irradiation time, the cooling and cutting of the activated sample, and the successive radiation measurement out-of-core. On the side of *active* neutron detection, thermal neutron detectors tailored for power-reactor applications include fission chambers and self-powered neutron detectors (SPNDs). A complete review of the design and application of these instruments in LWRs can be found in the textbook by Knoll [12]. In zero-power research reactors, due to the milder irradiation conditions and lower temperatures and pressures, a wider range of neutron detection systems can be employed, including gas-filled, scintillator, and solid-state detectors (discussed in the previous sections). In both commercial and zero-power reactors, neutron detectors should be able to work in mixed radiation fields, meaning that they need to be gamma blind to count only neutrons and disregard gamma contributions. Otherwise, background rejection or discrimination techniques are needed.

In addition, neutron detection in nuclear reactors is performed in-core, namely in between or within the fuel elements, or ex-core, meaning that the devices for neutron detection are placed inside the reactor vessel but not within fuel elements. Because of the reduced space inside the core, the tendency is to design in-core miniature detectors that fit inside instrumentation tubes or in the gap between fuel rods, while ex-core detectors have larger dimensions for a higher detection efficiency. Active neutron detectors for reactor application can operate in pulse mode, current mode, and Campbell mode. A detailed description of the different modes of operations is available in [12]. The attention of this work is placed on instruments to perform active in-core neutron detection in pulse mode in zero-power reactors.

2.6 Localized thermal neutron detection in nuclear reactors

Measuring thermal neutrons in a point-wise manner in nuclear reactor cores is a challenging task. The volume-averaging of the converter reaction rate over the active detector region limits the achievable spatial resolution of the measurements. In addition, if neutron measurements are intended to be performed in-core, additional constraints are set by the limited space available to position instrumentation. For these reasons, the availability of publicly available high-resolution neutronics experimental data is extremely limited.

Typical localized measurements of the neutron distribution in a reactor core are performed with neutron activation techniques. Highly-resolved in-core experiments with activation techniques have been performed in the past in the zero-power research reactor PROTEUS operated at Paul Scherrer Institut (PSI) from 1968 to 2011. Detailed power and reaction rate distributions were investigated for modern LWRs fuel designs. In particular, Macku et al. [44] measured the radial and the azimuthal within-pin ^{235}U fission reaction rate and ^{238}U capture reaction rate distributions with activation foils installed in a demountable experimental pin of a Westinghouse SVEA-96 Optima2 boiling water reactor fuel assembly. The experimental measurements were compared with CASMO-4 results and MCNP4C, concluding that the two codes are able to predict the radial and azimuthal distributions. Foil activation measurements were also used to measure the azimuthal flux distribution around fuel rods in the Toshiba Nuclear Critical Assembly (NCA) by Yoshioka et *al.* [45].

On the side of in-core active thermal neutron measurements, a previous experience is represented by a study within the LWR-PROTEUS program, where Murphy et *al*. [46] used standard miniature fission chambers (MFCs) to measure fission and capture distributions in the same SVEA-96 Optima2 assembly and compare the results with MCNPX predictions. More recently, high-resolution measurements were performed in the CROCUS zero-power reactor by Rais [19] with a miniature fission chamber attached to a movable system called TRAX (described in Section 3.2), installed in the central vertical plane of the core, with the purpose of validating the computational scheme, i.e., PARCS [47] kinetics models.

The scarcity of high-resolution experiments also moved the development of novel detection technologies. A prototype of a miniature detector based on the use of a ZnS(Ag):^{6}LiF screen painted on the tip of an optical fiber was developed at Nagoya University in 1994 by Mori et al. [40]. The detector was tested in the Studsvik R2 and R2-0 reactors [48] and the Kyoto University Critical Assembly (KUCA) [49]. This experience provided the first proof of the feasibility of online mm-wise neutronics measurements in nuclear reactors with such a technology. However, the system featured the use of a plastic optical fiber connected to a standard photomultiplier tube (PMT), limiting the possibility to parallelize the detector design.

The availability of miniature neutron detector technologies also allows for the distribution of a large number of detectors in the core for either detailed monitoring purposes or research activities. Typically, the number of neutron detectors present in-core in commercial LWRs is on the order of a few tens (12 × 6 SPND in the case of the EPR [50]). An exception is represented by the VVR-1000 having approximately 500 in-core neutron detectors by design [51]. However, as already mentioned, such proprietary data are often not available to the public and therefore are hardly used to validate calculation schemes of high-fidelity neutronics tools. In this framework, zero-power research reactors represent an excellent opportunity to build 3D core-mapping systems for measuring localized and space-dependent neutronics phenomena with better flexibility and without thermal feedback. However, up to the knowledge of the author, no 3D full-core mapping system has been installed yet in any research reactor.

Chapter 3

The CROCUS zero-power research reactor

The high-resolution neutronics experiments presented in this work are performed in the CROCUS zero-power research reactor [52]. This chapter is dedicated to the detailed presentation of the CROCUS design, extensively benchmarked in the International Handbook of Evaluated Reactor Physics Benchmark Experiments (IRPhE) [53], and to the presentation of past and ongoing experimental programs of interest for this work.

3.1 Core design

CROCUS is an experimental zero-power reactor operated by the Laboratory for Reactor Physics and Systems Behaviour (LRS) at the École polytechnique fédérale de Lausanne (EPFL) campus in Lausanne, Switzerland. The reactor's operations are dedicated to education and research activities. The maximum power allowed by regulations is limited to 100 W, corresponding to a total neutron flux of 2.5×10^9 $cm^{-2} \cdot s^{-1}$ at the core center.

CROCUS is a pool-type, light-water-moderated core using low-enriched uranium. The reactor core has a nearly cylindrical shape, with an active diameter of about 58 cm and a height of 1 m. A 3D model of the CROCUS reactor is depicted in Figure 3.1. The fuel is arranged in squared lattices in two different radial fuel zones, surrounded by a reflector, making CROCUS a unique heterogeneous core. As shown in Figure 3.2, the inner region is loaded with 336 uranium dioxide UO_2 rods with a 1.806% enrichment. In the standard core configuration, the outer core zone can accommodate between 172 and 176 metallic uranium U_{met} rods enriched to 0.947%. In Figure 3.2, 176 U_{met} fuel rods are arranged according to the COLIBRI configuration, called as such after the presence of the COLIBRI fuel rods oscillator (see Section 3.3). Unless clearly stated, this COLIBRI core configuration (or a variation of the latter) is mounted during the experiments presented in this work. The outer fuel zone is surrounded by a demineralized light water reflector extending up to a diameter of 130 cm. The core and reflector are contained within an aluminum water tank with a thickness of 1.2 cm and diameter of 132.4 cm.

Both the UO_2 and the U_{met} fuel rods are composed of fuel cigars cladded in aluminum, with helium filling the gap between the fuel cigars and the cladding. The fuel rod dimensions are reported in Table III. A stainless steel spring at the top of each rod holds the fuel cigars inside the aluminum cladding. All the rods sit on the core baseplate and are kept in a vertical position by two aluminum grid plates

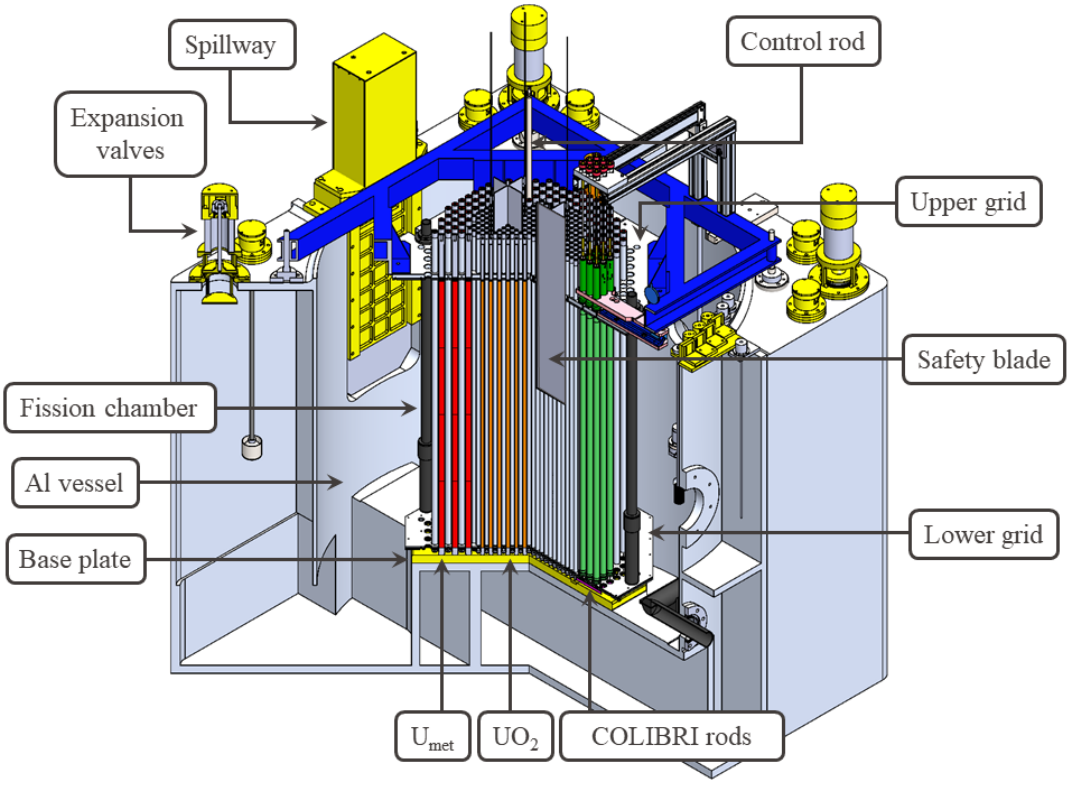

Figure 3.1 – 3D model of the CROCUS reactor in the COLIBRI configuration sectioned from the northwest side.

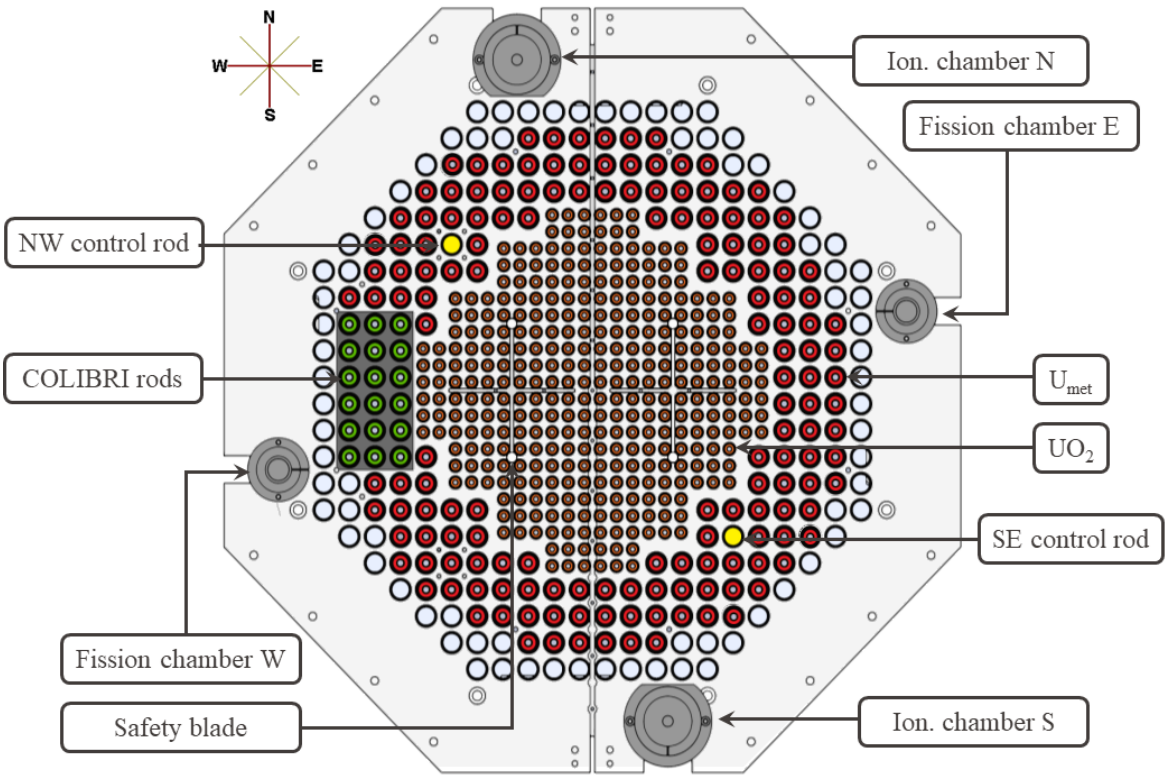

Figure 3.2 – Top view of CROCUS upper grid and fuel lattices in a configuration with 336 UO_2 rods, 176 U_{met}, and COLIBRI.

spaced 1 m apart, as shown in Figure 3.3. The lower grid is screwed to the core baseplate with 2.15-cm spacers, while the upper one is supported by a metallic structure standing above the core (visible in Figure 3.1). The upper grid is composed of two plates that leave a slit in the core center for instrumentation.

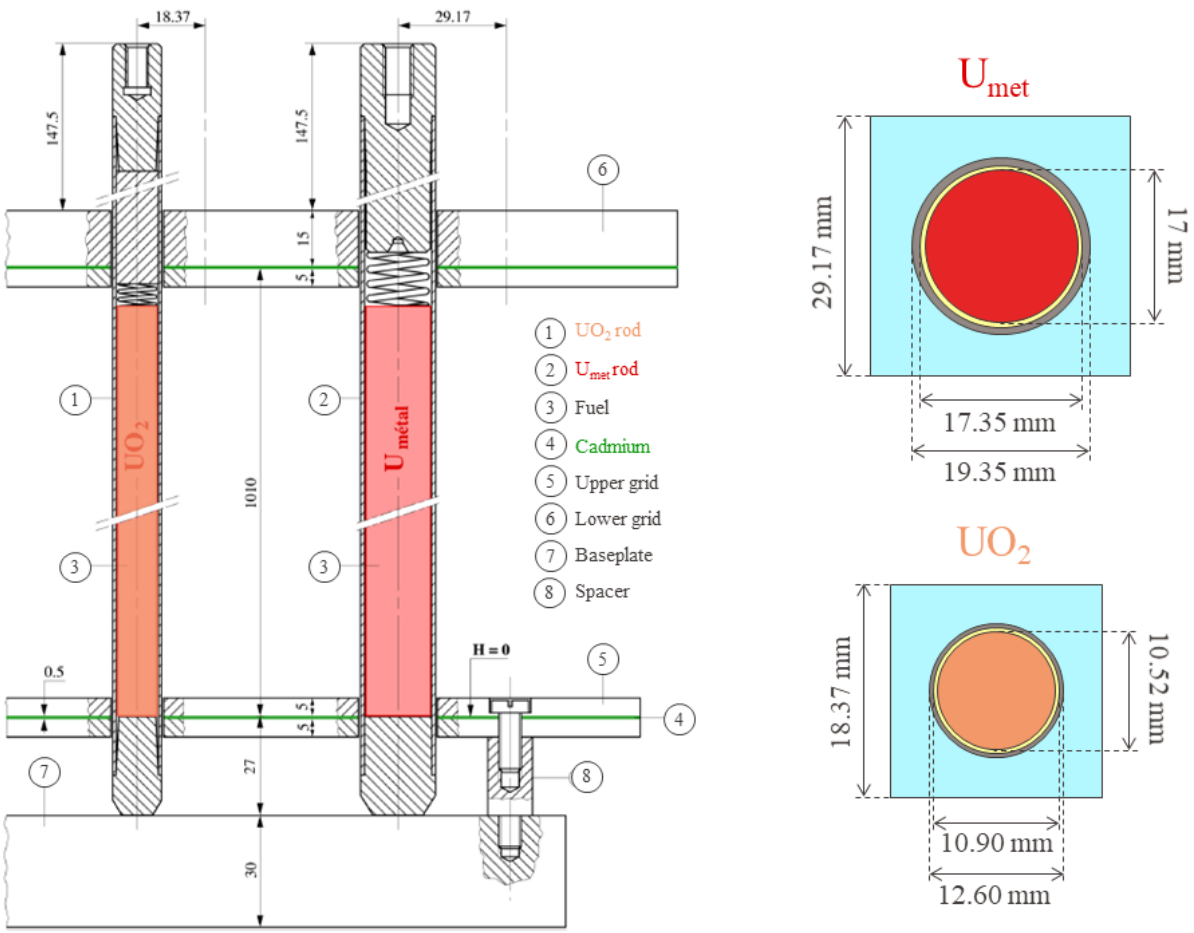

Figure 3.3 – Vertical and horizontal views of the CROCUS fuel, with dimensions from [52].

Table III – Dimensions of CROCUS fuel rods [52].

	UO_2	U_{met}
Fuel diameter (mm)	10.52	17.00
Internal cladding diameter (mm)	10.90	17.35
External cladding diameter (mm)	12.60	19.35
Fuel lattice pitch (mm)	18.37	29.17
^{235}U enrichment (%)	1.806	0.947
Fuel density (g/cm^3)	10.556	18.677

In the standard CROCUS configuration, both grid plates enclose a 0.5-mm thick cadmium (Cd) layer within the aluminum (in Figure 3.3). The purpose of the cadmium layer is to limit the thermal neutron flux in the axial direction. The fuel rods are designed so that the lower level of the active fuel

corresponds to the top surface of the lower cadmium layer. The lower level of the fuel is always the axial reference level for the experimental and computational studies presented in this document.

The core criticality and the power can be controlled in two ways: with the water level or with one or two boron-carbide B_4C control rods. A spillway is installed on the east side of the aluminum vessel (as visible in Figure 3.1) to control the water level in the core with a ±0.1 mm accuracy. The critical water level depends on the core configuration and is usually found with an "approach-to-critical" experiment. An increase in the water level with respect to criticality improves the moderation of neutrons, causing an exponential increase in the neutron population and in the reactor power. A reduction in the water level has the opposite effect. A variation of +1 mm in the water level of CROCUS corresponds to a reactivity insertion of 4 pcm. The water temperature is regulated via a secondary circuit and it can be varied by ±2.5 °C around the nominal temperature of 20 °C.

Instead of varying the moderator level, two B_4C rods can be inserted or withdrawn in the core through dedicated guide tubes in aluminum identical to the U_{met} fuel cladding. The control rods are connected to a motor that allows moving them with a precision of 1 mm at different speeds. The rods can be inserted or withdrawn from the core in less than one second, but the drop speed is limited by gravity. Each control rod has a reactivity worth of approximately 175 pcm [19], which is below the maximum reactivity insertion allowed in CROCUS by regulation and equal to 200 pcm. This means that, by design, an inadvertent ejection of the control rod does not bring the reactor to an uncontrolled state. The control rod guide tubes can be used, on occasion, as in-core experimental channels to accommodate instrumentation.

Six independent safety systems are in place in CROCUS. They include two cruciform cadmium safety blades and four water expansion tanks: each of these systems ensures a safe shut down of the reactor in less than a second. The two safety blades are suspended above the core and attached to two electromagnets during normal operations. The blades fall by gravity inside the UO_2 fuel lattice upon conventional shutdown or due to safety-related events. Each blade inserts more than 3000 pcm. In a similar way, the water pool of CROCUS is connected to four expansion thanks located in the corners of the aluminum vessel. Each expansion tank is connected with an expansion valve, which is closed during the reactor startup to fill the tanks with air. In case of reactor shutdown, the expansion valves are released, the expansion tanks are filled with water coming from the reactor pool, and the water level in the core drops by nearly half in less than a second.

3.2 Standard instrumentation

The monitoring of the neutron population in CROCUS is performed by four ex-core detectors: two compensated ionization chambers for general core monitoring and two power-calibrated [54] fission chambers used primarily for safety purposes. The four detectors, visible in Figure 3.2, are located in the core's periphery inside four detection channels attached to the upper grid plate.

The two fission chambers are Photonis CFUM21 double deposit fission chambers with ^{235}U coating enriched at more than 90 wt. %. They are used in pulse mode and are connected to the safety chains of CROCUS, where their output signal is translated into a power level according to a calibration factor. Their sensitivity to thermal neutrons was estimated to be approximately 10^{-3} cps/n_{th} [55]. In

this work, we often refer to these instruments as "monitors" of CROCUS and their reading is used to power-normalize the experimental data obtained from other devices.

The other two ex-core monitoring devices are Merlin Gerin CC54 ^{10}B-coated compensated ionization chambers working in current mode. Although the boron-coated electrode has as its primary function the detection of neutrons, it also interacts with the gamma field present in CROCUS during irradiations. Therefore, a second electrode without a thermal neutron converter is used to detect only gammas and remove the gamma-generated current from the main current output of the detector. Their sensitivity to thermal neutrons is about 8×10^{-2} nA/n_{th} [55].

Aside from the standard core instrumentation, an in-core miniature fission chamber (Photonis CFUF34) is used for local flux measurements in the central vertical plane of the core going from the north to the south direction. The fission chamber has an external diameter of 4.7 mm and a sensitive length of 85 mm loaded with approximately 1 mg of ^{235}U (~ 100 wt. % enriched). It is used in pulse mode and has a sensitivity to thermal neutrons of 10^{-4} cps/n_{th}. The fission chamber can be moved axially and radially with a 1-mm precision within the active core and reflector regions by a remote-controlled system called TRAX (the French acronym for Translateur Radial AXial). The detector's active part is mounted on a mechanical shaft that is suspended above the core and moves along rails running parallel to the slit present in between the two upper grids.

A series of other ex-core and in-core neutron detectors have been used over the years in CROCUS for different experimental campaigns. For instance, ^{3}He gas-filled neutron detectors of 32 mm in diameter and two 48-mm diameter Photonis CFUL01 ^{235}U fission chambers have been used for a series of neutron noise experiments being placed outside the core due to their large dimensions. On the contrary, BF_3 detectors (type Transcommerce MN-1 with 7.5 mm diameter) served for in-core neutron noise measurements during other experimental programs. Their smaller diameter allows inserting them in the control rod guide tubes used as an experimental channel or in similar experimental channels positioned in the available U_{met} lattice positions around the core active region. Moreover, various 3-mm diameter miniature fission chambers MFC (Photonis CFUR44/EP-M3 type with 130 µg of ^{235}U) and other advanced systems such as the Cividec sCVD diamond detector are available at LRS.

3.3 The COLIBRI fuel rods oscillator

In the framework of the COLIBRI (CROCUS Oscillator for Lateral Increase Between U_{met} Rods and Inner zone) experimental program at LRS, an in-core fuel rods oscillator device was installed in CROCUS in 2018 [56]. The device called here “COLIBRI” for the sake of conciseness is designed to laterally displace or oscillate up to 18 U_{met} fuel rods in the west region of the core of up to ±2.5 mm around their nominal lattice positions with a frequency in the Hz range. The CAD model of the COLIBRI oscillator is shown in Figure 3.4.

The device is composed of two moving plates axially positioned above and below the two core grids and rigidly connected by an aluminum beam. Each plate holds one extremity of the fuel rods selected to oscillate. The selection among the 18 U_{met} rods available to oscillate is performed by lifting the

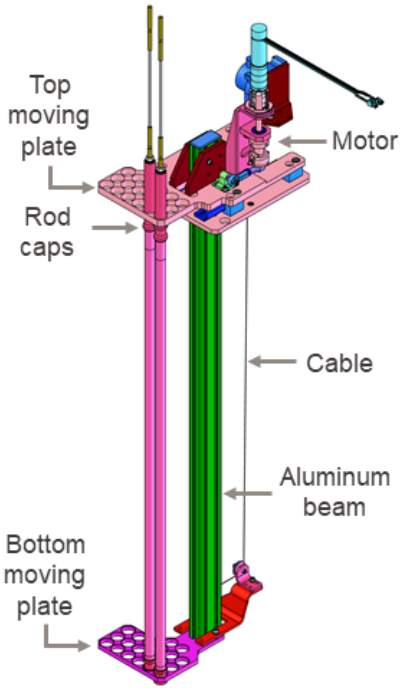

Figure 3.4 – CAD model of the COLIBRI fuel rods oscillator.

interested rods by 10 mm from the reactor baseplate in a way to insert them into the two COLIBRI moving plates. The insertion in the moving plates is made possible by the presence of top and bottom enlarged caps on the 18 rods. The top plate is set above the superior grid, installed on gliders, and connected to a motor. The motor rotation is translated into a linear translation of the top plate using an eccentric sheave and a connecting rod. The ideal movement of the top plate follows a sine function, whose amplitude is tuned by the selected sheave and whose frequency depends on the speed of the motor. The top movement is transferred to the bottom plate, unconstrained by gliders, via the transmission aluminum beam. Ideally, the top and bottom plates move in solidarity. However, the device calibration and the weight and inertia of the rods induce misalignments between their extremities (see Section 5.3.2 for a detailed study).

The standard lower grid and west upper half-grid were substituted by similar grids but with enlarged holes in correspondence of the 18 oscillating rods to be able to accommodate their movement. The device calibration ensures an oscillation amplitude within the available space, and in case of abnormal amplitudes, two stoppers dampen the movement of the lower plate at ±2.3 mm at maximum. Due to mechanical limitations in the manufacturing, the modified grids were produced with a Cd layer of 1 mm thickness instead of the standard 0.5 mm.

The oscillation is controlled and monitored with a LabVIEW software operating with 10 ms time-steps. A cable coder is used to measure the displacement of the lower moving plate with a ±0.1 mm precision. The software produces a .csv file output with the recordings of the motor position and speed and the position of the bottom moving plate from the cable.

COLIBRI is used especially for neutron noise studies, also called neutron modulation. In particular, three fuel rod oscillation campaigns [57]–[59] were carried out within the framework of the Horizon 2020 European project CORTEX for the validation of noise simulators. The analysis of the experiments demonstrated the observation of a spatial dependence of the induced noise [60]. In this work, COLIBRI is used solely for the study of the local flux changes induced by the displacement of fuel rods, as presented in Section 5.3.

Chapter 4

Development of MiMi neutron detectors

The present chapter covers the development of the miniature and minimalistic (MiMi) thermal neutron detectors designed for performing highly localized measurements in the zero-power reactor CROCUS. The various steps undertaken during the instrumentation development are detailed hereafter: from the initial development at PSI, to the construction and characterization of the first prototype, up to the design optimization targeting the installation of a 3D full-core mapping system in CROCUS. The work presented in this chapter is partially available in [61], [62], and [63].

4.1 Development of ZnS-based neutron detectors at PSI

The depletion of the ^{3}He reserves, the forecast of its limited production, and its consequent cost increase are driving the high demand for alternative neutron detectors with competitive efficiencies and lower prices [34]. Inorganic scintillator screens, and in particular ZnS, were selected as one of the most valuable candidates to replace ^{3}He technologies [64]. The Laboratory for Particle Physics (LTP) at Paul Scherrer Institute (PSI) has been developing since 2014 advanced neutron detectors based on ZnS(Ag) for different applications ranging from spallation source measurements [65]–[69] to, more recently, spent fuel characterization [70].

A 16-inches neutron detector [66]–[69] was developed by LTP to substitute the ^{3}He detectors at the POLDI time-of-flight diffractometer at the Swiss Spallation Neutron Source (SINQ) facility of PSI. The detector design, shown in Figure 4.1, consists of a sandwich of ZnS(Ag):^{6}LiF layers with embedded wavelength shifting fibers (WLS) uniformly distributed in the detection volume to transfer the scintillation light to a series of SiPMs. WLS are used to maximize the light collection efficiency inside the detector's active volume, which has a section of 2.4 × 2.8 mm and a length of 200 mm. Each detection channel is independent of the others. Several publications describe the development and testing of the innovative signal processing system based on the photon counting approach [66], [68] and the FPGA neutron/gamma discrimination algorithm [65], [71]. Indeed, it was shown that the long light emission time of ZnS(Ag) allows detecting with a good efficiency single-photon events with SiPMs, and by sampling the density of these photon events, the interactions of the thermal neutron can be distinguished from SiPM dark counts. This discrimination is performed by an FPGA digital algorithm using Moving Sum after Differentiation (MSD) filtering. The detector module was characterized by Stoykov et al. [68], and the direct comparison with the standard ^{3}He of the

diffractometer performed by Mosset et al. [69] showed a promising thermal neutron detection efficiency for such detectors, comparable or even superior to those of the standard ^{3}He detection system at SINQ.

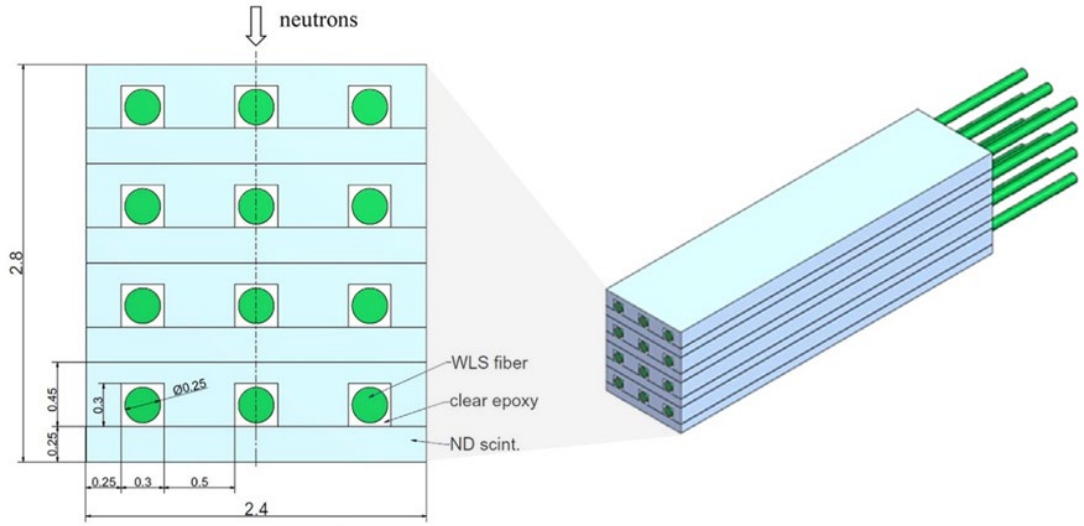

Figure 4.1 – Cross-section and 3D view of the sensitive volume of the 16-inches detection unit for the upgrade of the POLDI diffractometer [66], [69]. Dimensions are in millimeters.

A variation of this technology was recently designed at the LRT laboratory of PSI by Wolfertz et al. [70]. The target is the detection of fast neutrons in high gamma flux environments for the application to spent fuel characterization of fuel rods from Swiss nuclear power plants. The fast neutron sensitivity is achieved by relying on the elastic scattering of fast neutrons with the epoxy matrix embedding ZnS(Ag) crystals and by eliminating the ^{6}Li thermal neutron converter. A first prototype showed good gamma blindness when applying the same MSD algorithm [65], [71] used by its thermal neutron sensitive version.

4.2 Prototype development and testing

A collaboration between the LTP laboratory of PSI and the LRS laboratory of EPFL was established to adapt the SiPM-based ZnS(Ag):^{6}LiF technology to thermal neutron detection in the zero-power CROCUS reactor. In particular, the relatively high thermal neutron flux levels present in a reactor would allow for a reduction of the detector's active volume while still maintaining the high efficiency of the LTP detection system, shown to be comparable to that of standard ^{3}He detectors [69]. This triggered the idea to develop miniature thermal neutron detectors for in-core reactor applications based on the LTP technology.

The idea followed the previous experience of small thermal neutron detectors developed at Nagoya University [40] composed of a WLS optical fiber whose tip is covered with ZnS(Ag):^{6}LiF. These detectors were tested for measuring flux profiles in several reactors, e.g., Studsvik R2 and R2-0 reactors [48] and the Kyoto University Critical Assembly (KUCA) [49]. The main limitation of this design consists in the reduced system scalability due to the use of classical PMTs for light collection, which are expensive and bulky compared to the low-priced and compact SiPMs technology. Aside

from facilitating the system parallelization, the use of SiPMs and their dedicated signal processing is expected to improve the thermal neutron detection efficiency and the gamma blindness of similar instruments. Therefore, the combination and adaptation of this design with the technology developed at LTP would result in an efficient, cost-effective, parallelizable, and versatile miniature device suitable for localized and spatial-dependent measurements in the CROCUS reactor.

Miniature thermal neutron detectors were designed, built, and tested at EPFL since December 2017, in close collaboration with the LPT laboratory of PSI. The idea behind the design of the adapted thermal neutron detector in miniature dimensions is rather simple, as demonstrated by the schematics in Figure 4.2. A single layer of the same ZnS(Ag):^{6}LiF screen used by LTP for its excellent efficiency is cut into a piece of miniature dimensions. Due to its miniature dimensions, the piece is simply placed at the tip of a standard plastic optical fiber instead of being traversed by multiple WLS fibers, which are no longer required to maximize the light collection efficiency. The light emitted by the screen after a thermal neutron interaction with ^{6}Li is transported through the optical fiber outside the reactor biological shielding, where the SiPM is installed to prevent severe radiation damage. The SiPM collects the scintillation light and sends its output to the signal processing system, based on the LTP approach of converting photon-counting into an online thermal neutron counting. The signal processing employs either an analog readout, as done for the development of the first prototype, or the digital processing readout based on the MSD algorithm developed at LTP (used for the system upgrade in Section 4.3).

The final result is a device of Miniature dimensions and Minimalistic design that is named MiMi neutron detector after its two main characteristics. The first prototype of the detector is called MiMi-0. Measuring instruments of this type are of interest for the validation of high-fidelity neutronics codes because they can open up to the experimental investigation of both local and spatial-dependent neutronic effects.

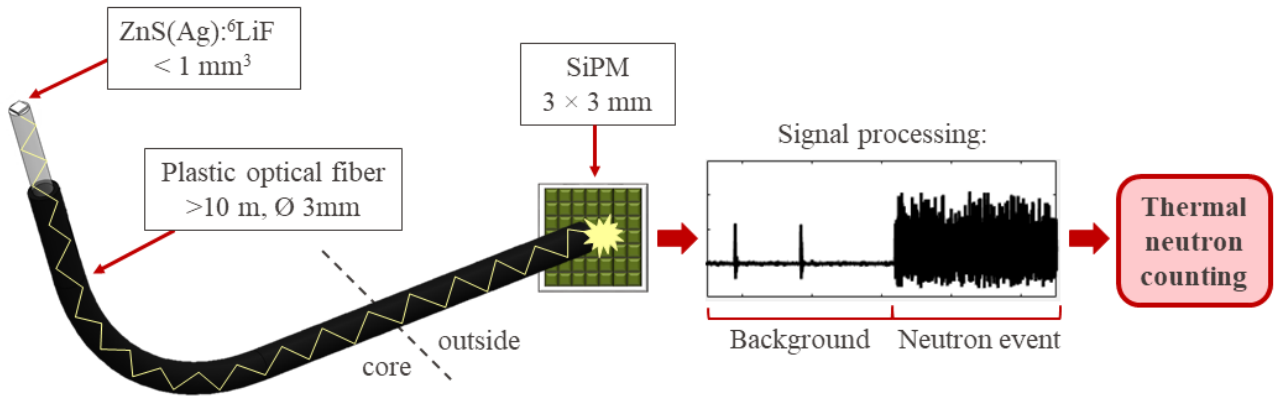

Figure 4.2 – Components and working principle of MiMi neutron detectors.

4.2.1 Detector design

4.2.1.1 Scintillator screen

The sensitive volume of the MiMi-0 neutron detector prototype relies on the commercially available ND2:1 scintillator screen manufactured by Scintacor [72]. The ND2:1 screen is composed of a

mixture of ^{6}LiF and ZnS(Ag) polycrystalline powders, both with grain size smaller than 10 µm, bonded within a poly(methyl methacrylate) (PMMA) matrix, as depicted in Figure 4.3. The interaction between an incoming thermal neutron and a ^{6}Li nucleus produces an α particle and a triton, as in Equation (2.12). The generated charged particles interact with the ZnS inorganic scintillator grains mixed into the same matrix, and fluorescence light is generated as a result of the de-excitation of the luminescence centers in the ZnS crystals. The screen sample used in this prototype version was cut at LRT and shows a nearly cylindrical irregular shape, with a total sensitive area of approximately 1 mm^2 and a thickness of 0.2 mm.

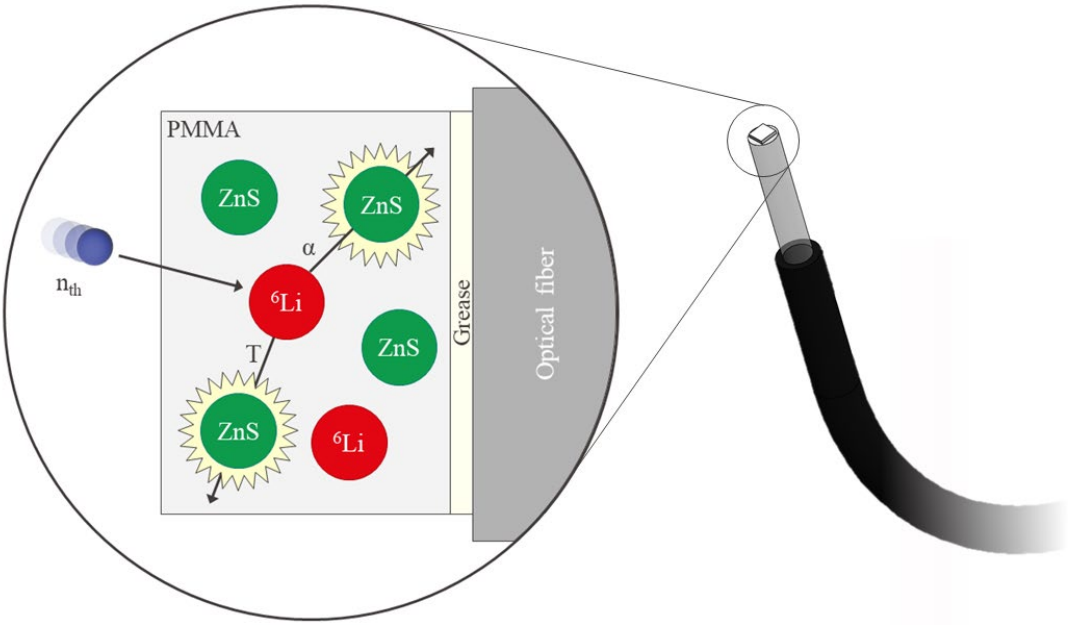

Figure 4.3 – Thermal neutron detection in the ND2:1 screen.

The 2:1 mass ratio between the two screen components and the high reaction cross section in the thermal range, i.e., about 10^3 barns [31], provide an excellent thermal neutron detection efficiency. In addition, the large reaction Q-value of 4.78 MeV translates into a high light production by the ZnS scintillator of approximately 160'000 photons/neutron [73]. The fluorescence light emitted by the ND2:1 has a typical emission spectrum lying in the blue range of the visible light, with a peak emission wavelength of 450 nm [72]. However, ZnS is a fairly opaque material limiting the transmission of the generated photons. In addition, the prolonged emission time of 80 µs for 90% of the light (according to the manufacturer) calls for signal processing techniques to discriminate neutron events from standard background light. Last but not least, ZnS is well-known to have a low sensitivity to gammas, which is further minimized due to the miniature dimensions of the screen (see Section 4.2.3 for experimental proof). An overview of the ND2:1 screen characteristics is reported in Table IV.

Table IV – ND2:1 screen characteristics for the MiMi-0 neutron detector prototype, based on [72], [73].

Formula	ZnS(Ag):^{6}LiF
Components state	Particulate blend
Mass ratio ZnS(Ag):^{6}LiF	2:1
^{6}Li atomic density	1.4×10^{22} atoms/cm^{3}
Density	2.2 g/cm^{3}
Light yield	160'000 photons/neutron
Decay to 10%	80 µs
Peak wavelength	450 nm
Sensitive area	1 mm^{2}
Thickness	0.2 mm

Figure 4.4 – Picture of the front-end MiMi-0 neutron detector prototype without its aluminum cap.

4.2.1.2 Optical fiber

The miniature ND2:1 scintillator screen is positioned at the tip of a polished plastic optical fiber, as shown in Figure 4.4.

The optical coupling between the ND2:1 screen and the SH8001 fiber is performed with the BC-630 grease manufactured by Saint-Gobain [74]. The purpose of the grease is to minimize the refraction of scintillation photons at the contact point between the ZnS(Ag):^{6}LiF and the optical fiber and ensure a better light transmission.

A 10-m long ESKA SH8001 plastic optical fiber, commercialized by Mitsubishi Chemical Co. [75], is selected for the MiMi-0 neutron detector prototype due to its dimensions, characteristics, and availability. The optical fiber is composed of a PMMA core with an average diameter of 1.96 mm and a refractive index of 1.49. The core is covered by a 0.04-mm thick fluorinated polymer cladding of lower refractive index for improving the light-guiding by total internal refraction. A 0.5-mm thick jacket, for a total external diameter of 3 mm, coats the whole fiber length. The jacket protects the core from external damages and avoids infiltrations of parasitic light from the environment. The transmission losses can be considered negligible considering the short fiber length compared to its standard applications.

The front-end part of the MiMi prototype is completed by an aluminum cap covering the ND2:1 scintillator and the optical fiber tip. The optical fiber is uncladded for about 1cm to accommodate the cap and avoid increasing the probe diameter to more than 3 mm. In this first detector version, the cap is secured to the optical fiber with black plastic tape. The purpose of the aluminum cap is twofold: first, it protects the optical fiber from external light photons that could affect the discrimination of neutron events, and second, it minimizes the light dispersion from the scintillator by reflecting the photons that are not emitted in the direction of the optical fiber.

4.2.1.3 Silicon photomultiplier (SiPM)

The rear end of the 10-m optical fiber is connected to a silicon photomultiplier (SiPM) to collect the light photons generated by a neutron interaction in the ND2:1 screen. SiPMs working principles were already discussed in Section 2.4.3.1. A black plastic guide is designed to ensure a perfect coupling between the optical fiber and the SiPM active area, minimizing the diffusion and dispersion of scintillation light photons. Similarly, the SiPM is kept in the dark by being wrapped in several layers of black cloth to reduce as much as possible the background contributions of external light photons interacting with the SiPMs.

The S13360-3050PE [76] SiPM of the Multipixel Photon Counter (MPPC) series produced by Hamamatsu is selected as the best candidate for MiMi neutron detectors. Its 3 × 3 mm area is covered with 3600 avalanche photodiodes (APDs) working in Geiger mode, called pixels. The pixels are connected in parallel and mounted on a monolithic silicon crystal [77]. The S13360-3050PE has a peak wavelength sensitivity of 450 nm, matching the emission peak wavelength of the ND2:1. Its breakdown voltage is 53 ± 5 V, and it can be operated with a recommended overvoltage of 3 V. With a 3 V overvoltage, the photon-detection efficiency is at 40% for 450 nm photons, and the SiPM gain is 1.7×10^6. An overvoltage increase improves the gain and the detection efficiency, but at the same time, it also increases the dark counts and the crosstalks [76]. Hence, an optimal overvoltage is found during the characterization phase of the MiMi prototype (see Section 4.2.2). All the main features of the S13360-3050PE SiPM are reported in Table V.

Table V - Specifications of the S13360-3050PE MPPC silicon photomultiplier by Hamamatsu [76]. (*)Photon detection efficiency does not include crosstalk or after pulses.

Pixel pitch	50 µm	Peak sensitivity wavelength λ_p	450 nm
Effective photosensitive area	3 × 3 mm	Photon detection efficiency PDE(*) $\lambda = \lambda_p$	40 %
Number of pixels	3600	Gain	1.7×10^6
Fill factor	74 %	Breakdown voltage V_{BR}	53 ± 5
Window material	Epoxy resin	Recommended operating voltage	V_{BR} + 3 V
Refractive index window material	1.55	Crosstalk probability	3 %
Operating temperature	-20 to 60 ˚C	0.5 p.e. dark counts	500 kcps (max. 1500 kcps)
Temperature coefficient at recommended operating voltage	54 mV/°C	Terminal capacitance C_t	320 pF
Spectral response range λ	320 to 900 nm	Quenching resistor R_q [77]	150 kΩ

The SiPM output of any detector arrangement similar to the MiMi-0 design would consist of current signals deriving from:

- Thermal neutron reactions with ZnS(Ag):^{6}LiF: generating a large number of photons for a long time period (the scintillator has a decay time of 80 µs to 10%) and reaching the SiPM surface via the optical fiber;

- Gamma interactions in the ZnS(Ag):^{6}LiF screen: expected to be in a limited amount due to the small scintillator thickness and with a small light production not comparable to that of thermal neutron events;
- Background photons: infiltrating at the uncovered part of the front-end optical fiber, along with the fiber jacket, at the coupling with the SiPM, or directly hitting the SiPM surface if not kept in perfect dark conditions.
- Thermally generated dark counts, crosstalks events, and afterglow pulses (as mentioned in Section 2.4.3.1).

It is straightforward that signal processing techniques must be implemented to discriminate thermal neutron events in order to be able to use MiMi neutron detectors in mixed neutron-gamma fields, i.e., in the CROCUS zero-power reactor.

4.2.1.4 Fast processing electronics

The S13360-3050PE SiPM output is processed by fast processing electronics, including a fast preamplifier designed and produced by the LTP group at PSI and a first discriminator stage to transform the SiPM output into a stream of photon counting events.

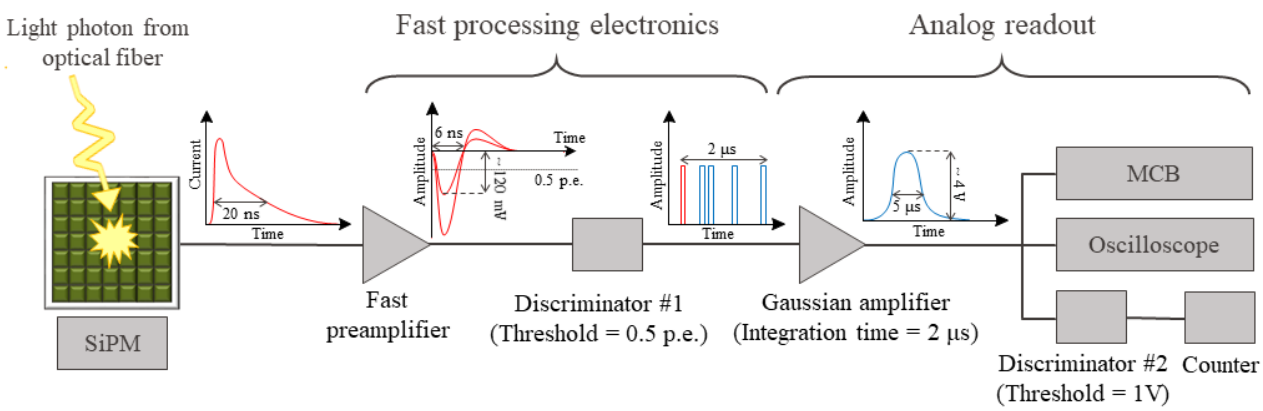

Figure 4.5 – Analog signal processing system for the MiMi-0 prototype with description of the output signal at each stage.

As shown in Figure 4.5, the fast preamplifier generates a short negative output signal in the range of a few ns with an amplitude in the order of hundreds of mV. The amplitude of the preamplifier output signal is proportional to the number of pixels discharged within the preamplifier integration time, which is smaller than the decay time of the SiPM signal. For a single-photon event, the preamplifier output has a unit amplitude of 1 p.e., while multiple single-photon events simultaneous or close in time (or even crosstalks) are represented by amplitudes which are a multiple of the 1 p.e. The preamplifier board includes a compensation circuit of the output signal amplitude depending on the operational temperature of the SiPM.

The following leading edge discriminator, a CAEN N84 4-channels fast discriminator [78], produces a square signal with a fixed amplitude when a preamplifier signal with an amplitude above 0.5 p.e. reaches its input. The prime intent of the first discriminator is to generate individual photon signals

and, at the same time, cut the SiPM and preamplifier electronic noise and the effect of crosstalks. The result is a train of equal square pulses, each corresponding to the detection of one or more photons in short time intervals, i.e., few ns. The density of these pulses strongly increases when a neutron interacts with the ZnS(Ag):^{6}LiF screen. Such density variation is exploited to discriminate thermal neutron events from gammas, background, and dark counts.

The first discrimination stage was included in the readout chain with the intention to count and process the photon train with the fast FPGA digital readout algorithm developed by LTP at PSI [65], [71]. However, in the first stages of the development of MiMi neutron detectors, the stream of photon pulses is read with a standard analog readout system available at LRS. This choice was motivated by the need to have a first assessment of the system's capabilities and set a reference for future upgrades to the readout process.

4.2.1.5 Analog readout

The analog readout system assembled at LRS includes a Gaussian amplifier (CANBERRA Model 2022 [79]), generating a Gaussian output signal of approximately 5 µs width, corresponding to an integration time of 2 µs given by the amplifier shaping time set to 1 µs. The Gaussian pulse amplitude, in the range of a few volts, depends upon the number of photon counting square pulses in the 2-µs time window. Amplifier output signals are either directly read by an oscilloscope (Teledyne Le Croy Wavesurfer 10 oscilloscope [80]), or processed by an MCB multichannel analyzer (ORTEC Model 926 Multichannel Buffer [81]), or sent to a second discriminator stage, as shown in Figure 4.5. The second discrimination, performed by a single channel analyzer (SCA) by Canberra (CANBERRA Model 2030 SCA [82]), produces fixed square signals only when the signal coming from the amplifier exceeds the defined threshold limit. The intent is to cut out noise and gamma contributions and count only thermal neutron events through a simple counter module.

4.2.2 Characterization with the CARROUSEL Pu-Be neutron source facility

After assembling the first prototype of a MiMi neutron detector, i.e., the MiMi-0, as discussed in the previous Section 4.2.1, a series of tests with a plutonium-beryllium (Pu-Be) neutron source installed in the CARROUSEL facility are conducted to characterize the behavior of the detection system and, in conjunction with its fast processing electronics and analog readout, prove that it is able to detect and count thermal neutrons.

4.2.2.1 The CARROUSEL facility

CARROUSEL is a nuclear facility operated in the LRS controlled area. It consists of a Pu-Be neutron source installed at the center of a cylindrical stainless steel (SS) tank filled with water. A three-dimensional section of CARROUSEL is shown in Figure 4.6.

Neutrons are produced via the (α, n) reaction between an α particle generated by the decay of ^{239}Pu and a ^{9}Be nucleus as

$$ {}^{9}_{4}Be + \alpha \rightarrow {}^{12}_{6}C^{*} + n \rightarrow {}^{12}_{6}C + n + \gamma. \tag{4.1} $$

The long ^{239}Pu half-life makes the source a permanent neutron emitter of 8.9 × 10^6 neutrons/s [83] without significant degradations. From this reaction, neutrons are born within an energy spectrum with an average energy of 3.5 MeV and maximum energy of 10.6 MeV. Although different shapes of the neutron emission energy spectrum of Pu-Be sources were measured by Stewart [84] and Anderson and Bond [85], the spectrum of the CARROUSEL source is not characterized. However, it was shown that the neutron spectrum becomes prevalently thermal after 10 cm of distance from the source center [86]. In addition, the de-excitation of the intermediate product ${}^{12}_{6}C^{*}$ produces gamma rays of 4.44 MeV. Consequently, the presence of a mixed neutron-gamma field in the CARROUSEL facility must be taken into account during detector calibration procedures.

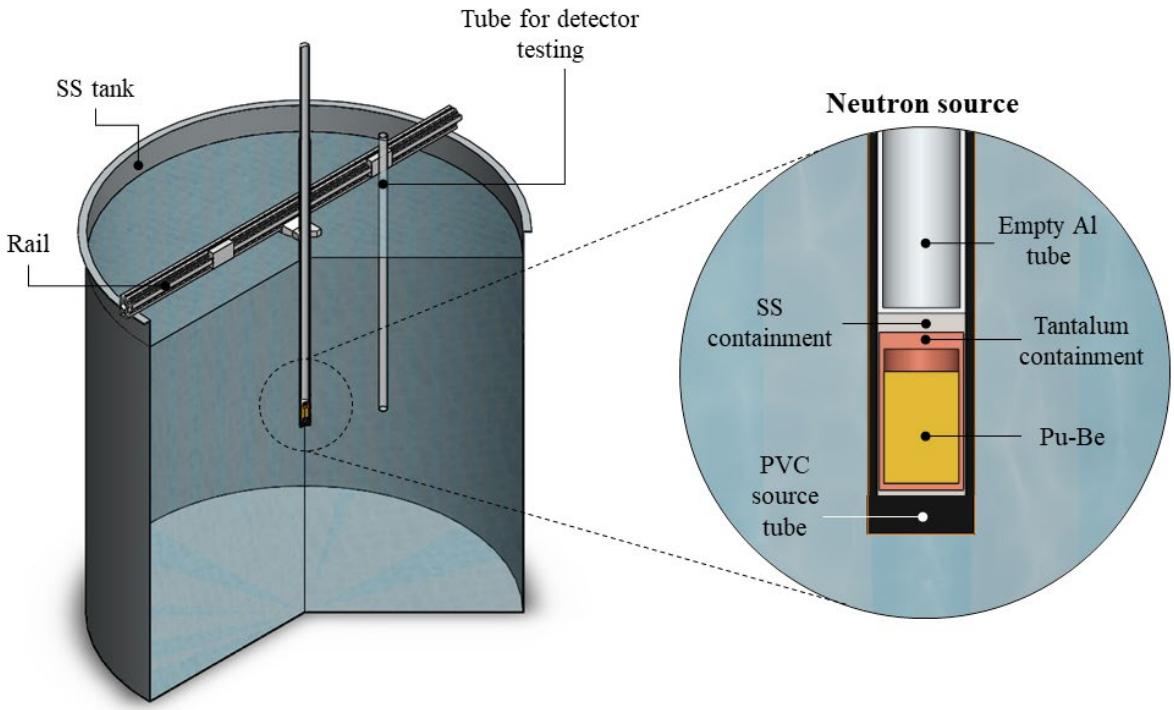

Figure 4.6 – Schematics of the CARROUSEL facility at LRS.

The Pu-Be source has a cylindrical shape, with a double-wall container made of tantalum and welded stainless steel, as shown in Figure 4.6. The source is connected to an aluminum tube for its handling. On occurrence, the source is inserted with the handling tube into a Polyvinyl chloride (PVC) tube of 40 mm of internal diameter and 3.2 mm thickness positioned in the central vertical axis of the water tank. The PVC tube, designed so that the Pu-Be source is located at mid-height of the water tank, is held in position by being attached to a horizontal rail installed above the tank. The same rail is also used to place and move plastic measurement tubes where different neutron detectors are installed at will for teaching and research purposes. Finally, the water tank is filled with industrial water at approximately 12 degrees, and it slowly gets to equilibrium with the controlled area temperature of 20 °C.

4.2.2.2 Experimental setup

The MiMi-0 neutron detector prototype is vertically inserted and positioned at the bottom of a 2-mm thick Plexiglass tube with an internal radius of 8.00 ± 0.05 mm. Considering the experimental channel

inner diameter, a plastic centering tool made of two plastic rings is designed to correctly position the sensitive part of the MiMi-0 detector inside the tube and reduce the uncertainty related to the radial position to ± 0.5 mm. The original purpose of this Plexiglass experimental channel was to accommodate BF_3 neutron detectors with an active volume of approximately 20 cm in height so that they would be aligned with the Pu-Be source. In this case, being only 0.2 mm thick, the active volume of the MiMi-0 is not directly facing the source, but it is offset by approximately -10 cm from the source mid-plane. For the purpose of this test, the axial detector offset is not deemed relevant as long as the same axial level is maintained throughout the test.

The output signals from the different electronic components described in Section 4.2.1.4 are studied. At first, the output signal from the fast preamplifier is studied for the prototype placed at 10.00 ± 0.05 cm distance from the center of the Pu-Be neutron source, and the first discriminator threshold is chosen accordingly. Second, the analog readout system is installed and characterized. In particular, the amplifier signal is thoroughly investigated with both the oscilloscope [80] and the MCB multichannel analyzer [81]. Lastly, the measurement tube and detector are moved at different distances from the Pu-Be neutron source, and the count rate as a function of the radial detector position is recorded.

4.2.2.3 Electronics setup: configuration and optimization

SiPM overvoltage

The amplitude of the fast preamplifier output was recorded as a function of the breakdown voltage applied to the SiPM. The goal was to choose the appropriate overvoltage to be supplied to the SiPM. The results are presented in Figure 4.7. The SiPM voltage of 56.50 V ± 0.05 V was chosen to be employed in all the following measurements because giving a preamplifier output signal greater than 100 mV (in absolute value). The selected value also complies with the range of recommended breakdown voltages declared by the SiPM manufacturer, as previously reported in Table V.

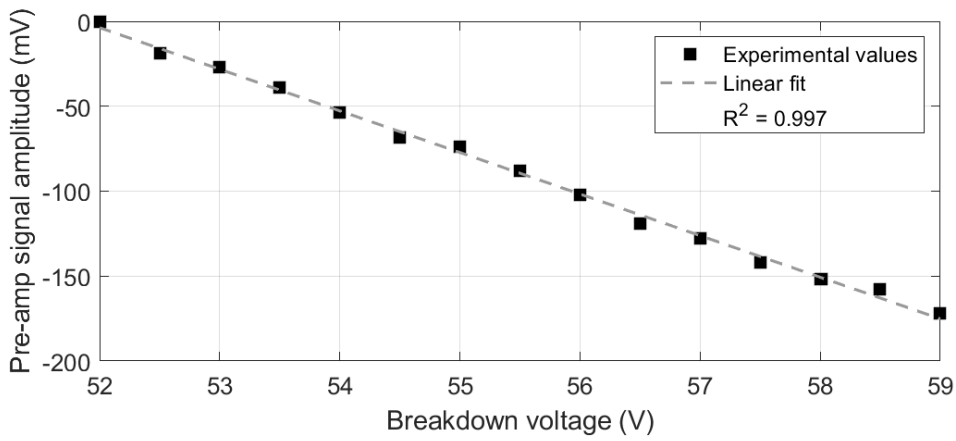

Figure 4.7 – Amplitude of the preamplifier output signal for a single-photon event (1 p.e.) as a function of the SiPM breakdown voltage.

Fast preamplifier signal

Figure 4.8(a) shows the fast preamplifier output signals for the chosen SiPM voltage recorded with the oscilloscope [80] at a sampling rate of 10 GS/s, with the detector positioned at 10.00 ± 0.05 cm.

The output signals have a full-width half-maximum (FWHM) of approximately 3 ns and a total duration of about 6 ns, without considering the overshooting of about 15 ns. As expected, the amplitude assumes discrete values in multiples of approximately 120 mV per single-photon event (p.e.). The discrete nature of the signal amplitude derives from the proportionality with the number of pixels triggered simultaneously in the SiPM, whilst each pixel generates the same amount of charges whether being hit by single or multiple incoming photons.

The same trend is also visible in the pulse height spectrum (PHS) in Figure 4.8(b), showing the number of signals sharing a similar amplitude. The PHS is reconstructed by post-processing the maximum amplitude of 11500 fast preamplifier output signals recorded with the oscilloscope. The maximum amplitude is plotted in absolute value in Figure 4.7(b). Unfortunately, the number of recorded events limits the spectrum statistics. Aside from noise contributions below ~50 mV, it is possible to distinguish one peak at 120 mV and two other peaks at 240 mV and 360 mV, corresponding to the detection of one, two, and three photons, respectively, within the preamplifier integration time. A series of pile-up events are visible between the prominent peaks, while it is reasonable to assume that the counts after ~550 mV correspond to the first light burst coming from a thermal neutron detection. Indeed, when a neutron interacts with the scintillator, a large quantity of light reaches the SiPM cells in the first instants so that the pre-amplifier signal amplitude may reach values up to 2 V. Only 1% of the recorded signal is above 1 V, and thus it is not displayed in Figure 4.8(b). The first light burst is then accompanied by a slow decay of the emitted light.

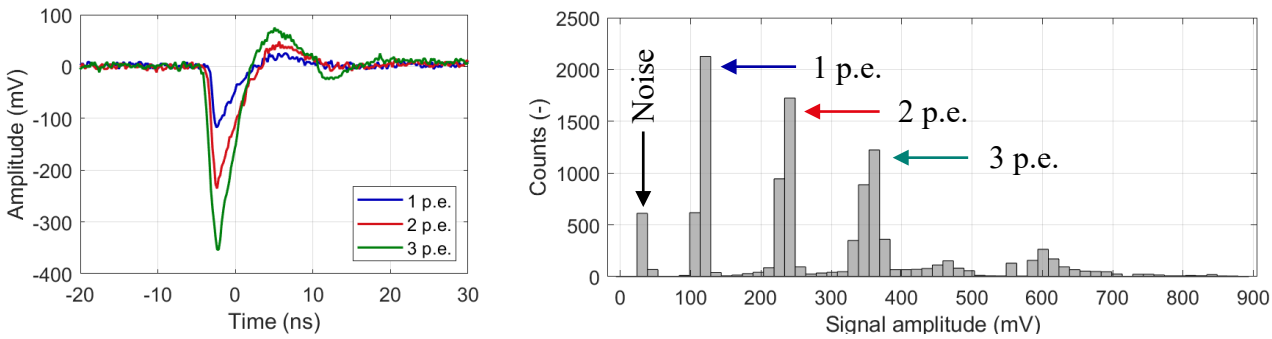

(a) (b)

Figure 4.8 – (a) Example of fast pre-amplifier output signal recorded with the oscilloscope. (b) Pulse height spectrum at the fast pre-amplifier output with an applied breakdown voltage of 56.0 ± 0.05 V.

SiPM threshold

The preamplifier PHS serves to determine the threshold at which the first discriminator is set to cut noise and convert in square pulses all the events, i.e., 1 p.e. and above. The threshold value, called from now on "SiPM threshold" to be distinguished from other discrimination levels discussed later, was set to half the amplitude of the single-photon signal (0.5 p.e.), corresponding approximately to -60 mV. The chosen first discriminator module, the CAEN N84 [78], has no indication of the threshold level on the analog regulation of the latter. Therefore, the SiPM threshold is set by simply testing the discriminator's capabilities to digitalize all the signals corresponding to one or more photon events.

Gaussian amplifier signal

As mentioned in Section 4.2.1.4 and shown in Figure 4.5, the first discriminator output is sent to a Gaussian amplifier in this analog configuration of the readout electronics. The amplifier output signal has an amplitude proportional to the density of photon counting events occurring within the amplifier module integration time of 2 µs. An example of the output signals from the electronic modules up to the Gaussian amplifier during a light burst, like the one following a thermal neutron interaction in the ZnS(Ag):^{6}LiF screen, is shown in Figure 4.9.

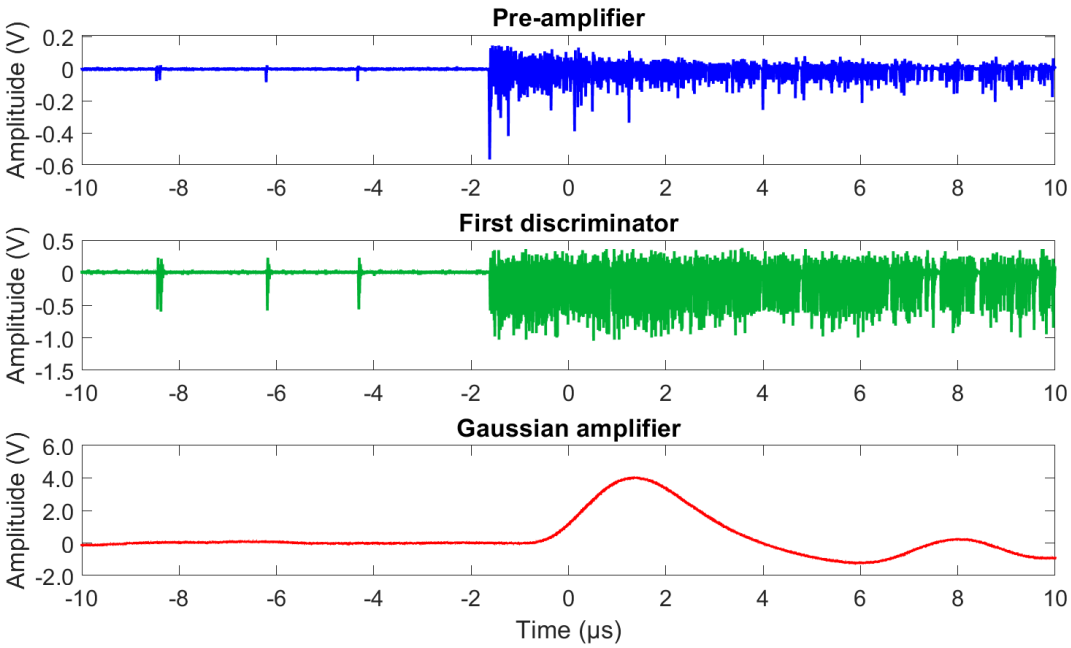

Figure 4.9 – Example of the output signal from different electronic components during the detection of a light-burst event, as the one due to a thermal neutron interaction in the ZnS(Ag):^{6}LiF screen.

A PHS of the amplifier output signal is recorded at the distance of 10.00 cm ± 0.05 cm via the MCB module connected to a computer. The amplifier PHS is visible in Figure 4.10. Aside from the noise contribution, the spectrum shows a clear peak and a tail toward lower amplitudes, corresponding to a lower density of the digital pulses in the photon train signal. Assuming that all the recorded events derive from a neutron interaction, a reduced density of photons can be caused by the escape of light from the screen, by the light attenuation in the screen volume itself being the ZnS an opaque material, and also due to possible light dispersion in the fiber length or in the coupling between the fiber and the SiPM. It is important to remark that no other peak is visible in the spectrum, suggesting that no other radiation types are detected in the miniature ZnS(Ag):^{6}LiF screen or, if detected, contribute only to the noise. In addition, the ORTEC MAESTRO-32 software [87] recording the amplifier PHS takes into account and corrects the counting by the system dead time, being the time interval in which the detector is not available for detecting other events. In this case, the system dead time is estimated to be 0.6%.

The calibration of the spectrum obtained with the MCB module is performed through the acquisition with the oscilloscope of 3.3×10^{3} signals and their postprocessing. As shown in Figure 4.11, it is possible to reconstruct the whole spectrum with this method, but the amount of data to be

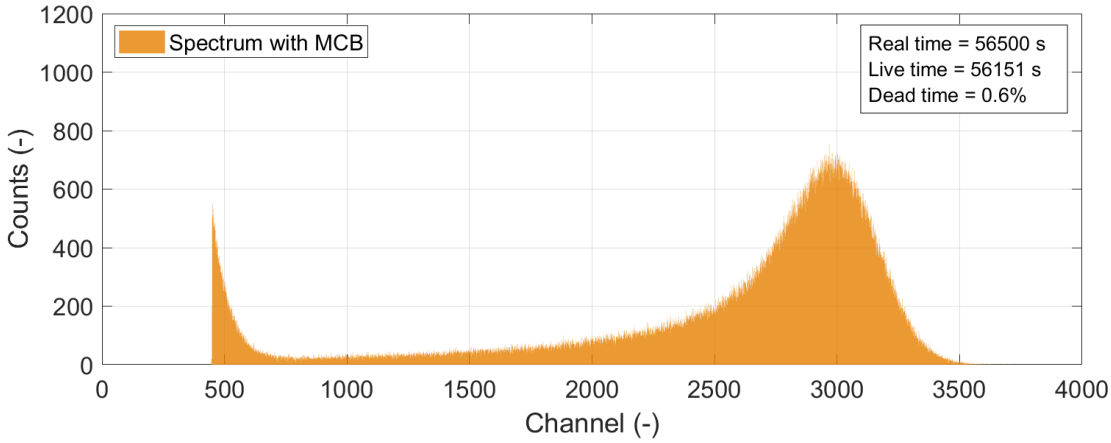

Figure 4.10 – PHS of the amplifier output signal, acquired for MiMi-0 prototype at a distance of 10.00 cm ± 0.05 cm from the Pu-Be source. The horizontal axis is not calibrated.

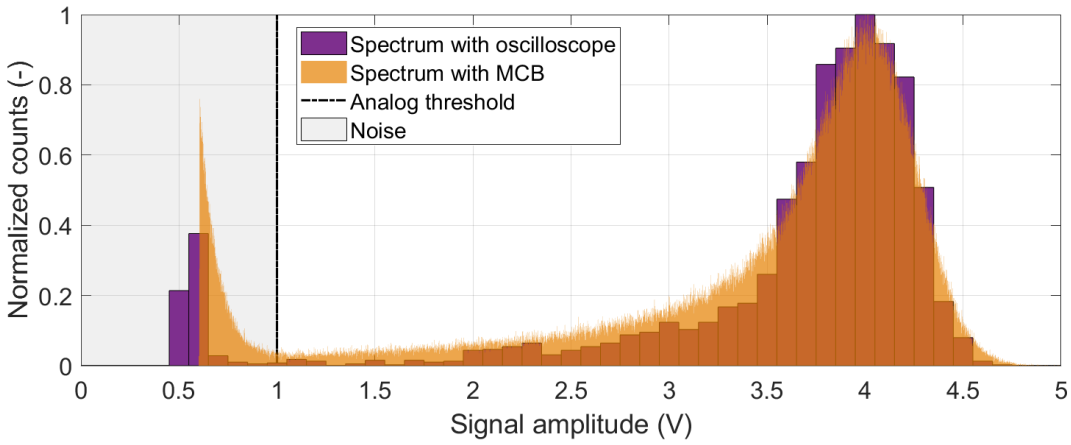

Figure 4.11 – Calibrated PHS, acquired with oscilloscope and MCB module for MiMi-0 prototype at 10.00 cm ± 0.05 cm from Pu-Be source.

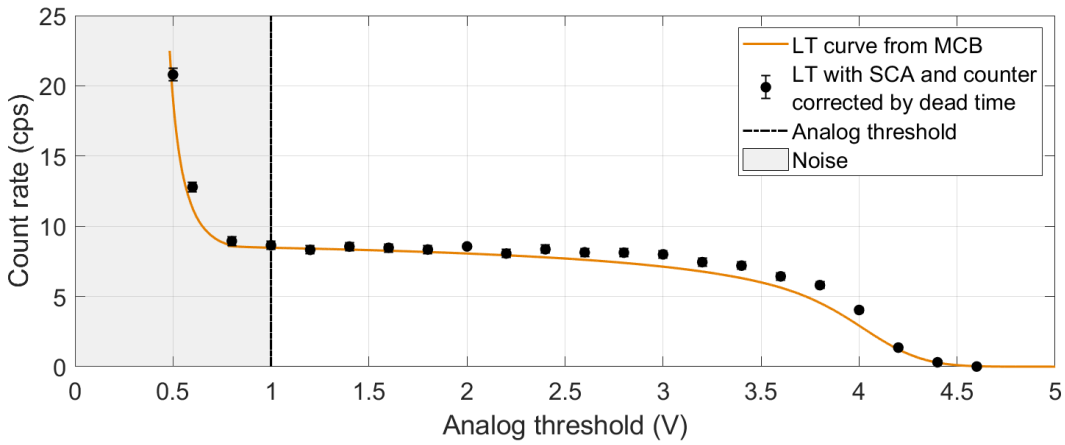

Figure 4.12 – Low-threshold (LT) curves reconstructed from the spectrum and acquired with an SCA and a counter. The uncertainty on the MCB-reconstructed LT curve of ±0.004 cps is not reported.

stored and the lack of time information make this approach less practical than using an MCB module. However, it is possible to characterize the peak amplitude of Gaussian signals, equal to approximately 4 V.

Analog threshold

Depending on the amplitude of the Gaussian amplifier signal, thermal neutron interactions occurring in the active volume of the MiMi-0 prototype are discriminated from the noise contributions. An "analog threshold" is set by an SCA on the Gaussian amplifier output signal. Every amplifier signal with an amplitude above the analog threshold is converted into a square pulse. The number of pulses is counted by means of a simple counter module.

By varying the selected analog threshold, it is possible to reconstruct the low-threshold (LT) curve for the Gaussian amplifier signal. The LT curve represents the count rate of amplifier signals above the analog threshold as a function of the threshold itself. The LT curve is directly reconstructed from the post-processing of the PHS obtained with the MCB and compared with the count rates recorded by the combination of an SCA with a variable analog threshold and a simple counter. The results, presented in Figure 4.12, show a general agreement between the trend of the two sets of count rate values. Based on the LT curve, the analog threshold for the MiMi prototype detector is chosen to be 1 V, as shown in Figure 4.11 and Figure 4.12. A 1-V threshold is deemed appropriate to discriminate relevant events from background noise. The assessment of the nature of such relevant events is discussed in Section 4.2.2.4.

Final output

The count rate recorded for the prototype of the MiMi-0 neutron detector positioned at 10.00 ± 0.05 mm from the Pu-Be source and connected to an analog readout electronics with the settings reported in Table VI is equal to 8.467 ± 0.012 cps.

Table VI – Settings of the analog signal processing electronics.

SiPM voltage	56.50 ± 0.05 V	
Fast pre-amplifier voltage	6 V	
SiPM threshold	about -60 mV	
Gaussian Amplifier	Coarse gain	30
	Fine gain	8.0
	Shaping time	1 µs (2 µs integration)
Analog threshold	1 V	

4.2.2.4 Proportionality check with Pu-Be source

After testing and characterizing the electronic components, it is necessary to assess if the event counting has a physical meaning. In particular, whether the count rate of the MiMi-0 neutron detector prototype is proportional to the volume-integrated and energy-integrated ^{6}Li reaction rate and thus to the total neutron flux at the detector position in the CARROUSEL facility, as described by Equation (2.10). Considering the miniature dimensions (< 1 mm^3) of the active volume of the MiMi-0 prototype, the proportionality is expressed as a function of the point-wise total neutron flux.

Assuming that the Pu-Be source is an isotropic point source in a non-multiplying spherical medium, the steady-state one-group diffusion equation (described in Section 2.1.5) at distance from the source is described by:

$$D\Delta\phi(r) - \Sigma_a\phi(r) + S = 0 \tag{4.2}$$

where Σ_a is the macroscopic absorption cross-section and S is the term describing the isotropic point source. The solution of Equation (4.2) yields to

$$\phi(r) = \frac{S}{4\pi D}\frac{e^{-r/L}}{r} \tag{4.3}$$

Where L is the diffusion length. Therefore, assuming that the detector count rate as a function of the radial coordinate CR is proportional to the neutron flux ϕ, the following linear trend should be followed by the detector response:

$$\ln(CR \times r) = -\frac{r}{L} \tag{4.4}$$

The count rate of the MiMi-0 prototype as a function of the radial distance from the CARROUSEL Pu-Be source is recorded by moving the experimental tube on which the detector is installed. The experimental results are shown in Figure 4.13.

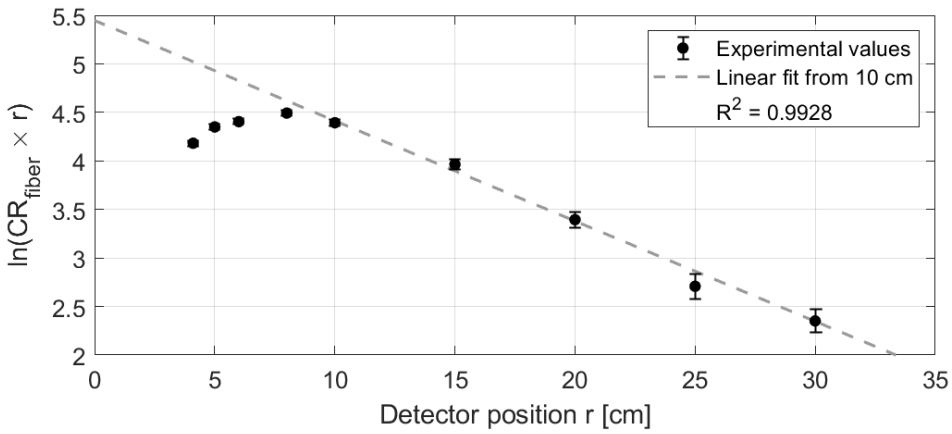

Figure 4.13 – Radial dependence of the MiMi-0 prototype count rate in the CARROUSEL facility.

The relationship described in Equation (4.4) is followed for radial distances above 10 cm from the neutron source, corresponding to the region where the neutrons born fast from the Pu-Be neutron source are slowed down to the thermal energy range. The linear fit of the experimental values after 10 cm is shown in Figure 4.13, and it proves the proportionality between the count rate of the MiMi neutron detector and the neutron flux in CARROUSEL. In particular, this result proves that the MiMi neutron detector prototype is successfully counting thermal neutrons.

At distances shorter than 10 cm, the experimental points are not represented by the linear fit because they are out of the applicability range of the diffusion theory from which the analytical solution is

derived. From an experimental point of view, the detector count rate saturates instead of exponentially increasing in the proximity to the Pu-Be neutron source. The saturation is caused by a combination of the harder neutron spectrum (due to the higher share of fast neutrons born from the source) with the exponential decrease of the ^{6}Li(n,α) reaction cross-section at high energies that reduces the number of neutron interactions within the ZnS(Ag):^{6}LiF scintillator. This spectral effect is taken into account if the experimental data are compared with the results of Monte Carlo simulations [86].

The experimental results obtained with this test are sufficient to conclude that the MiMi-0 neutron detector prototype counts predominantly thermal neutrons, proportionally to the energy-integrated ^{6}Li reaction rate in its miniature active volume. However, a mixed neutron-gamma field is present in the CARROUSEL facility. Therefore, it is necessary to assess if gamma rays interacting in the miniature scintillator volume contribute to the total counting.

4.2.3 Gamma sensitivity test

Although the induced ionization by a single gamma ray in a 0.2 mm^{3} ZnS(Ag) scintillator might be negligible due to the minimal energy release in such a small volume [12], multiple simultaneous gamma interactions could lead to an increased density of photon counting pulses. This gamma pile-up effect could generate a Gaussian amplifier signal similar in amplitude to the one obtained after a neutron interaction. Therefore, the goal of the current test is to complete the characterization of the MiMi-0 prototype by assessing its gamma sensitivity while exposing it to a pure gamma field, such as the one available from the SILC irradiator installed in the LOTUS cavity.

4.2.3.1 The LOTUS facility

The LOTUS facility, operated at LRS, was born as a facility to test materials for nuclear fusion technologies using a deuterium-tritium (DT) neutron generator [88]. It has recently been converted into an irradiation cavity with a 2.2-m thick concrete shielding. Inside the cavity, a gamma beam irradiator named System of Irradiation in the LOTUS Cavity (SILC) and designed by Hopewell Design, Inc. [89], contains a 10 Ci (370 GBq, as of October 2015) ^{60}Co gamma source [90] used for irradiation experiments. The device includes a shielded irradiator that allows for safe source usage and the possibility to irradiate with a horizontal collimated beam thanks to a tungsten and lead collimator. The ^{60}Co source is doubly encapsulated in stainless steel and hermetically sealed. The source is held by a steel and tungsten source rod and incorporated into the irradiator. The source is moved from the storage to the exposed position using a pneumatic system controlled from outside the cavity.

4.2.3.2 Experimental setup

The MiMi-0 active volume is placed in front of the aperture of the collimated gamma beam at a distance of about 25 cm from the ^{60}Co source. The ^{60}Co source activity is estimated to have an activity of approximately 250 GBq at the time of the experiment. The optical fiber is connected to the readout analog electronics placed outside the concrete shielding by passing through an experimental hole. The same settings of the analog readout electronics used during the tests in CARROUSEL are used in this test to avoid biases. A schematic of the experimental setup is shown in Fig. 14.

The number of interactions in the detector's active volume is acquired for two days and 17 h with the analog electronics connected to a counter. Afterward, the oscilloscope is used to acquire 1043 signals to be post-processed for the reconstruction of the PHS.

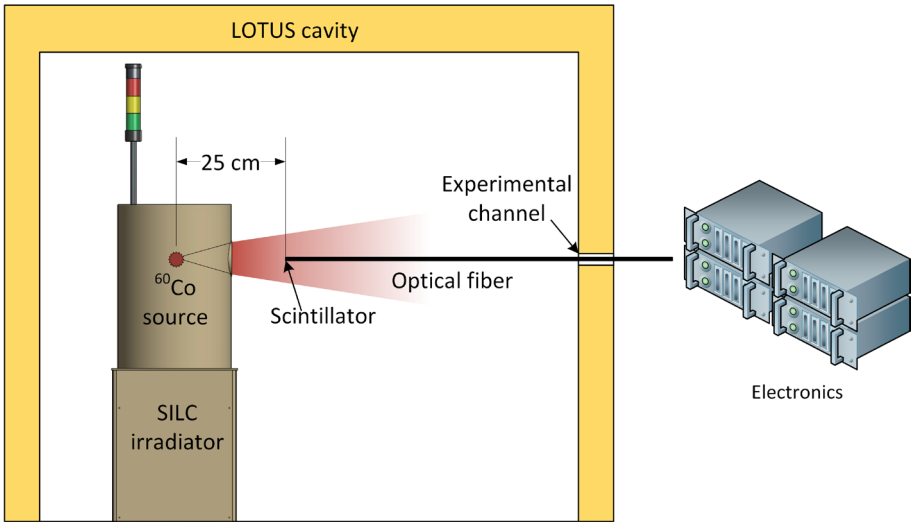

Figure 4.14 – Schematic of the experimental setup installed in the LOTUS cavity to test the gamma sensitivity of the MiMi-0 neutron detector prototype.

4.2.3.3 Results and discussion

In the first measurement performed in the LOTUS facility, only 204 recorded events showed an amplitude above the analog threshold of 1 V, for a count rate of $(8.7 \pm 0.6) \times 10^{-4}$ cps. It is reasonable to deduce that this small number of counts, for a count rate equal to the 0.01% of the one measured in CARROUSEL, might originate from either noise or gamma pile-up.

The amplifier PHS reconstructed after the postprocessing of 1043 signals acquired in LOTUS with the oscilloscope is compared to the one measured in CARROUSEL in Figure 4.15. Both spectra are shown on a logarithmic scale and are normalized by their maximum value. The LOTUS spectrum, obtained from the exposure of a pure and strong ^{60}Co source, presents an average amplitude of 0.4 V,

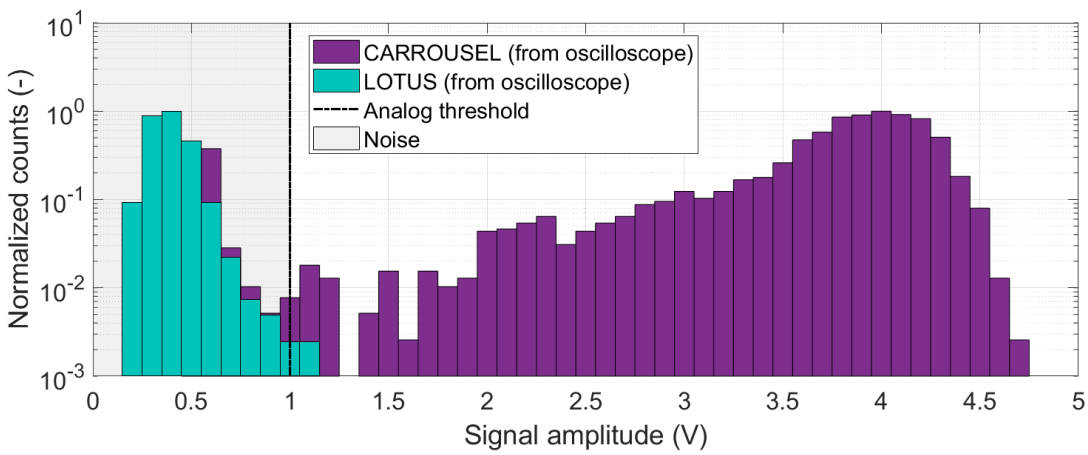

Figure 4.15 – Pulse height spectra reconstructed from post-processed oscilloscope signal in CARROUSEL and in LOTUS for the MiMi prototype.

with only two contributions above 1 V. These two events, being the 0.2% of the total registered counts, are the only ones with an amplitude of the Gaussian amplifier signal above or equal to 1 V, similarly to neutron interactions. Although the high statistical uncertainties, it is possible to conclude that gamma pile-up events represent a negligible contribution to the MiMi detector output measuring in the LOTUS gamma field.

The gamma flux and the average gamma energy in LOTUS are estimated by knowing the source activity, the decay scheme of ^{60}Co, and the source positioning, assuming that the ^{60}Co source is a point source. The gamma flux in the MiMi prototype's active volume is calculated as:

$$\phi_{LOTUS} = A \cdot \frac{\Omega}{4\pi} \cdot n_\gamma \cdot \frac{1}{S} \tag{4.5}$$

where A is the source activity, n_γ is the average number of gamma rays produced per decay, which is approximately two according to the ^{60}Co decay scheme, and S is the ZnS(Ag):^{6}LiF surface of 1 mm^2. The solid angle Ω between the ^{60}Co source and the scintillator surface is

$$\Omega = 2\pi \cdot \left(1 - \frac{d}{\sqrt{d^2 + r^2}}\right) = 1.6 \times 10^{-5} \tag{4.6}$$

Where d represents the distance of 25 cm between the source and the scintillator and r is the scintillator screen radius equal to 0.56 mm (calculated approximating the screen shape to a cylinder with a 1-mm^2 upper face).

The gamma flux in the scintillator volume during the test in LOTUS is calculated to be equal to 6.4×10^7 γ·cm^{-2}·s^{-1}, with average gamma energy of 1.25 MeV. On the basis of the measured count rate and the estimated gamma flux, the count rate per unit flux in a pure gamma field, equivalent to the gamma sensitivity of the MiMi detector, is $(1.37 \pm 0.09) \times 10^{-11}$ cps/(cm^{-2}·s^{-1}) for gammas at around 1.25 MeV.

4.2.4 Test in the CROCUS reactor

An experimental campaign in the CROCUS reactor is conducted to test and assess the performance of the MiMi-0 neutron detector prototype in a zero-power reactor environment. In particular, the primary intents are to prove the linear behavior of the thermal neutron count rate of the MiMi-0 neutron detector prototype as a function of the CROCUS reactor power and define its range of applicability in CROCUS.

4.2.4.1 Experimental setup in CROCUS

The front end of the MiMi-0 detector prototype is inserted into the empty guide tube of the northwest (NW) control rod guide tube of the CROCUS reactor, as indicated in Figure 3.2. The guide tube is dedicated primarily to inserting a B_4C absorber control rod for reactivity control. Since the reactor power level can also be controlled by adjusting the water level or inserting the other symmetrical control rod, the NW guide tube can be left empty and used as an experimental channel. The prototype is positioned so that the scintillator lies in the center of the control rod guide tube (with the aid of the same plastic centering tools used in the CARROUSEL testing) in correspondence to the active core geometrical mid-height of 50.0 cm ± 0.5 cm from the bottom of the fuel. At this position, the total

neutron flux is approximately at its maximum, depending on the critical water level. The 10-m plastic optical fiber passes through the reactor's lateral experimental channel and reaches the electronics, from the SiPM to the analog readout system, installed outside the biological shield of the reactor. The whole signal processing chain is set up by maintaining the same parameters chosen during the characterization in the CARROUSEL facility (see Section 4.2.2).

The detector thermal neutron count rate is acquired at several reactor conditions. At first, a background acquisition with the reactor in the shutdown state, i.e., without water in the reactor pool, is performed for 38.5h. The detector count rate is then recorded at different stages after the insertion of the external Pu-Be and the water filling-up procedure until the core criticality is achieved at a water level of 957.8 ± 0.1 mm and a power of 40 mW. Afterward, the detector count rate is measured at different power levels to test the linearity of the detector's response with increasing reactor power and neutron fluence rate.

4.2.4.2 Results and discussion

The in-core background measurement of 38.5 h shows a detector count rate of 1.7×10^{-4} cps with a 20% statistical error. This result proves that the detection system does not count a significant amount of events related to background radiation or fuel activation. Hence, it gives a first indication of the gamma insensitivity of the MiMi-0 prototype.

Once the external neutron source is inserted, an increase in the detector count rate is observed. A detector count rate of 6.0 ± 0.2 cps is recorded at the stable subcritical reactor configuration with the water level at 800.0 ± 0.1 mm. A further increase in the detector count rate is observed during the increase of the water level to approach the reactor's criticality, corresponding to 957.8 ± 0.1 mm of water in this reactor configuration. A count rate of 168.4 ± 1.0 cps (0.6% error) is measured at a critical reactor state for a power of 40 mW.

The linearity of the detector count rate is then tested by increasing the reactor power from 40 mW up to 10.8 W, corresponding approximately to a total neutron flux in the range from 10^5 to 10^8 $cm^{-2}\cdot s^{-1}$ in the detector position. The count rate acquired with the analog readout electronics is reported in Table VII and plotted in Figure 4.16 as a function of the reactor power. The reactor power is obtained from the out-core monitor fission chamber of CROCUS, which is calibrated using the gold foil activation technique [54].

The evolution of the count rate shows a good capability of the MiMi-0 prototype to linearly respond to the increase of the reactor power up to 6.5 W, corresponding to a total neutron flux of approximately 7.7×10^7 $cm^{-2}\cdot s^{-1}$ and a thermal neutron flux of 3.2×10^7 $cm^{-2}\cdot s^{-1}$ in the NW control rod guide tube at core mid-height, calculated with Serpent 2 Monte Carlo simulations. The loss of linearity above 6.5 W is expected to be caused by standard detection dead time. Indeed, the Gaussian amplifier integrates the pulses reaching its input in the time interval of 2 μs, and thus photon train pulses deriving from different neutron interactions might be read together, contributing to a single amplifier pulse. The difficulty in discriminating different events becomes relevant at higher reactor power, where the neutron count rate increases significantly. This limitation might be partially overcome by reducing the shaping time of the Gaussian amplifier to have better discrimination between different neutron events at higher neutron flux rates.

Table VII – Count rate of MiMi-0 prototype acquired at different power levels of CROCUS.

Power (W)	Count rate (kcps)	Error (%)
0.125	0.441 ± 0.002	0.5
0.2	0.677 ± 0.003	0.5
0.5	1.717 ± 0.007	0.4
0.8	2.778 ± 0.010	0.4
1	3.368 ± 0.018	0.5
1.25	4.37 ± 0.02	0.5
1.57	5.42 ± 0.02	0.4
2.035	6.99 ± 0.03	0.4
3	10.33 ± 0.03	0.3
4.9	16.57 ± 0.04	0.2
6.5	21.35 ± 0.05	0.2
8.85	25.48 ± 0.05	0.2
10.8	26.70 ± 0.05	0.2

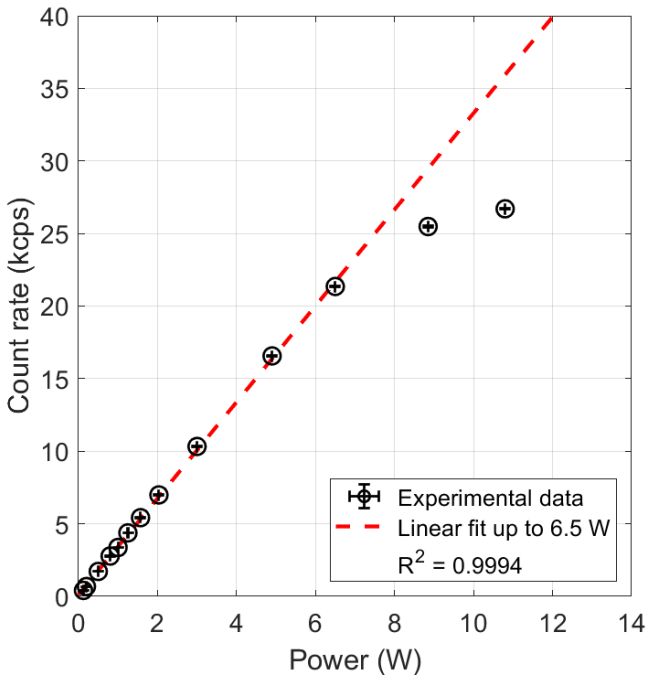

Figure 4.16 – MiMi-0 prototype count rate as a function of the CROCUS reactor power (with uncertainty < 0.1%). Data are linearly fitted up to 6.5 W.

The spectrum acquired with the MCB module in CARROUSEL (already shown in Figure 4.11) is compared to the one obtained in CROCUS at 100 mW in Figure 4.17 (a), using a logarithmic scale. The spectrum in the reactor presented here is acquired at the power of 100 mW to obtain better

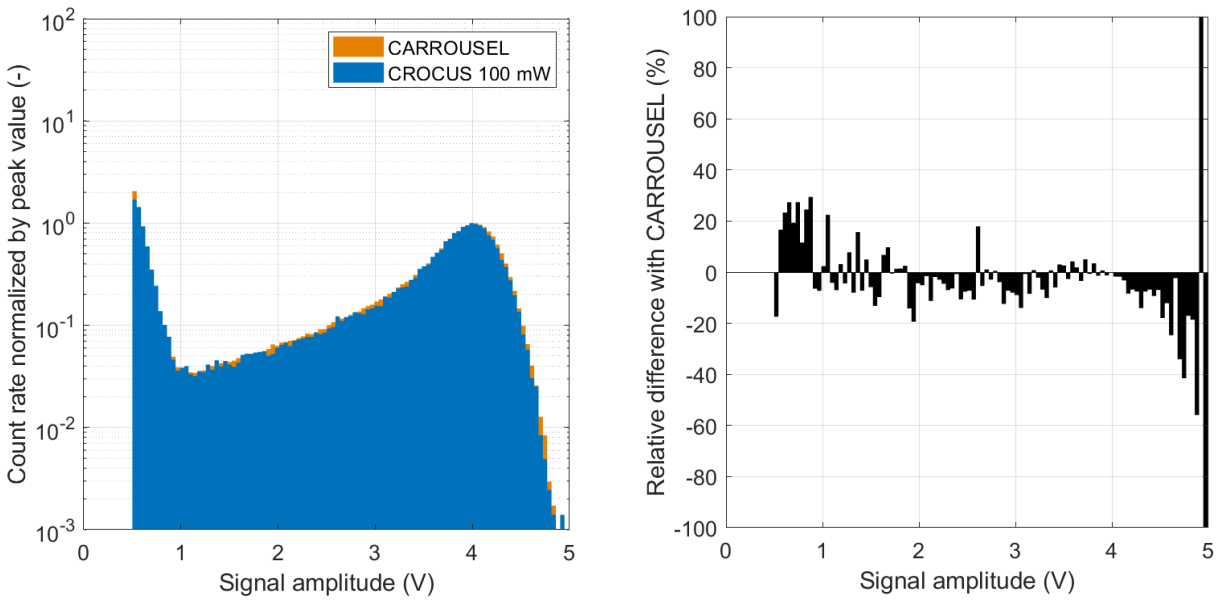

(a) (b)

Figure 4.17 – (a) Comparison between the spectra obtained in CARROUSEL and in CROCUS (critical at 100 mW) with the MCB. Both spectra are shown in logarithmic scale after re-binning. (b) Relative difference between the two spectra.

statistics. The two spectra, normalized by their peak value after re-binning in order to increase statistics, present a similar shape. The relative difference between the two spectra is shown in Figure 4.17(b).

4.2.4.3 Incident gamma flux on MiMi prototype in CROCUS

In the present subsection, the goal is to ensure that the count rate of the MiMi-0 neutron detector prototype in CROCUS is well representing only the thermal neutron interactions. Although the gamma spectra are different, the flux and average energy of the gamma rays interacting with the ZnS(Ag):^{6}LiF volume during the irradiation in CROCUS are estimated to be sufficiently comparable with the conditions of the LOTUS test.

The prompt gamma flux is estimated with a full-core coupled neutron-photon criticality calculation [91] with the Serpent 2 Monte Carlo code [91], based on previous work [92]. The volumetric prompt gamma flux at the detector position in the NW control rod of CROCUS is tallied for a reactor power of 100 mW. The water level was set at the critical level of 957.8 cm. The ENDF/B-VII.0 [93] nuclear data library is used for both neutron and photon transport. From the simulation results, the prompt gamma flux at the NW control rod mid-height is equal to $(6.9 \pm 0.5) \times 10^{5}$ gamma·cm^{-2}·s^{-1}, with a gamma energy spectrum with an average of about 1 MeV. In a Master's thesis work at LRS [94], the delayed gamma fraction in the NW control rod of CROCUS was estimated to be equal to approximately 30% of the total gamma flux, and thus an additional contribution is added to the simulated prompt gamma flux for a total of $(9.8 \pm 0.5) \times 10^{5}$ gamma·cm^{-2}·s^{-1}. The results from the evaluation of the irradiation conditions in LOTUS and CROCUS are summarized in Table VIII.

Table VIII – Comparison of gamma irradiations condition in CROCUS and LOTUS.

	Gamma flux (cm^{-2} · s^{-1})	Average gamma energy (MeV)	Gamma count rate in MiMi-0 prototype
CROCUS - NW control rod at 100 mW	$(9.8 \pm 0.5) \times 10^{5}$	~ 1.00	$(1.67 \pm 0.14) \times 10^{-5}$ cps (estimate)
SILC in LOTUS - (^{60}Co)	6.4×10^{7}	1.17 and 1.33 (1.25 on average)	$(8.7 \pm 0.6) \times 10^{-4}$ cps (measured)

For a comparable average gamma energy, the calculated gamma flux in CROCUS is approximately one order of magnitude smaller than in LOTUS at a 25-cm distance from the gamma source. Knowing the pure gamma sensitivity of $(1.37 \pm 0.09) \times 10^{-11}$ cps/(cm^{-2}·s^{-1}) from Section 4.2.3.3, it is possible to derive the count rate deriving from gamma events in the NW control rod guide tube of CROCUS at 100 mW. If a linear law is assumed to relate the detector count rate and the gamma flux, while the gamma energy is related by an inverse proportionality with the gamma absorption cross-section in the Compton regime [95], the gamma count rate would be approximately $(1.67 \pm 0.14) \times 10^{-5}$ cps. Despite the 9% uncertainty, this quantity represents a fraction of about 10^{-8} of the counts detected during the experimental campaign. Therefore, it is possible to conclude that the contribution of gamma interactions is negligible in a mixed neutron-gamma radiation field like the one inside the CROCUS reactor for the MiMi-0 neutron detection technology with a selected analog threshold of 1 V.

4.2.4.4 Comparison with other in-core instrumentation

Other measurements in the same position and irradiation conditions, i.e., criticality and same neutron and gamma spectra, were performed in CROCUS with other neutron detector designs in the years. All the neutron detectors were placed in the guide tube of the NW control rod at approximately 50 cm from the bottom of the active core zone (corresponding to the lower level of the fuel). The neutron count rate of a BF_3 proportional counter (PC, type Transcommerce MN-1) with an active length of 10 cm and a diameter of 7.5 mm placed in the same aforementioned position is about 180000 cps/W [96], whereas the value registered by the Cividec single-crystal vapor deposited (sCVD) diamond detector equipped with a ^{6}Li converter layer is 150 cps/W [33]. In the same position, a miniature fission chamber (MFC, Photonis CFUR44/EP-M3 type with 130 µg of ^{235}U) displays 560 cps/W, while the MiMi-0 neutron detector prototype gives a count rate equal to 3368 cps/W. The count rate comparison between the different neutron detectors is summarized in Table IX. In the same table, the order of magnitude of the sensitivity to the thermal neutron flux and its value per unit active volume are reported.

Table IX – Comparison of performances for different neutron detection technologies.

Detector type	Neutron count rate per unit power (kcps/W)	Sensitivity to thermal neutrons (cps/n_{th})	Sensitivity to thermal neutrons per unit active volume ($cps/n_{th}/cm^3$)
Cividec sCVD diamond	0.15	10^{-5}	10^{-2}
Photonis CFUR44 MFC	0.56	10^{-4}	10^{-5}
MiMi-0 prototype	3.37	10^{-4}	10^{0}
Transcommerce MN-1 BF_3 PC	180	10^{-2}	10^{-4}

4.2.5 Summary of MiMi neutron detectors features

The MiMi-0 neutron detector prototype was characterized and its performances in mixed neutron-gamma irradiation fields were assessed with the series of tests conducted in this section. The main characteristics of MiMi neutron detectors, based on the prototype testing, are summarized as follows:

- **Miniature dimensions**: the detector's active volume is below 1 mm^3, and the maximum detector dimension is represented by the optical fiber diameter of 3 mm. With such dimensions, a MiMi detector can be positioned in numerous in-core locations of interest in the CROCUS core, as done in Chapter 5 and Chapter 6, for high-resolution neutronics measurements;

- **Minimal flux perturbation**: it is reasonable to assume that the miniature dimensions contribute to a highly localized perturbation of the neutron flux map with minimal changes in the local moderation. Hence, the MiMi technology has the potential to be used for low-invasive measurements of neutronics effects and unperturbed 3D neutron flux maps;

- **High thermal neutron sensitivity**: compared to other neutron detection technologies, the MiMi-0 prototype shows an excellent thermal neutron sensitivity of 10^{-4} cps/n_{th}. The high counting efficiency, combined with the miniature dimensions, makes it a perfect candidate to study localized effects in the CROCUS reactor with an unprecedented spatial resolution (demonstrated in Chapter 5 and Chapter 6);

- **Linearity up to ~10^7 $cm^{-2}\cdot s^{-1}$ neutron flux**: even if the MiMi-0 prototype responds linearly only to a limited range of reactor power in CROCUS, it is possible to investigate in this range local and spatial-dependent neutronics phenomena with a good counting efficiency. It is reasonable to expect that the range of applicability can be extended by reducing the amount of sensitive material and thus limiting the dead-time effects;

- **Minimalistic design**: the simple detector design facilitates in-house manufacturing and drastically reduces production costs, lying mainly in electronics. The lack of an applied voltage to the active volume reduces the likelihood of being subject to radiation- or vibration-induced electronic noise as other standard technologies;

- **Flexibility:** the detector's active volume can be sized and shaped according to the desired application, taking into account that a reduction of the ZnS(Ag):^{6}LiF screen also causes a reduction in the detector sensitivity. In addition, multiple MiMi detectors can be arranged together to build detectors arrays (as in Chapter 6) or meshed instruments;

- **Online acquisition:** the local thermal neutron count rate can be acquired online with different readout systems. The characterization of the analog readout will be followed by the development of scalable processing electronics (in Section 4.3.1) to be used in combination with a multi-channel digital acquisition system (in Section 4.3.2);

- **Parallelization:** the easy manufacturing and the use of a multi-channel digital acquisition system with an FPGA algorithm based on MSD (designed by LTP) to convert photon counts into thermal neutron counts would allow the multiplication of the number of detection channels that can be acquired simultaneously. In the following Section 4.3, the upgrade to 160 channels is discussed.

4.3 Upgrade for multi-channel applications

Building an array of neutron detectors to investigate local and space-dependent phenomena in a reactor core requires, as a pre-requisite, the possibility to multiplicate the number of available detectors and the associated signal processing channels at an affordable cost. For this purpose, the MiMi neutron detectors are a straightforward choice due to their simplicity in design and their flexibility in applications, among their many features. However, the signal processing electronics and the readout system employed with the first prototype version impose limitations in the parallelization of the acquisition channels due to the high cost of standard modules.

In view of the installation of a large array of MiMi neutron detectors in CROCUS, a process of optimization of the MiMi neutron detector technology for multi-channels applications is initiated internally at LRS. In particular, the optimization concerns:

- The upgrade to scalable processing electronics, with stand-alone capabilities and optimized for Field Programmable Gate Array (FPGA) acquisitions;
- The upgrade of the readout electronics from analog to digital for simultaneous acquisition of the thermal neutron counting of a high number (>150) of MiMi detectors;
- The reduction of the total dimension of MiMi detectors for a better fit within the CROCUS double fuel lattice for 3D full-core mapping in inter-pin positions and potentially for intra-pin experiments.

4.3.1 Parallelizable processing electronics

The fast processing electronics and the analog readout system employed for the first testing of the MiMi-0 neutron detector prototype were designed specifically to acquire the thermal neutron count rate from a single detector. Indeed, the fast preamplifier stage, designed and produced by the LTP group at PSI to transform the SiPM currents into a stream of single-photon counts in reactor applications, could be connected only to a single SiPM. All the following signal processing steps to count and discriminate thermal neutron events from the background were performed with standard analog electronics modules available at LRS. This limits the possibility of acquiring the neutron counting from more than a few MiMi detectors due to the high cost of purchase and installation of a large number of such commercial modules.

In view of the parallelization of the MiMi detectors, the development of scalable processing electronics was initiated at LRS. As a first step, three boards for the fast processing of the SiPM signal were built to acquire the count rate of three MiMi neutron detector prototypes simultaneously. This design was then extended to the construction of six 32-channels stand-alone modules for the simultaneous online processing of the 32 detector signals each.

4.3.1.1 Testing PCB processing boards

The LRS laboratory technical division developed and built a SiPM housing and a dedicated printed circuit board (PCB) that performs the first fast preamplification stage of the SiPM current and the successive discrimination into photon-counting pulses. The testing versions of the SiPM housing and the PCB processing board are shown in Figure 4.18(a).

The same S13360-3050PE SiPM used in the prototype version is enclosed in an aluminum tube for external light shielding. The tube is coupled to a black plastic piece that ensures the perfect connection between the SH8001 optical fiber and the SiPM surface, limiting light losses. The rear-end of the tube presents two connectors: one to provide the SiPM with its 56.5 V bias and the second to collect the SiPM output and send it to the processing electronics.

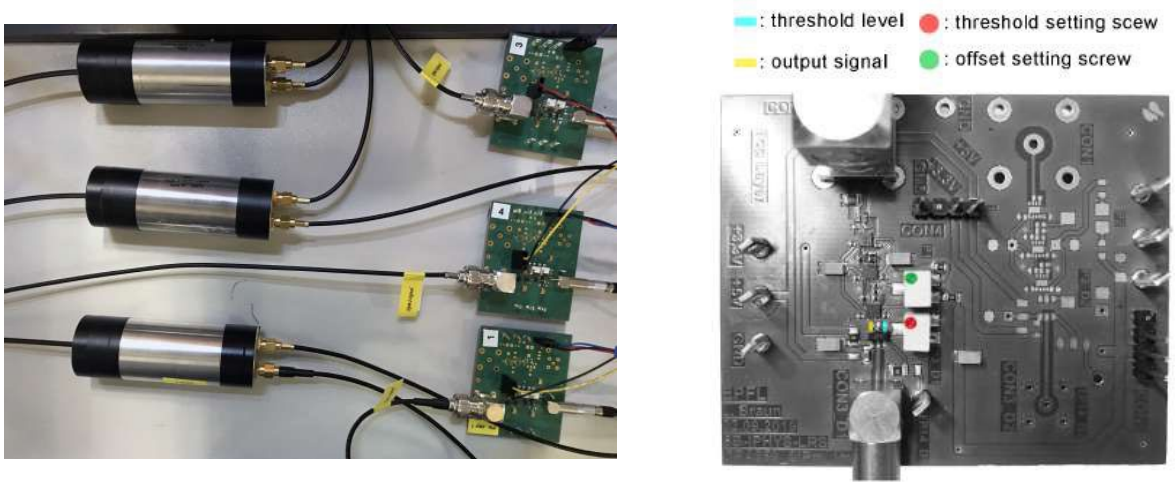

(a) (b)

Figure 4.18 – (a) Three SiPM aluminum housing connected to the PCB board under testing. (b) Outputs and regulations of the testing version of the PCB board [97].

The preamplification circuit is composed of three successive amplification stages of the SiPM output, performed with three OPA859 amplifiers [98] powered by a ±2.5 V power supply. The offset level of the output signal is manually adjustable and is tuned with the dedicated potentiometer installed on the PCB board so that the baseline of the output signal is at zero. Typical pre-amplified signals have a positive sign, contrary to the LTP processing electronics output, and an amplitude of approximately 2 V per photon event. The pre-amplified signal then goes through a high-speed comparator (LMH7220MK [99]) that converts the pre-amplified signals into 3.3 V square pulses on the basis of the SiPM threshold. The SiPM threshold for the comparator module can be regulated by a second potentiometer visible in Figure 4.18(b). As in the prototype signal processing system, the photon counting stream can be processed by either analog or digital readout electronics.

The three PCB boards were tested in CROCUS in the framework of a Master's thesis work at LRS and used for an experimental campaign in the SUR-100 zero-power reactor (see Appendix A for more details). For this test, each SiPM and PCB module was connected to a different MiMi neutron detector in an updated version with respect to the MiMi-0 prototype. This version is called MiMi-1, and the main differences with respect to the prototype version are:

- A higher active volume: the ZnS(Ag):^{6}LiF has a cylindrical surface with a surface of approximately 1 mm^2 and a thickness of 0.28 mm, for a total active volume 40% times bigger than the MiMi-0 prototype version;
- An optimized cap shape: the aluminum cap is reshaped into a new double-diameter piece to improve the coupling with the fiber and improve the detector positioning.

The three MiMi-1 detectors are positioned once again in the northwest control rod guide tube at mid-core height. The output of each PCB is read by a different analog readout chain, and the three thermal neutron count rates are recorded by the CAEN V2495 [100] FPGA board loaded with the PLUscaler firmware [101]. In this configuration, the CAEN V2495 FPGA is simply used as a multi-channel counter of TTL signals.

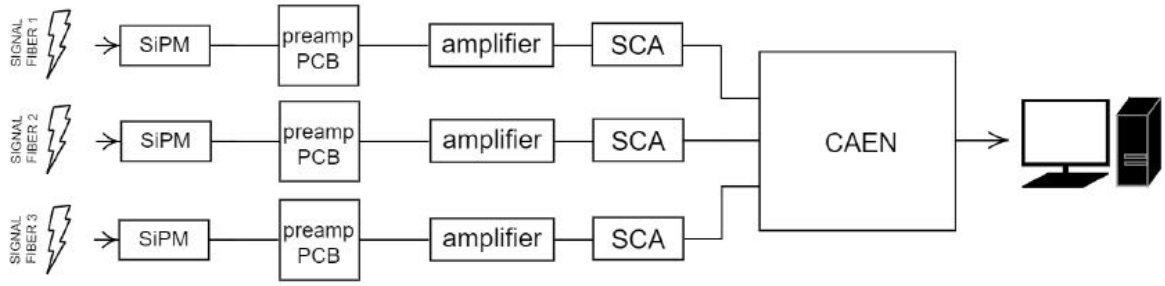

Figure 4.19 – Mixed signal processing system for the three MiMi-1 prototypes [97].

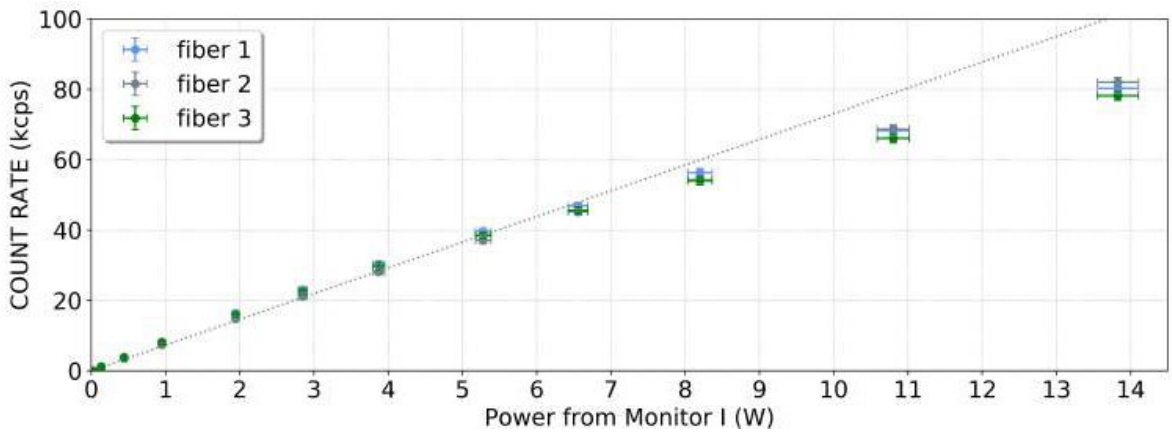

Figure 4.20 – Count rate of the three MiMi-1 prototypes as a function of the CROCUS reactor power [97]. Data are linearly fit up to 6.5 W.

The three MiMi-1 detectors show minimal differences in their counting capabilities, probably due to slight variations in the detector's active volume or in the positioning of the ND2:1 screen at the tip of the optical fiber. However, they all show comparable performances to their prototype version, with an increased counting efficiency due to the larger ZnS(Ag):^{6}LiF active volume. The detector count rate as a function of the CROCUS power is again confirmed to be linear up to approximately 6.5 W.

The same setup is employed to perform high-resolution experiments in the SUR-100 zero-power teaching reactor operated at Stuttgart University. The results of the experimental campaign in SUR-100 are summarized in Appendix A.

4.3.1.2 32-channels stand-alone processing modules

The excellent performances proved by the three testing PCB processing electronics boards triggered the upgrade of the acquisition system to the construction of six 32-channels stand-alone modules, built in-house at LRS and capable of simultaneously processing the output of 32 SiPMs and thus of 32 MiMi neutron detectors.

Each module presents 32 openings where each optical fiber is connected and coupled with its respective SiPM via a black plastic cylinder. The cylinders separate and keep in the dark the 32 SiPMs to minimize background noise and crosstalk events. All the SiPMs are installed on a small circular PCB board visible in Figure 4.21 and connected to the SiPM power supply. Each SiPM output is sent to one of 32 separated PCB processing boards, in Figure 4.22, produced on the basis of the testing design

described in the previous Section 4.3.1.1 and optimized for a multi-channel module. The PCB boards are all mounted on a motherboard visible in Figure 4.22 from above. Both the 32 SiPMs and the 32 PCB processing boards are powered by an internal alimentation module providing the 56.5V power supply to the SiPMs and the ±2.5V and +3.3 V to the processing electronics. The SiPM bias voltage applied and the SiPM threshold are selected with knobs on the module front panel, and their level is visualized on display.

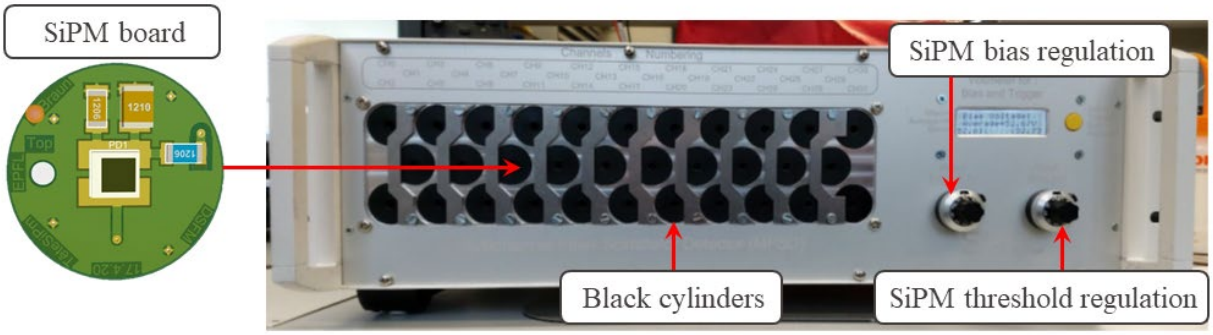

Figure 4.21 – SiPM PCB board and front-view of the 32 channels module.

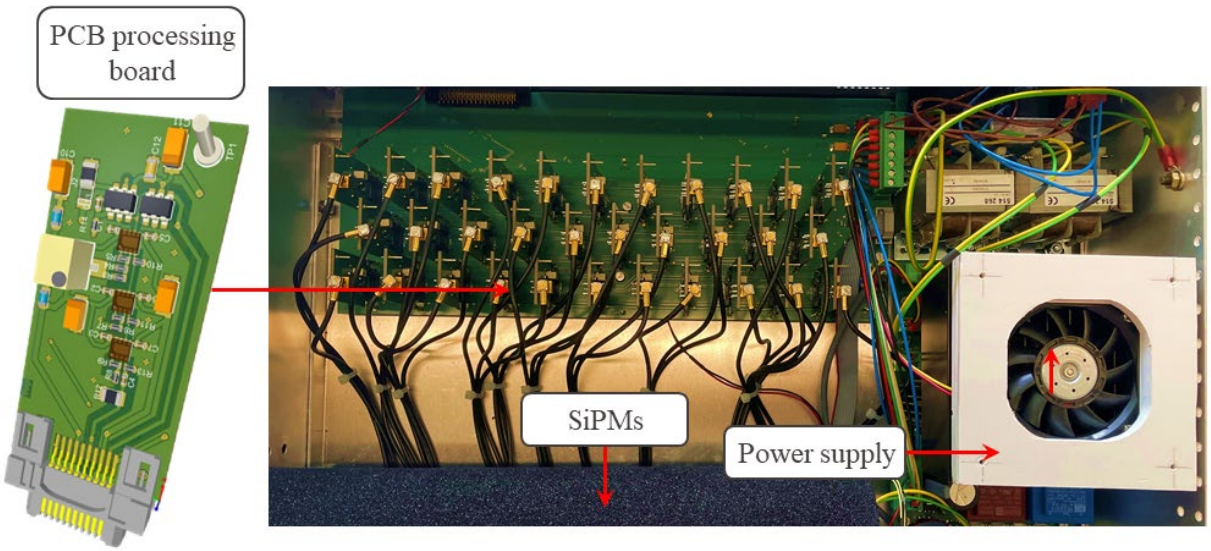

Figure 4.22 – PCB processing board and top-view of the 32 channels module.

The lack of a temperature compensation circuit for the amplitude of the preamplifier signal forced the installation of the 32-channel modules into an incubator [102]to maintain the operating temperature of the SiPMs constant and be independent of the environmental conditions. Side testing showed that a variation of 1°C in temperature corresponds to approximately 1% change in the detector counting.

The output of a single 32-channels module consists of the simultaneous photon counting stream in each of the 32 channels. These signals, using the LVDS standard, are optimized to be sent to an FPGA module mounting a processing algorithm that discriminates neutron events and performs thermal neutron counting.

A summary of the six 32-channels produced at LRS is shown in Table X. The performances of five 32-channel modules (the sixth is a backup) will be described, along with the development and use of the 3D full-core mapping system SAFFRON, detailed in Chapter 6.

Table X – Summary of the characteristics of 32-channels modules.

Multi-channel module	Channels	Bias voltage (V)	SiPM threshold (V)	Purpose
A	0 – 31	56.66	1	Counting
B	32 – 63	56.66	1	Counting
D	64 – 95	56.66	1	Counting
E	96 – 127	56.66	1	Counting
F	128 -159	56.66	1	Counting
G	-	-	-	Replacement

4.3.2 FPGA-based digital readout

The simultaneous use of five 32-channels processing electronics modules requires the online treatment of 160 photon counting signals at the same time. This computationally intense task can be performed only by a Field-Programmable Gate Array (FPGA) board.

In this work, the general-purpose programmable CAEN V2495 [100] FPGA board is used. The board has 64 build-in inputs that can be expanded to 160 by adding three mezzanine boards in the expansion slots to accommodate the 160 photon counting signals. The data acquisition from the board is controlled and programmed through the V1718 VME bridge module [103].

A custom-made proprietary firmware was developed by the LTP laboratory at PSI to process the photon counting into neutron counting. In this work, the firmware is loaded into the V2495 User FPGA, and it is used as a "black box", meaning that the firmware code cannot be modified or tailored for each specific measurement.

The firmware counts the number of photons in fixed intervals of time, whose length can be user-selected and ranges from 5 ns to 1.125 μs. The moving-sum-after-differentiation (MSD) algorithm developed by Mosset et al. [69] is then applied to the number of photons counted in each interval: the sum of photons in five consecutive intervals is compared with the sum of photons counted in the previous five, as shown in Figure 4.23. This moving-average technique allows to identify density variations in the number of photons and recognize the dense and long stream of photons originating from a neutron event in the ZnS(Ag):^{6}LiF screen. To perform this discrimination, a limit called “digital threshold” is set by the user to distinguish between low photon-density occurrences, i.e., background, and the high light-density events corresponding to neutron interactions. An additional parameter called “blocking window” can be tweaked by the user to provide a fixed dead-time after every neutron count and avoid erroneous discriminations. In conclusion, thermal neutron events are counted and recorded according to the selected digital threshold. The entire acquisition scheme is performed simultaneously by a single FPGA module in all the 160 available channels.

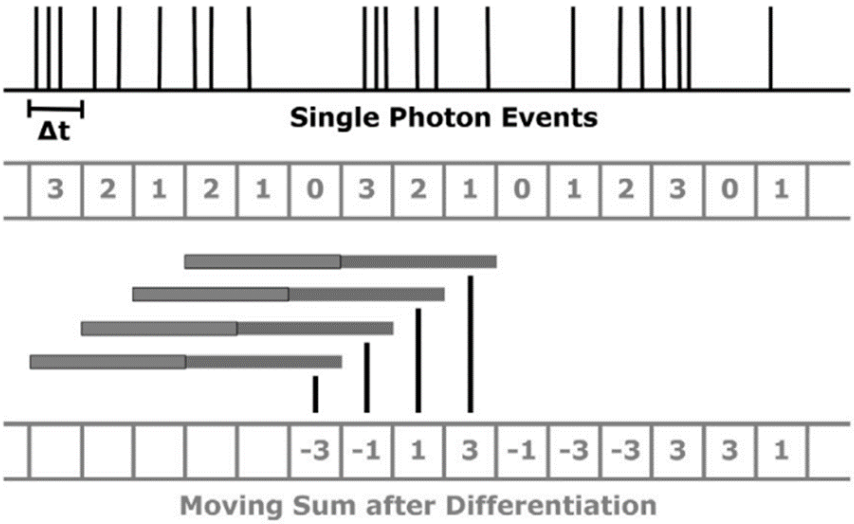

Figure 4.23 - Scheme of the MSD algorithm [70].

4.3.3 Optimization of detector design

The possibility of building in series MiMi neutron detectors and parallelizing the signal processing system paves the way for the realization of detectors arrays composed of a large number of detectors. In particular, the conception and installation of a 3D full-core mapping system in CROCUS (see Chapter 6) are foreseen in order to measure online 3D neutronics phenomena in CROCUS.

The 3D core-mapping system envisages the installation of a large number of MiMi detectors in inter-pin positions within the core fuel lattices at different radial and axial positions. For this purpose, a mechanical supporting structure to keep the detectors in positions in the inter-pin space must be installed in the core. The already small space available in between CROCUS fuel rods would be further reduced by the presence of such a supporting structure. For this reason, although the excellent performance of the first MiMi prototype (proven in Section 4.2.4) and of its updated version (in Section 4.3.1.1), the outer fiber diameter of 3 mm represents a significant constraint, as better explained in Section 6.1. Therefore, an optimization process of the dimensions of MiMi neutron detectors is initiated at LRS to allow for higher flexibility in the design of complex and localized detection systems.

The first step consists in reducing the maximal dimension of the detector, being the diameter of the plastic optical fiber. Four different plastic optical fibers are tested and compared to the prototype version, i.e., the ESKA SH8001 [75] called "fiber A", looking for a tradeoff between external and internal diameter and performances. The four optical fibers, whose characteristics are listed in Table XI, are all produced by Mitsubishi Chemical Co. [104].

The four fibers are tested in blank conditions, meaning without being exposed to a neutron source, in order to assess their background level. Signals corresponding to background photons arise from the light-tightening quality of the fiber tip coverage, the fiber jacketing, and the coupling with the SiPM. Considering that all four optical fibers have the same front-end tip cover and an identical pairing with

Table XI – Characteristics of the optical fibers tested for dimension optimization of MiMi neutron detectors based on the information in [104].

Optical fiber name	Model	Outer diameter (mm)	Core diameter (mm)	Jacket thickness (mm)
fiberA	SH8001	3	2	0.5
fiberB	SH4001	2.2	1	0.6
fiberC	SH4001-1.3	1.3	1	0.15
fiberD	SH2001	1	0.5	0.25

the SiPM, the number of background photons filtering from the polyethylene jacket in 1 ms is measured. The counting is performed using a CAEN V2495 FPGA [100] loaded with the PLUscaler firmware [101]. The test was repeated in two different light conditions to assess whether laboratory environmental conditions could bias the measurements.

The results presented in Figure 4.24 clearly show how the jacket thickness is a key parameter in the selection of the optical fiber. In dark conditions, the number of background photons is of the same order of magnitude for the four optical fibers. However, in daylight conditions, the number of background photons increases significantly for optical fibers with a thin jacket with respect to their counting in the dark. The number of photons measured in daylight decreases with the increase of the jacket thickness, up to a point where there is no difference between daylight or darkness conditions.

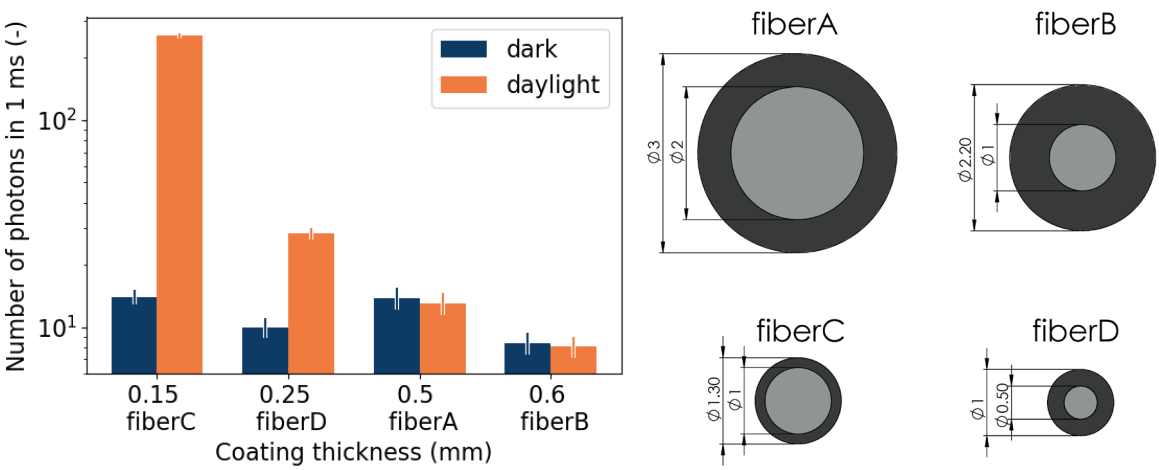

Figure 4.24 – Number of background light photons filtering from the jacket in 1 ms as a function of the jacket thickness, in two different light conditions, for the four optical fibers on the right.

Therefore, above a jacket thickness of 0.5 mm, the optical fiber is properly light-shielded and unaffected by the external light conditions. Looking at Figure 4.24, the only two optical fibers having a jacket thickness above 0.5 mm are fiberA (SH8001), corresponding to the optical fiber used for the MiMi-0 prototype version, and fiberB (SH4001), having a polymethyl methacrylate (PMMA) core of 1 mm in diameter and an outer diameter of 2.2 mm. According to the requirements, fiberB represents the perfect combination between the optical fiber performances and the dimensional constraints set by the installation of a 3D full-core mapping system in CROCUS (see Chapter 6).

4.3.3.1 Final MiMi detector design

The choice of fiberB, having a core diameter of 1 mm, leads to the optimization of the dimensions of the ZnS(Ag):^{6}LiF screen so that the level of thermal neutron sensitivity is maximized. A new Scintacor ND2:1 foil with 0.225 mm thickness [72] was precisely cut at EPFL into square pieces of 0.66 mm × 0.66 mm using a wire-cutting technique. This screen size allows for good coverage of the fiber tip and a possible reduction of the reactivity impact if compared to the MiMi-0 prototype version. In addition, smaller dimensions of the active volume reduce the possibility of gamma interactions.

The 0.66 × 0.66 mm screen is positioned at the tip of the sanded and uncovered tip of the optical fiber PMMA core with a layer of optical grease in between the two. The fiber tip is covered with an aluminum cap having the same external diameter as the optical fiber. The cap is glued to the optical fiber with an epoxydic adhesive (Araldite), used due to its excellent resistance in the water, fast setting, and good transparency. With this method, additional thicknesses on the fiber dimension are minimized, and the ZnS(Ag):^{6}LiF screen is secured in the aluminum cap to prevent both unwanted movements or loss of the screen in the CROCUS core. Although the good accuracy in the ZnS(Ag):^{6}LiF screens cutting and gluing, a detector inter-calibration with a Pu-Be source available at LRS is envisaged to be carried out before the performing measurements in the CROCUS core.

Figure 4.25 shows a schematic of the final optimized design chosen to build the 3D full-core mapping system in CROCUS. This design is simply called "MiMi" detectors for the sake of conciseness.

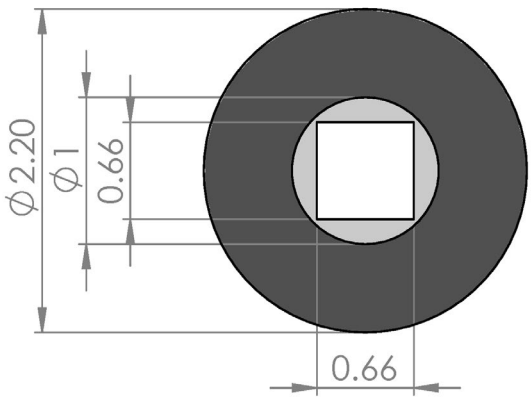

Figure 4.25 – Final design of the MiMi neutron detectors, viewed from the optical fiber tip (in black). The optical fiber core is represented in grey, and the ZnS(Ag):^{6}LiF screen is in white.

Chapter 5

High-resolution experiments in CROCUS

This chapter presents the experimental results of high-resolution neutronics experiments performed in the CROCUS zero-power reactor with the prototype version of the MiMi neutron detectors, namely the MiMi-0. In Section 5.1, the gradients and the azimuthal dependency of the count rate recorded with the MiMi-0 were measured inside an in-core experimental channel within a 13.3-mm space set at two core locations. In the same channel, the count rate as a function of the angular coordinate was measured, and the results are reported in Section 5.2. Section 5.3 shows the experimental results of a study about the local impact on the neutron distribution of millimetric lateral displacements of fuel rods using the COLIBRI device. In every section of this Chapter, experimental results are compared against the results of Serpent 2 simulations. Parts of the experimental results presented in this Chapter are available in [105] and [106].

5.1 Intra-channel flux gradients and azimuthal dependency

The first set of experiments performed in CROCUS with the MiMi-0 neutron detector prototype intends to prove the capability of the detection systems to perform online in-core neutronics measurements with an unprecedented spatial resolution, i.e., in the order of the millimeter. The objective is to measure the thermal neutron count rate from a single MiMi-0 neutron detector

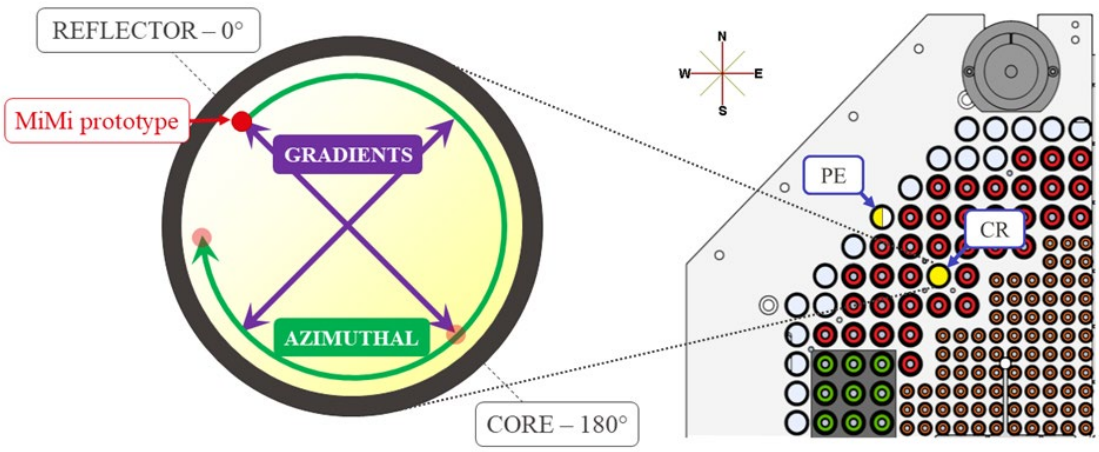

Figure 5.1 – Lattice positions and principle of the intra-channel flux gradients and azimuthal dependency experiments. The presence of an experimental tube is indicated in yellow: the CR tube must always be installed, the PE tube is positioned on occurrence.

prototype positioned by rotation at different azimuthal positions with a 13.3-mm diameter within the control rod guide tube of CROCUS used as an experimental channel and positioned at different in-core locations within the fuel lattice. For 180°-symmetrical azimuthal positions, as shown in Figure 5.1, it is possible to estimate the count rate gradient along the direction.

Being the detector count rate proportional to the volume-averaged and energy-integrated ^{6}Li reaction rate as shown by Equation (2.9), the experimental data are complemented with their comparison against the results of Serpent 2 Monte Carlo simulations for the same quantity. An agreement between experimental and simulation results would provide the first proof of the capabilities of the MiMi-0 neutron detector prototype to measure highly localized neutronics phenomena with minimal perturbation.

5.1.1 Experimental setup

Two in-core lattice positions of the COLIBRI configuration of CROCUS are selected to perform the first set of localized experiments with the MiMi-0 prototype: the northwest periphery (PE) and the northwest control rod (CR) positions, as shown in Figure 5.1. Both lattice positions lay along the same radial direction and are selected because of their vicinity to heterogeneous zones of the reactor. The PE position is situated in the water reflector surrounding the core, while the CR is close to the water gap between the two different fuel lattices of CROCUS.

The control rod guide tube, identical to the aluminum fuel cladding of CROCUS with a 17.35 mm internal diameter, is positioned at the CR position in the standard reactor configuration and, on occurrence, is moved to the PE position. When moved, an additional aluminum tube is then placed in the CR position to maintain the same lattice organization in the core. As in the first testing in CROCUS of the MiMi-0 neutron detector prototype, discussed in Section 4.2.4, the control rod guide tube is used as an experimental channel in both positions.

A goniometer piece was built at LRS for a precise azimuthal installation of the MiMi-0 prototype inside the guide tube. It consists of a POM plastic holder with a density of about 1.4 g/cm^3. Four holes are drilled around the holder circumference (see Figure 5.2(a)), each of which can accommodate the front-end of one MiMi-0 prototype taking into account the dimensions of the aluminum cap. However, at the time of the experiment, only one MiMi-0 prototype was available, and thus only one position was occupied. The detector is located at the hole radial distance of 6.65 ± 0.01 mm from the central vertical axis of the tube. Due to limitations in the detector design (related to the holding of the aluminum cap to the optical fiber) and in order to have an axial reference position, the MiMi-0 is inserted in the holder in a way that the flat face of the cap is at the same level of the bottom face of the POM. Considering a thickness of the aluminum cap of 0.5 mm, the mid-plane of the MiMi-0 active volume is located within the POM, at 0.6 mm from its lower face. The POM piece is connected to an aluminum bar with a movable plastic element that allows choosing the desired axial location in the core – in this study, 50.0 ± 0.1 cm from the bottom of the fuel. i.e., mid-height. The holding piece is equipped with a small metal pin that works as an indication for the azimuthal position of the detector with respect to the scale of the goniometer attached to the guide tube and arbitrarily oriented (in Figure 5.2(b) and Figure 5.2(c)). The experimental setup installed at the PE lattice location is shown in Figure 5.2(c). Similar to the testing phase, the optical fiber is connected to the SiPM located outside

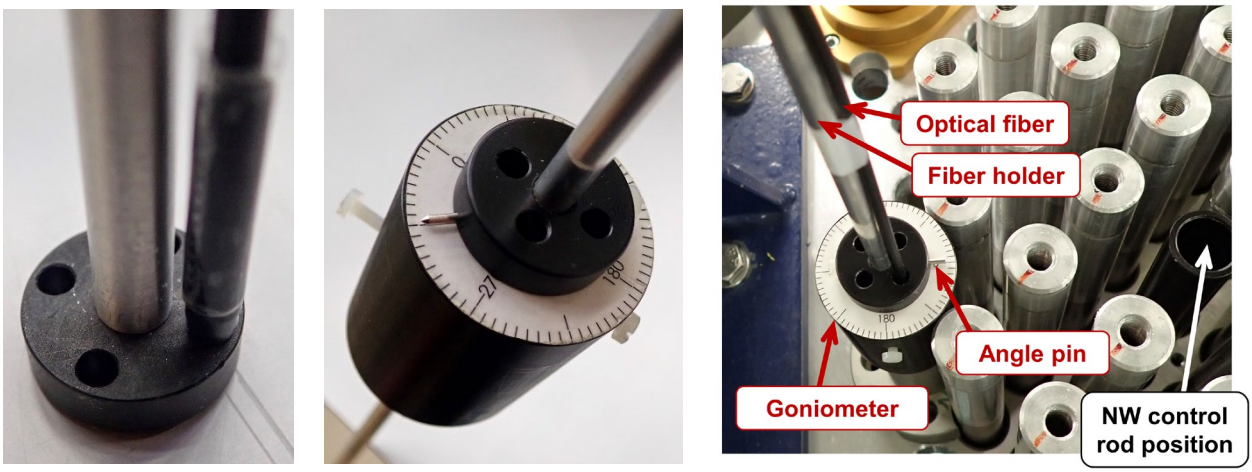

(a) (b) (c)

Figure 5.2 – (a) Plastic holder for the azimuthal positioning of the MiMi-0 detector front-end. (b) Goniometric piece for the azimuthal setting. (c) Experimental setup installed in the PE position of CROCUS.

the biological shielding of CROCUS, where also the PSI-built processing electronics and the analog readout electronics (described in Section 4.2.1.4) are installed.

The neutron count rate is recorded at four different angular positions in each of the two lattice locations. For the sake of simplicity, these azimuthal positions are named as their cardinal direction. Each measurement is carried out at a reactor power level of approximately 1 W for 60 and 45 minutes for PE and CR positions, respectively. The azimuthal position of the detector, joined together with the holding device, is manually modified after every measurement with the reactor in intermediate conditions (i.e., inserted safety blades and water level equal to 800.0 ± 0.1 mm) and after the dose rate inside the reactor cavity is under the allowance limit. Before every measurement, the reactor is brought to criticality, and variations of ± 0.1 mm from the average water level of 953.5 ± 0.1 mm for the PE and 953.3 ± 0.1 mm for the CR were observed when azimuthally turning the measuring setup. Such fluctuations are in the range of error of the water level gauge.

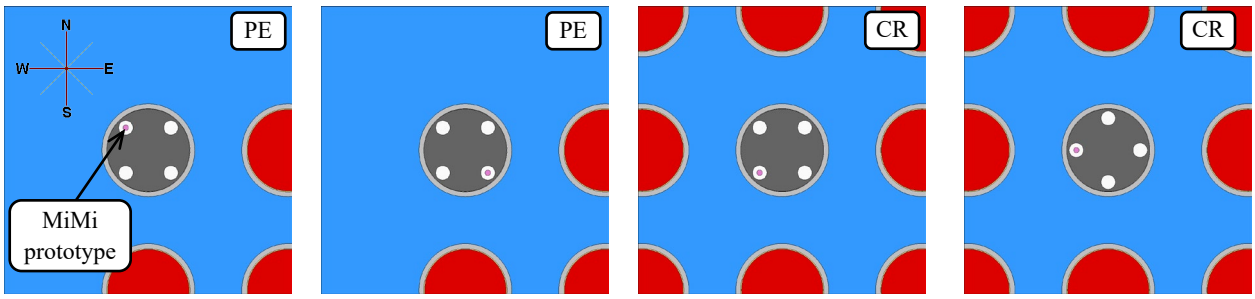

(a) (b) (c) (d)

Figure 5.3 - Examples of experimental measurement arrangements (taken from Serpent 2 plotting): (a) NW - 0° orientation in PE, (b) SE - 180° orientation in PE, (c) SW - 270° orientation in CR, and (d) W - 315° orientation in CR.

5.1.2 Experimental results and discussion

The relative results of the azimuthal counting experiments with the MiMi-0 prototype performed in the control rod guide tube placed at PE and CR are presented in Table XII and shown in Figure 5.4. The recorded number of counts is normalized by the sum of the counts acquired by both Photonis CFUM21 fission chamber safety monitors of CROCUS in the same time interval. The power-normalized values are normalized once again to the value obtained at the reference azimuthal position chosen to be the NW orientation (corresponding to 0 degrees).

The normalized count rate is accompanied by the total experimental uncertainty, combining the Poisson statistical uncertainty and the uncertainty on the count rate caused by the uncertainty of the axial detector positioning. Indeed, it was estimated that the variation within ±0.1 mm around the mid-core level, corresponding to the maximum of the axial cosine shape for a 1-m high core, is in the range of 0.03%. This uncertainty is propagated to the normalized count rate. In the same way, the effect of the variation of the critical water level on the count rate is calculated: a variation of ±0.1 mm between the periods of a cosine shape is in the order of 10^{-5} at around 50 cm. This effect is deemed negligible and thus not included in the total experimental uncertainty. An error of ±2.5°, corresponding to half of the goniometer resolution, is introduced on the azimuthal positioning of the detector.

Table XII – Normalized MiMi-0 count rate in the PE and CR positions as a function of the azimuth.

Position	Orientation	Azimuthal position (°)	Normalized MiMi count rate with total experimental uncertainty (-)
PE	NW	0.0 ± 2.5	1.0000 ± 0.0007 (0.07%)
PE	NE	90.0 ± 2.5	0.9865 ± 0.0007 (0.07%)
PE	SE	180.0 ± 2.5	0.9571 ± 0.0007 (0.07%)
PE	SW	270.0 ± 2.5	0.9743 ± 0.0007 (0.07%)
CR	NW	0.0 ± 2.5	1.0000 ± 0.0007 (0.07%)
CR	SE	180.0 ± 2.5	1.0437 ± 0.0008 (0.07%)
CR	SW	270.0 ± 2.5	1.0243 ± 0.0007 (0.07%)
CR	W	315.0 ± 2.5	1.0038 ± 0.0007 (0.07%)

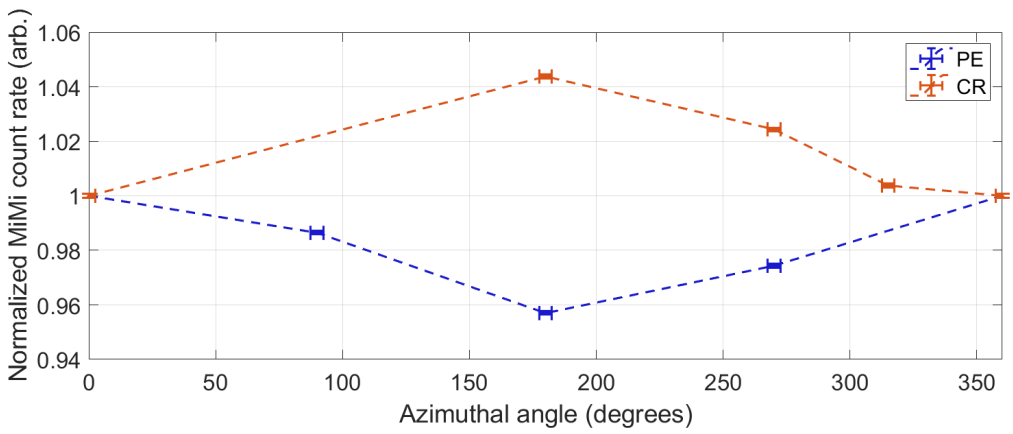

Figure 5.4 – Experimental results for the MiMi-0 count rate as a function of its azimuth within the control rod guide tube at PE and CR. The connecting dashed line is shown for visualization purposes.

The set of measurements carried out in the PE location shows a minimum towards the SE direction, i.e., 180°, corresponding to the orientation of pointing at the core center. Indeed, a higher share of thermal neutrons is present closer to the core water reflector (the NW direction), where the count rate measured by the MiMi prototype has its maximum. The gradient in the count rate profile along the radial direction in a range of 1.33 ± 0.02 cm at 30.939 ± 0.008 cm from the core center has been calculated to be equal to +(4.29 ± 0.10)%. The positive sign indicates that the gradient is oriented towards increasing radial coordinates, e.g., towards the core boundaries. The specular values (NE and SW) at the same PE position show a limited gradient of (1.25 ± 0.10)% in the NE direction, which might be caused by either unknown experimental biases or by a slight asymmetry in the CROCUS fuel lattice, as shown in Figure 5.1. Further investigations are needed to determine the source of the NE-SW gradient.

In the CR position, at 22.689 ± 0.008 cm from the core center, a gradient of -(4.37 ± 0.10)% is present between the NW and the SE detector positions, meaning that the higher neutron count rate is pointing towards the core center as expected due to the typical radial flux shape for a cylindrical core. The gradient along the NE-SW cannot be estimated due to the lack of experimental data for the NE direction in CR.

5.1.3 Comparison with Serpent 2 simulations

The comparison of the highly localized experimental results against Monte Carlo simulations in a full-core reactor geometry is accompanied by statistical issues, as discussed in Section 2.2.2. The need for low uncertainties to evaluate local effects in the order of a few percent difference is worsened due to the small tallying volumes involved in such simulations. For instance, the MiMi prototype sensitive volume of 0.2 mm^3 corresponds to a fraction of $\sim 10^{-10}$ of the total volume of the CROCUS core. Codes such as Serpent 2 offer the possibility to use track-length detectors, implemented and optimized for scoring events in optically thin volumes. Despite this capability, the computational power required to perform a full-core analog Serpent 2 simulation for recording the ^{6}Li reaction rate at different azimuthal positions in the real MiMi detector volume would be prohibitive. It was estimated that an uncertainty of 1% on the normalized ^{6}Li reaction rate in a real-size detector volume is achieved after approximately 10^4 CPU hours. Most of this computational power would be spent on tracking neutrons that have a very low probability of contributing to the 0.2 mm^3 detector tally. In order to reduce the required computational power, approximations in the modeling of the experimental setup are introduced, and a two-step approach is tested.

5.1.3.1 Direct simulations in smeared volumes

A first attempt at comparing the experimental data with Serpent 2 full-core criticality simulation results is made by virtually scoring the ^{6}Li reaction rate at different azimuthal positions with tally volumes 2000 times taller (40 cm around core mid-height) than the real ZnS(Ag):^{6}LiF. The virtual scoring of the ^{6}Li reaction rate with track-length detectors is justified by the assumption of a small and localized perturbation introduced by the MiMi neutron prototype due to the miniature dimensions of its active volume. Hence, the ^{6}Li volume is not included in the model geometry and the reaction rate is scored without taking into account the flux perturbation due to the detector presence. On the other hand, the increase of the Serpent 2 detector height allows to improve the results' statistic but introduces an averaging of the reaction rate over the axial height of 40 cm. If one requires absolute

estimates, the averaging can be corrected by estimating a form factor of the reaction rate axial profile. In the case of relative estimates, as in the case at hand, the form factor cancels out as the axial shape of the reaction rate can be considered constant within the radial difference of 1.33 ± 0.02 cm in which the measurements are performed. Considering the large smearing over 40 mm, modeling the local 5-mm thick POM holder in the geometry, as well as the miniature scintillator volume, would be redundant due to the averaging of their respective perturbations. With these assumptions, a Serpent 2 simulation with 36 virtual tallies of 40 cm, positioned every 10° at 6.65 cm from the central axis of the channel, is run per each lattice location. For the CR location, 1.5×10^9 neutron histories are simulated, while the double is run for the PE location to obtain comparable uncertainties. The relative simulation results, normalized by the tally at the zero degrees position (corresponding to the NW positions oriented towards the periphery of the core) and obtained using the ENDF/B-VII.0 [93] nuclear data library, are shown in Figure 5.5.

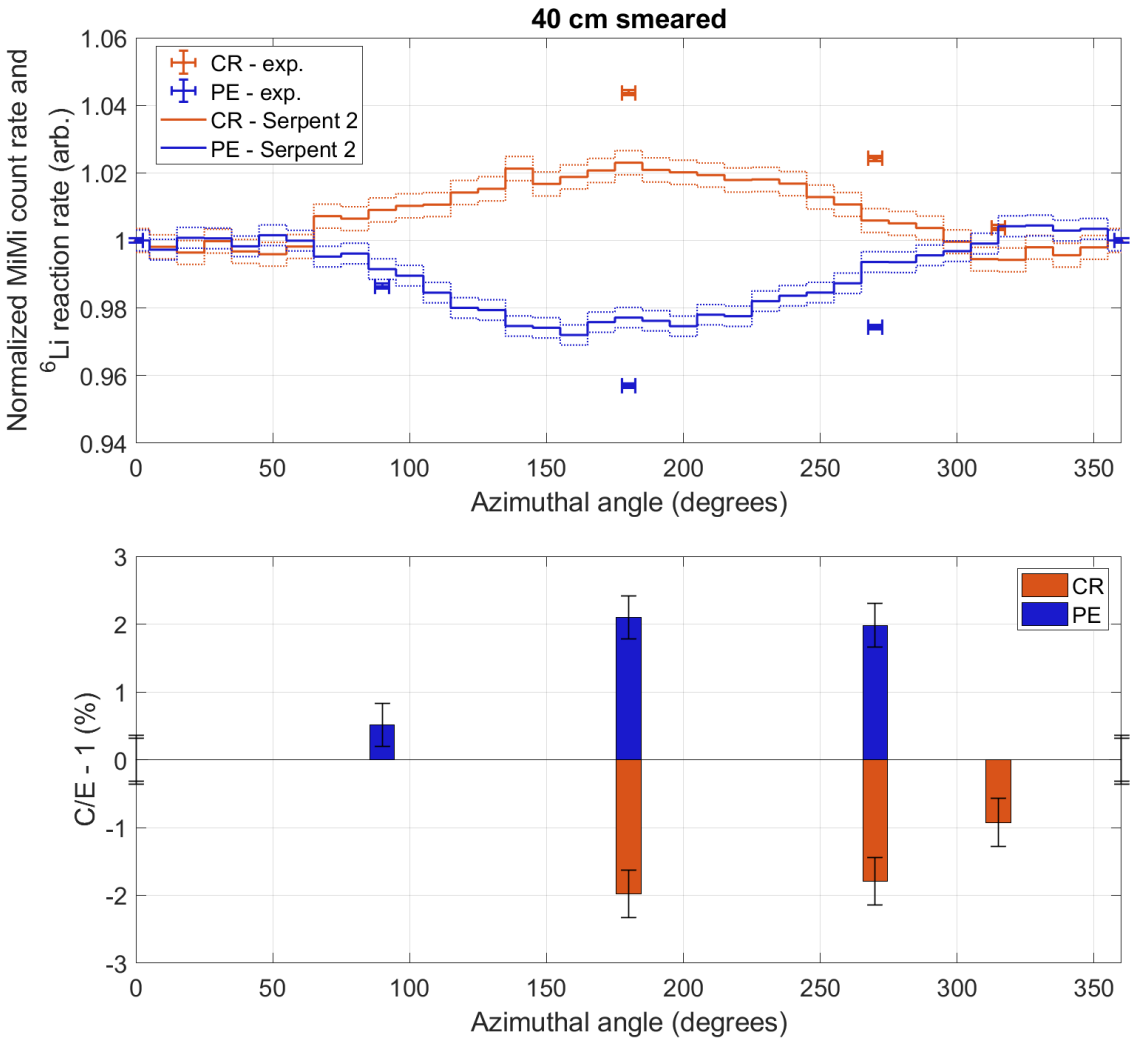

Figure 5.5 – Comparison between experimental results and direct Serpent 2 simulations for ±20 cm smeared virtual detectors, with no plastic holder modeling.

The simulation results of direct Serpent 2 simulations for tallies smeared over 40 cm show significant discrepancies with respect to the experimental data, with a maximum (C/E)-1 of 2.1 ± 0.3 % at the NW position (180 degrees) in the PE location. The reason for this disagreement is probably the

localized presence of the POM holder, not modeled in these simulations and surrounding the MiMi prototype active volume. The insertion of the plastic holder for experimental purposes is substituting the air present locally in the control rod guide tube with a moderating material having a higher density than water. Hence, it can be expected that the spectrum in the control rod guide tube is more thermal during the experiments than in the normal configuration without the plastic holder perturbation. The discrepancy observed in Figure 5.5 also suggests that the moderation effect might not be uniform in the channel and more relevant at higher fluxes.

This first attempt at simulating mm-wise effects in the CROCUS core uncovers the need to improve the modeling of the experiments to take into account also local perturbations introduced by the experimental setup and to improve the spatial resolution of the ^{6}Li reaction rate tally.

5.1.3.2 Two-step approach for simulations of local effects

With the intent to reduce the detector smearing and model the experimental setup explicitly, a two-step approach is tested to simulate the azimuthal dependency of the ^{6}Li reaction rate in 2-mm high virtual detector volumes. The methodology, partially inspired by [107], consists in performing consecutive Serpent 2 simulations: full-core criticality simulations are followed by source-mode simulations in a reduced geometry focusing around the location of interest. A visual representation of the two-step approach is shown in Figure 5.6.

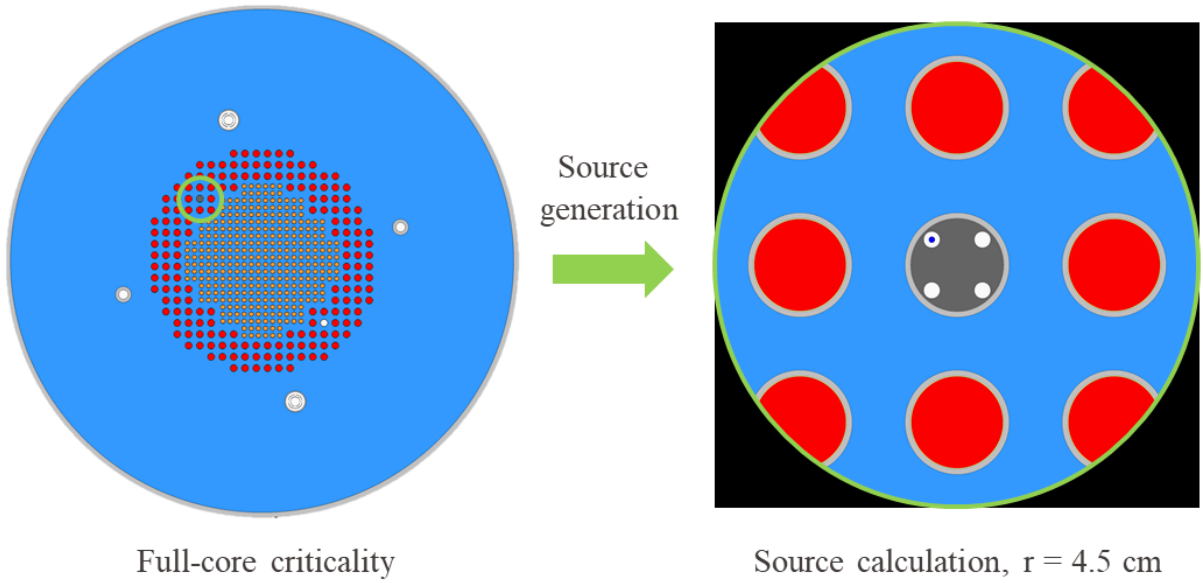

Figure 5.6 – Schematic of the two-steps methodology used for the computation of gradients and azimuthal trend in the CR position. The same approach is used in the PE position.

The first step consists of multiple full-core criticality simulations run with different seeds. During each simulation, the neutron histories crossing a spherical surface of 4.5 cm radius centered on the location of interest – CR or PE – are recorded in a source file in terms of positions, direction, and energy. In this case, the sphere volume contains the experimental setup explicitly modeled, including the POM holder and the MiMi active volume.

The choice of the sphere radius is arbitrary but has to be chosen as a trade-off between the statistical accuracy in the number of histories recorded uniformly on its surface and the distance from possible

perturbations. Indeed, if the same source file is intended to be successively used for a different configuration, one has to make sure that perturbations are either very localized within the sphere or far away from it. In this study, a sphere radius of 4.5 cm is chosen to obtain a good source sampling for studying effects within the control rod guide tube without being influenced by the presence or absence of this particular experimental setup. In particular, the perturbation introduced by the POM holder is expected to be localized within the diameter of the control rod guide tube.

In the CR position, approximately 1.9×10^{-2} neutron histories are recorded on the 4.5 cm sphere per neutron history run, while this number is approximately halved in the PE location. For each location, the output source files are then merged in a single file of 20 GB, containing approximately 300 million neutron histories recorded on a 4.5-cm radius sphere. The advantage of dividing the source generation in multiple runs is the possibility to split the simulation on multiple nodes of high-performance computers (HPC) and avoid the slowing down observed in the writing of large files. The merged source file is obtained in approximately 10^3 CPU hours for the CR location and 2×10^3 CPU hours for PE. The ENDF/B-VII.0 [93] nuclear data library is used for the generation of both sources.

In the successive second step, the merged source file is used as input for the simulation of neutron histories propagating within the geometry contained solely in the 4.5-cm radius sphere. In the standard configuration, the geometry modeled within the sphere matches that of the full-core criticality, including only parts of the control rod guide tube, parts of the adjacent fuel rods, and the experimental setup in place. The outside regions are set to void to conserve the total neutron flux within the sphere volume, which is set equal to the average of the total fluxes in the same region during the full-core criticality simulations. However, the flux normalization is not relevant for the simulation of the azimuthal experiments as only relative estimates are examined.

The main advantage of the methodology consists in the possibility of using multiple times the generated spherical neutron source to simulate a series of local effects within the selected region. This is valid as long as no strong perturbation modifying the shape of the neutron source at 4.5 cm is inserted in the geometry. By using the same seed for the simulation, it is possible to run multiple simulations involving minimal geometry perturbations, such as the rotation of the POM and the MiMi prototype in this set of measurements, and calculate the relative variation of the ^{6}Li reaction rate at the different positions with limited computational power. In a similar way, the local effect of the single components can be assessed under the assumption that their presence or absence is not influencing the spherical neutron source distribution. At the same time, performing the second step in a smaller geometry while maintaining a link to the full-core calculation – through the spherical neutron source and the flux normalization – allows for discarding neutron histories that are not in the vicinity of the detector volume while resolving local effects. However, it is important to remark that with this methodology, rare events might not be taken into account.

Although the re-utilization of the neutron source strongly reduces the simulation time needed to resolve local neutronics effects for an explicitly modeled experimental setup, it is straightforward that the results of the second step are biased by the number and the distribution of the neutron histories recorded in the first step. For this reason, the preliminary three-step methodology presented in [105] was replaced by this two-step method in order to limit the uncertainty connected to the source sampling and its propagation. The quantification of this bias is difficult, and for the purpose of this

work, a spherical source with at least 10'000 neutrons/mm^2 is deemed sufficiently converged for the simulation of mm-wise effects.

Local perturbations in CR location

As a first test, the ^{6}Li reaction rate is recorded in the reduced CR geometry within a real-diameter 2-mm high virtual tally with real MiMi diameter located at different positions and in various configurations. The 2-mm high virtual tally is selected as a trade-off between lowering statistical uncertainties and resolving as much as possible localized neutronic effects.

The two selected positions are the NW, corresponding to 0° and pointing towards the core periphery, and the SE, being at 180° and oriented towards the core center. The configurations that are compared are shown in Figure 5.7 and can be summarized as

- Unperturbed: the CR guide tube is empty, with no experimental setup and no MiMi detector;
- POM-only: the POM holder is included in the geometry as if it was installed alone in the CR guide tube. The tally records the effect of the holder on the ^{6}Li reaction rate;
- MiMi-only: the active volume of the MiMi prototype is modeled at the geometry without any support. The virtual tally takes into account the flux perturbation introduced by the detector;
- POM + MiMi: both the POM holder and MiMi active volume are explicitly modeled and their respective flux perturbation are taken into account.

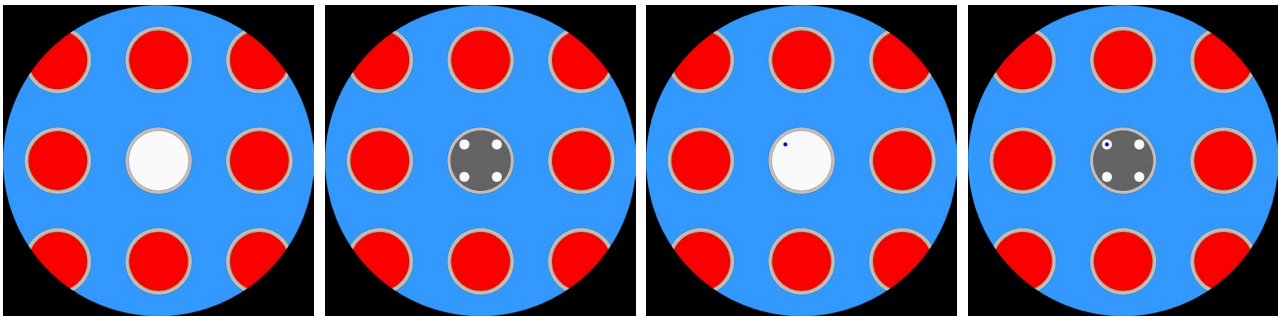

(a) (b) (c) (d)

Figure 5.7 – Second-step model geometry for (a) unperturbed, (b) POM only, (c) MiMi only, and (d) POM + MiMi configurations for testing local effects.

A single second-step simulation is performed for each position and for each configuration for a total of 16 source-mode simulations. The relative results of this study in the CR experimental channel, performed with the ENDF/B-VII.0 [93] nuclear data library, are reported in Table XIII. The uncertainty of the results is limited by the number of neutron histories recorded in the first step for the CR position, equal to approximately 300 million. Uncertainties below 1% are obtained with 4 CPU hours per simulation, for a total of 64 CPU hours.

Table XIII – Differences in ^{6}Li reaction rate at different positions and for different CR configurations. A positive value of the NW-SE gradient points towards the core center.

	Difference with unperturbed at NW - 0° (%)	Difference with unperturbed at SE - 180° (%)	NW-SE gradient (%)
Unperturbed	-	-	2.3 ± 0.9
POM-only	0.7 ± 0.9	2.5 ± 0.9	4.2 ± 0.9
MiMi-only	-7.0 ± 0.8	-7.0 ± 0.8	2.3 ± 0.9
POM + MiMi	-5.8 ± 0.8	-3.4 ± 0.8	5.0 ± 0.9

Despite the limited uncertainties of the results shown in Table XIII, the NW-SE gradient of 2.3 ± 0.9 % is in agreement with the results of the direct simulations shown in Figure 5.5. This result provides the first proof of the capability of the two-step methodology to simulate local neutronics effects in agreement with the relative results of smeared (and thus averaged) tallies obtained from a simple full-core calculation.

The insertion of the POM holder in the control rod guide tube introduces an increase in the ^{6}Li reaction rate due to the higher thermalization of neutrons by plastic materials, and as expected, the effect has a higher magnitude in the SE position closer to the core center. As a consequence, the NW-SE gradient in the POM-only configuration rises to 4.2 ± 0.9 %.

A strong reduction in the ^{6}Li reaction rate is instead caused by the MiMi prototype due to self-shielding effects in its volume. This decrease in the reaction rate, estimated to be around -7.0 ± 0.9%, is independent of the detector position in the core, meaning that the MiMi prototype is introducing a constant local perturbation. As proof, the NW-SE gradient is unaffected by the presence of the MiMi active volume with respect to the unperturbed configuration. The effect in terms of perturbation to the total neutron flux is also estimated to be in the order of -2.5 ± 0.5% and constant within the uncertainties in both the NW and the SE positions.

Lastly, the complete analog modeling of the experimental setup shows a counteraction of the ^{6}Li reaction rate decrease due to the presence of the MiMi detector by the higher local moderation introduced by the POM holder. The result is a NW-SE gradient of 5.0 ± 0.9%, which is in the range of uncertainty of the one calculated in the POM-only situation (i.e., one standard deviation). Therefore, it can be concluded that the major perturbation effect in this experimental setup is represented by the plastic POM holder due to its moderation effect in a region filled with air. The lesson learned from this study is that, when studying effects in air, the presence of the experimental setup cannot be easily taken into account by computational means. Therefore, setups minimizing the perturbation to the neutron flux should be used, e.g., the aluminum holder in the SUR-100 experimental campaign in Appendix A.

Azimuthal dependency for explicitly modeled experiments

Being aware of the flux perturbation introduced by the plastic holder, the experimental data must be compared with the results of simulations with this element modeled in the geometry. Hence, the azimuthal dependency of the ^{6}Li reaction rate is recorded at all the experimental positions for both CR and PE lattice locations with the same 2-mm high virtual tallies used in the previous study for

perturbation effects. Both the POM holder and the MiMi active volume are modeled in the geometry and together are rotated at the different within-channels orientations. The experimental and two-step simulation results, normalized at the 0° position (NW), are shown in Figure 5.8 with their (C/E)-1 plot. In Figure 5.8, an agreement between experimental and simulation results within one or two standard deviations is visible for both CR and PE locations of the control rod guide tube in which the measurements are performed.

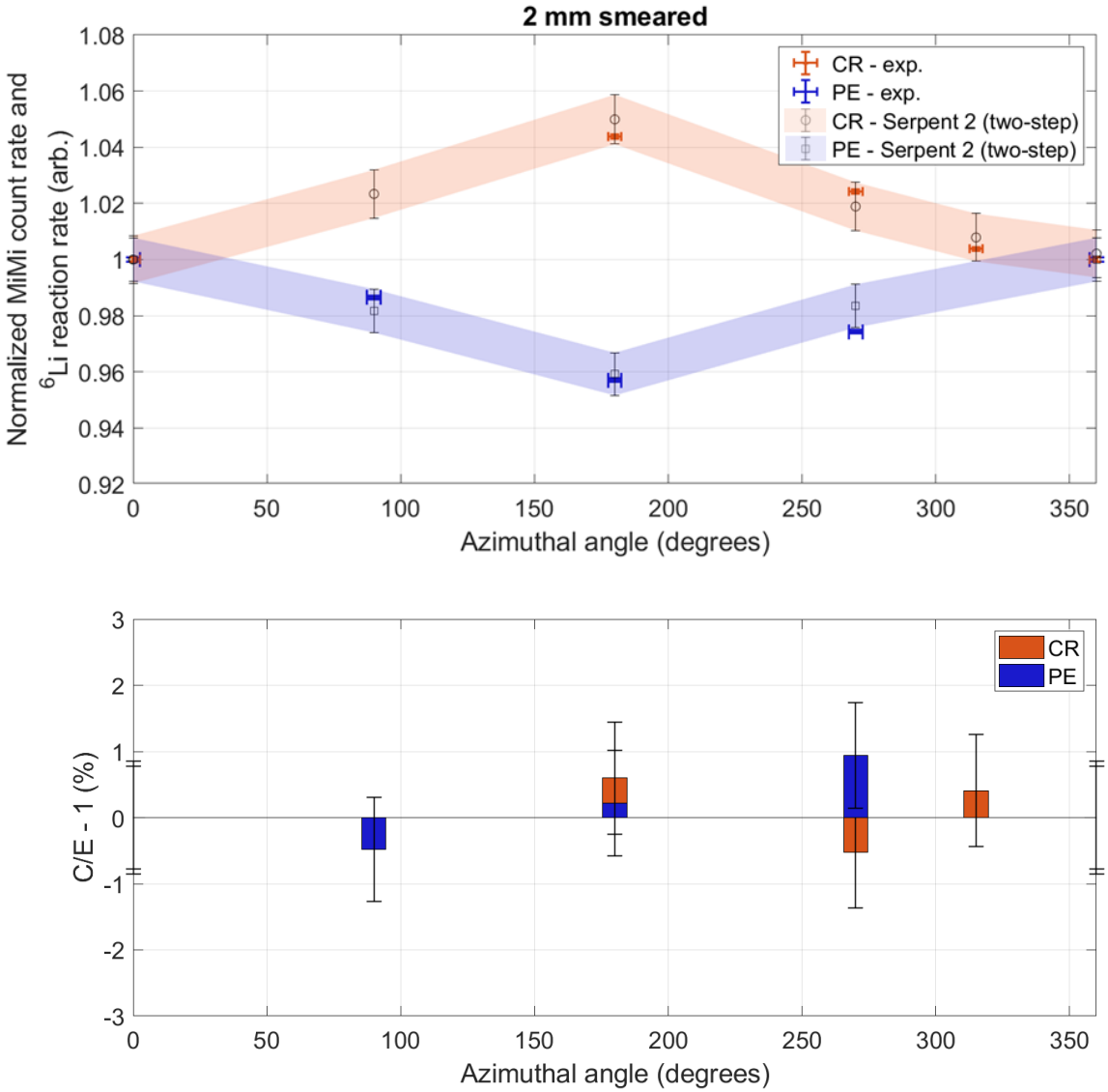

Figure 5.8 – Comparison between experimental results and two-step Serpent 2 simulations for ±1 mm smeared virtual detectors, with explicit modeling of POM holder and MiMi active volume.

5.1.4 Conclusions

The investigation of gradients and azimuthal dependencies in an experimental channel with the MiMi neutron detector prototype demonstrated that:

- The MiMi prototype is able to measure local variations of the ^{6}Li reaction rate, i.e., in the thermal range. In particular, reaction rate gradients were measured within 1.33 ± 0.02 cm inside an experimental channel in both CR and PE locations. In the CR location, a gradient of -(4.37 ± 0.10)% in the radial direction of the core is pointing towards the core center, while in the PE location, the measured gradient is +(4.29 ± 0.10)%, oriented towards the core reflector;
- The two-step approach with Serpent 2, even if with limitations, allow simulating local effects in the CROCUS core with limited computing power. The measured experimental values can be potentially used also for the validation of Monte Carlo variance reduction techniques;
- The 0.2 mm^3 active volume of the MiMi prototype perturbs the ^{6}Li reaction rate by -7.0 ± 0.9% and the total neutron flux by -2.5 ± 0.5%, both with the same magnitude at different core locations. Hence, if looking for relative results, its self-shielding effect can be neglected;
- The main local perturbation in the experimental setup is represented by the POM plastic holder around the detector's active volume. Hence, detectors must not be located within or close to local perturbations such as moderation materials (e.g., plastic) when measuring in an air channel.

5.2 Neutron flux directionality

The angular dependency present in the definition of the angular neutron flux (see Equation (2.1)) is particularly important for the solutions of problems that have a strong direction dependence, such as neutron streaming through a voided channel, the presence of a localized neutron source [17], or localized perturbations, e.g., fuel vibrations [108], [109]. The solution of these transport problems with deterministic neutronic codes requires the use of advanced methodologies for the treatment of the neutron flux directionality, which cannot be considered linearly anisotropic as in the diffusion theory [13]–[15]. The validation of these methodologies requires the comparison with experimental measurements of neutron currents in nuclear reactor cores.

However, at the experimental level, measuring the directionality of the thermal neutron flux is extremely difficult. Indeed, conventional thermal neutron detectors measure a quantity proportional to the volume-integrated reaction rate in the detector's active part, which can be related only to the scalar thermal neutron flux. Therefore, no information about the directionality of the thermal neutron flux can be retrieved from the output of a thermal neutron detector.

A possible workaround to this complex task is to enclose a thermal neutron detector in a partially-opened cadmium layer. The cadmium layer has the purpose of absorbing the thermal neutrons coming from the majority of directions and selecting only those going through the aperture. The detector output results in a measurement of partial neutron currents over a certain solid angle corresponding to the cadmium aperture. The feasibility of experimental measurements of this kind was proven by Lindén et al. [110] and Avdic et al. [111] with a Pu-Be neutron source.

In this experimental study, a first attempt at measuring the relative directionality of the thermal neutron flux in CROCUS with the MiMi-0 neutron detector prototype is performed. The MiMi-0

detector is enclosed at the center of a cadmium cylindrical box with a 40° vertical slit opening, as shown in Figure 5.9. By rotating the ensemble of the Cd box and the detector, the count rate as a function of the selected orientation of the Cd opening can be recorded. As in the previous study, the experimental results are compared with Serpent 2 simulations.

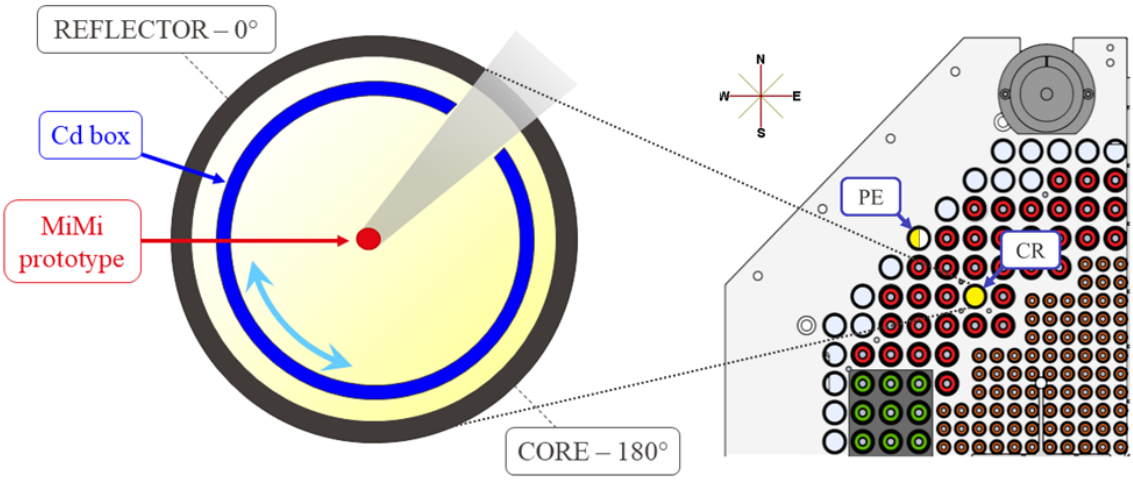

Figure 5.9 – Lattice locations and principle for experiments on the directionality of the neutron flux. The presence of an experimental channel is indicated in yellow: CR tube must be always installed, PE tube is positioned on occurrence.

5.2.1 Experimental setup

Among the available lattice locations, the same northwest control rod (CR) and northwest periphery (PE) lattice positions are selected for the measurements of the flux directionality due to their vicinity to the heterogeneities of the CROCUS core, i.e., water reflector and water gap, and following the characterization of their inner gradients for a possible unfolding of effects.

An experimental setup is designed at LRS to measure the directionality of the neutron flux with both the MiMi-0 detector and the CIVIDEC sCVD diamond detector, NEUTON. The shared parts of the setup include a hollow aluminum rod of 17.2 mm diameter with the possibility to attach at one extremity different plastic holders. The plastic holder, visible in Figure 5.10(a), is a 50-mm high plastic cylinder of POM of 13.3 mm diameter with a central passage of 4 mm to insert the 3-mm diameter optical fiber of the MiMi-0 detector. The larger passage is designed to accommodate the additional thickness of the black tape securing the aluminum cap to the optical fiber. Despite the knowledge acquired on the perturbation effect of POM with the azimuthal experiments, the measuring campaign is performed before the processing of the previous results, and thus the active volume of the MiMi-0 detector is positioned within the plastic at 1 cm from the lower face of the holder. Although the experimental flaw, the measurement results can still provide useful information on the thermal neutron flux directionality.

A 1-mm thick aluminum cap with the internal surface covered with cadmium encloses part of the POM holder with the MiMi-0 active volume in it. It is to be noted that the relatively large size of the cap box compared to the MiMi-0 detectors was dictated by the objective to repeat the experiment with the NEUTON detector using the same setup. The internal cadmium cover is composed of a

1-mm thick cadmium plate positioned at the bottom of the cap and a 1-mm cadmium sheet covering the lateral surfaces of the cap and leaving an aperture of approximately 4.9 ± 0.1 mm, corresponding to an angle of approximately 40°, as shown in Figure 5.9 and Figure 5.10(b). The lateral open cadmium layer selects the azimuthal direction from which thermal neutrons can enter the internal volume of the box, while the bottom plate limits the upward streaming. Due to practical limitations, it was not possible to include in the setup also an upper plastic cadmium plate to cut the downward streaming component. The lateral cadmium layer is at a radial distance of about 7.1 ± 0.1 mm from the central channel axis and from the MiMi-0 location.

The cadmium-covered cap is attached to the POM holder with a screw that is placed at the center of the cadmium opening (as visible in Figure 5.10(b)). The screw gives the reference for the cadmium orientation, which is selected in CROCUS using a similar system to that used for gradient and azimuthal measurements (in Section 5.1.1). A plastic holding piece runs along the 17.2 mm aluminum rod and can be set at different rod positions depending on the axial height in CROCUS at which the measurements are intended to be performed. In this case, the holding piece is regulated and fixed at a position that places the MiMi-0 active volume at 50.0 ± 0.1 cm with respect to the lower level of the CROCUS fuel. The holding piece is equipped with a metallic pin aligned with the central axis of the cadmium opening. The pin indicates the direction of the cadmium opening on the same goniometer piece shown in Figure 5.2(b) and placed on top of the experimental channel.

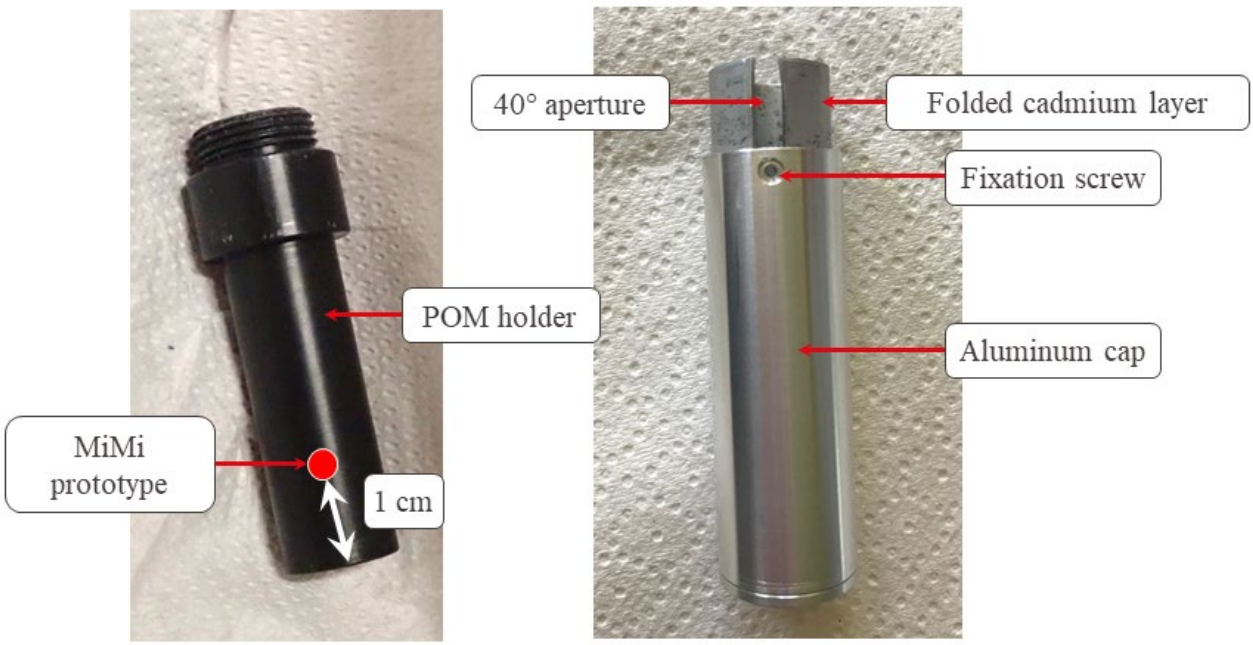

(a) (b)

Figure 5.10 – (a) Plastic holder for the MiMi-0 neutron detector prototype. (b) Aluminum cap with cadmium layer covering the internal surface (partially extracted for the picture).

The MiMi-0 count rate is recorded with the analog signal processing electronics (described in Sections 4.2.1.4 and 4.2.1.5) for different orientations of the cadmium opening in CR and PE lattice positions. During the measurements, CROCUS was operated at the power of 5 W to limit the counting time between one and two hours per direction while maintaining low statistical uncertainties, i.e., below 0.03%. A longer measurement time of two hours is necessary for measurements in the PE

location due to the -50% flux reduction estimated between CR and PE. Similar to azimuthal experiments, the rotation of the experimental setup is performed manually in an intermediate reactor state. After each rotation, the reactor criticality is achieved and the thermal neutron counting with the MiMi prototype is recorded. The critical water is set at an average value of 958.2 ± 0.1 mm with variations of ±0.2 mm depending on the Cd orientation for the measurements in the CR position and at 954.8 ± 0.1 mm for the PE measurements with variations of ±0.1 mm.

5.2.2 Experimental results

The directional-dependent count rates measured by the MiMi-0 neutron detector prototype in the PE and CR lattice positions are reported in Table XIV and shown in Figure 5.11. For each measurement, the total number of counts is power-normalized by the number of counts recorded by the two fission chamber monitors of CROCUS, like for the azimuthal experiments. The normalized count rate is then normalized to the one obtained at the reference orientation of the Cd opening, corresponding to the selection of the neutron entering the volume from ±20° around the direction pointing towards the core periphery (NW).

Similarly to Section 5.1.2, the total experimental uncertainty is the combination of the Poissonian statistical uncertainty and the 0.03% additional error arising from an error of ±0.1 mm in the axial detector positioning. Variations of the critical water level of about ±0.2 mm are observed during experiments in both CR and PE, corresponding to ± 0.8 pcm. The effect of such variation of the axial cosine flux shape at 50 cm is estimated to be in the order of 0.005%. This value is not included in the total computation of the final uncertainty because it is one order of magnitude smaller than the statistical uncertainty of the results.

Table XIV – Normalized MiMi-0 detector count rate as a function of the orientation of the Cd opening for both PE and CR positions.

Position	Orientation	Cd opening orientation (°)	Normalized MiMi-0 count rate with total experimental uncertainty (-)
PE	NW	0.0 ± 2.5	1.0000 ± 0.0007 (0.07%)
PE	NE	90.0 ± 2.5	0.9863 ± 0.0007 (0.07%)
PE	SE	180.0 ± 2.5	0.9206 ± 0.0006 (0.07%)
PE	S	225.0 ± 2.5	0.9084 ± 0.0006 (0.07%)
PE	SW	270.0 ± 2.5	0.9652 ± 0.0006 (0.07%)
PE	W	315.0 ± 2.5	1.0073 ± 0.0007 (0.07%)
CR	NW	0.0 ± 2.5	1.0000 ± 0.0006 (0.06%)
CR	NE	90.0 ± 2.5	1.0078 ± 0.0007 (0.07%)
CR	SE	180.0 ± 2.5	1.0774 ± 0.0007 (0.06%)
CR	S	225.0 ± 2.5	1.0601 ± 0.0007 (0.06%)
CR	SW	270.0 ± 2.5	1.0385 ± 0.0007 (0.07%)
CR	W	315.0 ± 2.5	1.0136 ± 0.0007 (0.07%)

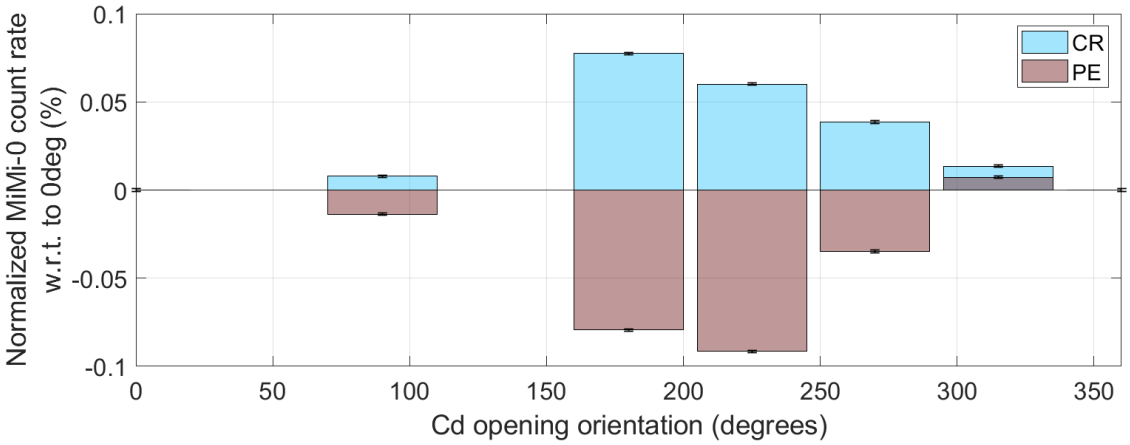

Figure 5.11 – Experimental results for the MiMi-0 count rate as a function of the orientation of the Cd opening in CR and PE. Histograms visually represent the integration over the 40° solid angle.

In the CR lattice position, the experimental results show a maximum increase of 7.74 ± 0.07 % in the counting of the MiMi prototype when the cadmium aperture is oriented towards the core center (SE - 180°) with respect to when it is pointing to the opposite direction. This means that a higher share of neutrons crossing the aperture of ±20° around the core direction, moving and interacting within the volume inside the cadmium-covered cap, is then incident on the MiMi-0 active volume. On the contrary, in the PE position close to the reflector, more thermal neutrons are counted when the cadmium opening is oriented towards the water reflector, which by definition has the purpose of sending back neutrons to the core. The minimum counting in PE is observed for a cadmium orientation towards the south direction, corresponding to 225°, with a magnitude of -9.16 ± 0.06 % with respect to the reflector direction.

5.2.3 Comparison with Serpent 2 simulations

The best approach to reproduce the experimental results of the neutron flux directionality study with Serpent 2 simulations is to explicitly model the experimental setup. Indeed, the positioning of the MiMi-0 detector within the plastic holder and the potential interactions of both thermal and fast neutrons in the plastic call for detailed modeling to allow for comparison. The ^{6}Li reaction rate must also be scored in a real detector-size tally volume or in a slightly axially smeared one, i.e., 2 mm height, to minimize the additional biases introduced by the smearing.

The two-step approach tested in Section 5.1.3.2, proven valuable at simulating relative localized effects, is applied to the simulation of the directionality experiments. As a first attempt, the source files generated from full-core criticality simulations for the azimuthal experiments, i.e., the first step, is assumed to be applicable also in this case. The source file for the CR lattice position is used to perform a series of second-step calculations with explicit modeling of the Cd layer in the 4.5 cm CR geometry, as shown in Figure 5.12.

The ^{6}Li reaction rate is virtually scored with track-length detectors within a tally volume of real-detector size and a smeared height of 2 mm positioned at the experimental location of the MiMi-0 neutron detector, i.e., at 1 cm above the lower level of the POM holder as shown in Figure 5.12(c). Different geometry configurations are investigated to assess the impact of the presence of the POM

holder and study the use of aluminum as a holder material for future improvements to the experimental setup. The simulated configurations can be summarized as follows:

- No holder: the holder is not modeled and the volume inside the Cd layer is filled with only air and with the MiMi-0 active volume geometry positioned as in the experiments;
- POM holder: the POM holder is modeled explicitly in the geometry. This configuration corresponds to the full-analog modeling of the experimental setup;
- Al holder: the material of the holder is switched from POM to aluminum.

For each configuration, two second-step simulations are performed: one with the Cd opening oriented at 0° (NW direction) and at 180° (SE direction) to observe the behavior of the relative difference between the two orientations. All the simulation results are obtained with the ENDF/B-VII.0 [93] nuclear data library. The simulation results are reported in Table XV.

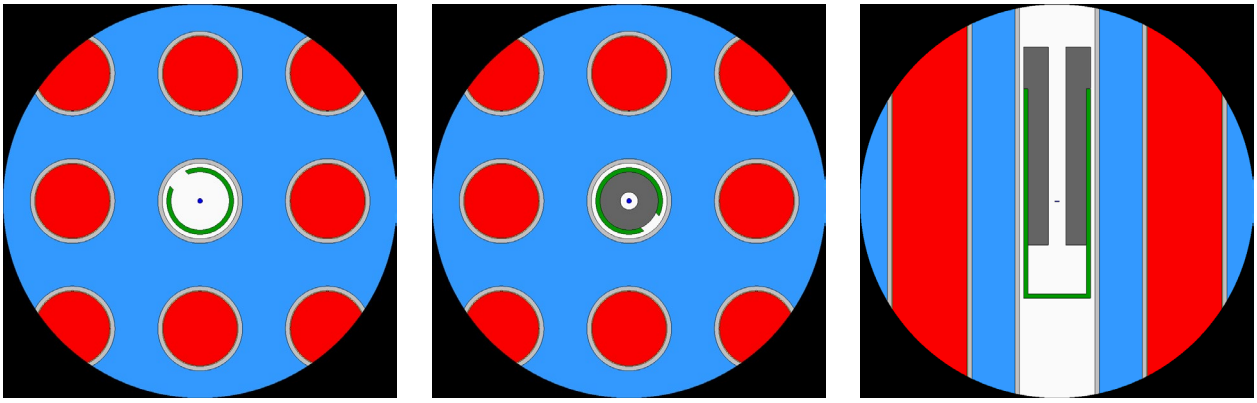

(a) (b) (c)

Figure 5.12 – Examples of second-step geometry configurations for the simulation of neutron flux directionality. (a) "No holder" configuration with Cd opening oriented at NW (0°). (b) Horizontal and (c) vertical cut of the "POM holder" configuration with Cd opening oriented at SE (180°). The MiMi-0 is always modeled at the experimental location.

Table XV – Differences in ^{6}Li reaction rate at different Cd orientations and configurations in the CR lattice location.

	Difference with no holder at NW - 0° (%)	**Difference with no holder at SE -180° (%)**	**180°-0° Cd orientation difference (%)**
No holder	-	-	22 ± 3
POM holder	30 ± 3	21 ± 3	13 ± 2
Al holder	-2 ± 2	-3 ± 2	20 ± 3

The second-step simulation results presented in Table XV show that, within the large uncertainties dictated by the size of the source file, the presence of the POM holder has a strong +30% positive effect on the ^{6}Li reaction rate measured within its volume with respect to a configuration where the POM holder is absent. This means that POM is adding a contribution to the counting of the MiMi-0 detector by thermalization of fast neutrons entering the aperture or crossing the cadmium layer. The

POM effect appears to be not homogenous and less effective in moderation when the Cd opening is oriented towards SE. This is probably linked also to an increase in absorptions in plastic.

For the full-analog configuration, i.e., with POM, the difference between the ^{6}Li reaction rate at different Cd orientations shows a strong reduction with respect to the unperturbed case. Nevertheless, this difference of +13 ± 2 % is almost double what the MiMi-0 neutron detector is measuring experimentally, corresponding to +7.74 ± 0.07 %. Despite the almost inexistent flux perturbation of aluminum, Table XV shows that the ^{6}Li reaction rate difference scored when aluminum is substituted with plastic is even higher and comparable to the unperturbed case. This might indicate that the discrepancy between simulated and experimental results is not connected to the choice of the holder material.

The assumption behind the second-step simulations was that the same source file recorded for the azimuthal experiments could be employed to simulate the flux directionality. However, some differences between the two experimental setups might play a role:

- The insertion in the reduced-model geometry of a strong perturbation, i.e., the Cd layer. Cadmium is a strong neutron absorber and it is possible that its perturbation to the flux map of CROCUS extends up to the 4.5-cm spherical surface at which the source file was recorded.
- The critical water level between the experiments is not the same. A difference in the order of 5 mm in water level exists between the two experimental setups in the CR lattice position. A difference in the critical water affects the axial shape of the flux map and thus the distribution of source histories on the 4.5-cm spherical surface used in the second-step simulations for the flux directionality.

The two effects are tested simultaneously by investigating the relative difference in the axial shape of the total flux in the CR lattice position for the control rod tube filled with, respectively, the POM holder for the azimuthal study and with the Cd-covered cap and the respective POM-holder for the flux directionality study. The results, shown in Figure 5.13, demonstrate that at the boundaries of the 4.5-cm sphere in the axial direction, the total flux is perturbed by the presence of the Cd piece. The maximum difference visible in Figure 5.13 is -5.6 ± 1.4 %. It could be expected that a similar effect, if not stronger, is present in the radial direction. The different critical, instead, does not seem to play a crucial role.

Therefore, it is possible to conclude that the perturbation introduced by the cadmium strongly biases the results of the second-step simulations presented in this Section, showing an additional limitation of the two-step method. For this reason, a new source file must be generated to have a consistent comparison of simulation results and experimental data.

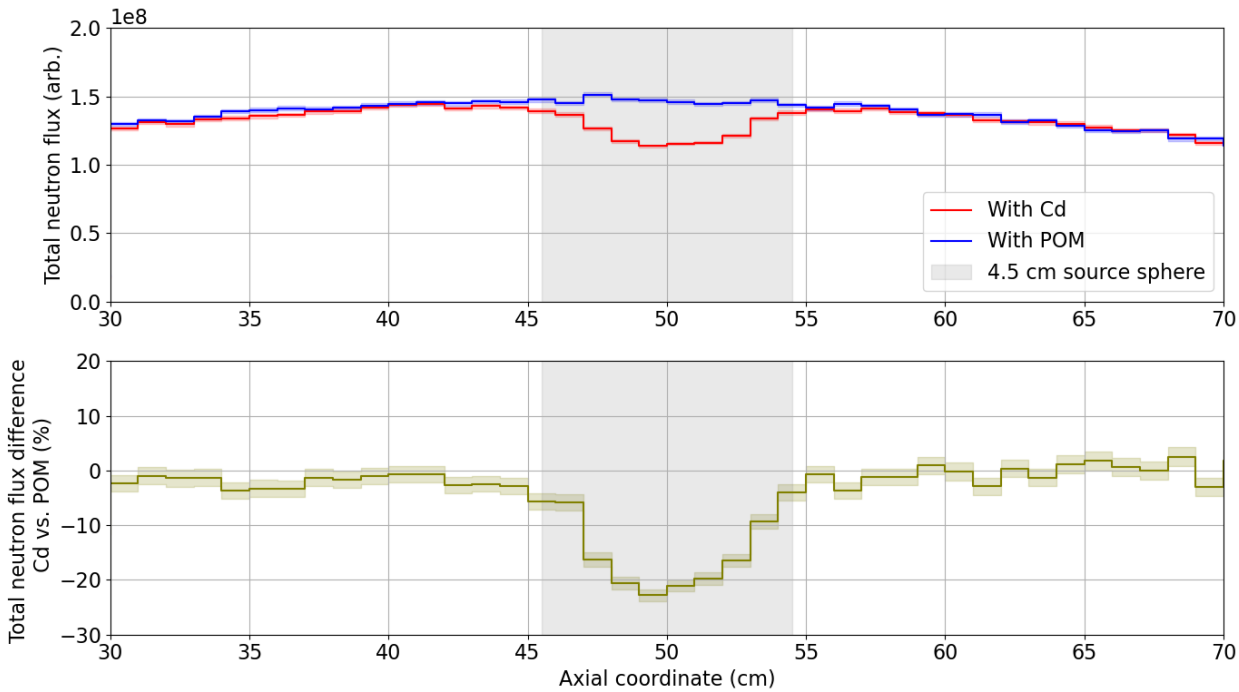

Figure 5.13 – Comparison of the axial total flux shape in the CR lattice position for azimuthal and directionally experiments. The portion of space where the 4.5-cm sphere for source recording is positioned is highlighted in grey.

5.2.4 Conclusions

The investigation of the directionality of the thermal neutron flux in the CROCUS experimental channels in CR and PE lattice positions with the MiMi-0 neutron detector prototype demonstrates that:

- A dependency on the directionality of the thermal neutron flux exists in both CR and PE lattice locations. In CR, the highest share of thermal neutrons is coming from the direction of the core center, while in PE, the opposite is observed, i.e., from the core reflector.
- The design of the experimental setup can be improved. The MiMi neutron detectors should be supported by a holder made of a material introducing a minimal perturbation of the neutron flux, such as aluminum. A tailored Cd-covered cap should be designed for its exclusive use with MiMi neutron detectors, minimizing the space between the cadmium opening and the detector to avoid dispersion of incoming neutrons in the cap volume;
- The application of the two-step methodology requires the generation of a neutron source taking into account the flux perturbations introduced by the experimental setup. In this study, the use of a previously generated source file is biasing the simulation results due to the insertion of the Cd-covered cap in the model geometry.

5.3 Millimetric fuel rods displacement experiments

In light water reactors (LWRs), several mechanical fuel deformations occur during the irradiation history and range across different spatial scales, from the µm to the mm. Typical mm-wise fuel deformation phenomena range from fuel assembly bowing [6] in normal operation conditions to rods ballooning during accident scenarios [112]. Such phenomena, happening within the spatial range of a few mm, might have an impact on both reactor safety – e.g., preventing the insertion of control elements or adding difficulties in the handling of spent fuel elements. At the same time, fuel displacements have an effect on the local neutron flux and power distribution in the core, as shown by Rochman et *al.*[24] with a computational study.

High-resolution pin-resolved neutronics codes could be used to predict the effects of fuel displacements on the local neutron population, prior validation against representative inter-pin experimental data. However, the general scarcity of inter-pin experimental data points, and in particular, the absence – up to the knowledge of the author – of localized thermal neutron flux measurements in the vicinity of fuel displacement, limit the validation exercise.

In this framework, the miniature dimensions of the MiMi neutron detectors are exploited to investigate the impact on the local thermal neutron flux of mm-wise static lateral fuel rod displacements in CROCUS. The possibility to laterally displace fuel rods in CROCUS is offered by the recent installation of the COLIBRI fuel rods oscillator (described in Section 3.3) in CROCUS. The second-version prototype of the MiMi neutron detectors, called MiMi-1 and described in Section 4.3.1.1, is attached to one of the laterally-oscillating fuel rods of COLIBRI as visible in Figure 5.14. The same rod or the adjacent one are moved alternatively at different lateral displacements within the ±2.5 mm allowed by the COLIBRI device and the MiMi-1 count rate is recorded.

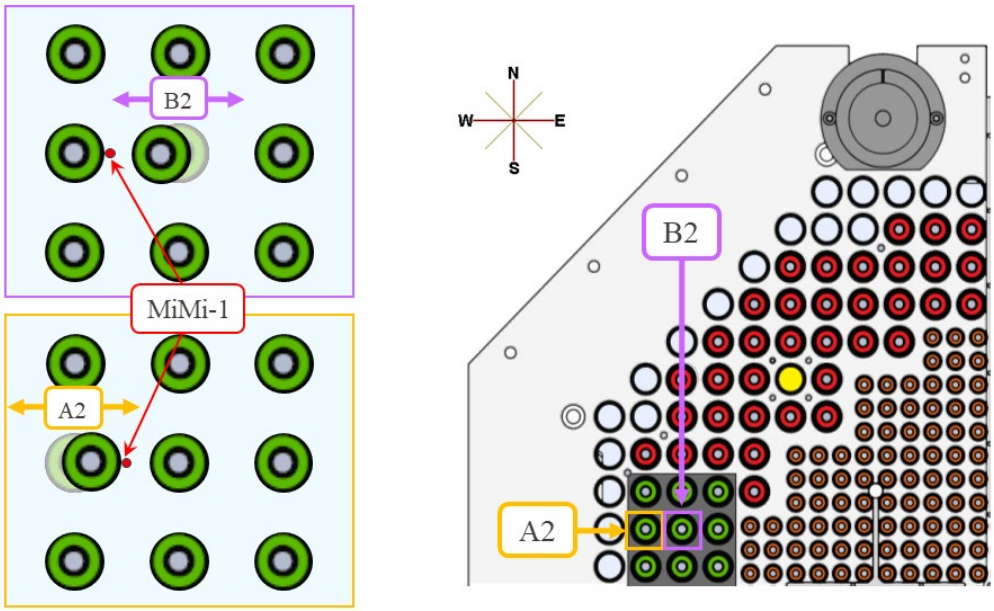

Figure 5.14 – Scheme of the fuel lateral displacement experiments, with indication of the COLIBRI rods involved and the position of the MiMi-1 neutron detector.

This experimental study aims at proving the feasibility of high-resolution online measurements for characterizing mm-range fuel displacements. The comparison with Serpent 2 simulations results in a preliminary assessment of possible biases in the applicability of nuclear data libraries for fuel displacements.

5.3.1 Experimental setup

The experimental campaign to study the local impact on the thermal neutron flux of millimetric fuel rod displacements was performed under a special temporary permit of the Swiss Federal Nuclear Safety Inspectorate (ENSI/IFSN) and therefore represents a unique measuring setup.

The A2 rod of the COLIBRI device, indicated in Figure 5.14, is instrumented with a MiMi-1 neutron detector. It is the same one used for the testing of the PCB boards described in Section 4.3.1.1 and for the experimental campaign in SUR-100 in Appendix A. The MiMi-1 detector is attached to the A2 rod by means of a Polytetrafluoroethylene (PTFE) holder (see Figure 5.15). The choice of a plastic holder is motivated by the need for safety. Metallic holders, even if more suitable to avoid flux perturbations, could cause damages to the fuel rod cladding.

The holder is a 15-mm high and 5-mm thick PTFE hollow cylinder surrounding the aluminum fuel cladding of the A2 rod. Five equally-spaced holes with a double diameter are drilled in the range between -90° and 90° (0° oriented towards east) and they are meant to accommodate up to 5 miniature detectors. The double-diameter of the holes matches that of the MiMi-1 aluminum cap for precise positioning of the instrument outside of the PTFE holder to avoid local perturbations around the detector's active volume. The MiMi-1 active volume is positioned at an axial distance of approximately 0.85 mm from the lower level of the PTFE holder. It is to be noted that the device was meant to be used with watertight miniature fission chambers as well, thus allowing results comparison with a ^{235}U fission rate, but the rigidity of their cable made the prospect impractical.

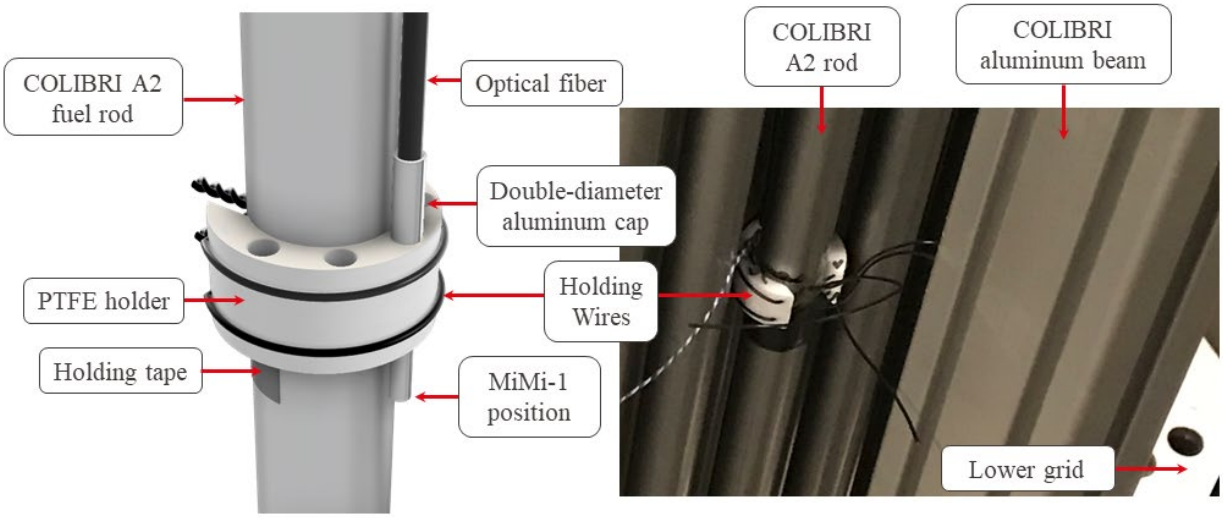

Figure 5.15 – 3D CAD model of the MiMi-1 holder installed on the A2 CROCUS fuel rod and picture of the experimental setup in CROCUS.

An opening of 15 mm on the west side is made to clip the holder to the rod thanks to its elastic deformation. This feature is designed to be able to position the holder without having to unload the fuel. Tape stoppers and two metallic wires running around the PTFE are used to sustain the holder, ensure its grip on the rod, and prevent any unwanted fall in the vessel. With the metallic wires, the whole holder thickness increases to 5.97 mm, leaving an acceptable margin of 1.35 mm from the adjacent fuel rods in case the maximum COLIBRI displacement of +2.5 mm is reached. In this study, all the positive displacements refer to movements towards the east direction and thus the core center, while negative ones are oriented towards the west and the reflector. In the axial direction, the holder is positioned on the A2 rod so that the miniature neutron detector active volume is set at the axial position of 53.6 ± 0.5 mm, zero being the nominal lower level of the active fuel.

The MiMi-1 prototype is connected to one of the PCB testing modules developed at LRS and described in Section 4.3.1.1. The photon counting is recorded with a standard counter module.

In this study, the COLIBRI device is not used for its original purpose of oscillating fuel rods, but it is simply used to laterally displace them online while the core is critical. This allows performing multiple measurements of fuel displacements during a single CROCUS operation. The selection of the lateral displacement within the ±2.5 mm allowed by the COLIBRI device is performed by launching low-frequency oscillations, i.e., 0.097 Hz, and interrupting the motor rotation to obtain static displacements of the selected fuel rod.

A first reference measurement at the ideally unperturbed lattice position is performed before starting the oscillations. The A2 rod is inserted in the COLIBRI device, which is set at its zero-motor position corresponding to a 0 mm displacement of the upper plate of COLIBRI and thus of the top of the A2 rod. Afterward, the neutron count rate of the MiMi-1 is recorded at different displacements of the A2 fuel rod while the CROCUS reactor is critical in a range of power between 5 and 6 W, and the results are normalized by the fission chamber monitors' recordings. A number of counts in the order of 9×10^6 is acquired to achieve statistical uncertainties in the order of 0.03%. The same procedure is repeated for the lateral displacement of the adjacent B2 rod.

5.3.2 Exact fuel displacement at MiMi-1 axial level

The COLIBRI motor and cable data are studied to reconstruct the movement of the two moving plates and to estimate the exact displacement of the A2 and B2 rods at the MiMi-1 axial level.

The first oscillation recording is analyzed and the results are reported in Figure 5.16(a). The upper plate movement obtained from the motor position data starts at the zero-motor position and, after initial inertia, it follows a sinusoidal function with a frequency of 0.097 Hz and an amplitude of 2.50 ± 0.15 mm. The amplitude is set by the selected eccentric sheave and its uncertainty is given by the tolerances between the upper plate holes and the rod caps. The movement of the lower plate is measured directly by the cable coder.

From the acquired data, it is possible to notice that the maximum amplitude of the lower plate oscillation is limited to 4.2 mm, while the stoppers would allow a total movement of up to 4.6 mm (±2.3 mm). In Figure 5.16(a), it is also visible how the movement presents a more prolonged flattening

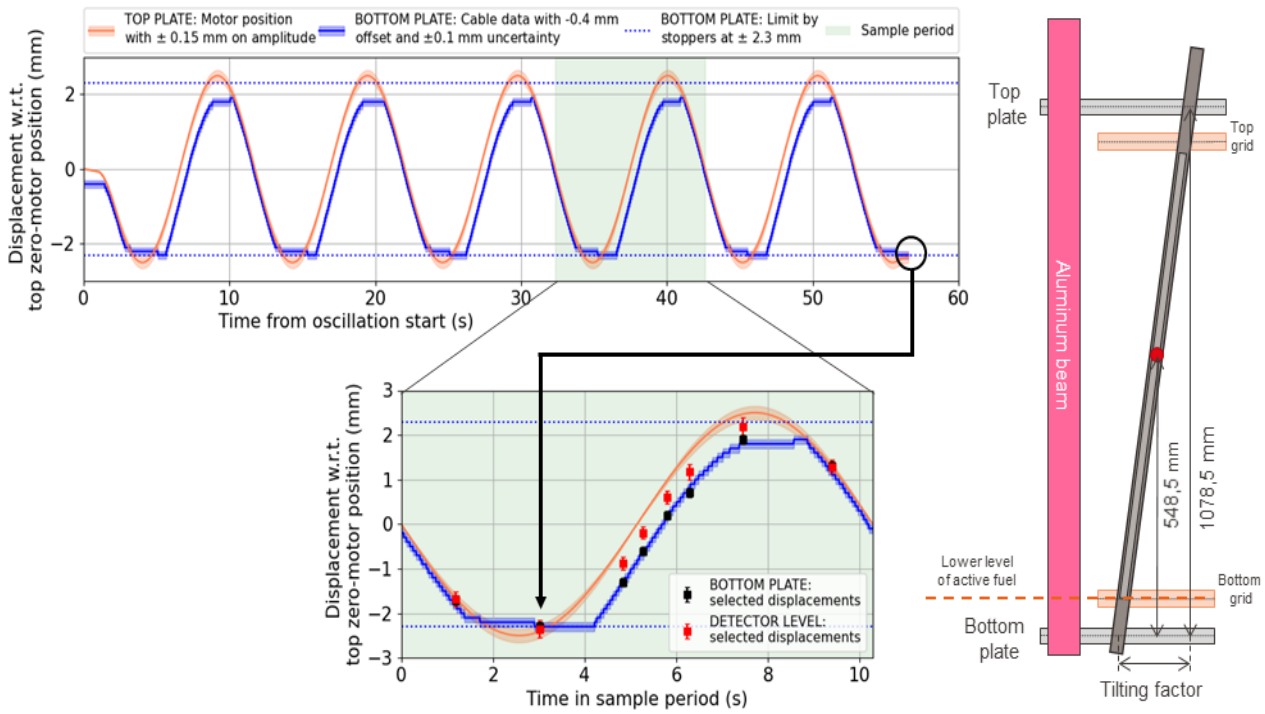

(a) (b)

Figure 5.16 – (a) Movement data of COLIBRI top and bottom plate and representation on a sample period of the selected displacements considered for this study. (b) Schematic for the calculation of the exact lateral displacement at the MiMi-1 detector axial level.

in the negative direction than in the positive. Hence, it is possible to conclude that due to the rod's weight and calibration limitations, the initial lower plate position had an offset of -0.4 mm with respect to the top plate. The -0.4 mm offset is represented in Figure 5.16(a) as a negative translation of the cable data.

Figure 5.16 shows that while the movement is directed from positive to negative, namely from the core center towards the periphery, the top and bottom extremities of the rod are aligned within their uncertainty. However, when the movement is reversed (from negative to positive), the lower end of the rod is not following the upper end, probably because it is withheld by the cable coder exerting tension towards the periphery. The different displacement of the two rod's extremities during part of the oscillation implies that, in some positions, the A2 rod was slightly tilted during the experiments.

The cable data at the end of each oscillation, performed to obtain different static lateral displacements, are plotted as a function of time within a sample oscillation period (points in black in Figure 5.16(a)). A tilting factor at the different measurement positions is estimated as the difference between the selected displacement point from cable data (in black) and the motor position (in orange). As a consequence, it is possible to estimate the exact displacement at the MiMi-1 axial level by knowing the tilting factor and the detector height with respect to the middle plane of the bottom moving plate. A schematic of this calculation process is shown in Figure 5.16(b) and the final estimated displacements corrected by the rod tilting are reported in red in Figure 5.16(a) and with the experimental results in Table XVI. The same movement analysis is repeated for the later displacement

of the B2 rod of COLIBRI and its exact lateral displacements at the MiMi-1 axial level are reported in Table XVII.

5.3.3 Experimental results

The thermal neutron count rate is measured for different static lateral displacements of the A2 rod and B2 rod with the MiMi-1 neutron detector installed on the A2 rod. The experimental results are reported in Table XVI for the A2 displacement and in Table XVII for the B2 displacement. The number of counts recorded by the MiMi-1 is power-normalized by the sum of both CROCUS fission chambers and then normalized again by the value obtained at the nominal position, corresponding to the displacement at the detector level when the motor is set at its zero position. In order to lower the counting statistic uncertainties, more than 10^7 counts are acquired at each lateral displacement. A visual representation of the results is shown in Figure 5.17.

Table XVI – MiMi-1 count rate power-normalized and divided by its value at the A2 nominal position (in bold) as a function of bottom and detector-height displacements of the A2 rod.

A2 rod at bottom position (mm)	A2 rod at MiMi-1 level (mm)	Distance A2-B2 at MiMi-1 level (mm)	Normalized count rate (-)	Critical water level (mm)
-2.30 ± 0.10	-2.3 ± 0.2	31.5 ± 0.2	1.0362 ± 0.0005 (0.05%)	954.3 ± 0.1
-1.70 ± 0.10	-1.68 ± 0.17	30.85 ± 0.17	1.0279 ± 0.0005 (0.05%)	954.5 ± 0.1
-1.30 ± 0.10	-0.88 ± 0.14	30.05 ± 0.14	1.0161 ± 0.0005 (0.05%)	954.4 ± 0.1
-0.6 ± 0.10	-0.19 ± 0.14	29.36 ± 0.14	1.0044 ± 0.0005 (0.05%)	954.6 ± 0.1
-0.40 ± 0.10	**-0.20 ± 0.10**	**29.37 ± 0.10**	**1.0000 ± 0.0005 (0.05%)**	**954.5 ± 0.1**
0.20 ± 0.10	0.60 ± 0.15	28.57 ± 0.15	0.9857 ± 0.0005 (0.05%)	954.6 ± 0.1
0.70 ± 0.10	1.17 ± 0.17	28.00 ± 0.17	0.9738 ± 0.0005 (0.05%)	954.6 ± 0.1
1.30 ± 0.10	1.29 ± 0.16	27.88 ± 0.16	0.9693 ± 0.0005 (0.05%)	954.8 ± 0.1
1.90 ± 0.10	2.2 ± 0.2	27.0 ± 0.2	0.9453 ± 0.0005 (0.05%)	954.7 ± 0.1

Table XVII – MiMi-1 count rate power-normalized and divided by its value at the B2 nominal position (in bold) as a function of bottom and detector-height displacements of the B2 rod.

B2 rod at bottom position (mm)	B2 rod at MiMi-1 level (mm)	Distance A2-B2 at MiMi-1 level (mm)	Normalized count rate (-)	Critical water level (mm)
-2.1 ± 0.10	-2.3 ± 0.2	26.87 ± 0.2	0.9303 ± 0.0005 (0.05%)	954.6 ± 0.1
-1.50 ± 0.10	-1.83 ± 0.18	27.34 ± 0.18	0.9530 ± 0.0005 (0.05%)	954.6 ± 0.1
-1.10 ± 0.10	-0.78 ± 0.14	28.39 ± 0.14	0.9727 ± 0.0006 (0.07%)	954.6 ± 0.1
-0.6 ± 0.10	-0.3 ± 0.14	28.87 ± 0.14	0.9865 ± 0.0005 (0.05%)	954.6 ± 0.1
-0.2 ± 0.10	**0.20 ± 0.10**	**29.37 ± 0.10**	**1.0000 ± 0.0005 (0.05%)**	**954.6 ± 0.1**
0.40 ± 0.10	0.7 ± 0.16	29.87 ± 0.16	1.0153 ± 0.0007 (0.07%)	954.6 ± 0.1
0.90 ± 0.10	1.1 ± 0.16	30.39 ± 0.16	1.0267 ± 0.0006 (0.05%)	954.6 ± 0.1

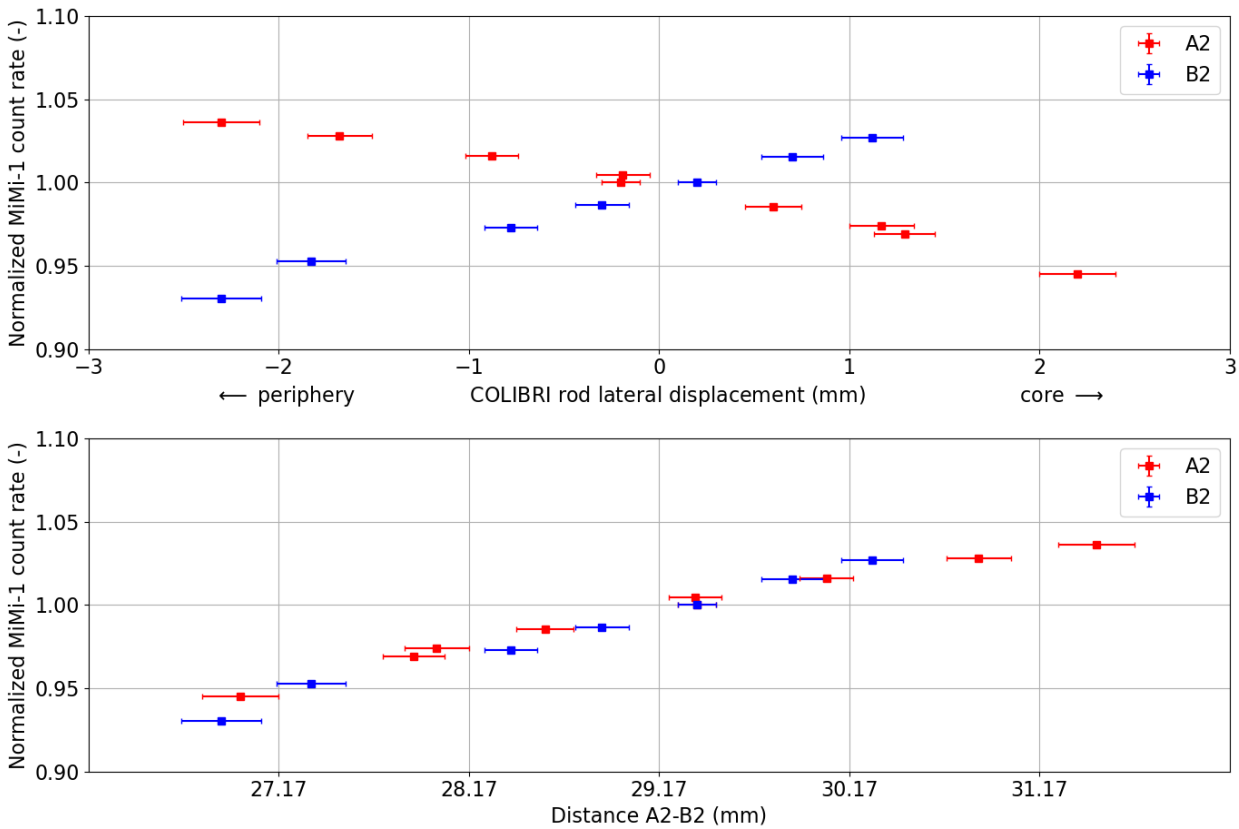

Figure 5.17 – Normalized MiMi-1 count rate as a function of the rod displacement for A2 and B2, and as a function of the variable distance between the two rods where the nominal pitch of U_{met} rods is 29.17 mm.

The experimental data represented in Figure 5.17 show the impact on the local thermal flux measured by the MiMi-1 neutron detector following a variation of the fuel gap between two U_{met} rods of CROCUS as a function of the rods' displacement (top) and the distance between the A2 and B2 rods (bottom). The order of magnitude of the effect is estimated to be +2.50 ± 0.01 %/mm of gap increase for both A2 and B2 displacement. The general trend indicates that in the positive direction, meaning for larger gap sizes, the thermal neutron flux is reduced, while the contrary happens when the gap is reduced. In fact, as CROCUS is by design an under-moderated core, when the moderation is further reduced by bringing rods closer, the neutron spectrum is locally hardened. As a consequence, the measured thermal neutron count rate is reduced. Similarly, a distance increase between the rods leads to a higher share of thermal neutrons in the detector area and a count rate increase.

In terms of relative displacements with respect to the nominal lattice position, the A2 and the B2 movement have opposite effects. The displacement towards the core periphery of the A2 rod causes an increase of the thermal neutron count rate by 3.62 ± 0.05 % at -2.3 ± 0.2 mm, while the same displacement for the B2 rod induces a reduction of -6.97 ± 0.05 % in the count rate. The difference in the magnitude of the effect is likely related to the increase of absorptions in water when the gap size is increased. For this reason, the A2 rod negative displacement shows a smaller increase in the count rate than the reduction in the same quantity for the negative displacement of the B2 rod. Unfortunately, the lack of experimental data for large positive displacement of the B2 rod does not allow us to conclude if the is a flattening due to absorption in the left-hand side of Figure 5.17.

5.3.4 Comparison with Serpent 2 simulations for A2 displacement

The full-core Serpent2 model of CROCUS is updated to represent the lateral fuel displacement experiments discussed in this Section. As already discussed in previous Sections, the computational cost of multiple standard full-core Serpent 2 simulations with the real detector size at different rod displacements would be prohibitive.

However, with the intent to increase the simulation efficiency, a series of assumptions can be introduced with the intent to virtually score the ^{6}Li reaction rate via full-core criticality simulations. The ^{6}Li reaction rate is recorded with track-length virtual tallies consisting of a smeared cylindrical tally at the MiMi-1 position, with a real-size detector surface and a height of ±20 cm with respect to the actual detector axial level. The use of virtual tallies over a smeared volume is justified by:

- The small neutron flux perturbation induced by the presence of a MiMi detector demonstrated in Section 5.1.3.2, i.e., a few percent. The modeling of the detectors materials and the aluminum cap is considered uninfluential on the averaging of the ^{6}Li reaction rate;
- The assumption that the perturbation introduced at the MiMi-1 detector level by the 0.85-mm distant PTFE holder is minimal. Nevertheless, the PTFE is modeled in the geometry;
- The assumption that the variation in the axial flux shape is constant along the rod height for different rod displacements. Hence, the relative simulation results should not be affected.

A single full-core simulation was run with 7.5×10^{8} neutron histories for each displacement position of the A2 rod, corresponding to one experimental point. Two similar sets of simulations were performed for different nuclear data libraries: ENDF/B-VIII.0 [31] and JEFF-3.1.1 [113]. The choice of not using an updated release of the JEFF library, i.e., JEFF-3.3 [114], depends on the version of Serpent 2 used in these calculations. The Serpent 2.1.31 version used in this study does not allow reading the JEFF-3.3 Thermal Scattering Law (TSL) sub-library in the continuous energy (ACE) format. As a consequence, JEFF-3.3 neutron cross-sections should be used together with the old JEFF-3.1.1 evaluation of the TSL sub-library, generating inconsistent results.

The two sets of simulation results for smeared detectors, normalized by the result value at the nominal position, are shown in Figure 5.18 alongside the experimental data. The propagated simulations' statistical uncertainties are within ±0.8%.

Figure 5.18 shows that the general trend of the experimental data is well represented by the simulation results for both nuclear data libraries. Indeed, the measured normalized count rates lie between 1 or 2 standard deviations of the simulation results, with maximum discrepancies in the order of 2.1 ± 0.7 %. Within the obtained uncertainties, it is difficult to conclude whether a trend in the discrepancies is present. Although the simulations are smeared along a considerably larger detector volume in height, the good agreement between experimental data and Monte Carlo calculations suggests good applicability of the nuclear data for the problem at hand.

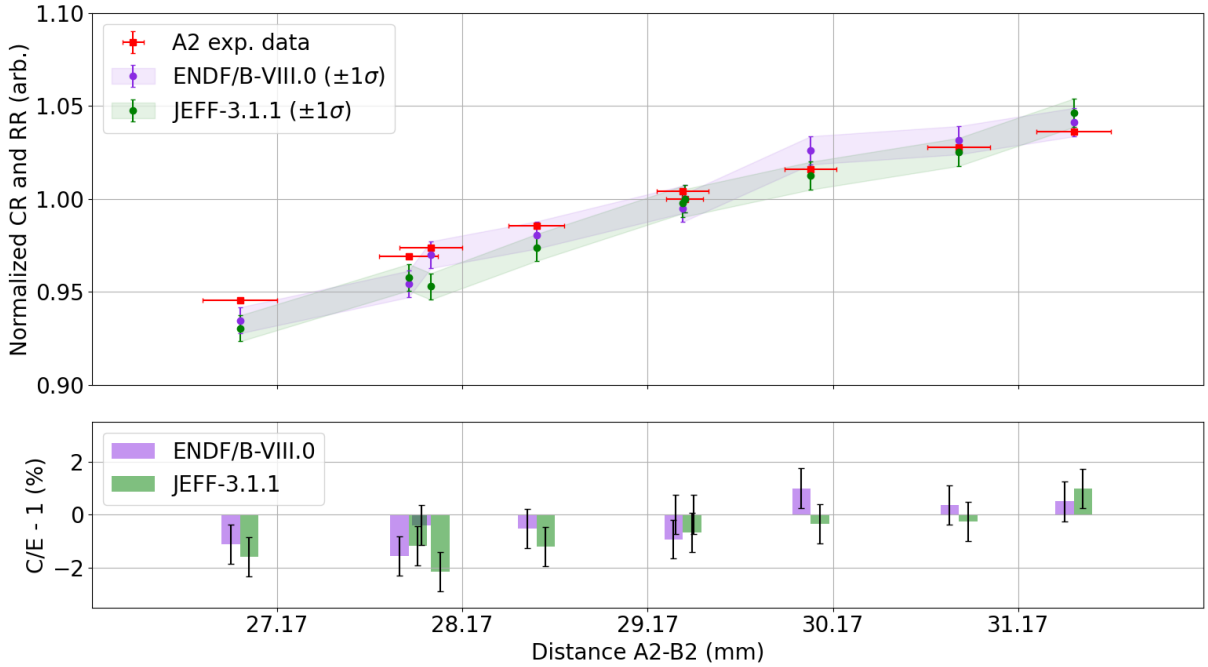

Figure 5.18 – Comparison of measured detector count rate and simulated smeared ^{6}Li reaction rate for different displacements of the A2 rod of CROCUS, using ENDF/B-VIII.0 and JEFF-3.1.1 libraries.

In addition, a variance reduction method based on the hit-distance to target [115] with Serpent 2 was used to perform a preliminary estimate of the ^{6}Li reaction rate for A2 displacements between -2.3 and +2.2 mm for a real-size and real-material detector volume. These preliminary simulations showed a variation of the ^{6}Li reaction rate of -9.0 ± 1.7 % across the whole displacement range of 4.5 mm, which is in agreement with the experimental value of -9.09 ± 0.07 %.

5.3.5 Conclusions

The local impact on the thermal neutron flux of lateral fuel rod displacements was investigated in CROCUS. The experimental data measured with the MiMi-1 neutron detector prototype and the simulation results of Serpent 2 calculations obtained with different nuclear data libraries allow concluding that:

- The variation of the pitch size between adjacent U_{met} fuel rods of CROCUS has an effect of +2.50 ± 0.01 %/mm of pitch increase. The effect is caused by the increase in the volume of water between the rods leading to a more efficient moderation of neutrons. From the experimental data, it is not possible to conclude if the increase of absorptions is playing a role;

- The comparison of measured normalized count rates with relative ^{6}Li virtual reaction rates scored via full-core Serpent 2 calculations in a smeared volume shows an agreement between the two quantities within one to two standard deviations, with maximum discrepancies of -1.6 ± 0.7 % for ENDF/B-VIII.0 and -2.1 ± 0.7 % for the JEFF-3.1.1 data library.

- Preliminary variance reduction simulations for the analog modeling of the experiment well reproduce the trend of the experimental data, demonstrating to be a viable solution for the simulation of highly localized in-core effect in nuclear reactor cores.

Chapter 6

SAFFRON: a 3D core-mapping system in CROCUS

SAFFRON (an acronym for Scintillator Array with optical Fibers For high-Resolution Online Neutron counting) is a full-core 3D mapping system designed to perform space-dependent neutronics experiments in the CROCUS zero-power reactor at EPFL. The system consists of an array of 149 MiMi neutron detectors spread in the inter-pin spaces of the CROCUS double lattice to count thermal neutrons at a wide range of radial and axial core positions.

The development of the MiMi neutron detectors (in Chapter 4) and their successful application for high-resolution experiments (in Chapter 5) paves the way for designing and installing a scaled-up measuring system in CROCUS. The multiplication of the number of detectors is made possible by the in-house development of the multi-channel signal processing electronics (in Section 4.3.1) used in combination with the digital FPGA algorithm for data acquisition. The reduction of the optical fiber diameter from 3 to 2.2 mm discussed in Section 4.3.3 opens the possibility of positioning the detectors at the most unattainable locations, including within the UO_2 fuel lattice, while leaving the available space for positioning devices. At the same time, the wide range of experiments performed with MiMi prototype detectors and the comparison of their results against Monte Carlo simulations proved that the detector technology is able to measure online highly localized neutronics effects, i.e., within a few mm, with minimal flux perturbations, e.g., flux gradients (in Section 5.1) and fuel pitch variations (in Section 5.3).

As a result, a 149-units array of optimized MiMi neutron detectors, i.e., SAFFRON, is designed for the CROCUS zero-power research reactor. The goal of SAFFRON is to measure online three-dimensional space-dependent neutronics effects and retrieve data useful for the validation of high-fidelity deterministic neutronics codes applied to both steady-state and kinetics problems. In particular, the SAFFRON system would allow measuring in CROCUS:

- The absolute shape of the neutron flux map in steady-state conditions, at different power levels and criticality states;
- The relative changes in the neutron flux map between different reactor configurations, i.e., with or without control rods inserted;

- The localized variation of the flux shape following dynamic events, i.e., control rod insertion or withdrawal, or lateral fuel displacements;
- Spatialization of perturbation noise induced by neutron modulation, e.g., by the COLIBRI oscillation, as observed in [60].

In this Chapter, the design of the SAFFRON system and the results of the first set of high-resolution neutronics experiments performed with it are discussed. In the first Section 6.1, the development and the final design of the SAFFRON system are presented, highlighting the synergies between the custom mechanical design, the MiMi neutron detectors dimensions, and the reactivity impact on the core criticality. Section 6.2 reports the results of the inter-calibration of the 149 MiMi neutron detectors of SAFFRON, performed with a Pu-Be source before the installation of the system. The loading of the system in CROCUS and the first criticality in the SAFFRON configuration are presented in Section 6.3. Finally, Section 6.4 and Section 6.5 present the experimental results of absolute and relative neutron flux maps measured in CROCUS at different experimental conditions and their comparison with preliminary Serpent 2 simulations.

6.1 System design

The installation of a large number of optimized MiMi neutron detectors, called from now on simply "MiMi detectors" for the sake of conciseness, in the inter-pin positions of CROCUS is a non-trivial task. Several factors must be taken into account during the design phase:

- **Detectors distribution**: the MiMi detectors must be evenly distributed in the inter-pin locations to have optimal radial and axial measurement of the core flux shape at any core configuration. The number of detectors can be increased in the proximity of specific locations of interest where flux perturbations could occur, e.g. close to the control rod guide and the COLIBRI fuel rods oscillator;
- **Core geometry**: the reference core configuration must not be modified to allow for the installation of SAFFRON. The arrangement of the fuel lattices, the top and bottom fuel grids of the COLIBRI configuration, and the standard core instrumentation must not be altered. Therefore, an additional mechanical supporting structure must be designed to insert and hold the miniature neutrons in the selected inter-pin positions;
- **Core safety**: the MiMi detectors and their supporting structure must not enter into contact or have friction against the aluminum cladding of the fuel rods to prevent any potential damage. All the additional components must be chemically inert in the demineralized water of CROCUS. The mechanical structure must be designed to be efficiently installed during out-of-vessel loading operations, also minimizing the exposure of the personnel to the CROCUS irradiated fuel;
- **Neutron economy**: all the SAFFRON components have to minimize the reactivity impact on the core criticality. Indeed, the large number of ZnS(Ag):^{6}LiF screens, ^{6}Li being a strong neutron absorber, already significantly reduces the number of neutrons available for propagating the fission chain. Preliminary simulations must be performed to ensure the core

criticality and eventually add fuel rods avoiding the exceedance of the limit reactivity reserve of CROCUS of 200 pcm. In addition, the ZnS(Ag):^{6}LiF screens must be safely secured to prevent any unwanted loss in the core.

6.1.1 Mechanical constraints

In CROCUS, a vertical insertion of the MiMi neutron detectors in the inter-pin space between fuel rods is made impractical by the presence of the upper fuel grids. Opening passages for the optical fibers would require extremely delicate machining of the grid due to the presence of the cadmium layer in it. Therefore, a horizontal insertion was preferred for the installation of the MiMi neutron detectors, even though the peculiar double-lattice fuel arrangement of CROCUS imposes severe limitations. Figure 6.1 shows the positions at which it is possible to cross both fuel lattices and indicates the maximum available space in mm to perform full or partial straight crossings. Partial crossings arise from the presence of the cruciform safety blades in the core center, whose run must be kept clear at all times for safety reasons. However, these partial crossings can be performed from both north and south directions. From Figure 6.1, and excluding the partial crossing of 3.48 mm, the minimum space available between fuel rods is equal to 4.59 mm. Hence, the maximum allowed thickness of material cutting across the core was set to 4 mm to leave a margin for possible mechanical tolerances. The 4-mm limit remains valid also when COLIBRI displaces the 18 fuel rods indicated in green in Figure 6.1 by ±2.5 mm and reduces the 9.87 mm margin to 7.37 mm.

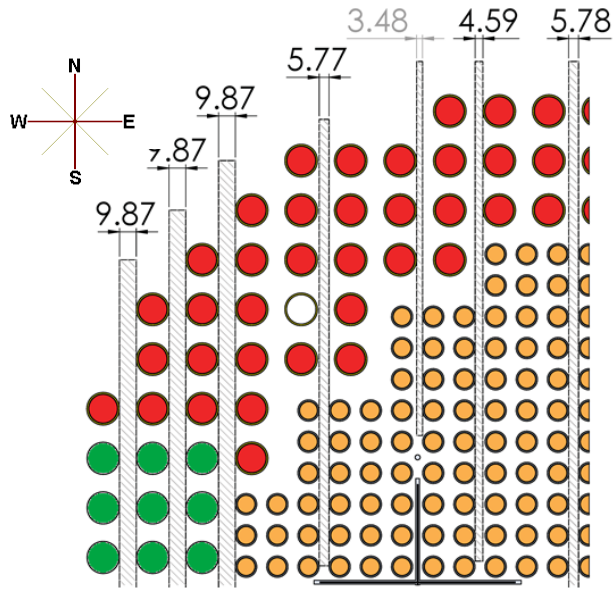

Figure 6.1 – North-west portion of the horizontal section of the CROCUS reactor with indication of the locations available to cross in a straight line the double fuel lattice. The maximum space available for the crossing is indicated in mm.

6.1.2 Mechanical design of supporting structure

Based on the lateral insertion strategy of the 149 detectors and the 4-mm space limit, a tailored mechanical structure to install and hold the SAFFRON system has been designed in-house at LRS. The already existing SolidWorks CAD model of CROCUS is updated with the full SAFFRON system installed, as shown in Figure 6.2.

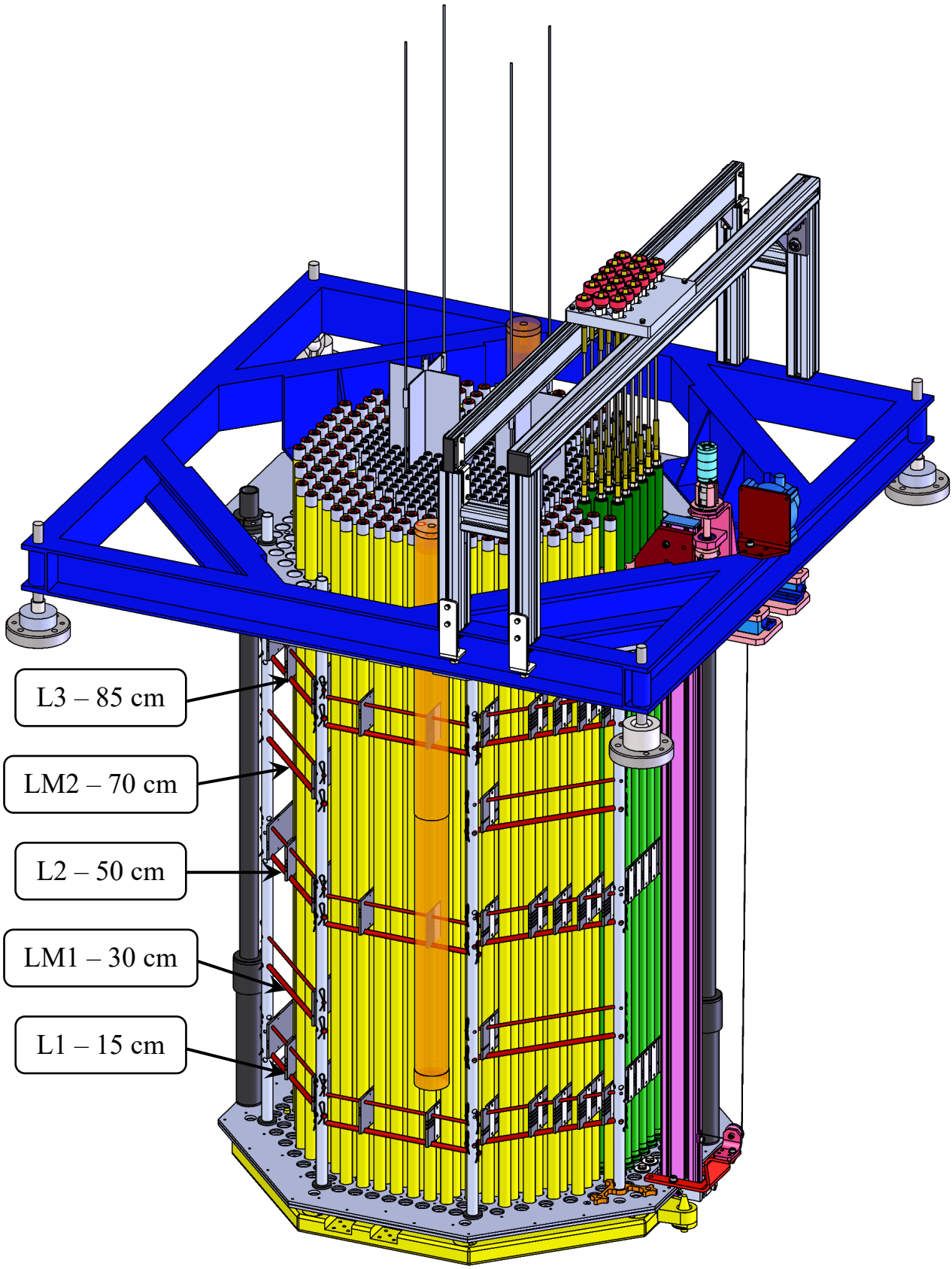

Figure 6.2 – 3D CAD model of the CROCUS core with the SAFFRON full-core mapping system installed. The U_{met} fuel cladding is shown in yellow and green (COLIBRI) for visualization purposes.

The main mechanical pieces composing the SAFFRON supporting structure are:

- 50 rectangular "rulers" of polyoxymethylene (POM-C) with a thickness of 4 mm and a height of 6 cm. A series of grooves in the ruler guide the optical fibers to the designated position for the MiMi neutron detectors' active volumes. The length of the rulers depends on their position in the fuel lattice: rulers can cross the whole core or be split in two to accommodate the presence of the cruciform safety blades. Non-crossing rulers are in correspondence with the UO_2 fuel lattice, and some of them are composed of two joint pieces that allow crossing both the U_{met} and the UO_2 lattice in the centerline of both fuel pitches. The detector positions are covered with a 1-mm white POM-C piece to add an additional light-shielding layer and to avoid exposing the detectors directly to water. An example of a ruler is shown in Figure 6.3. The black POM-C was selected as a material for the rulers due to its mechanical properties, its good resistance in the water, its excellent light opacity, and its density comparable to that of water (1.41 g/cm^3) to minimize the flux perturbation;

- 52 horizontal supporting rods made of anodized aluminum for holding and positioning the rulers among fuel rods at five different axial layers. For each layer, the lower horizontal rods support the rulers in the vertical position and the upper rods cross the rulers to secure their positions in the core with minimal tolerances, in the order of ±0.1 mm. A close-up of horizontal supporting rods is shown in Figure 6.4;

- 8 vertical 18-mm diameter hollow supporting rods of anodized aluminum in ex-core positions of the U_{met} lattice. The vertical rods support the horizontal rods and the rulers at the selected axial levels of the core. The three main levels – L1, L2, and L3 in Figure 6.2 – are positioned in a way that the MiMi detectors' active part is located at 15, 50, and 85 cm of core height, respectively. The two additional layers – LM1 and LM2 in Figure 6.2 – are at 30 and 70 cm to position additional MiMi detectors close to the northwest and southeast control rod guide tubes. The vertical rods are inserted within the fuel girds in the same way as the fuel rods, but with POM-C adaption pieces to match the diameter of the grid openings and minimize uncertainties on the MiMi detectors' positions. The horizontal rods are secured to the vertical rods with safety clips. Several apertures along the rods' height allow for the insertion of the horizontal rods from different angles and at different axial levels, when needed, and leave openings for the water intake in order to minimize the perturbation of the flux map. An aperture at the bottom lets the water level go down at core shutdown;

- 8 vertical 8-mm full supporting rods of anodized aluminum in in-core positions to hold the not-crossing rulers. The in-core rods are attached to the upper and bottom fuel grids by means of adaptation pieces in aluminum and POM-C. The adaptation pieces accommodate the vertical adjustments of the distance between the two fuel grids, in the order of a few mm, during loading procedures of the core without impacting the mechanical stability of the SAFFRON mechanical structure. The system to attach the in-core supporting rods to grids is shown in Figure 6.5.

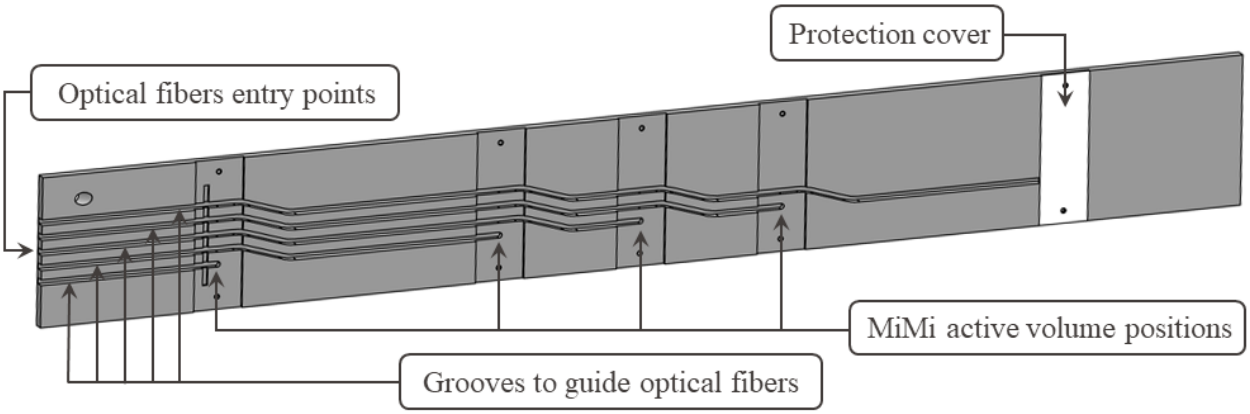

Figure 6.3 – Example of a POM-C ruler of SAFFRON.

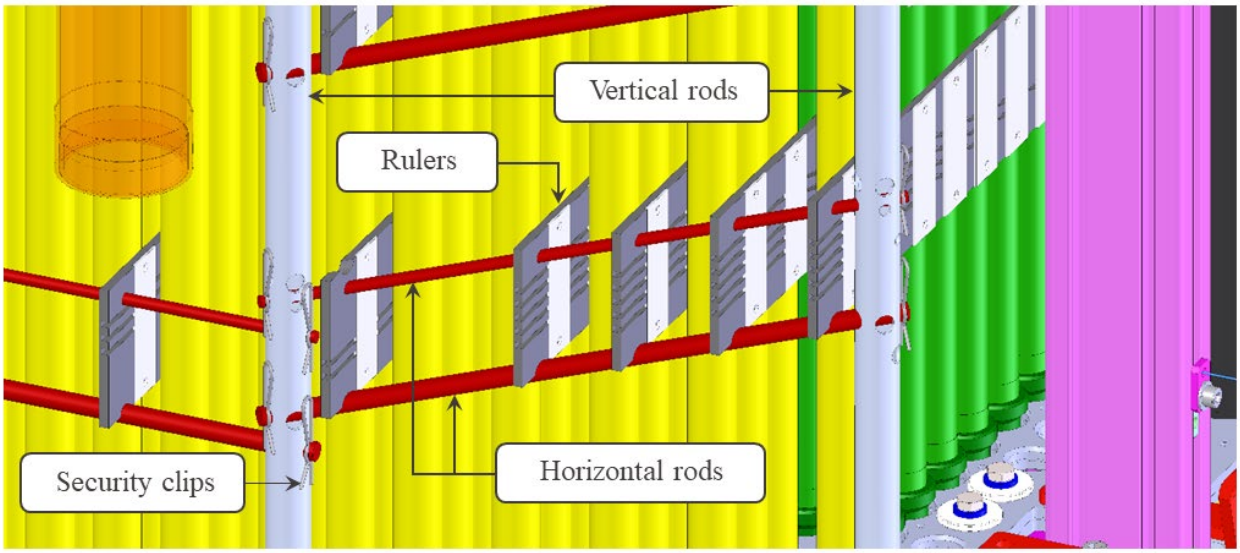

Figure 6.4 – Close up of the L1 layer of SAFFRON from the northwest side of the CROCUS core.

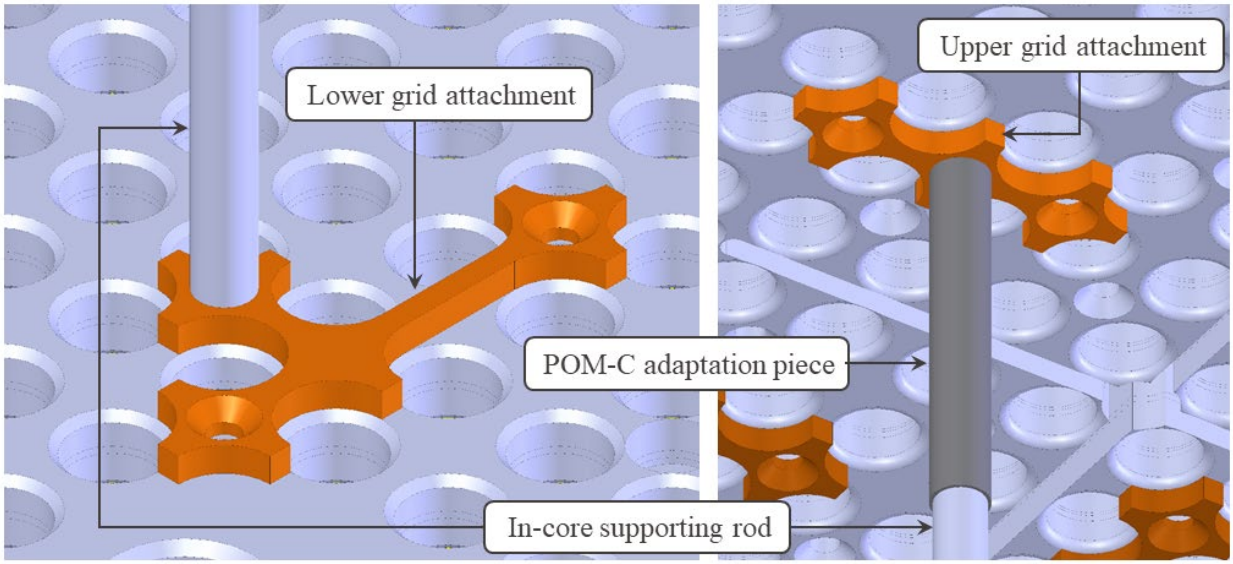

Figure 6.5 – Close up of the lower and upper grid attachments for in-core supporting rods of not-crossing rulers.

6.1.3 Positions of MiMi detectors in the CROCUS core

The final inter-pin positions selected for the installation of MiMi neutron detectors combine the mechanical design with the experimental needs. Each of the three main axial levels – L1, L2, and L3 – accommodate 47 MiMi neutron detectors distributed in between both UO_2 and U_{met} fuel rods. In these layers, the highest number of MiMi detectors per ruler is installed in correspondence with the COLIBRI fuel rods oscillator for future study of space-dependent effects of fuel rod oscillation. The MiMi detectors distribution for L1, L2, and L3 is presented in Figure 6.6, Figure 6.7, and Figure 6.8, respectively.

The two additional axial layers, i.e., LM1 and LM2, are designed to add two additional MiMi detectors next to the two control rod lattice positions at different axial levels. In this way, five MiMi detectors are distributed along the height of the northwest and southeast control rod guide tubes. For symmetry reasons, the same axial distribution of detectors is installed in the corresponding symmetric U_{met} rods in the northeast and southwest quadrants of the core. The distribution of MiMi neutron detectors in the LM1 and LM2 axial layers is shown in Figure 6.9 and Figure 6.10.

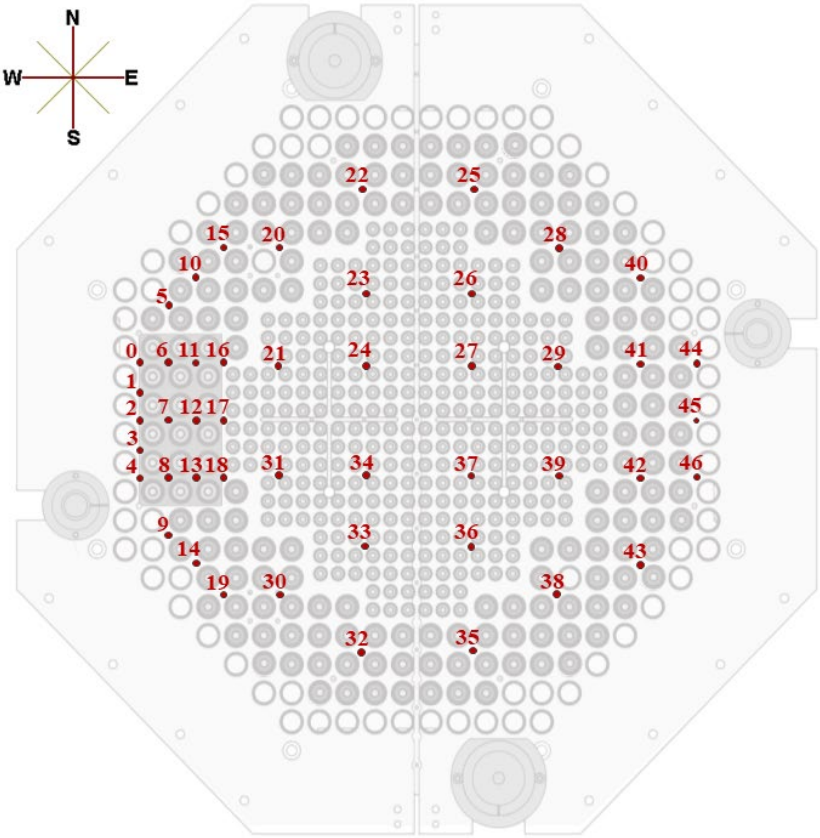

Figure 6.6 – MiMi detectors distribution at L1 axial layer, based on detector number.

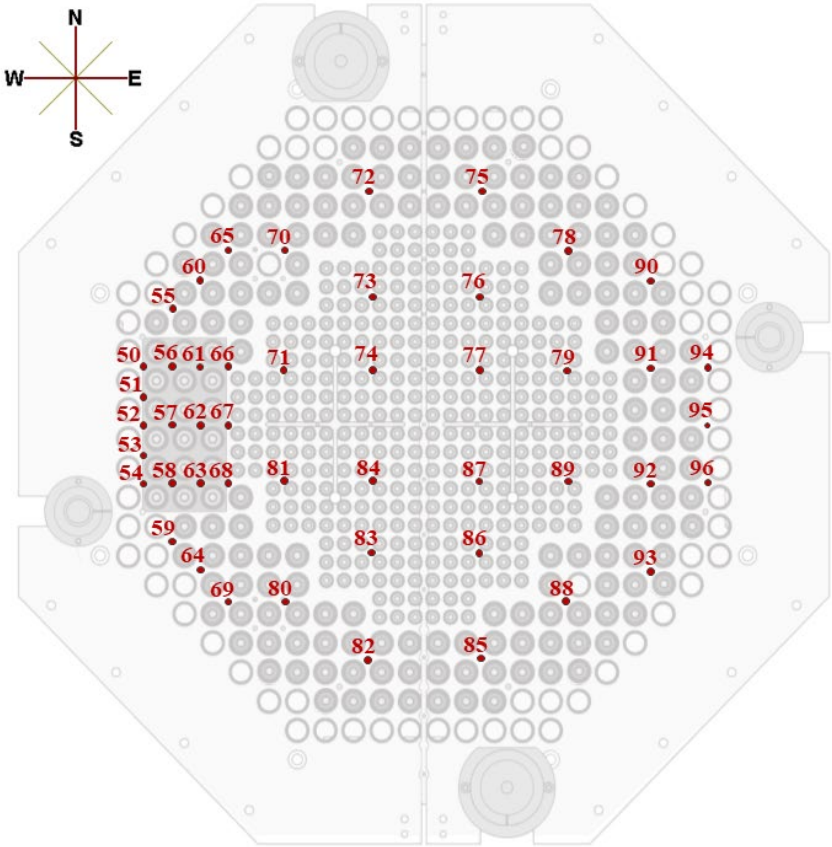

Figure 6.7 – MiMi detectors distribution at L2 axial layer, based on detector number.

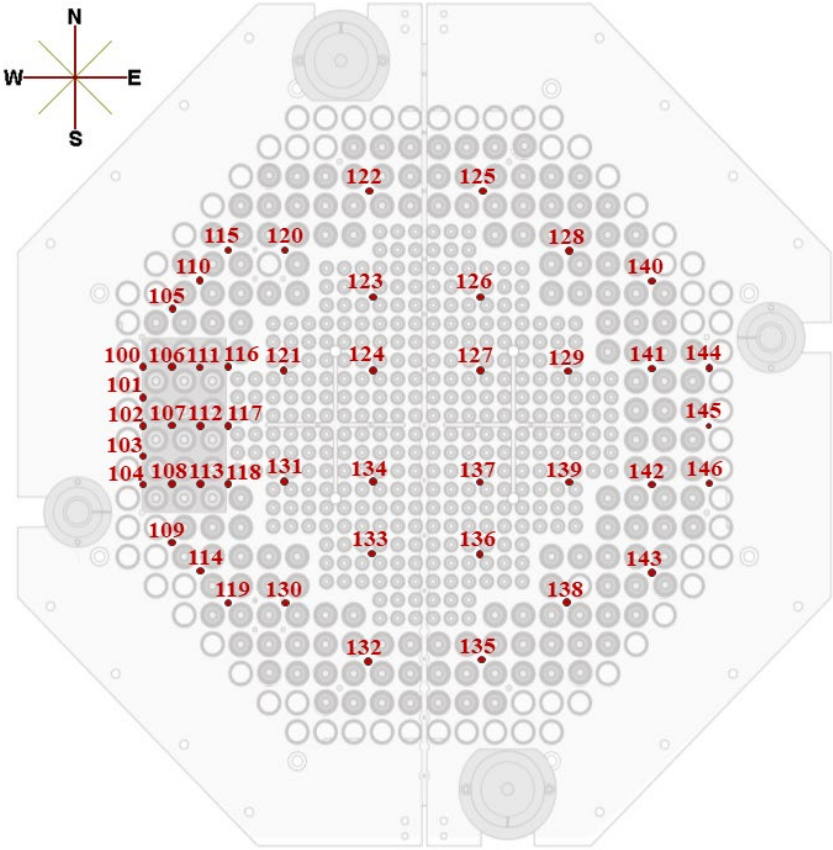

Figure 6.8 – MiMi detectors distribution at L3 axial layer, based on detector number.

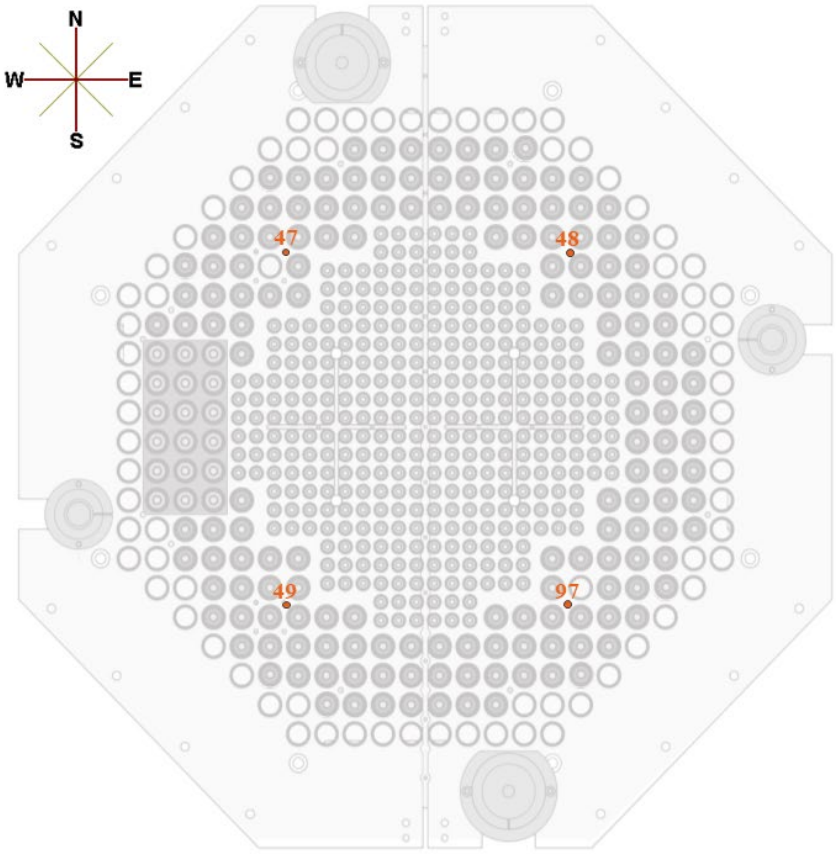

Figure 6.9 – MiMi detectors distribution at LM1 axial layer, based on detector number.

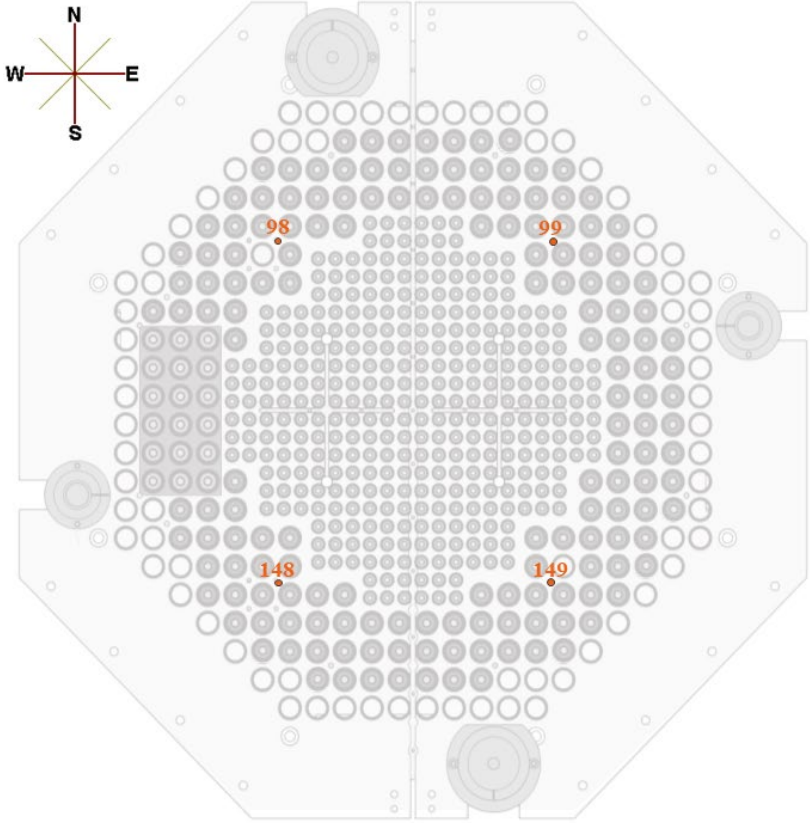

Figure 6.10 – MiMi detectors distribution at LM2 axial layer, based on detector number.

6.1.4 Impact on core criticality

The SAFFRON system, finally composed of 149 MiMi neutron detectors and the dedicated mechanical structure described in Section 6.1.2, is expected to have an impact on the reactor operation in terms of criticality. It is foreseen that the 149 ZnS(Ag):^{6}LiF scintillator screens introduce a strong negative reactivity insertion, which could be partially counteracted by the positive reactivity effect induced by the installation of the rulers in POM-C plastic, as it has a slightly higher density than water. By understanding the balance between these concurrent effects, it is possible to assess if the reactor can be operated in the authorized core configurations and within the safety limits.

The core criticality is studied computationally via Monte Carlo simulations performed with the MCNPX code version 2.4.0 [116], as required by the Swiss safety authority. A detailed MCNPX model of a typical configuration of CROCUS is used as a baseline and reference.

A key parameter to obtain reliable simulation results is represented by the material composition of the ZnS(Ag):^{6}LiF screen, and in particular, by the level of enrichment of ^{6}Li. Based on the supplier data and in order to obtain conservative results, a 95% ^{6}Li enrichment was used, and the resulting reactivity worth of the screen was compared with experimental results. Two testing MiMi detectors with different sensitive volumes were inserted alternatively in the north-west control rod guide tube of CROCUS and the critical level variation with respect to the standard configuration was recorded. The results of both experiments and simulations [117] are reported in Table XVIII, where a good agreement in the reactivity worth range of a few negative pcm is shown.

Table XVIII - Measured and simulated results for the reactivity worth in CROCUS of two MiMi neutron detectors with different sensitive volumes [117]. Simulations are performed with JEFF-3.1 [118] nuclear data library.

MiMi active volume (mm^3)	Measured reactivity worth (pcm)	Simulated reactivity worth (pcm)
0.2	-1.2 ± 0.2	-1 ± 2
0.09	-0.7 ± 0.2	-1 ± 1

Having confirmed the material composition, the entire 3D core-mapping system is modeled in MCNPX. For the sake of simplicity, rulers are modeled as single parallelepipeds, with no distinction between the optical fiber and the ruler material because both are made of similar plastics. The 0.66 × 0.66 × 0.225 mm ZnS(Ag):^{6}LiF screens are modeled explicitly in the predetermined positions (see Section 6.1.3). The rest of the supporting structure is included in the model following as much as possible the previously described mechanical design. Two different nuclear data libraries were used for the simulations: JEFF 3.1 [118] and ENDF/B-VII.1 [119]. The simulation results are presented in Table XIX.

Table XIX - Simulated reactivity worth for SAFFRON [117].

Configuration	JEFF-3.1 K_{eff} (-)	JEFF-3.1 worth (pcm)	ENDF/B-VII.1 K_{eff} (-)	ENDF/ B-VII.1 worth (pcm)
Standard	1.00240 (± 1 pcm)	0	1.00289 (± 2 pcm)	0
With SAFFRON	1.00189 (± 2 pcm)	- 51 ± 3	1.00245 (± 2 pcm)	-44 ± 4

The results in Table XIX show that the general effect of the installation of SAFFRON in CROCUS is a negative reactivity insertion. The strongest negative reactivity insertion corresponds to -51 ± 3 pcm, which is well below the maximum available reactivity reserve of CROCUS of +200 pcm. Therefore, the CROCUS reactor with the 149-detectors system installed in its core should be safely operated within its standard limits. At the same time, a larger reactivity margin might be needed to perform different experiments, e.g., control rod extractions with a small period, or to prevent that the future installation of additional absorbing devices, being neutron instrumentation or oscillating absorber elements [120], would deplete the core's reactivity reserve. Therefore, a permit request for the installation of SAFFRON with the addition of two to six U_{met} rods in the core periphery has been submitted to the Swiss regulatory authority ENSI/IFSN.

6.2 Detectors testing and inter-calibration

The MiMi detectors planned to be installed in CROCUS with the SAFFRON system are built in-house at LRS. Although the updated design presented in Section 4.3.3 is strictly followed during the realization phase, each detector is unique. In fact, different detectors measuring in the same neutron field, in terms of neutron flux level and spectrum, can show variations in their neutron counting capabilities. Such variations could be caused by:

- **Different amounts of ^{6}Li converter**: inhomogeneities in the mixing of ^{6}LiF and ZnS(Ag) may be present in the ND2:1 screen produced by Scintacor [72], causing spots with higher or lower converter concentrations resulting in detectors able to count more or fewer neutrons. In the same fashion, slight variations of screen thickness or size (after cutting) may affect the neutron count rate;

- **Photon yield variations**: the number of photons emitted after a neutron interaction may be affected by variations in the ZnS concentration, misalignments in the positioning of the scintillator screen at the tip of the optical fiber, and infiltrations of filtering materials as glue or dirt. A decrease in the light collection efficiency causes spectrum shifts and, consequently, a neutron count rate variation;

- **Efficiency of processing electronics**: the SiPM photon detection efficiency and the capabilities of the processing electronics to transform SiPM signals into photon counts might differ due to manufacturing. In this work, each scintillator screen is always paired with its own fixed SiPM and processing electronics, and no cross-connections are performed unless explicitly stated.

As mentioned in Section 2.4, the quantity describing the counting capabilities of a single neutron detector is the *intrinsic counting efficiency* ϵ, or *sensitivity*, which relates the detector output with the amount of radiation incident on the active detector volume [12].

In the high-resolution experiments presented in Chapter 5, a single MiMi prototype was moved at different locations within the CROCUS flux map and the changes in its count rate were estimated. In these cases, the relative experimental results are independent of the sensitivity of the single detector, assuming that it remained constant and that no degradation due to irradiation was occurring.

On the contrary, SAFFRON is an array of 149 MiMi detectors with unique characteristics exposed to different neutron flux levels, albeit with a comparable neutron spectrum shape, due to their distribution in the CROCUS core. Therefore, the thermal neutron count rate recorded by each detector depends on both the CROCUS flux map and the detector's sensitivity. As a consequence, the knowledge of the relative efficiency between MiMi detectors is essential to extrapolate the shape of the flux map from the experimental measurements.

The relative sensitivity $\varepsilon_{i,j}$ between two detectors i and j is defined as

$$\varepsilon_{i,j} = \frac{\epsilon_i}{\epsilon_j} \tag{6.1}$$

and is a characteristic parameter of the detector's duo. $\varepsilon_{i,j}$ can be considered independent of the experimental setup and the irradiation conditions in which it is measured, as long as the two detectors experience a similar neutron spectrum. In the particular case of the MiMi neutron detectors, it is also important to maintain the same connection between the ZnS(Ag):^{6}LiF screen and its SiPM to obtain reproducible values of $\varepsilon_{i,j}$.

The experimental procedure called *inter-calibration* aims at finding the relative sensitivity between different detectors in a similar neutron field to obtain spectrum-independent values. These values are successively applied for the rescaling of experimental measurements in unknown neutron fields.

This section presents the experimental inter-calibration of 160 MiMi neutron detectors with the Pu-Be neutron source installed in the CARROUSEL facility, described in Section 4.2.2.1. At first, the mathematical theory behind the inter-calibration procedure is formulated in Section 6.2.1. Then, the experimental measurements and their results leading to the estimation of the relative detector sensitivities are presented. The measured relative sensitivities are successively used in Section 6.4 to re-normalize the thermal neutron count rates obtained from SAFFRON to obtain the thermal flux map of CROCUS.

6.2.1 Mathematical formulation

Considering a generic neutron source located in the center of a non-multiplying media, the sensitivity ϵ of a neutron detector, positioned at a radial distance r from the source with an azimuthal angle θ and a polar angle φ, within a neutron energy spectrum $\chi(E)$, can be defined as:

$$\epsilon(m, g, \chi) = \frac{CR(m, g, \chi, r, \theta, \varphi)}{S(g, \chi, r, \theta, \varphi)} \tag{6.2}$$

where:

- $CR(m, g, \chi, r, \theta, \varphi)$ is the detector count rate. It depends on the detector properties – i.e., material composition m and detector geometry g, the neutron energy spectrum χ, and the detector position;
- $S(\chi, g, r, \theta, \varphi)$ is called here "source factor" and represents the amount of neutrons with a χ spectrum incident on the detector geometry g placed at r, θ, φ coordinates;

- $\epsilon(m, g, \chi)$ is the intrinsic detector efficiency, depending only on the detector properties and the neutron energy spectrum $\chi(E)$.

If the radial distance *r* and the polar angle φ at which the detector is positioned with respect to the point source are fixed, and the neutron spectrum is constant at different azimuthal coordinates θ, Equation (6.2) can be simplified as:

$$\epsilon(m, g) = \frac{CR(m, g, \theta)}{S(g, \theta)} \tag{6.3}$$

The *relative sensitivity* $\varepsilon_{i,j}$ between two neutron detectors *i* and *j* with similar geometrical properties $g_i \approx g_j$ but different material composition $m_i \neq m_j$, positioned respectively at the azimuthal angles θ_i and θ_j is defined as:

$$\varepsilon_{i,j} = \frac{\epsilon(m_i)}{\epsilon(m_j)} = \frac{CR(m_i, \theta_i)}{S(\theta_i)} \cdot \frac{S(\theta_j)}{CR(m_j, \theta_j)} = \frac{CR_{i,\theta_i}}{CR_{j,\theta_j}} \cdot \frac{S_{\theta_j}}{S_{\theta_i}} \tag{6.4}$$

In case the two detectors are positioned alternatively at the same azimuthal position $\theta_i = \theta_j = \bar{\theta}$, or if the source factor shows an isotropic azimuthal profile $S(\theta) = const.$, the relative sensitivity $\varepsilon_{i,j}$ between the two detectors becomes simply the ratio of their count rates:

$$\varepsilon_{i,j} = \frac{CR_i}{CR_j} \tag{6.5}$$

On the contrary, if the azimuthal profile of the neutron field $S(\theta)$ is unknown, the prior estimation of the *relative source factor* $s_{\theta_i,\theta_j} = S_{\theta_i}/S_{\theta_j}$ is essential to derive the relative sensitivity between similar detectors without having to inter-calibrate by positioning them one by one in constant irradiation field conditions $S(\bar{\chi}, \bar{r}, \bar{\theta}, \bar{\varphi})$.

6.2.2 Source factor characterization

The characterization of the source factor consists in finding the profile of $S(\theta)$ with respect to its value at a reference position $S(\theta_{ref})$, at fixed radial $\bar{r}$ and polar $\bar{\varphi}$ coordinates and in a constant neutron spectrum $\bar{\chi}$. The methodology for the characterization of the source factor is explained through a simple case with two detectors only, to be then extended to the practical configuration with 18 MiMi neutron detectors installed in CARROUSEL.

6.2.2.1 Methodology for a simple case

Two detectors of similar geometries, called detector 0 and detector 1, are located respectively at the azimuthal positions α and β, and both are at the same fixed $\bar{r}$ and $\bar{\varphi}$ coordinates within a similar neutron spectrum $\bar{\chi}$. According to Eq. (6.4), the count rates measured by the two detectors, having similar geometrical properties, are:

$$CR_{0,\alpha} = \epsilon_0 \cdot S_\alpha \tag{6.6}$$
$$CR_{1,\beta} = \epsilon_1 \cdot S_\beta \tag{6.7}$$

If the azimuthal positions of the two detectors are switched, the successive measurement yields to

$$CR_{0,\beta} = \epsilon_0 \cdot S_\beta \tag{6.8}$$
$$CR_{1,\alpha} = \epsilon_1 \cdot S_\alpha \tag{6.9}$$

By summing the independent experimental output obtained with different detectors placed at the same azimuthal position, the two following quantities are found:

$$CR_{0,\alpha} + CR_{1,\alpha} = \epsilon_0 \cdot S_\alpha + \epsilon_1 \cdot S_\alpha = S_\alpha(\epsilon_0 + \epsilon_1) \tag{6.10}$$
$$CR_{0,\beta} + CR_{1,\beta} = \epsilon_0 \cdot S_\beta + \epsilon_1 \cdot S_\beta = S_\beta(\epsilon_0 + \epsilon_1) \tag{6.11}$$
$$\rightarrow \frac{S_\alpha}{S_\beta}$$

The ratio between the right-hand terms of Eq. (6.12) and Eq. (6.13) leads to the estimation of the relative source factor $s_{\alpha,\beta} = S_\alpha/S_\beta$. In a similar way, the ratio of the sums of count rates measured with the same detector at different azimuthal angles gives the relative detector efficiency $\varepsilon_{0,1} = \epsilon_0/\epsilon_1$:

$$CR_{0,\alpha} + CR_{0,\beta} = \epsilon_0 \cdot S_\alpha + \epsilon_0 \cdot S_\beta = \epsilon_0(S_\alpha + S_\beta) \tag{6.12}$$
$$CR_{1,\alpha} + CR_{1,\beta} = \epsilon_1 \cdot S_\alpha + \epsilon_1 \cdot S_\beta = \epsilon_1(S_\alpha + S_\beta) \tag{6.13}$$
$$\rightarrow \frac{\epsilon_0}{\epsilon_1}$$

The strength of this methodology consists in the possibility to estimate at the same time both the relative source term and the relative detector efficiency, independently from each other. In this simple case of inter-calibration of two detectors, only two experimental measurements are required to obtain independent relative parameters. However, if the number of detectors to be inter-calibrated becomes large, the number of independent measurements required grows linearly, and the procedure becomes cumbersome. Indeed, 160 measurements would be required to perform a full inter-calibration of 160 MiMi detectors. In practice, this methodology is applied only with a limited number of detectors with the intent to reconstruct the shape of the source factor solely.

6.2.2.2 Extension to real case

The simple methodology is extended to the use of 18 detectors azimuthally equally spaced, all at the same radial and polar coordinate. By positioning each detector at each azimuthal position, for a total of 18 measurements, the relative source term profile $s_{\theta,0} = S(\theta)/S(0)$ with respect to the zero-angle position can be characterized with a 20 degrees resolution. At this stage, such azimuthal resolution was deemed appropriate to find a global shape of the source term around the neutron source. Hence, local source effects within 20 degrees are neglected. A visual illustration of the method extended to 18 detectors is shown in Figure 6.11.

6.2.2.3 Experimental setup

The 18 MiMi detectors chosen to characterize the relative source term profile are positioned at 15 cm of radial distance from the Pu-Be neutron source of CARROUSEL with an azimuthal spacing of 20 degrees and at the same level of the source mid-height, giving a zero polar coordinate. The radial distance of 15 cm, considerably larger than the neutron slowing-down length of Pu-Be neutrons in water [121], was chosen to ensure that the scintillator screens are in a thermal neutron spectrum, as demonstrated in [86].

= 1st meas. = 2nd meas. = 3rd meas. = 17th meas.

Detector number \ Azimuthal angle (deg)	0	20	40	…	320	340	
0	$\epsilon_0 \cdot S_0$	$\epsilon_0 \cdot S_{20}$	$\epsilon_0 \cdot S_{40}$	…	$\epsilon_0 \cdot S_{320}$	$\epsilon_0 \cdot S_{340}$	$\frac{\epsilon_0}{\epsilon_0} = 1$
1	$\epsilon_1 \cdot S_0$	$\epsilon_1 \cdot S_{20}$	$\epsilon_1 \cdot S_{40}$	…	$\epsilon_1 \cdot S_{320}$	$\epsilon_1 \cdot S_{340}$	$\frac{\epsilon_1}{\epsilon_0}$
2	$\epsilon_2 \cdot S_0$	$\epsilon_2 \cdot S_{20}$	$\epsilon_2 \cdot S_{40}$	…	$\epsilon_2 \cdot S_{320}$	$\epsilon_2 \cdot S_{340}$	$\frac{\epsilon_2}{\epsilon_0}$
⋮	⋮	⋮	⋮	.	⋮	⋮	
16	$\epsilon_{16} \cdot S_0$	$\epsilon_{16} \cdot S_{20}$	$\epsilon_{16} \cdot S_{40}$	…	$\epsilon_{16} \cdot S_{320}$	$\epsilon_{16} \cdot S_{340}$	$\frac{\epsilon_{16}}{\epsilon_0}$
17	$\epsilon_{17} \cdot S_0$	$\epsilon_{17} \cdot S_{20}$	$\epsilon_{17} \cdot S_{40}$	…	$\epsilon_{17} \cdot S_{320}$	$\epsilon_{17} \cdot S_{340}$	$\frac{\epsilon_{17}}{\epsilon_0}$
	$\frac{S_0}{S_0} = 1$	$\frac{S_{20}}{S_0}$	$\frac{S_{40}}{S_0}$		$\frac{S_{320}}{S_0}$	$\frac{S_{340}}{S_0}$	

Figure 6.11 – Visual illustration of the methodology used to characterize the source factor profile in CARROUSEL with 18 miniature neutron detectors.

The detectors' positioning around the neutron source is performed with a dedicated plastic structure designed and built at LRS for testing and inter-calibrating all 160 MiMi detectors of SAFFRON. The structure, shown in red in Figure 6.12 for visualization purposes, consists of two black POM-C disks of 30.7 cm diameter and 3 cm thickness, chosen with an identical composition to the SAFFRON ruler to avoid introducing biases in the inter-calibration process. The disks, inserted around the CARROUSEL source tube, are held together by three vertical plastic rods dimensioned to position the detectors' active volume at the source mid-level. At the same time, the rods force the upper and lower disk to rotate in solidarity around the source tube. The lower POM-C disk is machined with 180 blind holes of 2.3 mm diameter and 2.2 cm depth, distributed every 2 degrees at 15 cm from the disk center. Each blind hole can accommodate one of the MiMi detectors (with dimensions described in Section 4.3.3.1), safely held in position by a rubber O-ring through a later aperture, as visible in Figure 6.12. For this experiment, the 18 detectors are positioned one every five holes to respect the desired 20 degrees of spacing. The upper POM-C disk serves as a reference for the azimuthal position of the lower disk. The 36 through holes of 5 mm diameter distributed every 10 degrees around the upper disk define the unit of a rotational step that the structure can perform. A plastic piece attached to the rail running over CARROUSEL allows for the precise selection of the azimuthal coordinate via the insertion of a metallic pin bounding the piece itself and the upper disk through one of its holes. At the initial conditions, the reference MiMi detector is positioned in correspondence with the piece fixating the rotation, oriented towards the west and defining the 0° azimuthal position. The rest of the detectors are distributed counter-clockwise in the lower POM-C disk.

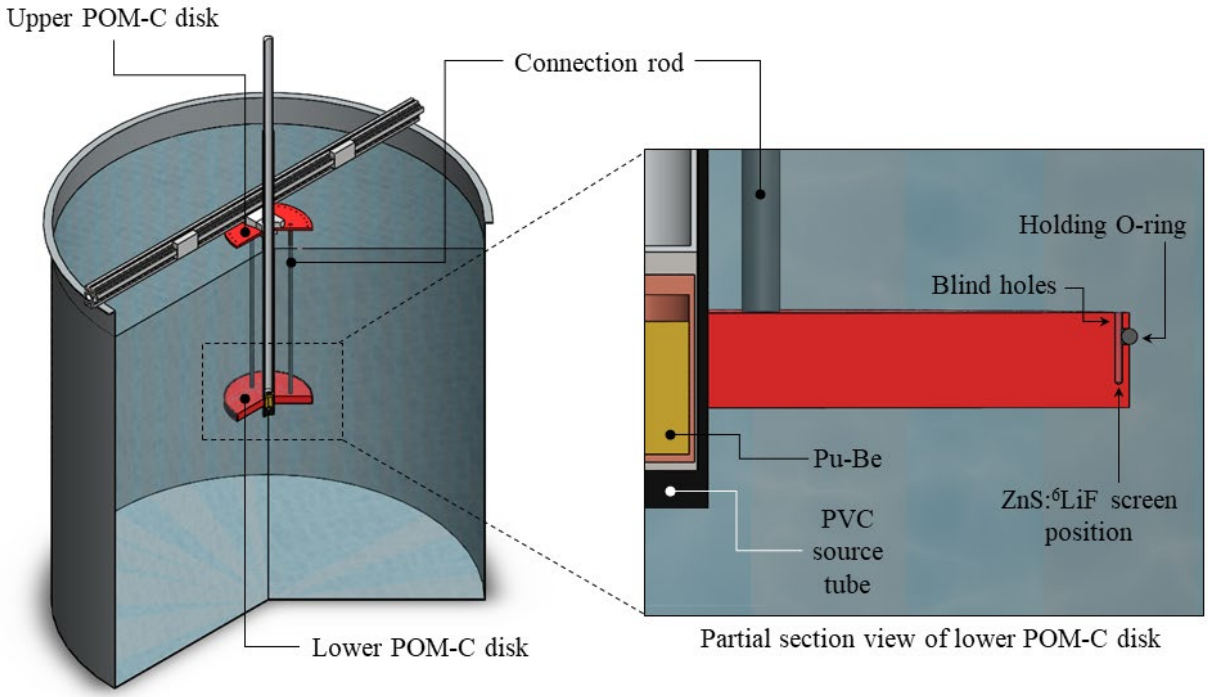

Figure 6.12 – Experimental setup in CARROUSEL for inter-calibration procedure.

The front-end of each of the 18 MiMi detectors is inserted in the lower disk and is connected via the optical fiber to its own counting channel, composed of a SiPM and a processing board. The counting channels used in this test are between the ones available in the six multi-channel stand-alone processing modules developed at LRS and described in Section 4.3.1.2. In this particular case, the processing channels from ch.65 to ch.82 of module D are used to process the scintillation light. Module D is stored, together with the other five operational modules, in the Memmert IPP750eco incubator [102], kept at a stable temperature of 20 ± 0.1 °C. SiPMs are operated with a high voltage of 56.66 V, and the conversion of the SiPM output into photon counting is performed with a threshold of 1 V. As described in Section 4.3.2, the photon counting is digitally processed by the CAEN V2495 FPGA with the proprietary PSI firmware developed at PSI, and the resulting thermal neutron counting per channel is sent to the acquisition computer via the CAEN V1718 VME bus.

The FPGA proprietary firmware based on the MSD algorithm, described in Section 4.3.2, was set via software with a sampling period of 800 ns. Hence, the number of photon counts is recorded every 800 ns and the MSD algorithm calculates the differences in the photon density. By setting a digital threshold on the photon density variation (see Section 4.3.2), the highly luminous neutron events can be discriminated from the background. The selection of the appropriate digital threshold is performed prior to the beginning of the measurements for the source factor characterization.

The holding structure is installed and equipped with the 18 MiMi detectors while the water tank of CARROUSEL is empty and the Pu-Be source is not present in the tube. After the installation, the tank is filled with industrial water flowing at around 12 °C of temperature. Three heaters are installed on the side of the water in order to speed up the attainment of the thermal equilibrium between the industrial water and the controlled zone environment, kept constant at around 20°C. Once the water equilibrium temperature is reached, the series of 18 measurements by rotation of the structure is

started. Each counting measurement is named as the azimuthal position of det. #0. The selection of the azimuthal position is optimized to obtain preliminary results and, for this reason, it is not performed following the increase of the azimuthal angle with respect to the initial position (corresponding to the reference detector at position 0°) linearly. All the measurements are performed continuously, with only interruptions of a few minutes to manually rotate the holding structure and the 18 MiMi detectors together with it. In this way, potential drift due to external conditions, such as the water temperature, can be taken into account and quantified. The minimum measuring time at each azimuthal position is about 2 hours, while five sub-measurements of approximately 20 minutes are automatically run by the digital readout. The measuring time at each azimuthal position was chosen to have an uncertainty of at least 0.5% on the measured count rate of each MiMi detector at every azimuthal position. Longer measurements - performed with continuous sub measurements during nights and weekends - contribute to lowering the final uncertainty of the source factor profile. After summation of the contributions, this corresponds to an uncertainty on the relative source factor profile $S(\theta)/S(0)$ below 0.2%.

6.2.2.4 Results and discussion

A series of counting experiments with the 18 MiMi neutron detectors installed in CARROUSEL is performed varying the digital threshold level of the MSD algorithm. The resulting low-threshold (LT) curve is shown in Figure 6.13. The curve trend resembles the one shown in Figure 4.12 for the MiMi prototype, with a noise region at low thresholds followed by a relatively stable region. The selected value of the digital threshold, chosen to be 20, marks the limit between the noise and the counting regions. The average count rate displayed by the detectors is 6.9 cps, with a standard deviation of 0.8 cps. Such counting capabilities are comparable with those of the MiMi prototype, despite the reduction of the active volume, the reduction of the fiber diameter, and the use of different electronics.

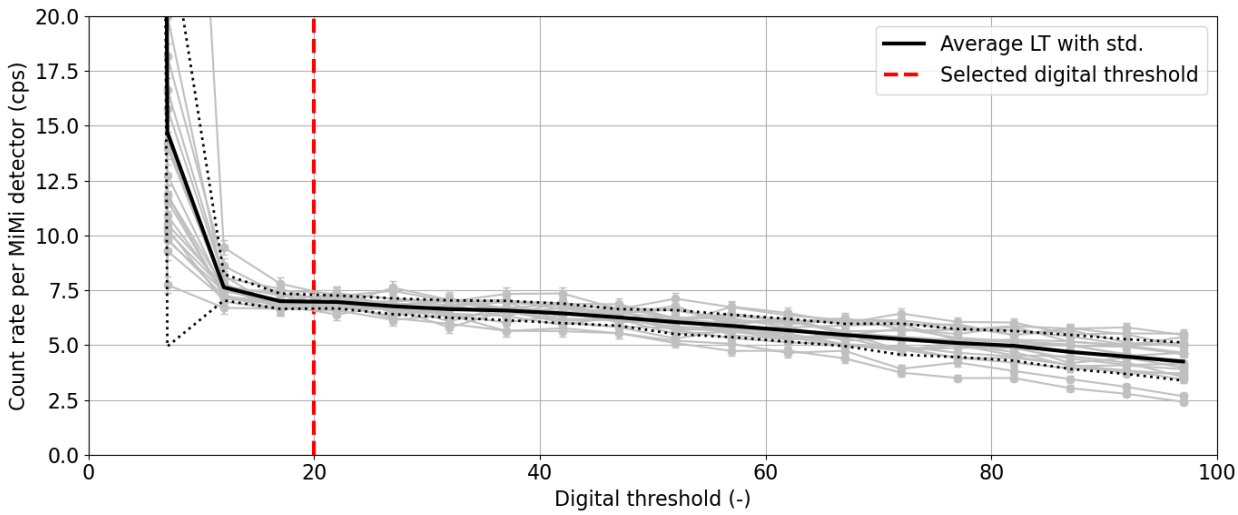

Figure 6.13 – Count rate per MiMi detector at 15 cm from the Pu-Be neutron source as a function of the digital threshold. The selected digital threshold level is indicated in red.

The trend of the total count rate for the 18 miniature detectors during the whole measuring time is shown in Figure 6.14, normalized to its value at the first 20-min sub-measurement. The choice of studying the total trend is connected with the magnitude of the statistical uncertainties, which are large when studying the response in time for a single detector.

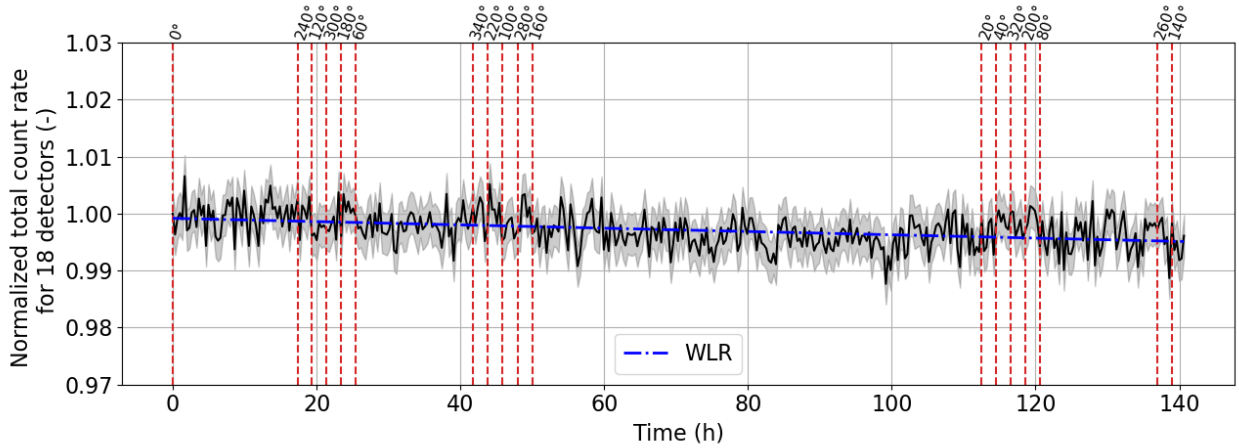

Figure 6.14 – Total count rate for the 18 MiMi detectors used for source characterization as a function of the measuring time in CARROUSEL. Vertical red lines represent a change in the detector position, indicated as the azimuthal coordinate of det. #0. The trend from linear regression of data is in blue.

The normalized total count rate for the ensemble of 18 MiMi detectors in Figure 6.14 presents a slight negative drift. The drift magnitude was estimated with a weighted linear regression, leading to a slope coefficient β_1 of $-(2.9 \pm 0.3) \times 10^{-5}$. A t-test for the regression slope is performed to assess the significance of the linear regression. The following null and alternative hypotheses are used:

- **H_0**: $\beta_1 = 0$ (the slope is equal to zero)
- **H_A**: $\beta_1 \neq 0$ (the slope is not equal to zero)

The calculated t-statistic is 8.709, with a corresponding p-value << 0.05. Hence, the null hypothesis is rejected, concluding that there is a statistically significant trend in the total count rate of 18 MiMi detectors.

The statistically significant drift in the total count rate results in a reduction of the latter of -0.48 ± 0.05 % at the end of the measuring time with respect to the initial conditions. The cause of this drift is yet to be clarified. The different azimuthal positions cannot cause the drift because they are not selected in a specific order. However, after careful investigation and testing of each possible cause, it is likely that the drift is related to the change in the water temperature from 19°C to 22°C observed between the beginning and the end of the measurement. It is estimated that such a temperature variation has a negligible impact on the moderation properties of water and plastic. Hence, the suspect is that a temperature variation is influencing the optical properties of the ZnS(Ag):^{6}LiF screen, increasing its opacity, thus reducing the amount of photons emerging from the screen and transported to the SiPM. This affects the delta in the density of photon counts, shifting the spectrum towards lower delta values. The relative spectrum shape measured over the 18 detectors between the initial conditions of det. #0 at 0° and the final one at 140° is shown in Figure 6.15. The variation is not expected to affect the SAFFRON measurements in CROCUS, where the temperature is set by the secondary circuit with a precision of ±0.01 °C. The impact of the total count rate drift on the source factor characterization is estimated by correcting the data under the assumption that the drift is constant and equal for all 18 detectors.

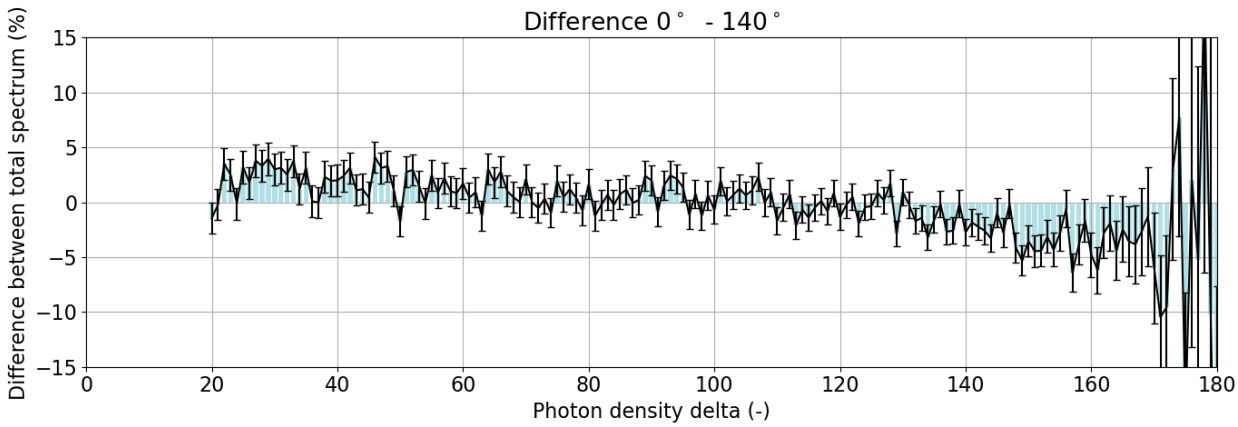

Figure 6.15 – Spectral difference for the total counting of 18 detectors between initial and final measuring conditions.

Both the corrected and uncorrected count rates of each detector at each azimuthal position were rearranged in the matrix form proposed in Figure 6.1. The vertical sum of the contributions, normalized to the sum at 0° position, provides the profile of the relative source factor distribution at 15 cm from the Pu-Be neutron source of CARROUSEL. The variation in the shape of the source factor due to the drift correction is estimated to be in the order of 0.001% and therefore neglected. The source factor shape for the uncorrected data is presented in Figure 6.16. The uncertainty on the relative source factor is in the order of 0.14%.

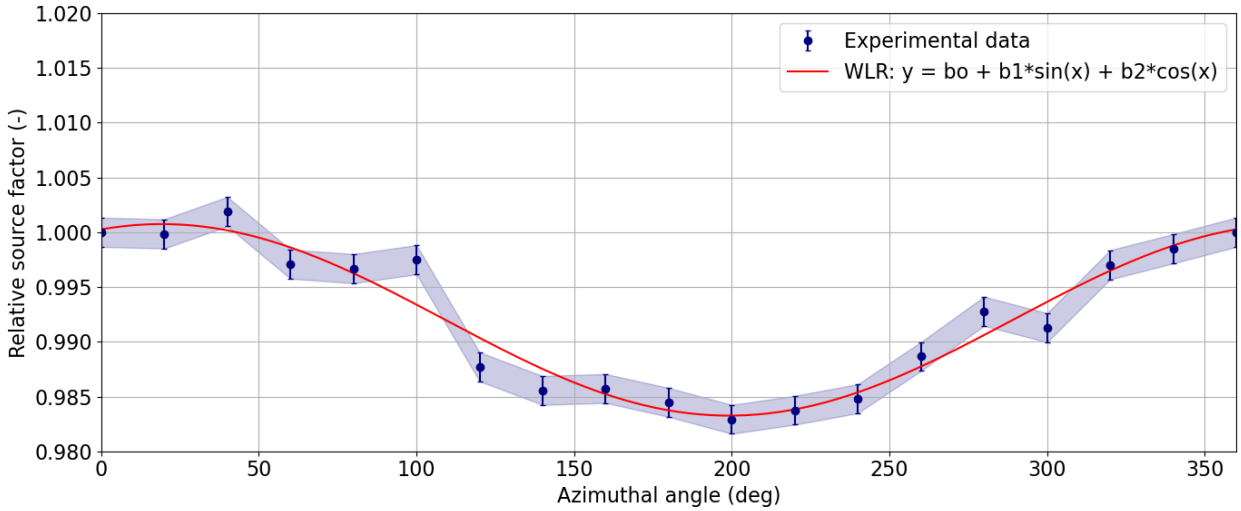

Figure 6.16 – Relative source factor at 15 cm from the Pu-Be source in CARROUSEL.

The results in Figure 6.16 show a reduction of -1.5% in the source factor shape at 15 cm from the source corresponding to the 200 degrees azimuthal angle. Assuming that the detector positioning is perfectly aligned, the causes for such reduction could be:

- An anisotropy of the Pu-Be source of CARROUSEL, attenuated by the water volume and the lower disk plastic at 15 cm;
- A miss-centering towards the azimuthal direction of 200° of the Pu-Be source in its dedicated tube.

The experimental data are fitted with a sine function having a 2π period, linearized as

$$y = b_0 + b_1 \cdot \sin(x) + b_2 \cdot \cos(x) \tag{6.14}$$

The WLR results are shown in Table XX, with the uncertainty on the regression parameters, and the resulting function is plotted in Figure 6.16. The statistical F-test on the regression model confirms the presence of a sine trend in the experimental data.

Table XX – WLR parameters for the linearized sine function describing the relative source factor in the CARROUSEL facility.

Regression parameter	Value	Standard error
b_0	0.992	< 0.001
b_1	0.003	0.001
b_2	0.008	0.001

6.2.3 Relative sensitivity of MiMi detectors

Knowledgeable of the relative source factor of the Pu-Be source of CARROUSEL, it is possible to inter-calibrate a large number of detectors positioned at the selected radial $\bar{r}$ and polar $\bar{\varphi}$ coordinates and subject to a similar neutron spectrum. Following Equation (6.4), the relative count rate between two detectors at different azimuthal positions can be rescaled by the relative source factor existing between the same positions. In this way, the relative detector efficiency $\varepsilon_{i,j}$ between two detectors is estimated. In particular, 160 MiMi neutron detectors are inter-calibrated simultaneously by being all positioned at 15 cm around the Pu-Be neutron source of CARROUSEL.

6.2.3.1 Experimental setup

The 160 MiMi detectors built for the inter-calibration are labeled with numbers going from det. #0 to det. #159. The same labeling scheme is maintained during the installation of SAFFRON.

The same mechanical structure used for the source factor characterization, and described in Section 6.2.2.3, is used for the estimation of the relative sensitivity. The detectors from #0 to #155 are installed in the lower POM-C disk occupying the azimuthal positions from 0° to 310° with a 2° spacing. The remaining 4 MiMi detectors are spread in the last 50° to cover the entire range of azimuthal coordinates. Hence, these detectors are positioned every 10° and are accompanied by two small fictive detectors in the neighboring azimuthal positions to reproduce potential self-shielding effects between detectors as in the other 156.

The five stand-alone processing modules A, B, D, E, and F are installed inside the Memmert IPP750 eco incubator [102] set at 20 ± 0.1 °C, together with the digital read-out electronics composed of the FPGA and the VME bus from CAEN. Each optical fiber is connected to one of the counting channels of the multi-channel processing electronics. The connection follows the detector numbering in a way that det. #0 is connected to ch. 0, det. #1 is connected to ch. 1, and so on. The same connection between the MiMi active volume and its processing channels must be maintained when installing the detectors in-core for SAFFRON.

All the MiMi detectors are inter-calibrated with respect to the det. #0, positioned in the reference 0° azimuthal position of CARROUSEL. The duration of the counting experiment is dictated by the need for low statistical uncertainties in the counting. Considering the count rates recorded during the source factor characterization (discussed in Section 6.2.2.4), a total acquisition time above 40h is estimated sufficient to obtain uncertainties in the order of 0.1% on the single detector count rate. The acquisition is divided into consecutive automatic sub-measurements of approximately 15 minutes each in order to observe potential trends over time and split the result data files.

At the starting time, the heaters installed in CARROUSEL are left intentionally powered after already two hours of functioning to observe if there are effects related to the water temperature increase. They are tuned off after approximately four hours, and the water is mixed at the same time, reaching the temperature of 21°C at approximately the mid-height level of the tank water. The data acquisition from the next 16 hours is discarded to let the CARROUSEL tank reach equilibrium with the environment, followed by 42 hours of useful data acquisition.

6.2.3.2 Experimental results

The trend in time of the total number of counts acquired is shown in Figure 6.17. At the time of water mixing, an increase in the total count rate in the order of 1% is clearly visible. This represents an ulterior proof of the influence of the water temperature on the detector counting capabilities. However, further investigations are necessary to conclude if the direction of the change is caused by an increase in the water temperature. After the stabilization time, the normalized total count rate for 160 MiMi detectors shows as well a slight positive drift quantified by WLR with a slope parameter of $(2.5 \pm 0.6) \times 10^{-5}$. A statistical t-test shows the presence of a trend also in this case.

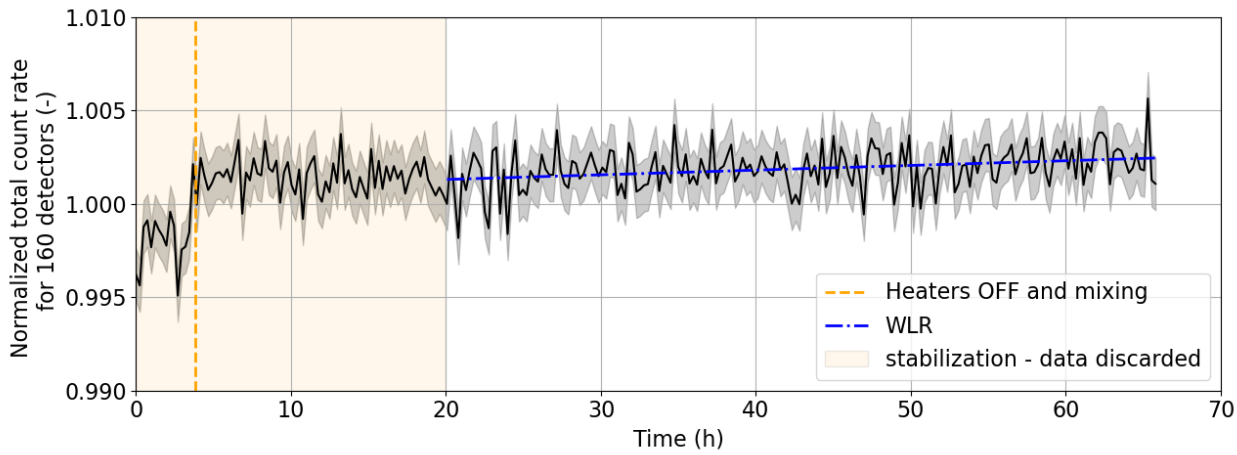

Figure 6.17 – Normalized total count rate for 160 MiMi detectors as a function of the acquisition time during inter-calibration.

The count rate for each MiMi neutron detector acquired over the entire acquisition time is first corrected by the drift, under the assumption that it is constant and equal for all the detectors, and then normalized by the same value for the det. #0 positioned at the 0° reference position of CARROUSEL. Following Equation (6.4), each normalized count rate is divided by the value of the linearized sine function, representing the relative source factor at 15 cm in CARROUSEL as estimated in Section 6.2.2.4. The final values obtained are the relative sensitivities of the 160 MiMi neutron detectors with

respect to det. #0. The maximum uncertainty of 0.13% measured on the relative source factor azimuthal points is added to the final computation of uncertainties for conservative purposes. The relative detector sensitivities $\varepsilon_{i,0}$ for corrected data are shown in Figure 6.18.

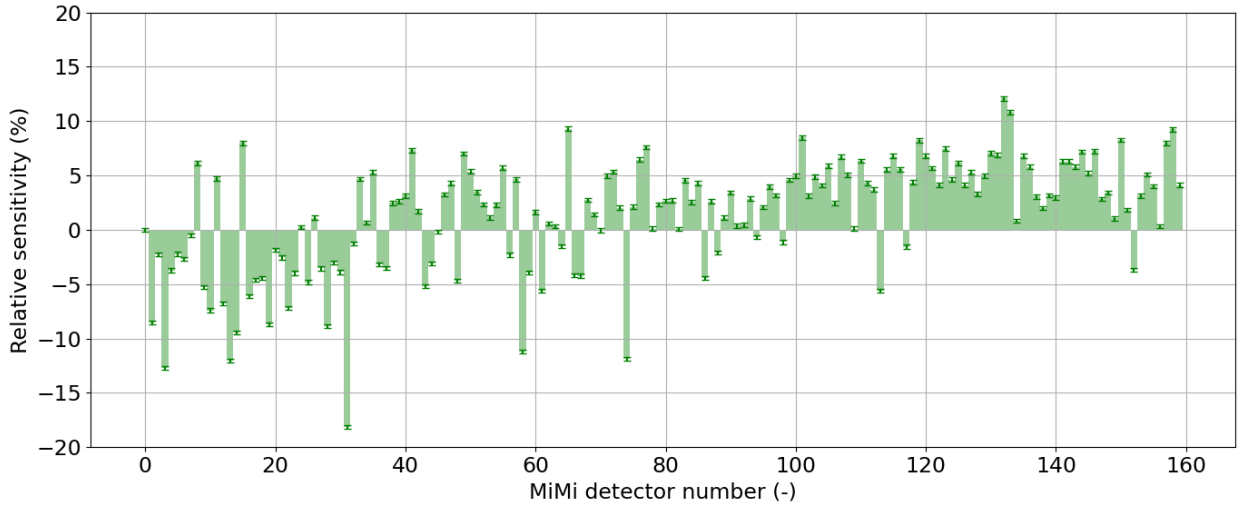

Figure 6.18 – Relative sensitivity for 160 MiMi detectors with respect to det. #0. The values shown are for data corrected by the total count rate drift.

The 160 MiMi neutron detectors show differences in the relative sensitivity between -18.2 ± 0.2 % and 12.1 ± 0.2%. The average uncertainty is 0.2%. The difference between corrected and uncorrected data is calculated to be within the final uncertainty and indicates that the total count rate drift can be neglected in the estimation of the relative sensitivities.

6.3 System loading and criticality

SAFFRON was installed in the CROCUS core in January 2022. As a first stage, the mechanical supporting structure and the 149 MiMi neutron detectors foreseen in the SAFFRON configuration are installed out-of-vessel in an unloaded core configuration. In other words, the installation is performed without the presence of the fuel rods of CROCUS in between the two core grids. This strategy reduces the exposure to radiation of the personnel involved in the installation of the SAFFRON system.

After loading the 336 UO_2 and178 U_{met} fuel rods, performed by regulations always out-of-vessel, the core is moved in its cavity and positioned in the vessel together with the SAFFRON mechanical structure and the 149 MiMi neutron detectors, including all the 17-m long optical fibers rolled and fixated above the core.

Once the CROCUS core is loaded into its vessel, the 149 optical fibers are unrolled and taken out from the core cavity through the experimental channel. Each optical fiber is connected to its dedicated and calibrated channel of the five multi-channels stand-alone modules (A, B, D, E, and F) installed inside the incubator. The connection order between optical fibers and SiPMs set in the calibration is respected. The incubator is positioned away from the opening of the experimental channel to avoid radiation damages to the electronics, and more in particular, to the SiPMs.

An approach to critical experiment was requested by the Swiss safety authority before operating at power the CROCUS reactor with the SAFFRON system installed. The purpose is to prove the reactor's capability to reach criticality and to ensure that the excess reactivity limit of 200 pcm is not overcome. An approach to critical experiment is performed for each of the configurations reported in Table XXI. The SAFFRON configurations differ for the number of U_{met} fuel rods installed in the core. The approach to critical for the SAFFRON0 configuration, corresponding to the COLIBRI configuration, shows a limited excess reactivity of ~115 pcm. For this reason, first two and then four U_{met} fuel rods are installed in the core periphery at the lattice locations indicated in Figure 6.19.

The behavior of the SAFFRON system with the reactor's power is demonstrated linear up to approximately 1 W. The reduction of the linearity range, if compared to the previous testing with analog and digital prototypes, seems to arise from limitations in the data transfer with the VME bridge.

Table XXI – CROCUS configurations during the SAFFRON experimental campaign.

Core configuration	$U0_2$ rods (-)	U_{met} rods (-)	Critical water level (mm)	Excess reactivity (pcm)
SAFFRON0	336	176	971.3 ± 0.1	~ 115
SAFFRON1	336	178	962.4 ± 0.1	~ 150
SAFFRON2	336	180	953.1 ± 0.1	~ 188

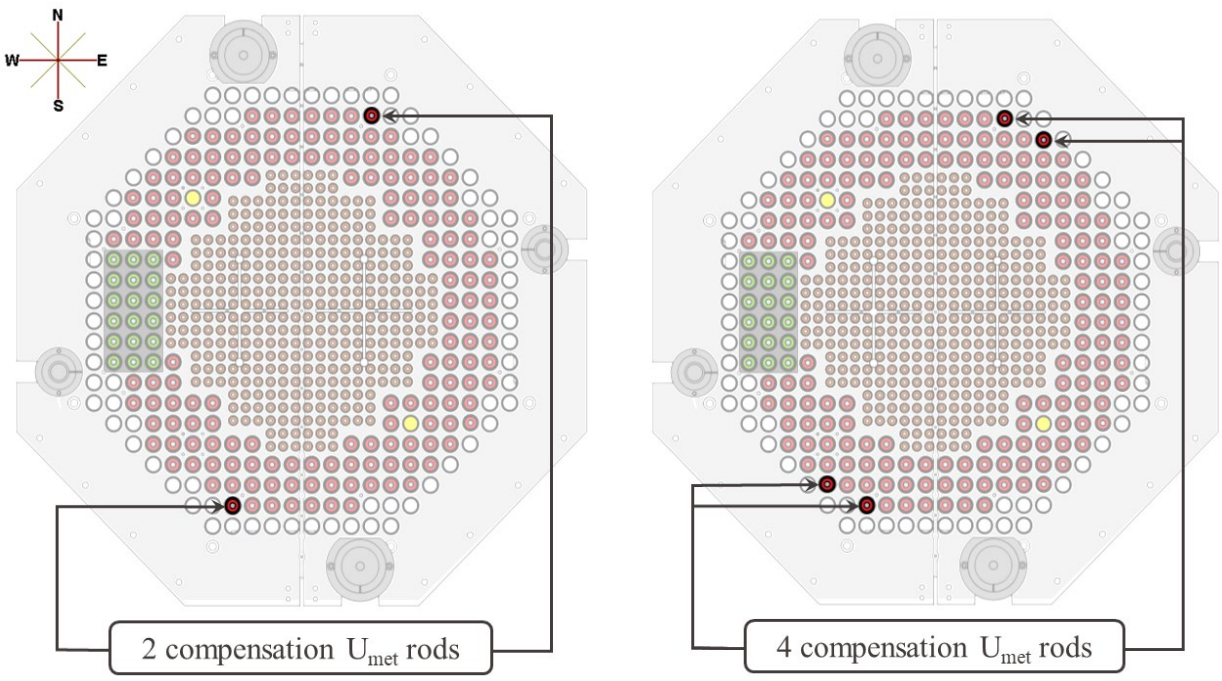

(a) (b)

Figure 6.19 – Positions of the additional U_{met} rods for reactivity compensation in (a) SAFFRON1 and (b) SAFFRON2 configurations.

6.4 Static flux map

The first objective of SAFFRON is to reproduce in an online manner the 3D shape of the thermal neutron flux map in CROCUS. For this purpose, the inter-calibration of the 149 MiMi neutron detectors installed in the inter-lattice positions is fundamental. The knowledge of the relative sensitivity $\varepsilon_{i,0}$ between any detector i and det. #0 allows reconstructing the shape of the thermal flux map with respect to the reference det. #0 as:

$$\frac{\phi_{th,i}}{\phi_{th,0}} \propto \frac{RR_i}{RR_0} = \frac{CR_i}{CR_0} \cdot \frac{1}{\varepsilon_{i,0}} \tag{6.15}$$

where $\phi_{th,i}$ is the thermal neutron flux at the position i and RR_i is the ^{6}Li reaction rate at position i.

6.4.1 Experimental conditions

The thermal flux map in static conditions is measured in the SAFFRON1 configuration (see Table XXI) of CROCUS at a stable power of 0.095 W. The criticality is set by regulation of the water level, with the two B_4C control rods completely withdrawn. The critical water level is set at 962.4 ± 0.1 mm and maintained stable throughout the measurement. The water temperature at the time of measurement is stable at 20.22 °C in the core center with fluctuations in time of ±0.01 °C.

The signal processing and acquisition electronics are operated with the same settings used for the detectors' inter-calibration to avoid introducing biases that would invalidate the previously measured relative detector sensitivities. These settings include a 56.66 V operational voltage of the SiPMs, a SiPM threshold of 1V, a sampling time of 800 ns of the MSD FPGA algorithm, and a digital threshold equal to 20. On the basis of preliminary tests, data are acquired for approximately one hour in order to reach an uncertainty on the counting statistics of about 0.2% per MiMi neutron detector.

Following Equation (6.15), the count rates acquired with the 149 MiMi neutron detectors are normalized by the count rate of det. #0 and further divided by the relative sensitivities $\varepsilon_{i,0}$. The resulting values should follow the shape of the thermal neutron flux map of CROCUS.

6.4.2 Experimental results and discussion

The thermal flux map of CROCUS at 0.095 W, based on the normalized and sensitivity-rescaled count rates of the 149 MiMi neutron detectors, is shown in Figure 6.20 as a function of the distance from the core center of the corresponding MiMi neutron detector. The uncertainty on the distance from the core is estimated to be in the order of ±0.1 mm, and thus it is not shown in Figure 6.20.

As expected, the experimental points represented in Figure 6.20 show a greater magnitude of the thermal flux map towards the core center for the three main axial layers L1, L2, and L3. In addition, the flux map is higher in the axial layer corresponding to the mid-core height, i.e., L2, due to the axial cosine shape typical of cylindrical reactors.

However, counting values of inter-calibrated detectors at the same distance from the core center, meaning in equivalent lattice positions for a perfectly symmetrical core configuration as SAFFRON1,

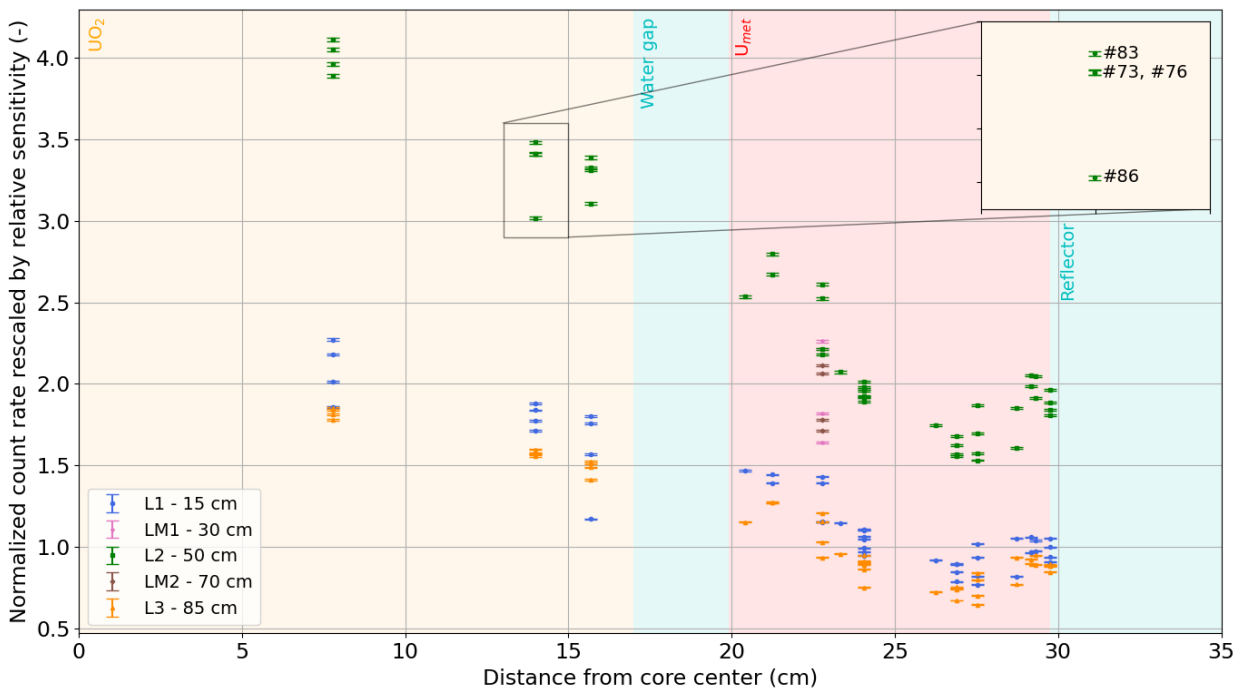

Figure 6.20 – Shape of the thermal flux map of CROCUS measured as a function of the distance from the core center. The color coding of points represents the different axial layers of SAFFRON, while the background colors indicate the core regions. The ±0.1 mm uncertainty on the detectors' positioning is not shown for visualization purposes.

present large discrepancies, in the order of a few tens of percent. For instance, as shown in the zoom-in of Figure 6.20, the MiMi detectors #73, #76, #83, and #86 count thermal neutrons with a relative difference of about ±16%, despite the rescaling for the inter-calibration relative sensitivity. These detectors are all positioned at the same distance from the core center of 14.0 ± 0.1 mm within the perfectly symmetrical UO_2 fuel lattice (see Section 6.1.3).

In order to study this abnormal behavior, the spectrum of the photon density difference recorded by the digital readout electronics is studied. The spectra in CARROUSEL and in CROCUS of the four abovementioned MiMi detectors, normalized by their total area for comparison purposes, are presented in Figure 6.21 with their relative difference. The four spectra for the photon density delta show variations in their shape between the measurements performed in CARROUSEL during inter-calibration and the measurements in CROCUS. In particular, det. #86 presents the most significant difference in the spectra with almost a ± 100% difference maximum. The reason behind the spectral shift is yet to be understood. Potential causes for the shift in spectra could be the bending of the optical fibers inside the POM-C plastic rulers of the SAFFRON mechanical structure or power-related phenomena due to the different power levels at which the MiMi detectors are exposed. The effect of the water temperature on the spectra is considered negligible since the small amplitude of its temporal and spatial fluctuations is considerably smaller than those measured during the CARROUSEL experiments, in the order of 0.3 °C and 3 °C, respectively.

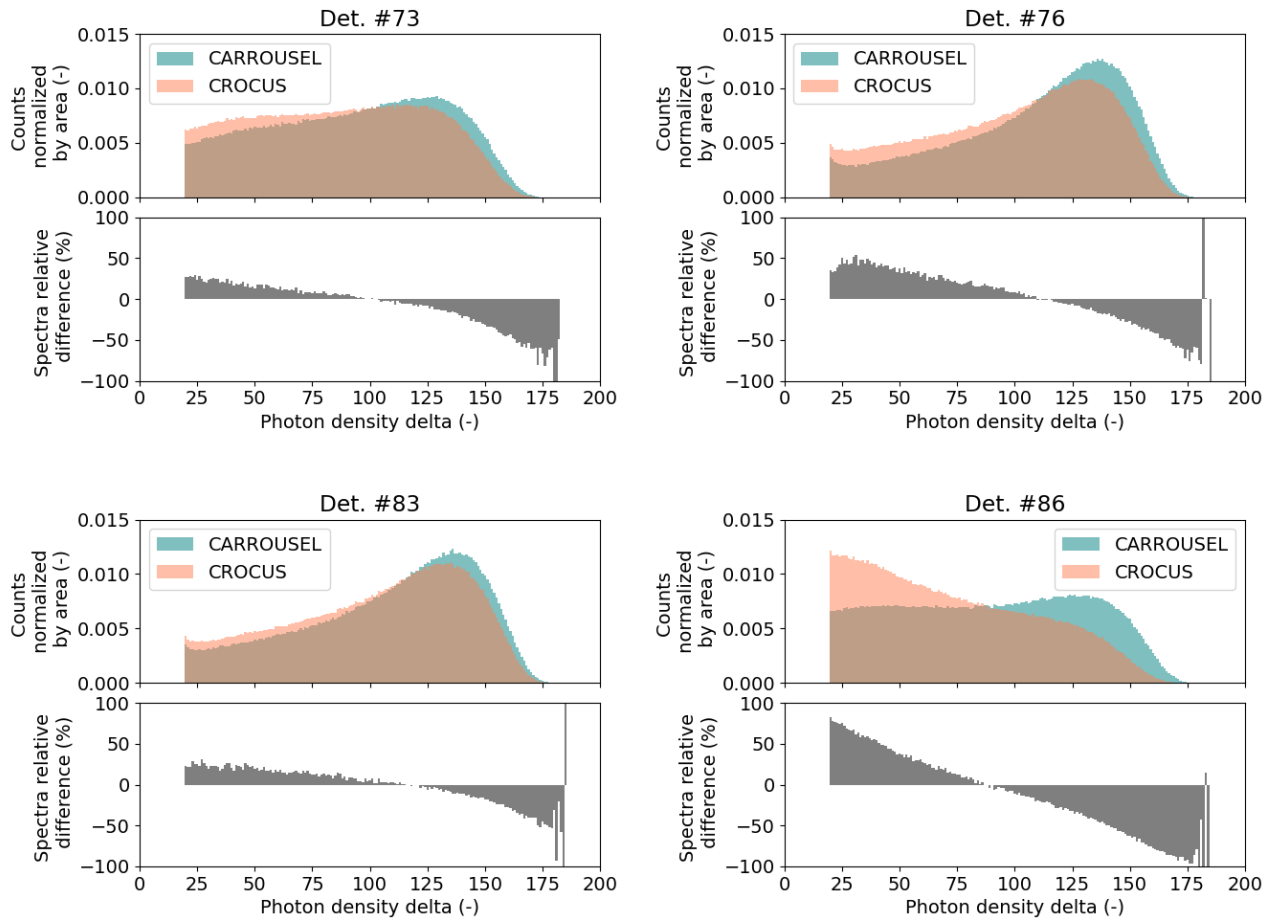

Figure 6.21 – Spectra of the photon density delta for MiMi det. #73, #76, #83, #86 in CARROUSEL (during inter-calibration) and in CROCUS. Uncertainties per bin are in the order of 1 to 2% for both cases.

The spectral shift is quantified on the basis of the absolute value of the difference between the two spectra acquired in CARROUSEL and CROCUS. The evolution of the spectral shift as a function of the number of optical fibers' bends is shown in Figure 6.22(a), while the dependency on the distance from the core center for the mid-core height L2 layer is given in Figure 6.22(b). In both cases, statistical testing is inconclusive in determining the presence of a trend.

The distribution of spectral shifts is represented in Figure 6.23(a), with the distribution mean and standard deviation. A criterion on the spectral shift is applied to all the detectors to select those that do not experience severe spectrum shifts. The selected detectors correspond to the left tail, i.e., below one standard deviation, of the spectral shift distribution. A representative example of a selected MiMi detector is shown in Figure 6.23(b). On the basis of the criterion, 23 MiMi neutron detectors are selected, and 19 detectors are rejected, i.e., being on the right tail of the distribution in Figure 6.23(a). The thermal flux map obtained with selected detectors highlighted is displayed in Figure 6.24.

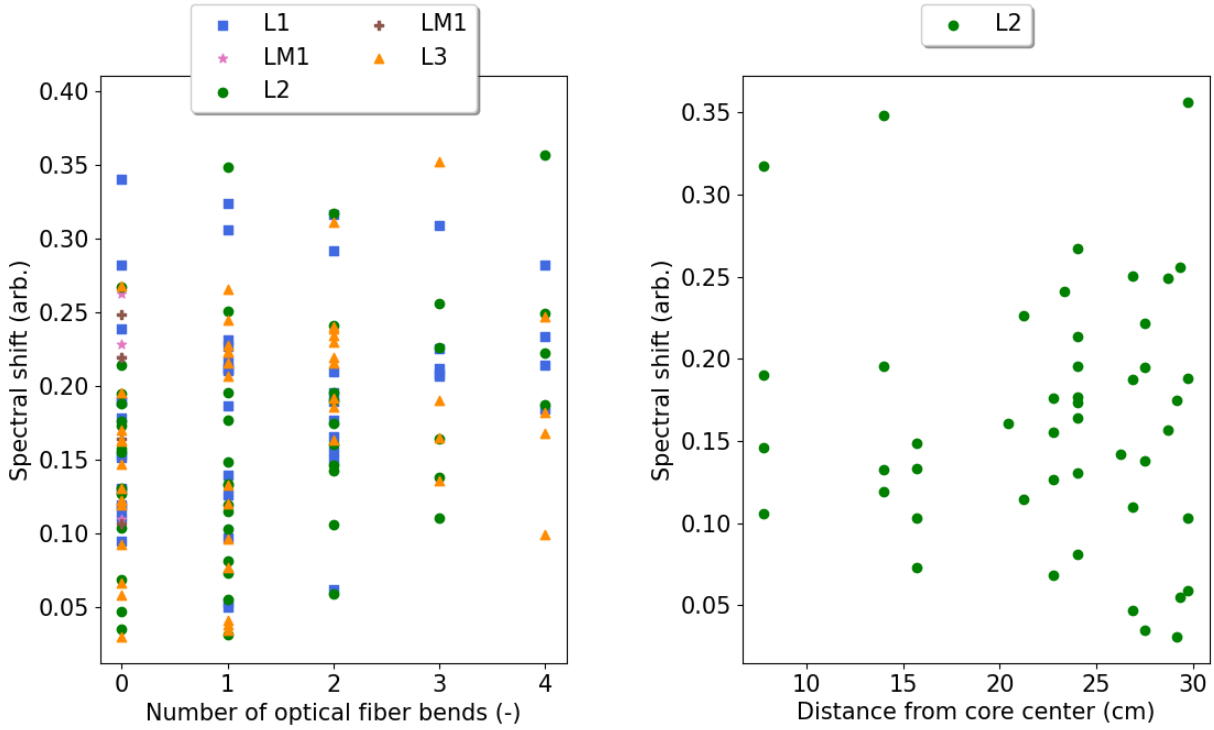

(a) (b)

Figure 6.22 – Spectral shift as a function of (a) the number of bends of the optical fibers in SAFFRON and (b) the distance from the core center for the L2 layer (mid-core height).

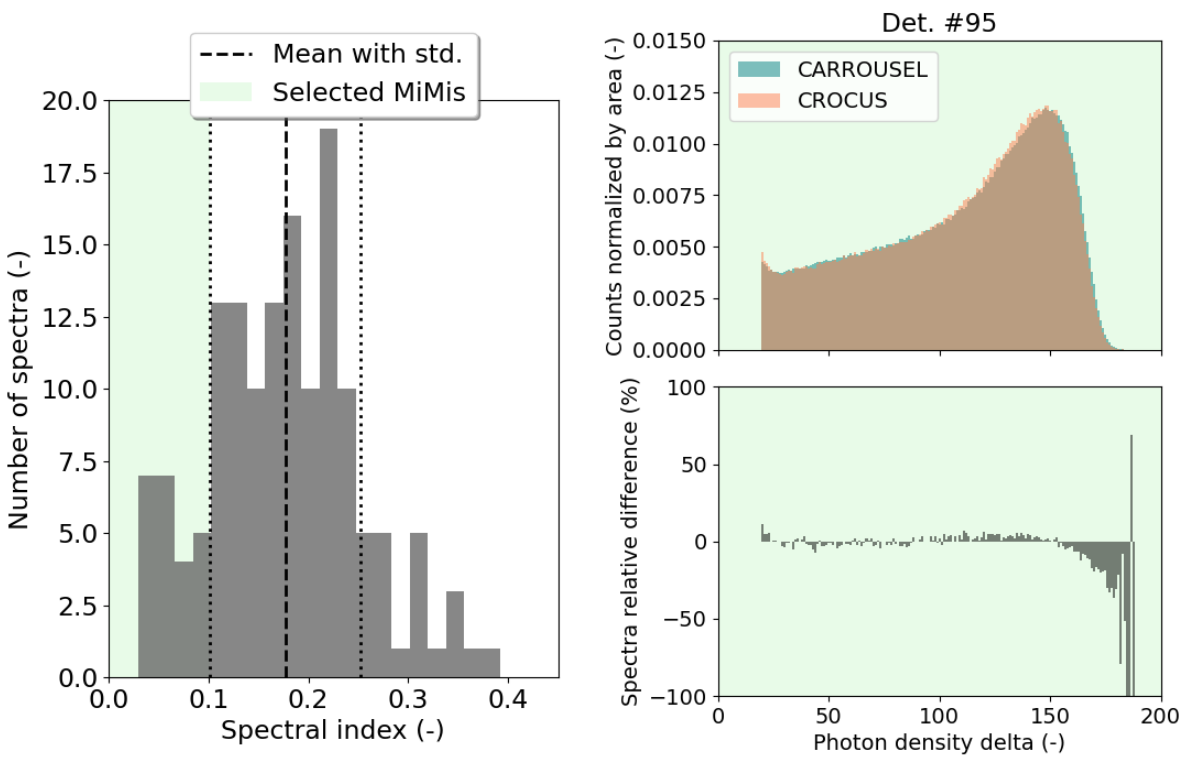

(a) (b)

Figure 6.23 – (a) Spectral shift distribution with selection of MiMi detectors with low spectral shift. (b) Spectrum of photon density delta for det. #95, as an example of a selected detector.

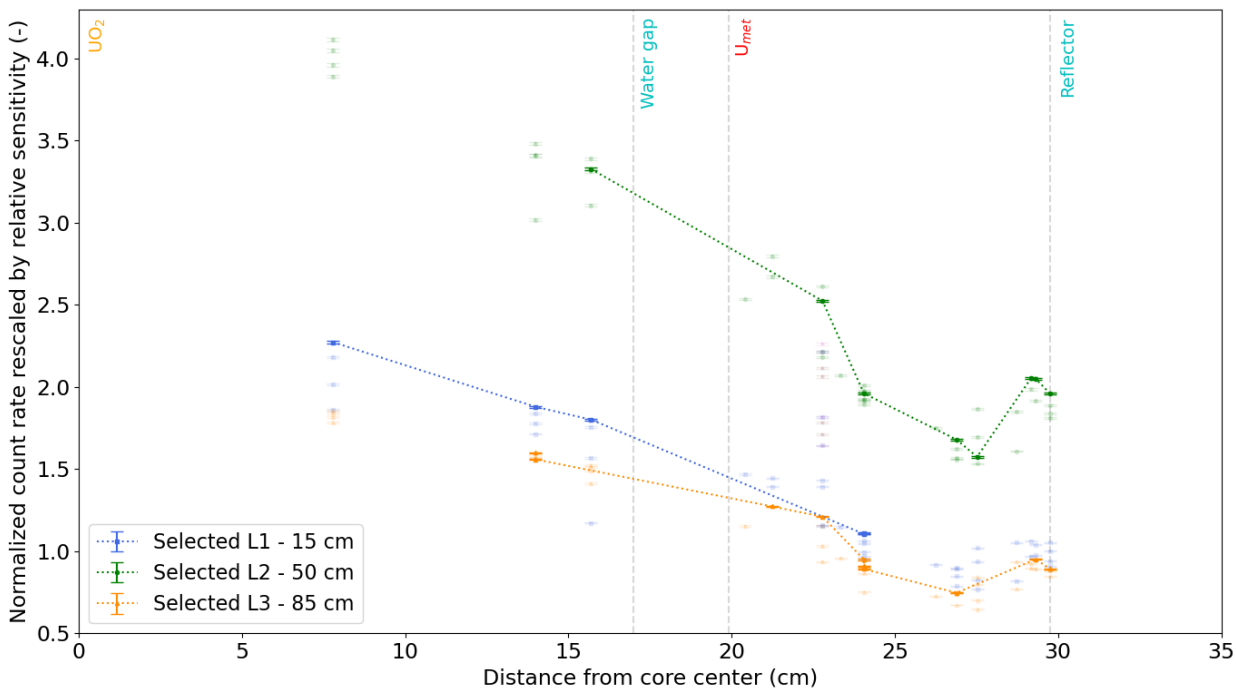

Figure 6.24 – Shape of the thermal flux map of CROCUS for selected MiMi neutron detectors with low spectral shift as a function of the distance from the core center. Rejected detectors are shaded. Dotted connecting lines are shown for visualization purposes. No detectors from LM1 and LM2 are selected.

6.4.3 Comparison with preliminary Serpent 2 simulations

As a first approach to modeling SAFFRON in Serpent 2, 149 track-length tallies recording the ^{6}Li reaction rate are positioned in correspondence with the 149 MiMi neutron detectors of SAFFRON without explicitly modeling neither the detectors nor the mechanical supporting structure. Under these conditions, the assumption is that the POM-C rulers are not strongly perturbing the neutron flux. Contrary to the azimuthal study in Section 5.1, the POM-C with a density of 1.41 g/cm^3 substitutes water instead of air, and thus its perturbation effect should be milder.

Each tally corresponds to an 8-mm side cube centered at the detector position. The tallies are smeared with respect to real MiMi detectors' size with the intent to reduce statistical uncertainties and computational time in this preliminary full-core criticality simulation. However, one must be aware that a form factor correction might be needed to be taken into account.

Full-core criticality simulations are run with 4 billion neutron histories in 2×10^5 active cycles. Two sets of simulations are run to compare experimental results with different nuclear data libraries, i.e., ENDF/B-VIII.0 [31] and JEFF-3.1.1 [113]. The reason behind the choice of an older version of the JEFF library is the same discussed in Section 5.3.4.

The results of the two sets of simulations are shown together with experimental data in Figure 6.25. Both experimental and simulation data are normalized by the corresponding value of det. #0. The C/E-1 values are plotted as a function of the MiMi detector number in Figure 6.26, highlighting the MiMi detectors selected on the basis of the spectral shift analysis.

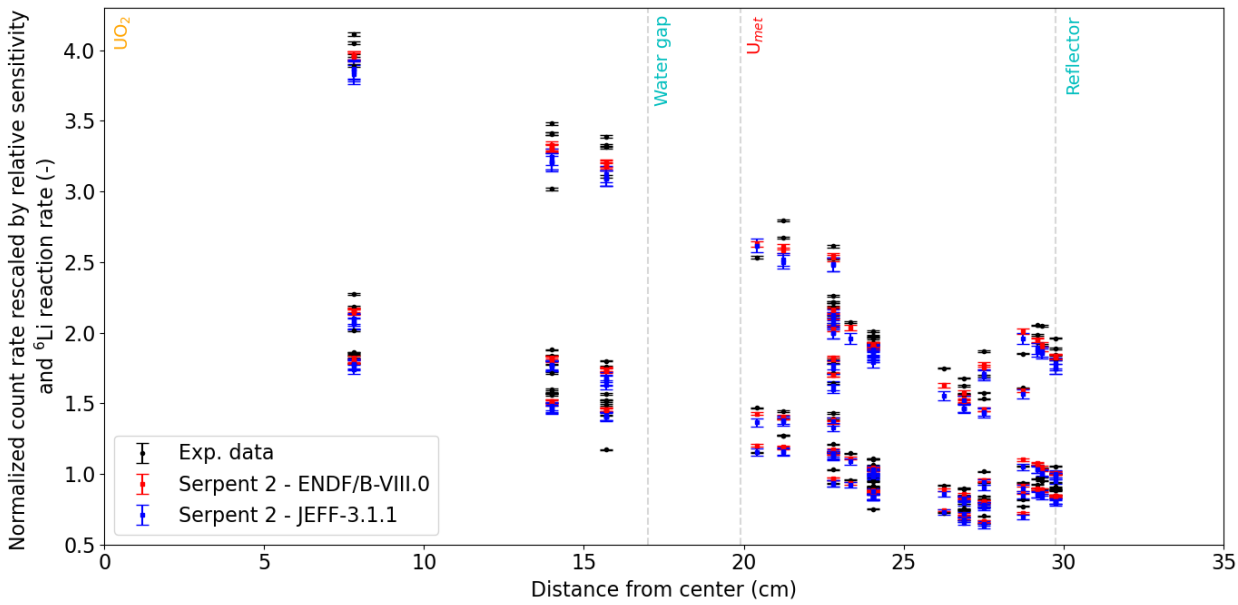

Figure 6.25 – Comparison of thermal flux map experimental data (for all detectors) against the results of Serpent 2 simulations for ENDF/B-VIII.0 and JEFF-3.1.1 nuclear data libraries. Both simulation and experimental results are normalized by the corresponding output of det. #0.

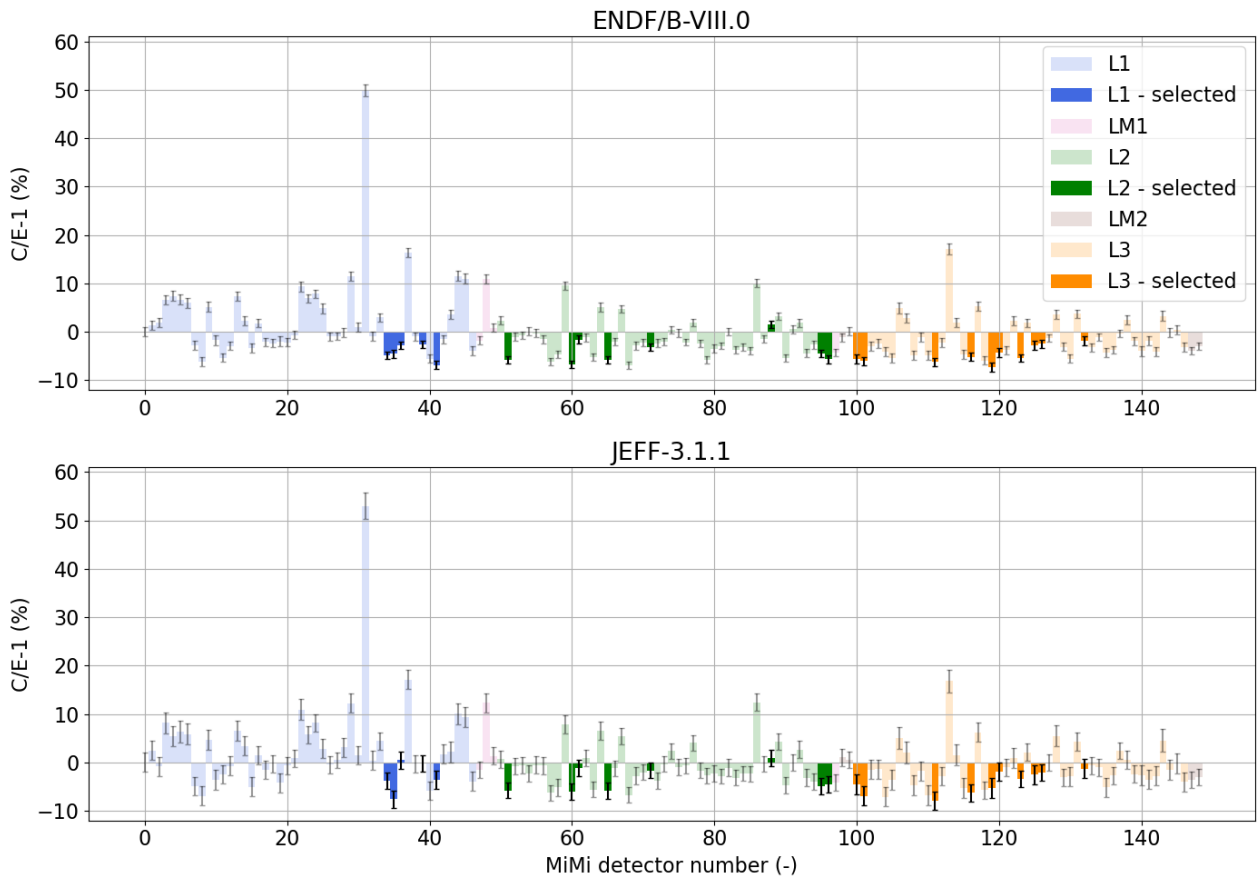

Figure 6.26 – C/E-1 values as a function of the MiMi detector number for ENDF/B-VIII.0 and JEFF-3.1.1 nuclear data libraries. Both simulation and experimental results are normalized by the corresponding output of det. #0.

The results of Serpent 2 simulations presented in Figure 6.25, in general, follow the shape of the thermal flux map measured by SAFFRON. However, the C/E-1 plots in Figure 6.26 show significant discrepancies between simulation and experimental results, which range from 49.8 ± 1.2 % to -7.3 ± 0.9 % for the ENDF/B-VIII.0 data library and from 53 ± 3 % to -8 ± 2 % for JEFF-3.1.1. By restricting the detector range to only those selected by the spectral analysis, the C/E-1 reduces to 1.6 ± 0.8% to -7.3 ± 0.9% for ENDF/B-VIII.0. An example of rejected detectors is det. #31, presenting the 49.8 ± 1.2 % discrepancy. The relationship between the spectral shift and the C/E-1 values is investigated in Figure 6.27 for ENDF/B-VIII.0 results.

Figure 6.27 demonstrates a relationship between the C/E-1 value and the spectral shift. Indeed, the MiMi detectors rejected by the spectral shift analysis have the highest C/E-1 positive values. It is likely that these discrepancies are due to the fact that rejected detectors are losing a significant amount of counts that overcome the digital threshold due to the spectrum shift towards lower photon densities. On the contrary, for detectors with low spectral shifts – the selected ones – the simulation results tend to underestimate the experimental values. It should be noted that the normalization to det. #0, which is among the rejected, induces a general offset in the results that causes the underestimation of the C/E-1 for the selected detectors. Other biases are to be researched on the simulation side and could be:

- Inadequate smearing of the Serpent 2 tallies: the relatively large (8-mm side cube) smearing in both axial and radial directions can affect the results, which must be corrected by a form factor. A reduction of the tallies dimensions might improve the simulation results;
- Influence of mechanical structure: the plastic POM-C rulers are not modeled, and although the perturbation introduced in water should be milder than in air, they might still affect the neutron spectrum in the region of the detectors;
- Possible biases in nuclear data libraries: the applicability of nuclear data to measurements in inter-pin positions could be proven inadequate, as their validation is one of the experiment goals.

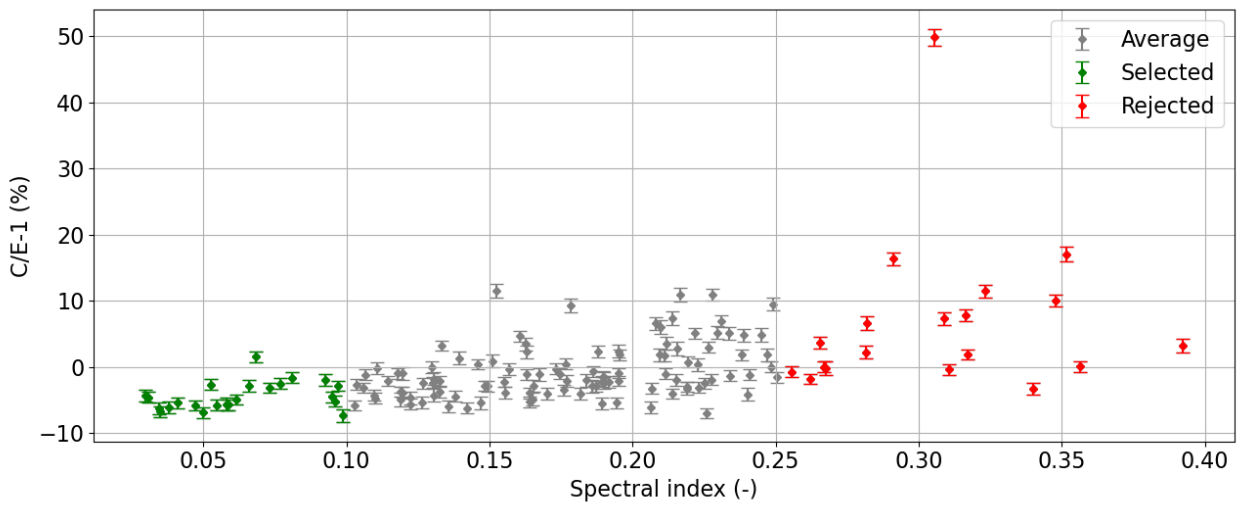

Figure 6.27 – C/E-1 as a function of the spectral shift for simulation data obtained with ENDF/B-VIII.0.

The C/E-1 values for the simulations performed with ENDF/B-VIII.0 are also plotted in Figure 6.28 as a function of the distance from the core center for the three main axial layers to analyze if there is a connection with the varying reactor power across the core. The C/E-1 for the two intermediated layers are not shown because they are all positioned at the same distance from the core center, and none of them was selected as a detector with a low spectral shift. In all the C/E-1 plots, the MiMi detectors selected on the basis of the spectral shift are highlighted.

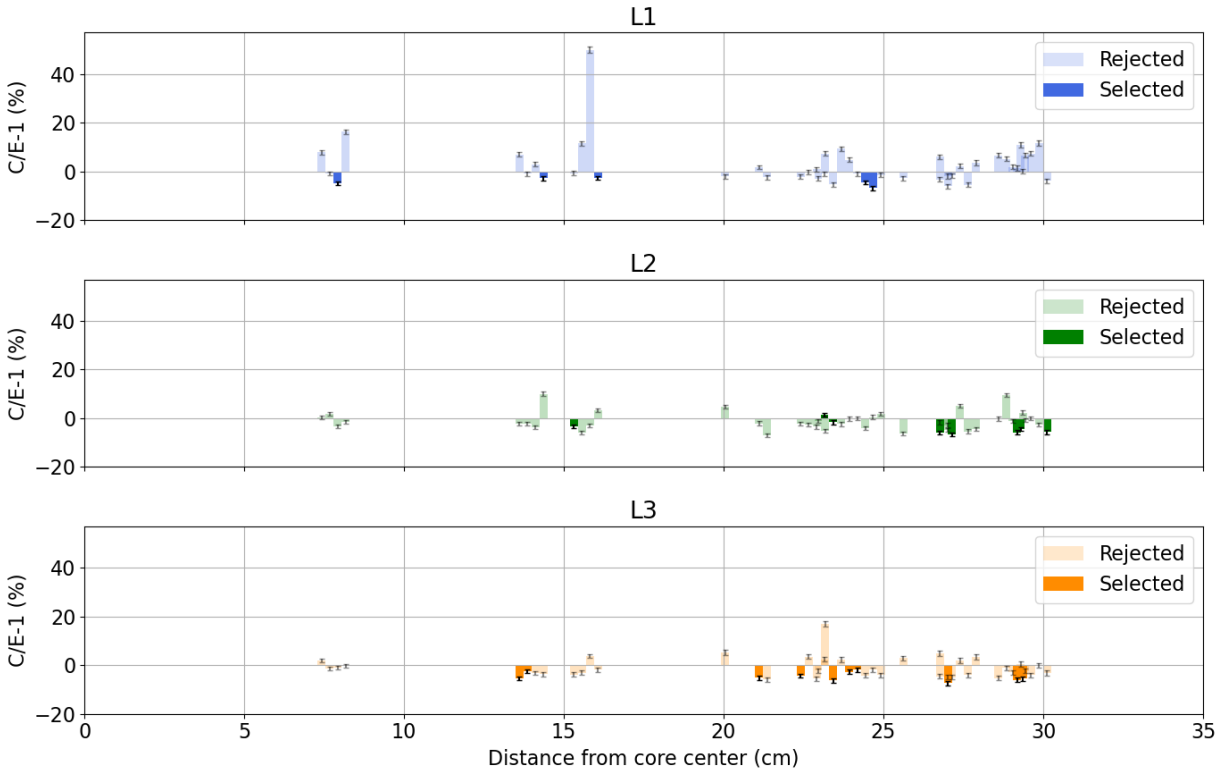

Figure 6.28 – C/E-1 values as a function of the distance from the core center for ENDF/B-VIII.0 for the three main axial levels of SAFFRON.

6.5 Relative variations of the flux map

The shift in the photon density spectrum for a portion of the MiMi detectors discussed in the previous Section 6.4 does not affect the relative counting capabilities of the detectors. The count rate of each MiMi detector acquired in certain core conditions can be compared to the same value acquired in a different state or configuration of the core to study relative variations of the thermal neutron flux map of CROCUS. Since the relative quantities involve count rates acquired with the same MiMi neutron detector, rescaling for the inter-calibration parameters is not needed either.

In this Section, the relative variations of the thermal flux map of CROCUS are studied for:

- Different reactor's criticality states, i.e., water level critical vs. control rod critical;
- Different reactor's powers, i.e., 2 mW and 160 mW vs. 1.1 W;
- Different reactor's subcritical states, i.e., critical at 953.1 mm of water vs. 910, 920, 930, 940, and 950 mm of water with the start-up Pu-Be source.

6.5.1 Control rod perturbation

Criticality is achieved in CROCUS by either water level regulation or by total or partial insertion of two absorbing B_4C control rods. Depending on the excess reactivity available, set by the core configuration, the reactor can be brought to critical with the insertion of the northwest control rod only, with the southeast control rod only, or with both. In this study, the effect of the presence of a single control rod on the shape of the thermal neutron flux map at a stable core criticality is investigated.

6.5.1.1 Experimental setup

The thermal neutron flux map is measured with SAFFRON at two different criticality states of the SAFFRON1 core configuration. In the first measurement, the critical state is achieved by raising the water level at its maximum, i.e., 1000.0 ± 0.1 mm, and inserting the northwest control rod up to the critical axial level of 215.0 ± 0.5 mm. The same procedure is repeated for the second measurement, where instead, the southeast control rod is inserted at 215.0 ± 0.5 mm. The same settings for the signal processing electronics of SAFFRON described in Section 6.4.1 are also used for these measurements. Each acquisition is performed at a reactor power of approximately 0.1 W for approximately 7 minutes. The statistical uncertainty on the counting of single MiMi detectors is in the order of ±0.5%.

The flux maps obtained at criticality with control rods are compared to the flux map obtained at criticality with water level regulation, i.e., without control rods inserted. For the comparison, the experimental results of the previous Section 6.4 are used. They correspond to the flux map measured in a stable critical state of the reactor with a critical water level of 962.4 ± 0.1 mm. Before comparison, the counts acquired in all the three measurements at hand are power-normalized by the total number of counts registered by the sum of the two fission chamber monitors. The relative difference between power-normalized data of different criticality states is calculated for each MiMi neutron detector.

6.5.1.2 Results and discussion

The relative difference of the thermal neutron flux map in CROCUS due to the presence of the northwest (NW) control rod with respect to the flux map at critical with no rods inserted and water level control is shown in Figure 6.29. The equivalent results for the presence of the southeast (SE) control rod are presented in Figure 6.30.

Figure 6.29 and Figure 6.30 highlight a strong perturbation of the neutron flux map due to the presence of a single control rod in the CROCUS configuration. The five MiMi detectors in close proximity to the control rod guide tubes witness the strongest variations in their count rate and thus in the thermal neutron flux map when a control rod is present. The L1 layer detectors, positioned below the level of insertion of the control rods, show a decrease in the range of -5% for both the NW and the SE cases. This means that the flux map at the L1 layer is simply pushed down in the proximity of the absorber rod. On the other hand, the presence of the NW control rod causes a maximum flux perturbation of -28.5 ± 0.3 % in the counting of the LM1 MiMi neutron detector located the closest to the rod extremity in the positive axial direction. The specular detector is affected by the presence of the SE control rod by a similar quantity, i.e., -28.4 ± 0.5%. The magnitude of the local perturbation decreases on the axial layers above LM1, up to the L3 layer, where the flux close to the rod is perturbed

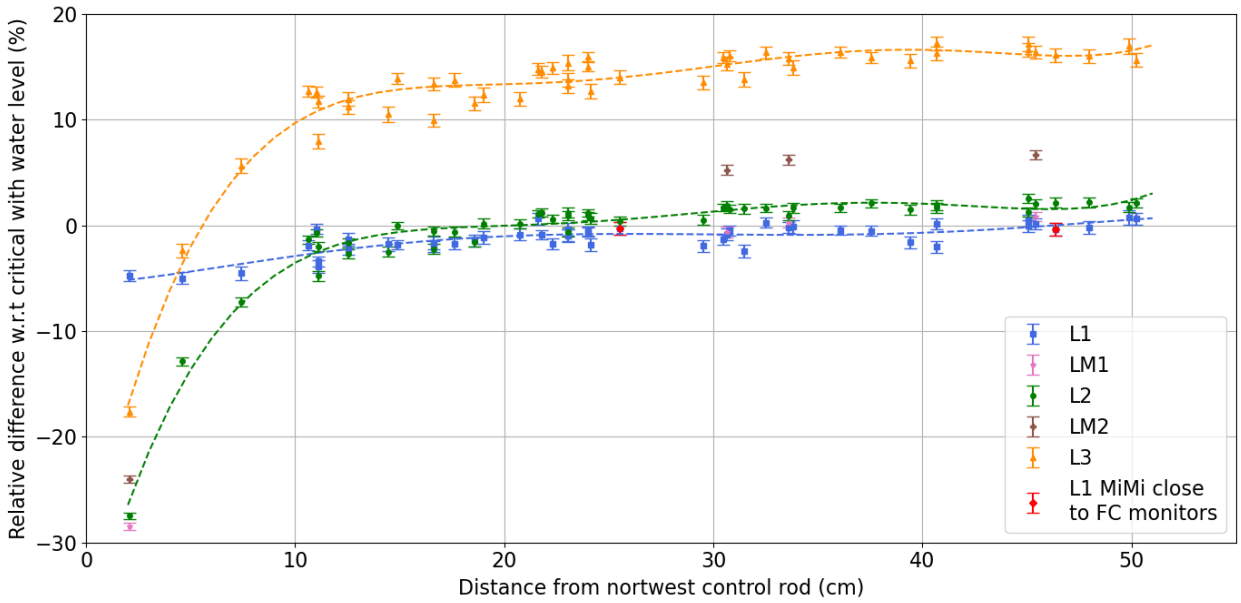

Figure 6.29 – Relative difference of the critical flux map with northwest control rod with respect to the critical flux map with water level. A polynomial fit is shown for visualization purposes for the three main axial layers of SAFFRON.

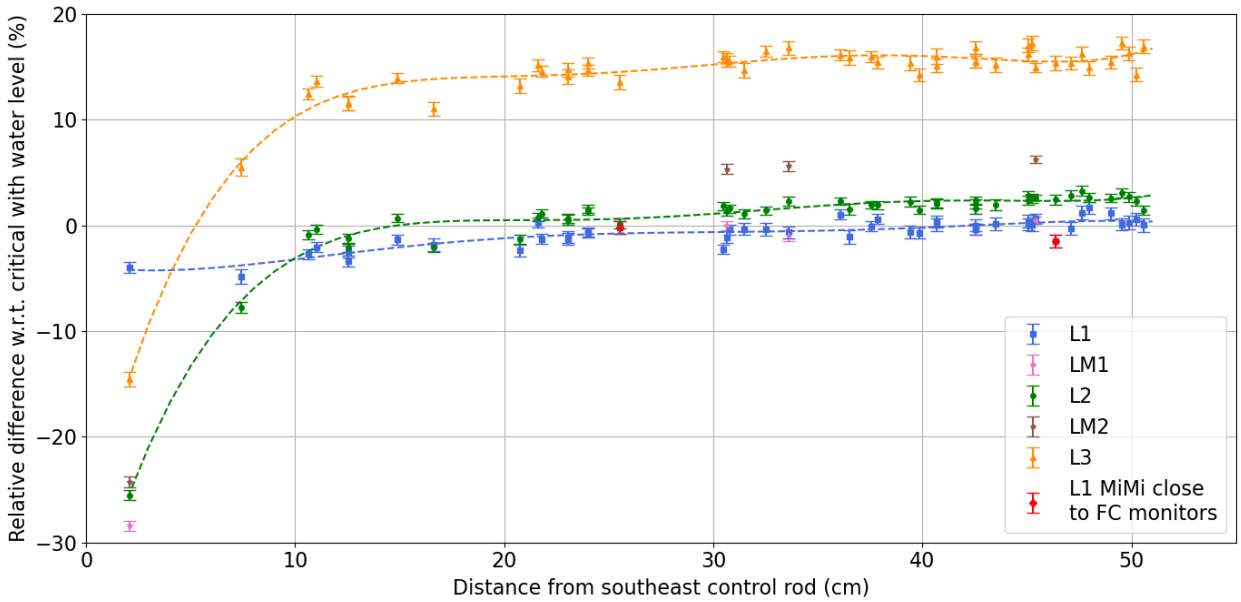

Figure 6.30 – Relative difference of the critical flux map with southeast control rod with respect to the critical flux map with water level. A polynomial fit is shown for visualization purposes for the three main axial layers of SAFFRON.

By approximately -17.6 ± 0.5 % for NW and -14.5 ± 0.7 % for SE. In fact, the local perturbation introduced by the rod is compensated by the global upward shift of the thermal neutron flux map caused by the higher water level in the critical configuration with a rod inserted, i.e., 1000 ± 0.1 mm vs. 962.4 ± 0.1 mm. Indeed, far from the control rod perturbation, a nearly constant increase in the flux map is clearly visible in both Figure 6.29 and Figure 6.30. The upward shift is at its highest for

the upper layer of SAFFRON, i.e., L3, where the flux map increase by approximately 16% with respect to the critical core configuration obtained with water regulation.

By analyzing the variation in the count rate of the two MiMi neutron detectors positioned in proximity of the fission chamber monitors of CROCUS, a first assessment of potential biases due to changes in the critical configuration in the power readings of the monitors can be performed. Indeed, the power monitors are power-calibrated for a critical configuration of CROCUS obtained by regulation of water level. As a consequence, their readings in the reactor control room could be affected by the shift of the thermal neutron flux due to the insertion of a rod. The monitor fission chambers are axially located close to the lower axial level of SAFFRON, and thus the most representative detectors are det. #4 and det. #44. The relative differences between critical configurations for such detectors are shown in red in Figure 6.29 and Figure 6.30. The only significant deviation is observed for det. #4 when the southeast control rod is inserted and is in the order of -1.5 ± 0.6%.

6.5.2 Reactor power and intrinsic source

A recent experimental and computational study by Dumonteil et *al.* [122] showed the relevance of intrinsic neutron sources due to spontaneous fissions of ^{238}U at low reactor power. If the fission rate in the reactor core is low, the average neutron emission rate of 1 n/s/g from ^{238}U spontaneous fissions [122] adds a non-negligible contribution to the neutron flux map in the core. As compared to the power fission source, the spontaneous fission source is evenly distributed throughout the fuel. In CROCUS, it was estimated that 10^6 n/s are emitted from ^{238}U spontaneous fission, representing approximately 1% of the total neutron source at the reactor's power of 1 mW.

Following these results, the variation of the thermal neutron flux map measured in CROCUS with SAFFRON is investigated in a range between the low-power states of the reactor and the nominal power. In particular, neutron flux maps at 2 mW and 160 mW are compared to that at 1.1 W. The comparison between flux maps would provide a preliminary experimental assessment of the importance of the intrinsic neutron source of CROCUS on the reactor behavior and possibly some orientation for further experiments testing the validity of the model developed by Dumonteil et *al.* [122].

6.5.2.1 Experimental setup

The thermal neutron flux map is recorded in the SAFFRON2 core configuration at the reactor powers of 2 mW, 160 mW, and 1.1 W. The criticality is set by the regulation of the water level. The signal processing electronics and the readout system are set with the same electronics settings defined in Section 6.4.1. The duration of each data acquisition is set to obtain statistical uncertainties below ±1% on the count rate of single MiMi detectors.

Before comparing different power levels, MiMi detectors countings are summed up by axial layer to improve the statistical uncertainty of the results and resolve differences in the axial neutron flux shape in the order of 1%. The axial profiles measured at 2 mW and 160 mW are divided by those obtained at the nominal power of 1.1 W.

6.5.2.2 Results and discussion

The relative differences between axial profiles at different low reactor powers with respect to 1.1W are shown in Figure 6.31.

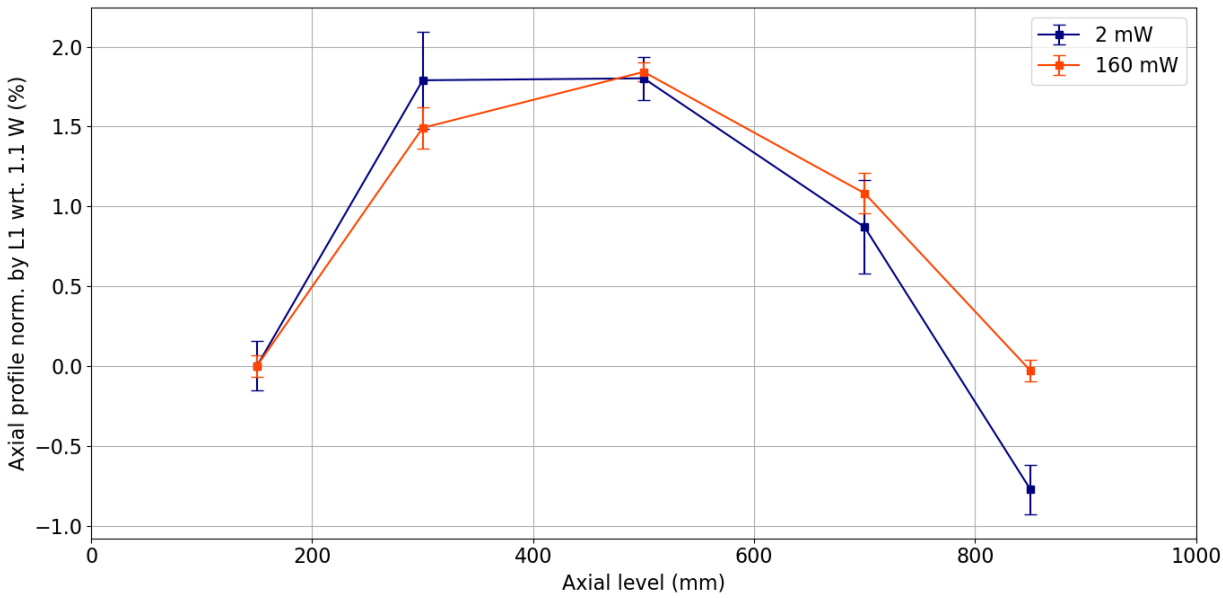

Figure 6.31 – Relative difference of the thermal flux axial shape in CROCUS as a function of the axial coordinate between critical at low power (2 mW and 160 mW) and critical around nominal (1.1W).

At the reactor power of 2 mW, an increase of approximately +1.8 ± 0.3 % in the axial profile of the thermal neutron flux is visible in correspondence to the LM1 and L2 levels of the SAFFRON system, respectively at 30 and 50 cm of core height. The order of magnitude of this increase agrees with the expected importance of the intrinsic neutron source of CROCUS and suggests that, at 2 mW, CROCUS might be operated at subcritical and driven by the intrinsic source of spontaneous fissions. This is consistent also with the observed decrease of the critical water level, set at 951.4 ± 0.1 mm at 2 mW, while at 1.1 W, it is found at 952.8 ± 0.1 mm, i.e., a reactivity difference of approximately 6 pcm. The reduction of the critical water level also affects the compared axial shape in Figure 6.31 with a maximum decrease of -0.8 ± 0.2 % for the L3 upper layer of SAFFRON (at 85 cm).

However, the axial flux shape measured at 160 mW shows an increase of +1.8 ± 0.1 % in the core center, similar to that measured at 2mW. This same level of increase, despite the two orders of magnitude of difference in reactor power, suggests a potential influence of the MiMi detectors' dead-time in the normalization values measured at 1.1W. The hypothesis is supported by the fact that the importance of such an effect is stronger at the core mid-height, where the reactor power is higher. Repetitions after verification of dead-time issues are necessary to assess if the visible effect in Figure 6.31 actually derives from the intrinsic neutron source of CROCUS. In addition, updated results should be tested against the theoretical developments proposed in [122].

6.5.3 Subcritical states

The variations in the shape of the thermal flux map at different subcritical states of the CROCUS reactor are investigated with SAFFRON. The knowledge of the flux map at subcritical is of interest

for a variety of studies and experiments, in particular branching noise [55] and neutron modulation experiments at subcritical states.

6.5.3.1 Experimental setup

The thermal neutron flux map is recorded in the SAFFRON2 core configuration at different subcritical states of the reactor. The water level is set below its critical value and the CROCUS Pu-Be neutron source is inserted at the bottom of the core to maintain a stable level of the neutron population. The different subcritical levels correspond to the water level in the core and are 910, 920, 930, 940, and 950 mm, with ±0.1 mm of uncertainty. The reactor power shown by the power-calibrated fission chamber monitors of CROCUS varies between 7 mW and 80 mW for 910 ± 0.1 mm and 950 ± 0.1 mm, respectively. The power-normalized subcritical flux maps are compared with the flux map obtained at criticality with water level at 953.1 ± 0.1 mm for a reactor power of 100 mW. As around criticality the reactivity worth per water level variation is about 4 pcm/mm, it should be noted that the studied subcritical levels correspond to approximately -170, -130, -90, -50, and -12 pcm, respectively.

The same signal processing and the readout settings of Section 6.4.1 are used in this series of measurements. The acquisition time is tuned at each measurement to obtain statistical uncertainty on each MiMi detector below 1%. At each subcritical state, the total number of counts recorded by each MiMi neutron detector is normalized by the sum of counts recorded by the fission chamber safety monitor 1 in the same period. The comparison between measurements provides an indication of the evolution of the thermal neutron flux map from subcritical to critical.

6.5.3.2 Results and discussion

The relative variation of the shape of subcritical thermal flux maps with respect to the critical map is illustrated in Figure 6.32 as a function of the axial level of the 149 MiMi neutron detectors.

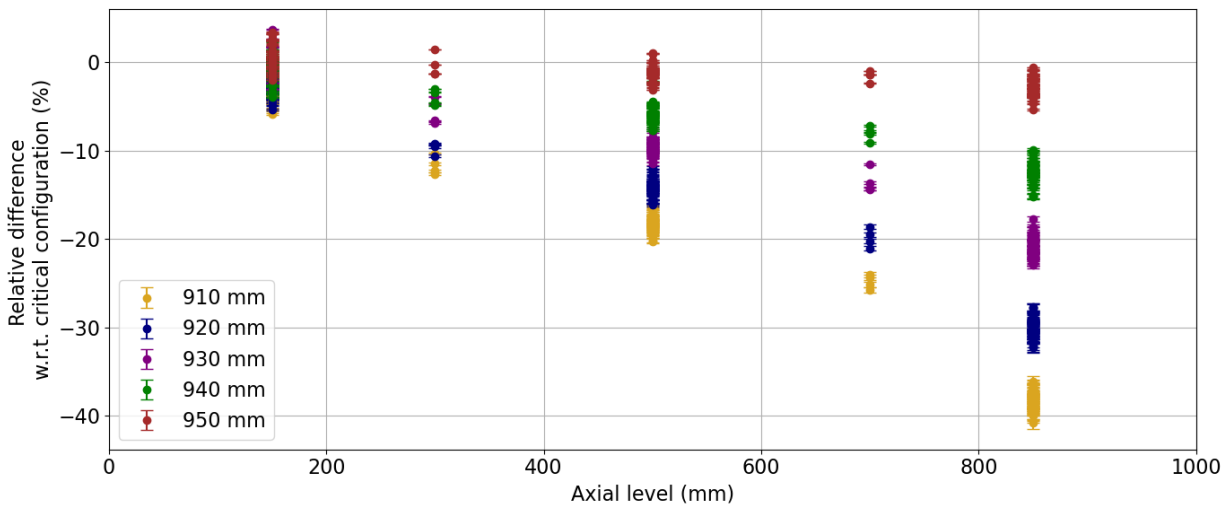

Figure 6.32 – Relative difference of the thermal flux map in CROCUS as a function of the axial level between subcritical reactor states and the critical reactor configuration.

At low subcritical regimes, the thermal neutron flux map concentrates close to the rector bottom, where the Pu-Be neutron source is inserted. For instance, at subcritical with 910 mm of water, the relative difference with respect to the critical flux map is in the order of a few percent in

correspondence with the L1 layer of SAFFRON, installed at 150 mm from the lower level of the fuel. On the contrary, the thermal flux map decreases by nearly -40 % in the L3 upper layer, at 850 mm.

The thermal flux maps of the successive subcritical states, i.e., 920, 930, and 940 mm, tend to approach the critical flux shape by growing towards the upper part of the core. At subcritical at 950 mm, the flux map is equivalent to the critical one for the L1, LM1, and L2 layers (at 150, 300, and 500 mm of core height), while the maximum discrepancy is visible at the L3 layer and is in the order of only a few negative percents.

Chapter 7

Conclusions and Outlook

In the present thesis, the main experimental results on the development of miniature neutron detectors and their application for online high-resolution neutronics measurements in the CROCUS zero-power reactor were presented.

Miniature and minimalistic (MiMi) neutron detectors were developed by adapting a novel neutron detection technology in development at PSI for in-core applications in low-flux reactors, e.g., the CROCUS zero-power reactor operated at EPFL. The detector features a ZnS(Ag):^{6}LiF screen of miniature dimensions, i.e., between 0.1 and 0.3 mm^{3} depending on the version, positioned at the tip of a plastic optical fiber and coupled with a silicon photon-multiplier (SiPM) for light collection. The principle of thermal neutron counting is based on the variation in time of the photon density detected by the SiPM following a neutron interaction in the ZnS(Ag):^{6}LiF screen.

Starting from a simple prototype called MiMi-0, the detection chain and the associated analog readout electronics were characterized in the CARROUSEL facility, which consists of a Pu-Be neutron source set in a water tank. It provided a first assessment of the capability of such technology to count thermal neutrons in mixed neutron/gamma radiation fields. The MiMi-0 prototype, when tested in CROCUS, presented a sensitivity to thermal neutrons in the order of 10^{-4} counts/n_{th} and a linearity in the count rate as a function of power up to 6.5 W, corresponding to a total neutron flux of about 10^{8} cm^{-2}·s^{-1} in the tested position. The thermal neutron sensitivity was one order of magnitude higher than other instruments of comparable active volume, such as MFC and sCVD diamond detectors. In addition, the MiMi-0 prototype showed the best sensitivity to thermal neutrons per unit of active volume with respect to the same instruments. By exposing the detector prototype to a 250 Bq ^{60}Co gamma source, its gamma sensitivity was estimated to be in the order of 10^{-11} cps/(cm^{-2}·s^{-1}) for 1.25 MeV gamma rays, mainly caused by pile-up effects of gamma interactions in the active volume. Comparing the gamma irradiation conditions between CROCUS and the ^{60}Co source, it was possible to conclude that the fraction of gamma pile-up interactions is a negligible contribution in the range of application of the MiMi-0 detector in CROCUS, making the detector practically gamma-blind.

Updated versions of the MiMi neutron detector prototype were developed to extend the capabilities and applications of the MiMi detection technology in the CROCUS reactor. In particular, the upgrade to a multi-channel signal processing and acquisition system was targeted to allow for the

multiplication of MiMi neutron detectors. Testing PCBs were built in-house to combine the pre-amplification and first-discrimination stage of the SiPM signals in a modular solution optimized for the digital counting of photons signals. The new electronics were tested in CROCUS and in the SUR-100 zero-power reactor at the University of Stuttgart. Despite the slight modification of the detector front-end design, i.e., increased active volume and optimized aluminum cap, count rates comparable to the MiMi-0 prototype version were recorded in CROCUS within a similar range of linearity with respect to the first tests. The proven measuring capabilities of the testing PCBs allowed to scale up the processing electronics: six 32-channels stand-alone modules were built to process simultaneously the input of 32 MiMi neutron detectors into streams of photon counting signals. The high number of detection channels available with the 32-channel modules called for the upgrade of the readout electronics from the analog version of the MiMi-0 prototype to a digital FPGA-based acquisition scheme. The FPGA firmware process online the photon counting signals received from the 32-channels modules into neutron counting on the basis of a moving-sum-after-differentiation (MSD) algorithm. The combination of the 32-channels modules with the digital FPGA acquisition allows for the simultaneous thermal neutron counting in up to 160 channels, corresponding to 160 MiMi neutron detectors. In addition, the MiMi detectors' dimensions were optimized in view of their use for a 3D full-core mapping system in CROCUS.

The demonstration of the feasibility of thermal neutron detection with the MiMi-0 prototype, combined with the miniature dimensions, the excellent thermal neutron sensitivity, and the gamma insensitivity, make the MiMi detection technology an efficient and practical solution for the investigation of local in-core neutronics phenomena in CROCUS. A series of high-resolution measurements were performed in the CROCUS reactor to build a dataset of experimental data viable for the validation of high-fidelity neutronics codes.

As a first attempt at performing high-resolution measurements in CROCUS, the azimuthal dependency of the thermal neutron flux and its gradients were measured within a 1.33 ± 0.02 cm experimental channel positioned in the northwest control rod position and in a northwest periphery position, i.e., in the water reflector. A gradient of +4.29 ± 0.10% within the experimental channel was measured in the periphery position, i.e., with a higher share of thermal neutrons nearer the core periphery. On the contrary, in the control rod position, which is set within the U_{met} lattice, the observed gradient is -4.37 ± 0.10% inward-oriented. These two sets of experiments proved the feasibility of performing highly spatially-resolved measurements in CROCUS with the MiMi neutron detectors and showed the possibility of resolving count rate gradients of a few percent within the cm range. The experimental data were compared with the results of Serpent 2 simulations either using full-core calculations with largely smeared tallies volumes or local estimates with a two-step approach. While discrepancies in the comparison are visible for full-core simulations, the two-step calculations showed a good agreement of the results, i.e., within one standard deviation. In addition, the two-step approach showed that the local thermal neutron flux depression introduced by a single MiMi-0 detector was equivalent to a reduction of the ^{6}Li reaction rate in the order of -7.0 ± 0.9%.

The dependency of the directionality of the thermal neutron flux was measured by enclosing the MiMi-0 detector in a cadmium (Cd) box with a 40° vertical opening in the same experimental channels. In general, it was found that in the northwest control rod lattice position the highest share of thermal neutrons is coming from the core center, while the opposite is observed in the periphery,

i.e., from the core reflector. Limitations in both the experimental setup and in the modeling with the two-step simulations were identified, opening up to the future improvement of both aspects to accurately measure the directionality dependency of the thermal neutron flux.

A unique experimental setup was installed in CROCUS to study the impact on the local thermal neutron flux of millimetric lateral displacements of U_{met} fuel rods. An updated version of the MiMi neutron detector prototype, called MiMi-1, was installed on one of the laterally moving U_{met} fuel rods, i.e., A2, of the COLIBRI fuel rods oscillator. Static measurements following the displacement of the instrumented rod (A2) and the adjacent one (B2) were achieved at core criticality. It was observed experimentally that a variation of the distance between U_{met} fuel rods has an effect of about +2.50 ± 0.01 %/mm of gap increase and -2.50 ± 0.01 %/mm of gap decrease, both with respect to the nominal U_{met} pitch size. These effects are caused by the changes in the water moderation in the region between the two rods. The comparison of the experimental data for the A2 rod displacements against full-core Serpent 2 criticality simulations performed with the ENFD/B-VIII.0 nuclear data library showed a good agreement within one to two standard deviations, although the ^{6}Li reaction rate was scored on smeared tally volumes. The agreement, further confirmed by preliminary simulations with variance reduction, provides as well an indication of the applicability of nuclear data libraries to the modeling of such localized phenomena.

The proven applicability of MiMi neutron detector technology for online in-core high-resolution neutronics experiments, their simple design, and their parallelization capabilities with advanced multi-channel processing electronics allowed their use for multiple simultaneous localized measurements in the CROCUS reactor. In this optic, a full-core 3D mapping system called SAFFRON was designed for the CROCUS zero-power reactor. The system distributes 149 MiMi detectors in three main axial layers (and two additional middle layers) of the CROCUS core at multiple inter-pin radial positions. A tailored mechanical structure was designed to support and hold in position the 149 MiMi neutron detectors in the CROCUS core. Eleven complementary detectors are available for adaptable positioning, e.g., core center.

The measurement of the absolute shape of the thermal flux map in CROCUS required the prior inter-calibration of the 160 MiMi detectors in a well-known neutron field. The detectors, inter-calibrated at 15 cm with a Pu-Be neutron source in CARROUSEL, showed variations in their relative sensitivity between -18.2 ± 0.2 % and +12.1 ± 0.2% with respect to the reference detector, caused by potential differences in the amount of sensitive material, in the detector mounting, and in the dedicated processing electronics.

The absolute shape of the thermal neutron flux map was measured in CROCUS with SAFFRON. It presented significant discrepancies for MiMi detectors at perfectly symmetrical radial locations in the core. The investigation of the causes behind these discrepancies highlighted that a shift in the photon density spectrum existed for some of the MiMi neutron detectors between the measuring conditions in CROCUS and in the inter-calibration with the Pu-Be neutron source. Although the reason for this spectral shift is yet to be understood, the comparison with full-core criticality Serpent 2 simulations showed that there is a relationship between the discrepancies in the C/E-1 results and the spectral shift. Indeed, the highest discrepancies between experimental and simulated results, in the order of +50% for both ENDF/B-VIII.0 and JEFF-3.1.1, corresponded to MiMi detectors with significant

spectral shifts. A criterion on the magnitude of the spectral shift was applied to select detectors that are usable for static flux map experiments, resulting in the selection of 23 MiMi detectors over the 149 installed.

The spectral shift in the majority of the MiMi neutron detectors of SAFFRON did not affect the capabilities of the system to measure relative variations of the thermal flux map between different configurations. In particular, the effect of the presence of a partially-inserted (215 mm from core bottom) highly-absorbing B_4C control rod on the shape of the flux map was investigated. A reduction in the count rate, and thus in the thermal neutron flux, of about -28% with respect to the critical configuration with water level was measured in the close proximity of the control rod guide tubes by the nearby MiMi detectors at 300 mm. In turn, a constant increase of the thermal neutron flux map was observed at distance from the local perturbation in the upper axial layers of SAFFRON. The effect, in the order of +16% for the L3 layer (at 85 cm), is caused by the upward shift of the neutron flux map deriving from the higher water level set for the core configuration with a control rod inserted. The local perturbations and the global upward shift are equivalent, within the range of uncertainties, for the critical configurations with the presence of the northwest or the southeast control rod.

Preliminary experimental results on the differences in the flux map between different power levels at criticality. In particular, an increase within +2% of the thermal neutron flux is observed when measuring at 2 mW with respect to 1.1W. These results possibly indicate the influence of the intrinsic ^{238}U neutron source of the fuel at low-power regimes. However, further investigations are needed to test the data trend with theoretical models and to exclude the presence of possible biases due to detectors' dead time. Finally, variations of the thermal neutron flux between different subcritical states of the CROCUS core were investigated. The subcritical flux map in CROCUS evolves upwards in the axial direction from being localized mostly at the bottom of the core, close to the Pu-Be start-up neutron source, at 910 ± 0.1 mm of water (-170 pcm), to approaching the critical flux shape at 950 ± 0.1 mm of water (-12 pcm).

7.1 Outlook

Further developments in the design and applications of the MiMi neutron detectors in CROCUS and in other facilities are foreseen in the next future.

Aside from the investigation of the reasons for the spectral shift of SAFFRON in CROCUS after the inter-calibration, different configurations of the MiMi front-end electronics are planned to be studied. The use of analog readout electronics turned out to be a steady, reliable, and versatile acquisition system for a low number of MiMi detectors, especially when used in coordination with conventional detectors and acquisition systems. Hence, further experimental campaigns in CROCUS are expected to still benefit from the reading of MiMi neutron detectors with analog readouts. For prospects requiring more channels and thus a digital readout, improvements in the processing electronics should be considered, including the addition of a temperature compensation module for the SiPM signal on the processing PCBs. Upgrades of the custom-built processing electronics would also allow the development of portable processing electronics modules for experimental campaigns at other reactor facilities.

In this same direction, a preliminary study to extend the operational range of operation of the MiMi neutron detectors was carried out in the framework of a Master's thesis at EPFL [123]. The study first showed that a reduction in the MiMi detector's active volume, or in the amount of its sensitive material, could extend its operational range to higher reactor fluxes. In addition, an alternative triggering method based on the amplitude of the SiPMs pre-amplified signals was tested to discriminate neutron events from the background. This method, or the use of the MiMi detectors in current or Campbell mode, would have the potential to reduce dead time limitations at higher fluxes. Although further investigations are needed, improving the counting capabilities of the MiMi detectors for higher flux ranges would allow performing high-resolution multi-physics experiments in power research reactors with thermal feedback. The immediate next step would consist in assessing the capabilities of the optical fibers and the scintillator material to withstand higher thermal neutron fluxes and adapting them accordingly while checking whether the associated signal processing is able to handle the change. Finally, the building of position-sensitive block arrays of MiMi neutron detectors is prospected to perform local mapping in space-dependent experiments and towards the development of full “neutron current detectors”.

On the side of experiments, a revision process of the high-resolution experiments performed in CROCUS is expected to be initiated with the intent to submit the experimental results to international benchmarks. In this optics, improvements in the design of the presented high resolutions experiments are in preparation, including the repetition of the measurements for the directionality of the neutron flux with a more appropriate aluminum holder and a redesigned Cd-covered box. From an analysis point of view, the experimental data were compared against the results of Serpent 2 Monte Carlo simulations with several limitations connected to the large computing power required to score localized tallies in full-core model geometries. Hence, the analysis of the high-resolution experimental data would benefit from the use of more advanced Monte Carlo methods with variance reduction, as was developed for other programs in CROCUS [115], and from the development of the high-fidelity GeN-Foam model of CROCUS [11].

Last but not least, SAFFRON opened up to the investigation of a wide range of space-dependent neutronics phenomena beyond the measuring of simple static flux maps. The spatialization of dynamic experiments, fission chain correlations, and induced neutron modulations are only examples of the potential capabilities and perspectives of SAFFRON. Measurements of the control rods' insertion or withdrawal were already attempted, but issues in the FPGA data transfer system made the results of such first tests inconclusive. An upgrade of the data transmission is currently ongoing. Modulation campaigns with COLIBRI and the PISTIL rotating absorber are foreseen for the coming year, and a Master thesis will be carried out in 2023 on correlation studies. Aside from the exploration of “exotic” reactor physics phenomena, SAFFRON would allow the validation of both 3D kinetics codes and the most recent theoretical development on the spatialization of neutron noise.

Bibliography

[1] International Atomic Energy Agency (IAEA), *Power Uprate in Nuclear Power Plants: Guidelines and Experience*. No. NP-T-3.9, Vienna, 2011.

[2] International Atomic Energy Agency (IAEA), *High Burnup Fuel: Implications and Operational Experience*. IAEA-TECDOC-1798, Vienna, 2016.

[3] International Atomic Energy Agency (IAEA), *Cost Drivers for the Assessment of Nuclear Power Plant Life Extension*. IAEA-TECDOC-1309, Vienna, 2002.

[4] J. G. Marques, "Review of Generation-III/III+ Fission Reactors," in *Nuclear Energy Encyclopedia*, S. B. Krivit, J. H. Lehr, and T. B. Kingery, Eds. Hoboken, NJ, USA: John Wiley & Sons, Inc., 2011, pp. 231–254.

[5] International Atomic Energy Agency (IAEA), *Water Chemistry and Clad Corrosion/Deposition Including Fuel Failures*. IAEA-TECDOC-CD-1692, Vienna, 2013.

[6] International Atomic Energy Agency (IAEA), "Structural behaviour of fuel assemblies for water cooled reactors," IAEA-TECDOC-1454, Vienna, 2005.

[7] M. Seidl, K. Kosowski, U. Schüler, and L. Belblidia, "Review of the historic neutron noise behavior in German KWU built PWRs," *Prog. Nucl. Energy*, vol. 85, pp. 668–675, Nov. 2015.

[8] U. Farinelli, "Nuclear Data and Integral Experiments in Reactor Physics." Comitato Nazionale per l'Energia Nucleare - RIT, Centro di Studi Nucleari, Casaccia (Rome), Italy.

[9] G. Bignan, P. Fougeras, P. Blaise, J.-P. Hudelot, and F. Mellier, "Reactor Physics Experiments on Zero Power Reactors," in *Handbook of Nuclear Engineering*, D. G. Cacuci, Ed. Boston, MA: Springer US, 2010, pp. 2053–2184.

[10] U. C. Bergmann and J. King, "TRITON11 - Westinghouse 11*11 BWR fuel design," in Proceedings of TOP FUEL 2016, Boise, ID, USA, 2016.

[11] T. Mager, M. Hursin, C. Fiorina, and A. Pautz, "Development of a High Fidelity Model of the CROCUS Experimental Reactor," in Proceedings of PHYSOR2022, Pittsburgh, PA, USA.

[12] G. F. Knoll, *Radiation Detection and Measurement*, 4th edition. John Wiley & Sons, Inc., 2010.

[13] J. J. Duderstadt and L. J. Hamilton, *Nuclear Reactor Analysis*. John Wiley & Sons, Inc., 1976.

[14] W. M. Stacey, *Nuclear Reactor Physics*, Second Edition, Completely Revised and Enlarged. WILEY-VCH Verlag GmbH & Co., 2007.

[15] J. C. Lee, *Nuclear reactor physics and engineering*. John Wiley & Sons, Inc, 2020.

[16] Y. Azmy and E. Sartori, *Nuclear Computational Science*. Springer Netherlands, 2010.

[17] A. K. Prinja and E. W. Larsen, "General Principles of Neutron Transport," in *Handbook of Nuclear Engineering*, D. G. Cacuci, Ed. 2010.

[18] D. Knott and A. Yamamoto, "Lattice Physics Computations," in *Handbook of Nuclear Engineering*, D. G. Cacuci, Ed. Boston, MA: Springer US, 2010, pp. 913–1239.

[19] A. Rais, "Performance assessment of a 3-D steady-state and spatial kinetics model for the CROCUS reactor," Ph.D. thesis, École polytechnique fédérale de Lausanne (EPFL), 2018.

[20] A. Hébert, *Applied Reactor Physics - Third Edition*. Presses internationales Polytechnique, 2020.

[21] C. J. Werner *et al.*, "MCNP Version 6.2 Release Notes," LA-UR--18-20808, 1419730, Feb. 2018.

[22] J. Leppänen, M. Pusa, T. Viitanen, V. Valtavirta, and T. Kaltiaisenaho, "The Serpent Monte Carlo code: Status, development and applications in 2013," *Ann. Nucl. Energy*, vol. 82, pp. 142–150, Aug. 2015.

[23] S. W. Mosher *et al.*, "ADVANTG An Automated Variance Reduction Parameter Generator," ORNL/TM-2013/416, 1105937, Nov. 2013.

[24] D. Rochman *et al.*, "Bowing effects on power and burn-up distributions for simplified full PWR and BWR cores," in Proceedings of M&C2017- International Conference on Mathematics & Computational Methods Applied to Nuclear Science & Engineering, Jeju, Korea, 2017.

[25] D. J. Walter, B. K. Kendrick, V. Petrov, A. Manera, B. Collins, and T. Downar, "Proof-of-principle of high-fidelity coupled CRUD deposition and cycle depletion simulation," *Ann. Nucl. Energy*, vol. 85, pp. 1152–1166, Nov. 2015.

[26] CASL, "The Consortium For Advanced Simulation Of Light Water Reactors (CASL)," *CASL*. https://casl.gov/

[27] MPACT team, "MPACT Theory Manual," Oak Ridge National Laboratory, CASL-U-2019-1874-001, 2019.

[28] MPACT team, "MPACT User Manual," Oak Ridge National Laboratory, CASL-U-1873-001, 2019.

[29] N. Choi, H. Park, H. G. Lee, S. Jae, S. Jeon, and H. G. Joo, "Recent capability and performance enhancements of the whole-core transport code nTRACER," *EPJ Web Conf.*, vol. 247, p. 06033, 2021.

[30] C. Fiorina, A. Pautz, and N. Paul Scherrer Institut PSI OST, 5232 (United States)], "Status and Ongoing Developments for the GeN-Foam Multi-Physics Solver," *Trans. Am. Nucl. Soc.*, vol. 115, Jul. 2016.

[31] D. A. Brown *et al.*, "ENDF/B-VIII.0: The 8th Major Release of the Nuclear Reaction Data Library with CIELO-project Cross Sections, New Standards and Thermal Scattering Data," *Nucl. Data Sheets*, vol. 148, pp. 1–142, Feb. 2018.

[32] F. H. Ruddy, A. R. Dulloo, J. G. Seidel, S. Seshadri, and L. B. Rowland, "Development of a silicon carbide radiation detector," *IEEE Trans. Nucl. Sci.*, vol. 45, no. 3, pp. 536–541, Jun. 1998.

[33] M. Hursin *et al.*, "Testing of a sCVD diamond detection system in the CROCUS reactor," *Eur. Phys. J. A*, vol. 54, no. 5, p. 82, May 2018.

[34] International Atomic Energy Agency (IAEA), *Modern Neutron Detection: proceedings of a technical meeting*. IAEA-TECDOC-1935, Vienna, 2021.

[35] J. R. Lakowicz, *Principles of fluorescence spectroscopy*, 3rd ed. New York: Springer, 2006.

[36] R. Stedman, "Scintillator for Thermal Neutrons using Li ^{6}F and ZnS (Ag)," *Rev. Sci. Instrum.*, vol. 31, no. 10, pp. 1156–1156, Oct. 1960.

[37] R. T. Kouzes *et al.*, "Neutron detection alternatives to 3He for national security applications," *Nucl. Instrum. Methods Phys. Res. Sect. Accel. Spectrometers Detect. Assoc. Equip.*, vol. 623, no. 3, pp. 1035–1045, Nov. 2010.

[38] T. Nakamura *et al.*, "A time-of-flight neutron imaging detector using ZnS/6LiF scintillator and wavelength shifting fibers with high spatial resolution and with low gamma-ray sensitivity," in *2014 IEEE Nuclear Science Symposium and Medical Imaging Conference (NSS/MIC)*, Seattle, WA, USA, Nov. 2014, pp. 1–3.

[39] N. J. Rhodes, A. G. Wardle, A. J. Boram, and M. W. Johnson, "Pixelated neutron scintillation detectors using fibre optic coded arrays," *Nucl. Instrum. Methods Phys. Res. Sect. Accel. Spectrometers Detect. Assoc. Equip.*, vol. 392, no. 1–3, pp. 315–318, Jun. 1997.

[40] C. Mori *et al.*, "Simple and Quick Measurement of Neutron Flux Distribution by Using an Optical Fiber with Scintillator," *J. Nucl. Sci. Technol.*, vol. 31, no. 3, pp. 248–249, Mar. 1994.

[41] T. Nakamura *et al.*, "Development of a ZnS/$^{10}B_2O_3$ scintillator with low-afterglow phosphor," *J. Phys. Conf. Ser.*, vol. 528, p. 012043, Jul. 2014.

[42] Hamamatsu Photonics K.K., "S13360-3050PE," *www.hamamatsu.com*. https://www.hamamatsu.com/eu/en/product/optical-sensors/mppc/mppc_mppc-array/S13360-3050PE.html

[43] Y. Musienko, D. Renker, S. Reucroft, R. Scheuermann, A. Stoykov, and J. Swain, "Radiation damage studies of multipixel Geiger-mode avalanche photodiodes," *Nucl. Instrum. Methods Phys. Res. Sect. Accel. Spectrometers Detect. Assoc. Equip.*, vol. 581, no. 1–2, pp. 433–437, Oct. 2007.

[44] K. Macku *et al.*, "Radial and Azimuthal ^{235}U Fission and ^{238}U Capture Distributions in BWR UO_2 Pins: CASMO-4 and MCNP4C versus Activation Foil Measurements," *Nucl. Sci. Eng.*, vol. 155, no. 1, pp. 96–101, Jan. 2007.

[45] K. Yoshioka, T. Kitada, and Y. Nagaya, "Azimuthal flux distribution measurements around fuel rods in reduced-moderation LWR lattices," *Prog. Nucl. Energy*, vol. 82, pp. 7–15, Jul. 2015.

[46] M. F. Murphy, M. Plaschy, F. Jatuff, U. Bergmann, and R. Chawla, "Fission and capture rate measurements in a SVEA-96 OPTIMA2 BWR assembly compared with MCNPX predictions," in Proceedings of PHYSOR2006, Vancouver, BC, Canada, 2006.

[47] T. J. Downar *et al.*, "PARCS: Purdue advanced reactor core simulator," in Proceedings of PHYSOR2002, Seoul, Korea, 2002.

[48] Y. Yamane, A. Uritani, T. Misawa, J. K.-H. Karlsson, and I. Pázsit, "Measurement of the thermal and fast neutron flux in a research reactor with a Li and Th loaded optical fibre detector," *Nucl. Instrum. Methods Phys. Res. Sect. Accel. Spectrometers Detect. Assoc. Equip.*, vol. 432, no. 2–3, pp. 403–409, Aug. 1999.

[49] T. Yagi, T. Misawa, C. H. Pyeon, and S. Shiroya, "A small high sensitivity neutron detector using a wavelength shifting fiber," *Appl. Radiat. Isot.*, vol. 69, no. 1, pp. 176–179, Jan. 2011.

[50] M. Pfeiffer and S. Sala, "EPR reactor neutron instrumentation," presented at the 2013 3rd International Conference on Advancements in Nuclear Instrumentation, Measurement Methods and their Applications (ANIMMA), in Proceedings of ANIMMA2013, Marseille, France, Jun. 2013.

[51] V. I. Mitin *et al.*, "Advanced In-core Monitoring System for High-power Reactors," presented at the 16th Symposium of AER on VVER Reactor Physics and Reactor Safety, in Proceedings of 16th Symposium of AER on VVER Reactor Physics and Reactor Safety, Bratislava, Slovakia, 2006.

[52] V. Lamirand, "Installation nucléaire CROCUS - Rapport de sécurité," Techical report RT-100-104-17-48, 2017.

[53] Nuclear Energy Agency (NEA), "IRPhE Handbook 2020." International Reactor Physics Evaluation Project Handbook (database), 2020.

[54] V. Lamirand, A. Laureau, O. Pakari, P. Frajtag, and A. Pautz, "Power calibration methodology at the CROCUS reactor," *EPJ Web Conf.*, vol. 225, p. 04022, 2020.

[55] O. V. Pakari, "Experimental and numerical study of stochastic branching noise in nuclear reactors," École polytechnique fédérale de Lausanne (EPFL), Lausanne, 2020.

[56] V. Lamirand *et al.*, "The COLIBRI experimental program in the CROCUS reactor: characterization of the fuel rods oscillator," *EPJ Web Conf.*, vol. 225, p. 04020, 2020.

[57] V. Lamirand *et al.*, "Experimental report of the 1st campaign at AKR-2 and CROCUS," COR-TEX-D2.1, 2018.

[58] V. Lamirand *et al.*, "Experimental report of the 2nd campaign at AKR-2 and CROCUS," CORTEX - D2.2, 2021.

[59] V. Lamirand, A. Knospe, K. Ambrožič, F. Vitullo, and C. Lange, "Experimental report of the 3rd campaign at AKR-2 and CROCUS," CORTEX - D2.4, 2021.

[60] V. Lamirand *et al.*, "Analysis of the first COLIBRI fuel rods oscillation campaign in the CROCUS reactor for the European project CORTEX," in *EPJ Web of Conferences*, 2021, vol. 247, p. 21010.

[61] F. Vitullo *et al.*, "Developing and testing a miniature fiber-coupled scintillator for in-core neutron counting in CROCUS," in *EPJ Web Conferences*, 2020, vol. 225.

[62] F. Vitullo *et al.*, "A mm^3 Fiber-Coupled Scintillator for In-Core Thermal Neutron Detection in CROCUS," *IEEE Trans. Nucl. Sci.*, vol. 67, no. 4, pp. 625–635, Apr. 2020.

[63] F. Vitullo *et al.*, "Design of a 150-miniature detectors 3D core-mapping system for the CROCUS reactor," *EPJ Web Conf.*, vol. 253, 2021.

[64] J. H. Ely *et al.*, "Final Technical Report for the Neutron Detection without Helium-3 Project," PNNL-23011, 1115838, Nov. 2013.

[65] J.-B. Mosset, A. Stoykov, V. Davydov, M. Hildebrandt, H. Van Swygenhoven, and W. Wagner, "Upgrade of the POLDI diffractometer with a ZnS(Ag)/ ^{6} LiF scintillation detector read out with WLS fibers coupled to SiPMs," *J. Phys. Conf. Ser.*, vol. 528, p. 012041, Jul. 2014.

[66] A. Stoykov, J.-B. Mosset, U. Greuter, M. Hildebrandt, and N. Schlumpf, "A SiPM-based ZnS:6LiF scintillation neutron detector," *Nucl. Instrum. Methods Phys. Res. Sect. Accel. Spectrometers Detect. Assoc. Equip.*, vol. 787, pp. 361–366, Jul. 2015.

[67] M. Hildebrandt, A. Stoykov, J.-B. Mosset, U. Greuter, and N. Schlumpf, "Detection of thermal neutrons using ZnS(Ag):6LiF neutron scintillator read out with WLS fibers and SiPMs," *Nucl. Instrum. Methods Phys. Res. Sect. Accel. Spectrometers Detect. Assoc. Equip.*, vol. 824, pp. 204–207, Jul. 2016.

[68] A. Stoykov, J.-B. Mosset, and M. Hildebrandt, "Trigger Efficiency of a ZnS: ^{6} LiF Scintillation Neutron Detector Readout With a SiPM," *IEEE Trans. Nucl. Sci.*, vol. 63, no. 4, pp. 2271–2277, Aug. 2016.

[69] J.-B. Mosset *et al.*, "A 16-ch module for thermal neutron detection using ZnS:6LiF scintillator with embedded WLS fibers coupled to SiPMs and its dedicated readout electronics," *Nucl. Instrum. Methods Phys. Res. Sect. Accel. Spectrometers Detect. Assoc. Equip.*, vol. 845, pp. 494–498, Feb. 2017.

[70] A. Wolfertz, R. Adams, and G. Perret, "First tests of a gamma-blind fast neutron detector using a ZnS:Ag-epoxy mixture cast around wavelength-shifting fibers," *Nucl. Instrum. Methods Phys. Res. Sect. Accel. Spectrometers Detect. Assoc. Equip.*, vol. 971, p. 164003, Aug. 2020.

[71] J.-B. Mosset, A. Stoykov, U. Greuter, M. Hildebrandt, and N. Schlumpf, “Digital signal processing for a thermal neutron detector using ZnS(Ag):6LiF scintillating layers read out with WLS fibers and SiPMs,” *Nucl. Instrum. Methods Phys. Res. Sect. Accel. Spectrometers Detect. Assoc. Equip.*, vol. 824, pp. 319–321, 2016.

[72] Scintacor, “Neutron screens,” 2020. [Online]. Available: https://scintacor.com/wp-content/uploads/2015/09/Datasheet-Neutron-Screens-High-Res.pdf

[73] C. W. E. van Eijk, “Inorganic scintillators for thermal neutron detection,” *Radiat. Meas.*, vol. 38, no. 4–6, pp. 337–342, Aug. 2004.

[74] Saint-Gobain Crystals, “BC-630 SILICONE GREASE - MATERIAL SAFETY DATA SHEET.” 2005.

[75] Mitsubishi Chemical Co., “ESKA SH8001 data sheet.” 2019. [Online]. Available: https://i-fiberoptics.com/pdf/sh-8001.pdf

[76] Hamamatsu Photonics K.K., “MPPC S13360 sereis datasheet.” 2016. [Online]. Available: https://www.hamamatsu.com/content/dam/hamamatsu-photonics/sites/documents/99_SALES_LIBRARY/ssd/s13360_series_kapd1052e.pdf

[77] A. Ghassemi, K. Sato, and K. Kobayashi, “MPPC.” HAMAMATSU PHOTONICS K.K., 2021. [Online]. Available: https://www.hamamatsu.com/content/dam/hamamatsu-photonics/sites/documents/99_SALES_LIBRARY/ssd/mppc_kapd9005e.pdf

[78] CAEN, “CAEN N84 - Technical Information Manual.” 1991. [Online]. Available: https://wwwusers.ts.infn.it/~rui/univ/Acquisizione_Dati/Manuals/CAEN%20N84.pdf

[79] CANBERRA, “Model 2022 Spectroscopy Amplifier.” 2010. [Online]. Available: https://www3.nd.edu/~wzech/Model-2022-SS-M3833.pdf

[80] TELEDYNE LECROY, “WaveSurfer 10 Oscilloscopes.” 2015. [Online]. Available: https://cdn.teledynelecroy.com/files/pdf/wavesurfer10-datasheet.pdf

[81] ORTEC, “926-M32-USB Multichannel Analyzer.” [Online]. Available: https://www2.pd.infn.it/elettronica/Strumenti/926-m32-usb.pdf

[82] CANBERRA, “Single Channel Analyzer Model 2030.” 1976. [Online]. Available: http://www.nuclearphysicslab.com/npl/wp-content/uploads/canberra_2030_Single_Channel_Amplifier.pdf

[83] NUMEC-USA, “Shipping document Pu-Be source.” 1961.

[84] L. Stewart, “Neutron Spectrum and Absolute Yield of a Plutonium-Beryllium Source,” *Phys. Rev.*, vol. 98, no. 3, pp. 740–743, May 1955.

[85] M. E. Anderson and W. H. Bond, “Neutron spectrum of a plutonium-beryllium source,” *Nucl. Phys.*, vol. 43, pp. 330–338, May 1963.

[86] E. L. Brunetto, “Validation of the Serpent 2 model for the CARROUSEL facility,” École polytechnique fédérale de Lausanne (EPFL), Semester project, 2020.

[87] ORTEC, “MAESTRO®-32 v6.08 - MCA Emulation Software.” [Online]. Available: http://lab3ct.altervista.org/Manuale_Software_MAESTRO32.pdf

[88] P.-A. Haldy *et al.*, “Experimental Program at the LOTUS Facility,” *Fusion Technol.*, vol. 10, no. 3P2A, pp. 931–939, Nov. 1986.

[89] Hopewell Designs Inc., “Operation Maintenance Manual for Model 10-1-2600-10Co Gamma Beam Irradiator.” 2015.

[90] V. Lamirand, “Plan de radioprotection pour l’utilisation de l’irradiateur gamma dans la cavité LOTUS,” Laboratory for Reactor Physics and Systems Behaviour, École polytechnique fédérale de Lausanne, Lausanne, Switzerland, RE-100-106-15-43, 2015.

[91] J. Leppänen, T. Kaltiaisenaho, V. Valtavirta, and M. Metsälä, “Development of a coupled neutron/photon transport mode in the Serpent 2 Monte Carlo code,” in Proceedings of M&C2017-International Conference on Mathematics & Computational Methods Applied to Nuclear Science & Engineering, Jeju, Korea, 2017.

[92] O. Pakari *et al.*, “Design and Simulation of Gamma Spectrometry Experiments in the CROCUS Reactor,” *EPJ Web Conf.*, vol. 225, p. 04016, 2020.

[93] M. B. Chadwick *et al.*, “ENDF/B-VII.0: Next Generation Evaluated Nuclear Data Library for Nuclear Science and Technology,” *Nucl. Data Sheets*, vol. 107, no. 12, pp. 2931–3060, Dec. 2006.

[94] T. Mager, O. Pakari, V. Lamirand, and A. Pautz, “The LEAF system and gamma detection applications in CROCUS,” Master’s thesis in Nuclear Engineering, Grenoble INP Phelma, Dept. Nucl. Eng Politecnico di Torino, École polytechnique fédérale de Lausanne (EPFL), 2020.

[95] G. Gilmore, *Practical gamma-ray spectroscopy*. Chichester: Wiley, 2008.

[96] G. Perret, G. Girardin, P. Frajtag, and M. Hursin, “Decay constant and delayed neutron fraction measurements in CROCUS,” Paul Scherrer Institut, Villigen, Switzerland, TM-41-14-02, Rev. 1, 2014.

[97] E. L. Brunetto, “Measurements and Monte Carlo simulations with miniature neutron detectors for flux characterization in the SUR-100 zero power reactor,” Master’s thesis in Nuclear Engineering, Politecnico di Torino and École polytechnique fédérale de Lausanne (EPFL), 2020.

[98] Texas Instruments, “OPA859 Datasheet.” 2018.

[99] Texas Instruments, “LMH7220 Datasheet.” 2013.

[100] CAEN, “V2495/VX2495 VME Programmable Logic Unit.” 2019.

[101] CAEN, “PLUscaler_DAQ DT5495-V2495,” *https://www.caen.it/download/?filter=V2495*.

[102] Memmert Gmbh, “DS_Memmert Peltier-cooled incubator IPP750eco.” [Online]. Available: https://www.memmert.com/products/incubators/peltier-cooled-incubator/IPP750eco/

[103] CAEN, “V1718/VX1718 - VME - USB 2.0 Bridges.” 2020.

[104] Mitsubishi Chemical Co., “ESKA optical fibers.” https://www.pofeska.com/pofeskae/product/02/index.html

[105] F. Vitullo, V. Lamirand, P. Frajtag, G. Perret, and A. Pautz, “Highly localized azimuthal measurements in the CROCUS reactor towards the validation of high-fidelity neutronics codes,” in *EPJ Web of Conferences*, 2021, vol. 247, p. 08014.

[106] F. Vitullo *et al.*, “Millimetric fuel rod displacements: an experimental study of the impact on local thermal neutron flux in the CROCUS reactor,” in Proceedings of PHYSOR2022, Pittsburgh, PA, USA, 2022.

[107] V. Radulovic *et al.*, “Multi-step Monte Carlo calculations applied to nuclear reactor instrumentation — Source definition and renormalization to physical values,” in *2015 4th International Conference on Advancements in Nuclear Instrumentation Measurement Methods and their Applications (ANIMMA)*, Lisbon, Apr. 2015, pp. 1–6.

[108] V. Verma, D. Chionis, A. Dokhane, and H. Ferroukhi, “Modelling and Analysis of Fuel Assembly Vibrational Modes in PWRs using SIMULATE-3K,” *EPJ Web Conf.*, vol. 247, p. 21008, 2021.

[109] A. Vidal-Ferràndiz *et al.*, “Modelling and simulations of reactor neutron noise induced by mechanical vibrations,” *Ann. Nucl. Energy*, vol. 177, p. 109300, Nov. 2022.

[110] P. Lindén, J. K.-H. Karlsson, B. Dahl, I. Pázsit, and G. Por, “Localisation of a neutron source using measurements and calculation of the neutron flux and its gradient,” *Nucl. Instrum. Methods Phys. Res. Sect. Accel. Spectrometers Detect. Assoc. Equip.*, vol. 438, no. 2–3, pp. 345–355, Dec. 1999.

[111] S. Avdic, P. Lindén, and I. Pázsit, “Measurement of the neutron current and its use for the localisation of a neutron source,” *Nucl. Instrum. Methods Phys. Res. Sect. Accel. Spectrometers Detect. Assoc. Equip.*, vol. 457, no. 3, pp. 607–616, Jan. 2001.

[112] P. V. Uffelen, R. J. M. Konings, C. Vitanza, and J. Tulenko, “Analysis of Reactor Fuel Rod Behavior,” in *Handbook of Nuclear Engineering*, D. G. Cacuci, Ed. Boston, MA: Springer US, 2010, pp. 1519–1627.

[113] OECD/NEA Data Bank, “The JEFF-3.1.1 Nuclear Data Library,” JEFF Report 22, 2009.

[114] A. J. M. Plompen *et al.*, “The joint evaluated fission and fusion nuclear data library, JEFF-3.3,” *Eur. Phys. J. A*, vol. 56, no. 7, p. 181, Jul. 2020.

[115] A. Laureau, V. Lamirand, D. Rochman, and A. Pautz, “Uncertainty propagation for the design study of the PETALE experimental programme in the CROCUS reactor,” *EPJ Nucl. Sci. Technol.*, vol. 6, p. 9, 2020.

[116] L. S. Waters, “MCNPX User’s Manual, Version 2.4.0,” Los Alamos National Laboratory, LA-CP-02-408, Sep. 2002.

[117] V. Lamirand, F. Vitullo, K. Ambrožič, O. Pakari, L. Braun, and D. Godat, “Report on the development of fibre-based scintillator,” CORTEX-D2.3, 2021.

[118] OECD/NEA Data Bank, “The JEFF-3.1 nuclear data library,” JEFF report 21, 2006.

[119] M. B. Chadwick *et al.*, “ENDF/B-VII.1 Nuclear Data for Science and Technology: Cross Sections, Covariances, Fission Product Yields and Decay Data,” *Nucl. Data Sheets*, vol. 112, no. 12, pp. 2887–2996, Dec. 2011.

[120] Y. Jiang *et al.*, “PISTIL, a reactivity modulation device to probe the transfer function of the nuclear reactor CROCUS,” *EPJ Web Conf.*, vol. 253, p. 04007, 2021.

[121] D. F. Shook, R. L. Alexander, D. Bogart, and M. Krueger, “Ages of plutonium-beryllium neutrons in tungsten-water media,” National Aeronautics And Space Administration, Washington, D.C., NASA TN D-3695, 1966.

[122] E. Dumonteil *et al.*, “Patchy nuclear chain reactions,” *Commun. Phys.*, vol. 4, no. 1, p. 151, Dec. 2021.

[123] C. Rochat, “Extension of miniature neutron scintillators features in CROCUS: novel acquisition scheme and extended flux range,” Master’s thesis in Physics, École polytechnique fédérale de Lausanne (EPFL), 2021.

[124] E. L. Brunetto *et al.*, “High resolution measurements with miniature neutron scintillators in the SUR-100 zero power reactor,” *EPJ Web Conf.*, vol. 253, p. 04029, 2021.

Appendix A

SUR-100 experimental campaign

In the framework of a collaboration between LRS at EPFL and the Institut für Kernenergetik und Energiesysteme (IKE) of the University of Stuttgart, high spatial resolution experiments with MiMi neutron detectors are performed to characterize the thermal neutron flux distribution inside experimental channels of the SUR-100 zero-power reactor. The experimental results are compared with Serpent 2 Monte Carlo simulations. The experimental and computational results presented in this Appendix were the object of a Master's thesis performed at LRS [97] and of a conference publication [124].

A.1 The SUR-100 reactor

The Siemens Training Reactor SUR-100, in Figure A.1, is a thermal zero-power reactor used mainly for educational purposes, built in 1964 and located at the University of Stuttgart. The reactor has a maximum thermal power output of 1 W, with a nominal power of 100 mW. The homogenous core is composed of solid cylindrical slabs of moderator with fuel particles dispersed inside. The core is provided with a lifting mechanism moving the lower core section axially with respect to the upper one. The core halves are separated for the shutdown and brought together for the startup of the reactor. The reactivity regulation is performed with two cadmium control plates, which are steered into the core from below. The reactor is provided with various experimental channels, which allow the insertion of nuclear instrumentation into the core or in its proximity.

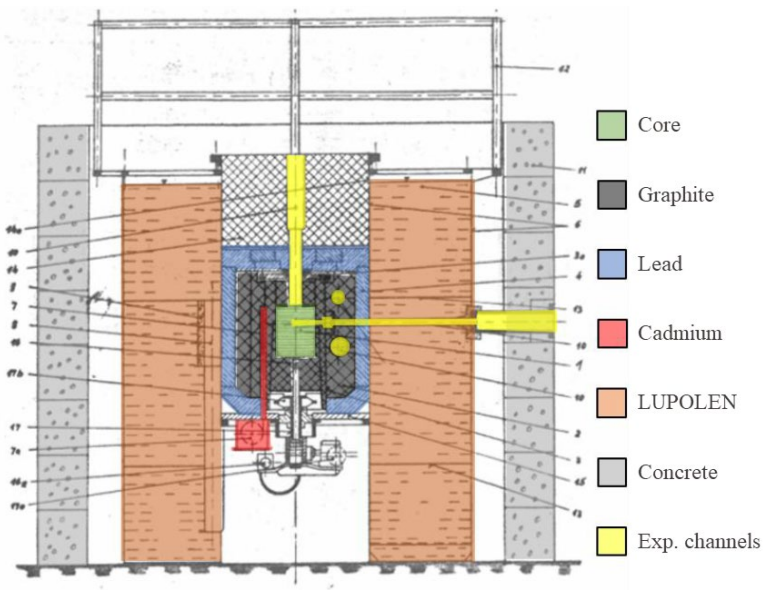

Figure A.1 – Scheme of the SUR-100 reactor design.

A.2 Experimental setup

Three MiMi-1 neutron detectors are used for the SUR-100 experimental campaign. An aluminum holder housing the three detectors' tips is manufactured at a diameter of 26 mm, corresponding to the internal diameter of the experimental channel I. Given the difference in diameter of the experimental channels, the diameter of the holding tube has the possibility to be adapted to a larger diameter (54 mm) by means of aluminum spacer rings. To move the detectors along the experimental channels, the front-end holder is mechanically coupled to an aluminum tube manufactured by the IKE laboratory, which is graduated to select the detectors' position inside the channels. The tube's handle allowed to adjust the angular orientation of the detectors inside the experimental channels. The choice of aluminum for the holding equipment is given by its small influence on thermal neutron flux, its availability, its low neutron absorption cross-section, and fast decay of the induced activity.

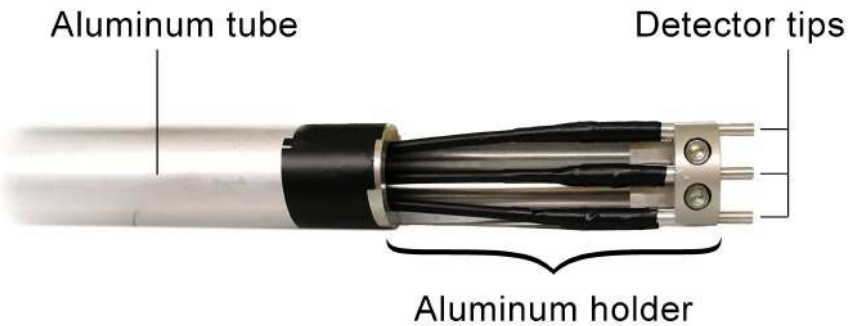

Figure A.2 – Aluminum positioner used for the experimental campaign in SUR 100.

Steady-state measurements with the three MiMi-1 detectors were carried out during the campaign to characterize the thermal flux, namely to measure thermal neutron flux profiles:

- along the central experimental channel I: [-40,+40] cm around the core center,
- along the tangential channel II: [-8,+46] cm around the core center,
- across the diameter of both channels I (vertically) and II (horizontally).

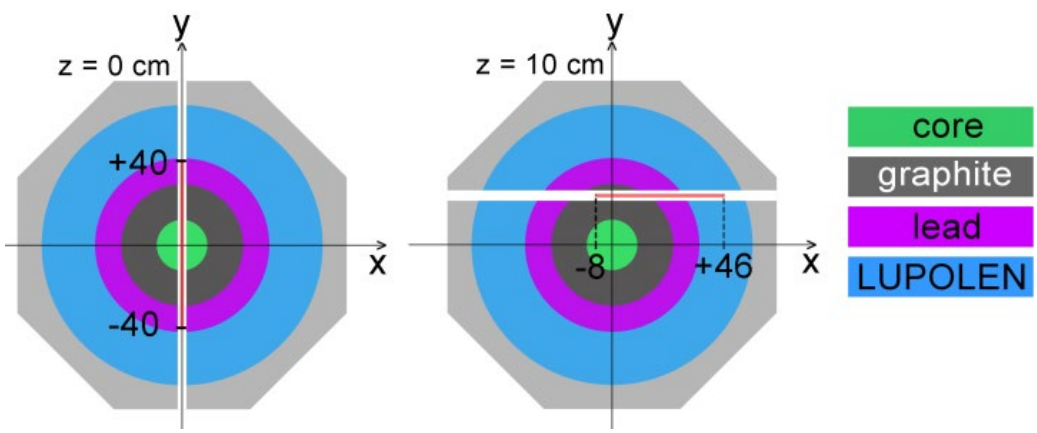

Figure A.3 – Simplified schemes of the profile measurements inside channel I (left) and channel II (right). The red lines indicate the spatial range in which measurements are performed.

An explanatory scheme of the performed measurements is presented in Figure A.3. The number of detectors used varied according to the needs of each experiment. In most of the experiments, one MiMi-1 detector is removed from the holder and used for power monitoring. Count rates were recorded at each position for the time necessary to have statistical errors in the order of 0.1%.

A.3 Experimental and simulation results

The neutron thermal flux profile is measured along central channel I. The results of the measurements are shown in Figure A.4. The count rates are normalized twice: first by the monitor MiMi, then by the maximum measured value. The profile is symmetric with respect to the core center, given the overall agreement of the data measured on each side of the core. A slight difference is found to exist between the points lying in the interval from 20 to 28 cm far from the core center, with a disagreement in the order of 10 %.

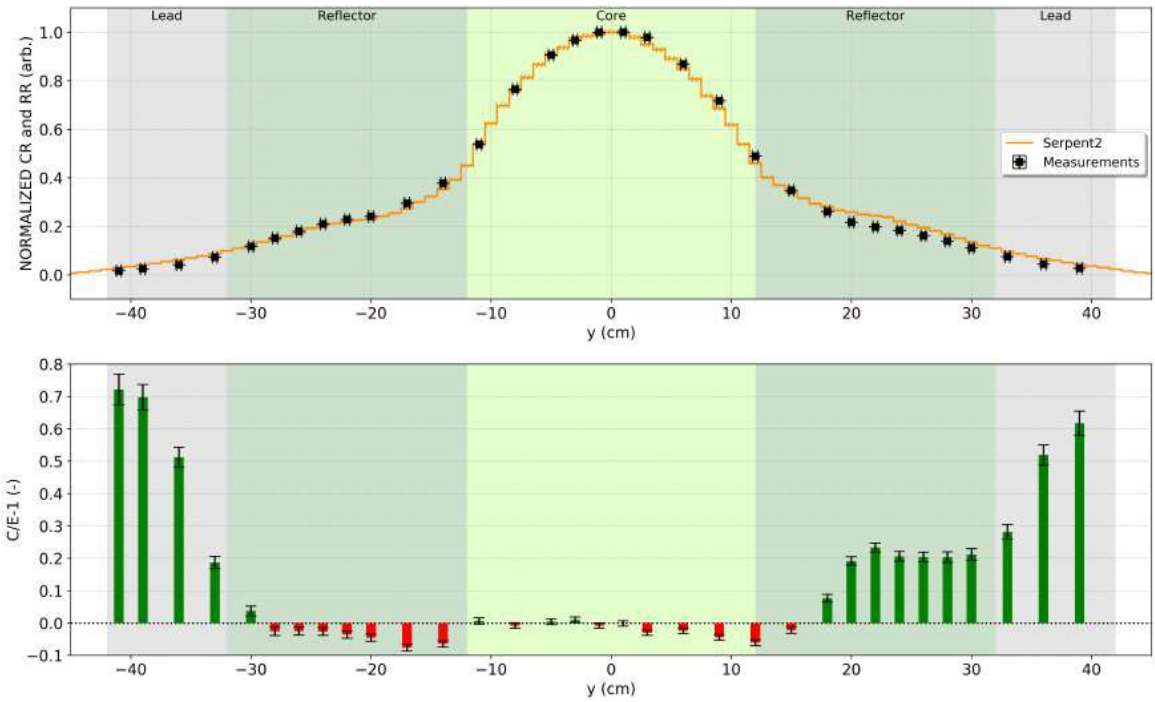

Figure A.4 – Comparison of normalized experimental count rates against ^{6}Li reaction rates estimations with Serpent 2 along experimental channel I (top) and observed discrepancies (bottom).

The measured data are then compared with computational results obtained with Serpent 2 model. The real configuration of the reactor (i.e., power level, control plates position, and filling of experimental channels) at the time of measurement is implemented in the computational model in order to reproduce the experiments as faithfully as possible. Cylindrical virtual detectors with the same radius of the channel (26 mm) and a thickness of 1 cm are used to score the neutrons reaction rate with ^{6}Li in every cm of the experimental channel in the range [-45;45] cm. The modeling of real-size detectors, given the miniature dimensions of the scintillators, was deemed to be unnecessary for the scope of the work at hand. However, the smearing of the detectors is expected to introduce a discrepancy with the measured data since the Monte Carlo results are in this way averaged on larger volumes. A

depiction of the comparison of experimental and simulated data is also given in Figure A.4 as well as the C/E-1 estimates.

The experimental results are seen to be particularly in agreement with the simulated data in the spatial range [-30,18] cm, with a C/E-1 value lower than 10 %. It is worth noting that this overall good agreement proves the negligible neutron flux perturbation induced by the miniature detectors, not modeled for the computational simulation.

An asymmetry in the radial profile is found in the zone of the graphite reflector between +20 and +30 cm away from the core, and it is not foreseen by the simulations. This discrepancy, which causes a disagreement of about 20 %, could be caused by a localized change in material composition or some geometric asymmetry not considered in the computational model. Further away from the core center, a higher discrepancy is found to exist symmetrically from 30 to 40 cm, with a C/E-1 value that reaches about 70 %. Given the presence of the lead shielding in the zone of highest disagreement, such a discrepancy could be motivated by the uncertainties in material composition or in its cross-section. Since the data series are normalized for their maximum value (which is located in the core center), the disagreement observed could not necessarily be attributed to the peripheral zones and, therefore, to the lead shielding region. Nevertheless, the main suspicions fall on the lead shielding area, as it is mechanically and chemically less known than the core central region.

Similar to the central channel I, thermal neutron flux distribution along the upper tangential channel is characterized. No experimental data on the flux distribution was available beforehand due to the difficulties of performing activation measurements in a region too far from the core center. The experimental results are shown in Figure A.5, together with a comparison against simulated data. For

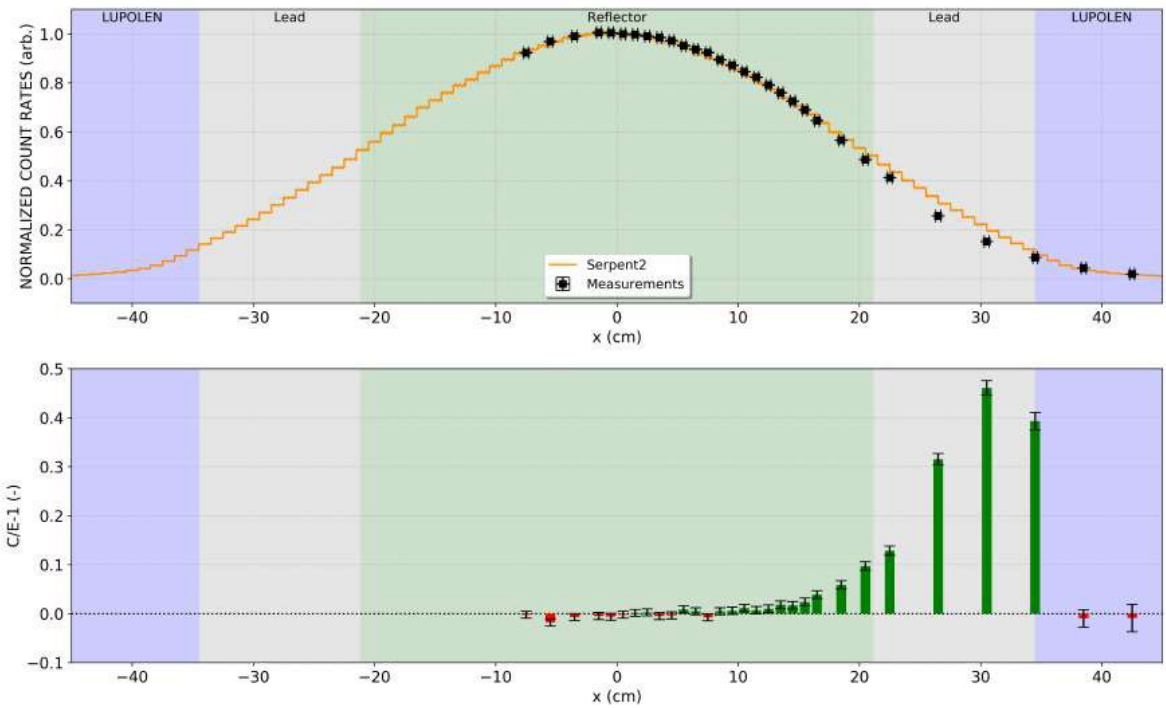

Figure A.5 – Comparison between experimental and simulated results for the thermal neutron flux distribution in tangential channel II (top) and discrepancies with simulations (bottom).

the Serpent 2 simulation, virtual track-length detectors with a cylindrical dimension as big as the channel (54 mm diameter) are used to characterize the thermal flux profile.

The experimental results show excellent agreement with most of the simulated points, except for the data lying in the interval [20;35] cm, where the disagreement reaches values of about 50 %. Again, the discrepancy is localized in the zone occupied by the lead shielding, which might have substantial differences in composition with respect to the modeled one.

The gradient in both channel I and channel II is measured by the rotation of 180° of the aluminum holder, switching the detectors' positions. Experimental results show the absence of a vertical gradient in channel I, being the reaction rate distribution almost flat in the core center. However, for the tangential channel II, the existence of a horizontal gradient of (9.09±0.20) % from the innermost to the outermost radial position is measured with the MiMi-1 neutron detectors.